2013

Experimental and Computational Assessment of Mechanical Circulatory Assistance of a Patient-Specific Fontan Vessel Configuration

Steven Chopski
Virginia Commonwealth University

Experimental and Computational Assessment of Mechanical Circulatory Assistance of a Patient-Specific Fontan Vessel Configuration

A dissertation submitted in partial fulfillment of the requirements for the degree of Doctor of Philosophy in Engineering at Virginia Commonwealth University.

by

STEVEN GABRIEL CHOPSKI
B.S. in Biomedical Engineering, Virginia Commonwealth University, 2008
M.S. in Mechanical Engineering, Virginia Commonwealth University, 2010

Director: Dr. Karla M. Mossi, Ph.D.
Co-Advisor, Mechanical and Nuclear Engineering

Dr. Amy L. Throckmorton, Ph.D.
Co-Advisor, Mechanical and Nuclear Engineering

Virginia Commonwealth University
Richmond, Virginia

October 2013

School of Engineering

Virginia Commonwealth University

This is to certify that the dissertation prepared by Steven Gabriel Chopski entitled "Experimental and Computational Assessment of Mechanical Assistance of a Patient-Specific Fontan Vessel Configuration" has been approved by his committee as satisfactory completion of the requirement for the degree of Doctor of Philosophy in Engineering

Dr. Karla M. Mossi, Ph.D., Co-Advisor and Associate Professor, Mechanical and Nuclear Engineering, VCU School of Engineering, Committee Chair

Dr. Amy L. Throckmorton, Ph.D., Co-Advisor and Associate Professor, Mechanical and Nuclear Engineering, VCU School of Engineering

Dr. William Moskowitz, M.D., Chairman, Division of Pediatric Cardiology, VCU School of Medicine

Dr. Mohamed Gad-el-Hak, Ph.D., Professor, Mechanical and Nuclear Engineering, VCU School of Engineering

Dr. Ramana M. Pidaparti, Ph.D., Associate Professor, Mechanical and Nuclear Engineering, VCU School of Engineering

Dr. Steven W. Day, Ph.D., Associate Professor, Mechanical Engineering, Kate Gleason College of Engineering, Rochester Institute of Technology

Dr. Gary L. Tepper, Ph.D., Professor, Department Chair, Mechanical and Nuclear Engineering, VCU School of Engineering

Dr. Barbara D. Boyan, Ph.D., Dean of the VCU School of Engineering

Dr. F. Douglas Boudinot, Dean of the VCU School of Graduate Studies

Date: October 2013

Signatures on file in the VCU Graduate School

Acknowledgement

When I started my college career, oh so many years ago, I never dreamed that I would end up with a Doctor of Philosophy degree in Engineering, Mechanical Engineering, no less. So with this dissertation, I would like to thank the following people who helped make this doctoral work possible. A big thank you goes to Dr. Amy Throckmorton, for all that you have ever done for me. I never could have done it without you. I would like to thank the U.S. Department of Education GAANN fellowship program for financial support. I would also like to thank the Dynamic Duo, Allison Bell and Courtney Culbreth, who helped me with the logistics and administrative issues that are involved in a large project. A special thank you goes to the staff of the MNE machine shop whose combined experience in machining helped to make the experimental side of this dissertation project possible. I thank my family for their love and support. Thank you as well to all of my dear friends for supporting me in this endeavor.

I would like to thank my good friends Ross and Amanda Walenga, Dale Farkas, Michael Sciolino, Landon Holbrook, Carson Fox, and Dhyaa Kafagy. In addition, I would like to thank my fellow mechanical engineers Jessica Nowak, Jason Teichert, James Carr, Jordan Brown, Jonathan Welch and Steve Hill, for lending a helping hand when I needed it. A special thank you goes to Owen Rangus for his creative insight in software development using MATLAB. Also, I would like to thank Dr. William Moskowitz for his guidance in the continued development of the cavopulmonary assist device and his unsurpassed knowledge of pediatric cardiology, particularly in Fontan physiology. I would like to thank Dr. Emily Downs for her diverse medical knowledge and her skills at performing medical modeling. I thank you all for helping me at various stages in this tough endeavor it has truly been a wonderful journey.

Table of Contents

xi

<u>List of Tables</u>

Page

List of Figures

List of Abbreviations

2-D	two-dimensional
3-D	three-dimensional
δt	delta time or delta 't'
BPM	Beats per minute
BT	Blalock-Tussig Shunt
CAD	Computer Aided Drafting
CCD	Charged Coupled Device
CFD	Computational Fluid Dynamics
CO	Cardiac Output
DNS	Direct Numerical Simulation
ECMO	Extracorporeal Membrane Oxygenation
FEM	Finite Element Methods
FVM	Finite Volume Methods
FFT	Fast Fourier Transforms
IVC	Inferior Vena Cava
k-ε	k-ε turbulence model
k-ω	k-ω turbulence model
LA	Left Atrium
LES	Large Eddy Simulation
LPA	Left Pulmonary Artery
LPM	Liters per minute (L/min)

LV	Left Ventricle
LVAD	Left Ventricular Assist Device
PA	Pulmonary Arteries
PIV	Particle Image Velocimetry
RA	Right Atrium
RANS	Reynolds-Averaged Navier-Stokes
RMS	Root Mean Square
RPA	Right Pulmonary Artery
RPM	Rotations Per Minute
ROI	Region of Interest
RV	Right Ventricle
SNR	Signal to Noise Ratio
SLA	Stereolithography
SST	Shear Stress Transport
SVC	Superior Vena Cava
SV	Single Ventricle
TCPC	Total Cavopulmonary Connection
VAD	Ventricular Assist Device
VC	Vena Cava

Abstract

Experimental and Computational Assessment of Mechanical

Circulatory Assistance of a Patient-Specific Fontan Vessel

Configuration

By Steven Gabriel Chopski, MS

A Dissertation submitted in partial fulfillment of the requirements for the degree of Doctor of Philosophy in Engineering at Virginia Commonwealth University.

Virginia Commonwealth University, 2013

Major Director: Dr. Karla M. Mossi, Ph.D.
Co-Advisor, Department of Mechanical and Nuclear Engineering

Dr. Amy L. Throckmorton, Ph.D.
Co-Advisor, Department of Mechanical and Nuclear Engineering

The treatment of single ventricle anomalies is a formidable challenge for clinical teams caring for patients with congenital heart disease. Those patients fortunate to survive surgical palliation contend with lifelong physical limitations and late stage pathophysiology. A mechanical blood pump specifically designed to increase pressure in the great veins would augment flow through the lungs and provide hemodynamic stability until a donor heart is located. To support the development of such medical devices, this research characterized the fluid dynamics of mechanical assistance in the Fontan

circulation by performing numerical analyses and particle image velocimetry (PIV) studies in a patient-specific *in vitro* model. This project investigated the performance of three pump prototype configurations. ANSYS-CFX was used to conduct the computational studies for a range of operating conditions and degrees of Fontan dysfunction. Pressure generation, blood trauma predictions, shear stresses, fluid streamlines, and velocity profiles were examined. Three-dimensional PIV studies were completed and compared to the numerical estimations. Computational findings and experimental data correlated to within literature expectations. Blood damage levels, shear stresses, and fluid residence times remained reasonable or below threshold limits. The blood pump configurations met expectations by achieving target design specifications for clinical application. The pumps enhanced the rate of hydraulic power gain in the cavopulmonary circuit, reduced inferior vena cava pressure, and minimally increased pulmonary arterial pressure. The blood pump with the twisted protective stent produced the most rapid increase in the rate of power gain and the highest pressure generation. The PIV measurements illustrated a strong dependency of the fluid dynamics on the patient-specific vessel geometry and the particular pump design. The pump having the twisted cage outperformed the other designs and had a dominating impact on the blood flow distribution in the cavopulmonary circuit. A strong rotational component in the flow was observed leaving the pumps. These results confirm that mechanical cavopulmonary assistance is a viable therapeutic option. Significant knowledge into a new class of blood pumps and how these pumps interact with a single ventricle physiology was gained, thus advancing the state-of-the-art in mechanical circulatory support and addressing a significant human health problem.

CHAPTER 1: Motivation and Significance

1.1. Introduction

Every year an estimated four million babies are born in the United States. Of these births, 35,000 infants are born with significant congenital heart anomalies (8 in 1000 births) [1]. Most heart defects are minor and may even be corrected during growth cycles in early childhood without intervention. Infants who are born with the multiple and complex congenital heart defects typically require corrective surgery to survive. A special subset of those babies with complex congenital heart defects exhibit a rare condition called a univentricular physiology [2].

The incidence of single ventricle anomalies is approximately 2,000 babies per year in the U.S. [3]. This condition is derived from a failure of either the right or the left ventricle to adequately develop, and is usually due to other structural defects, such as missing or poorly developed heart valves. In these patients, a single functioning ventricle is surgically configured to provide the energy that is required to drive blood flow through the entire cardiovascular system - one pumping chamber that does the equivalent workload of two normal heart chambers or ventricles.

1.2. The Normal Cardiovascular System

In a normal cardiac physiology, two pumping chambers or ventricles are present to drive blood through both the left (systemic) and right (pulmonary) circulations. Blood flows from the left ventricle during systole (ventricular contraction) through the aortic valve into the great arteries and then out into the capillary beds in the tissue, muscle, and end organs. In the capillaries, vital nutrients are passed to the cells, metabolic waste produces are removed and gas exchange occurs with the release of O_2 and the removal of CO_2 by the red blood cells. Blood

1

then flows back toward the right side of the heart through the venules and veins. The venous return or blood flow return to the right atrium comes from the superior vena cava (upper trunk of the body) and the inferior vena cava (lower trunk and extremities). Contraction of the right atrium pushes blood into the right ventricle through the tricuspid valve. When the right ventricle contracts, blood flows to the lungs through pulmonary valve into the pulmonary arteries for gas exchange in the pulmonary beds with CO_2 being released by the red blood cells and as O_2 is collected. Blood then returns to the left side of the heart through the pulmonary vein and fills the left atrium during diastole (ventricular relaxation). Contraction of the left atrium serves to force blood into the left ventricle to complete filling through the mitral valve. The contraction of the left ventricle forces blood into the aorta to complete the cardiac cycle [4, 5]. **Figure 1.1** illustrates the flow of blood through the heart.
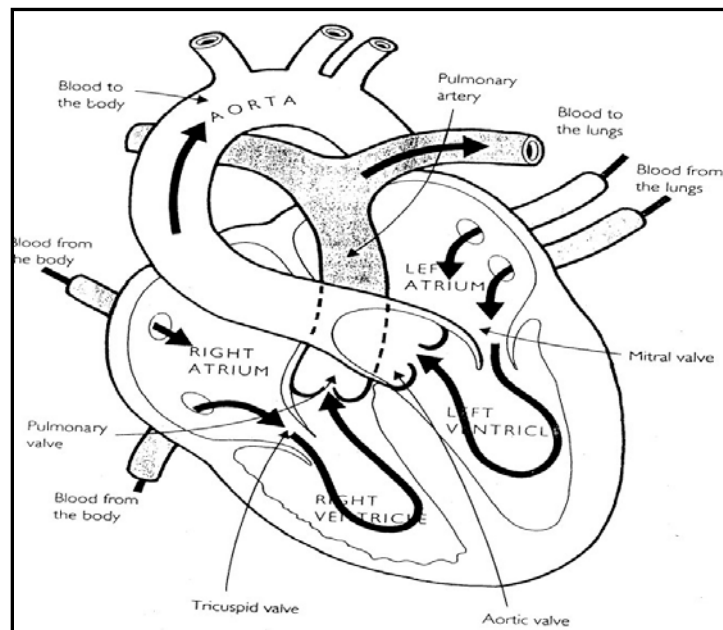
Figure 1.1: The Normal Heart Anatomy [1, 5]

1.3. Congenital Heart Defects

In contrast to a normal cardiovascular configuration, a single ventricle physiology comprises only one ventricular pumping chamber is unique in that it is a configuration produced through a set of surgical procedures, and is ultimately a "man-made" physiology to facilitate perfusion of the body and the lungs.

A single ventricle anomaly arises from the inability of the either the right or the left ventricle in the heart to develop properly. The under-developed ventricle is compounded by additional defects in the malformed heart such as deformed vasculature (coarctation of the aorta) deformed or missing valves (tricuspid atresia) and defects in the septum, the thick wall that normally separates the ventricles, which allows the mixing of blood between the systemic and pulmonary circulations (patent ductus arteriosus, ventricular septal defects) [2, 5].

Infants born with severe congenital heart defects struggle to survive. Immediate medical intervention takes place shortly after birth when the ductus arteriosus closes transitioning the cardiovascular system from being an open system on cardiac bypass through the mother to being an independent closed system. The newborn may become cyanotic due to poor oxygen delivery between the lungs and the tissues as the result of a septal defect in the malformed heart. With the full burden of having the workload of two normal ventricles thrust upon it, the overloaded single ventricle heart begins to fail. The infant will be given medications to reopen the ductus arteriosus and in some cases placed on a cardiac assist system such as ECMO [5-8].

Palliative surgeries that are conducted to form a single ventricle physiology are the only possible treatment. In order for the patient to survive, the pulmonary and systemic circulations must be separated to increase oxygen transport to the tissues and to provide hemodynamic stability by off-loading the failing single ventricle heart. The ventricle that is functioning adequately, as determined by the surgeon or cardiologist, becomes the systemic (i.e. left)

ventricle and drives blood through the body, tissue, muscle, and end organs. In this configuration, there is no pulmonary (i.e. right) ventricle, and the vena caval blood or venous return flows passively into the pulmonary arteries. The vena cavae are connected directly to the pulmonary arteries as opposed to the right ventricle [9].

A set of staged palliative surgeries are conducted to create this single ventricle physiology. **Figure 1.2(A)** illustrates the staged surgical procedures; each of which has its own mortality and morbidity [9]. The Norwood procedure was originally developed for treatment of patients with hypoplastic left heart syndrome but its use has been extended to the correction of other congenital heart defects. The procedure concentrates on reconstruction of the aortic arch to increase blood flow to the major arteries. The surgery may also include the placement of the modified Blalock-Taussig (BT) shunt between the pulmonary artery and the aorta. The shunt increases blood flow to the lungs and helps to offset cyanosis with increased oxygen transport to the tissues. Typically, the Norwood procedure occurs within the first two weeks of life [9].

The Glenn procedure, also referred to as the Hemi-Fontan procedure, seeks to further correct congenital defects and reconstruction. The procedure will remove the previously placed BT shunt and will attach the superior vena cava directly to the pulmonary artery. This surgery is performed between 4 and 12 months of age but may occur as late as 2 years depending upon growth of the vasculature and the growth of the patient [9]. **Figure 1.2(B)** shows the changes to the vessels and the heart from the surgery [10].
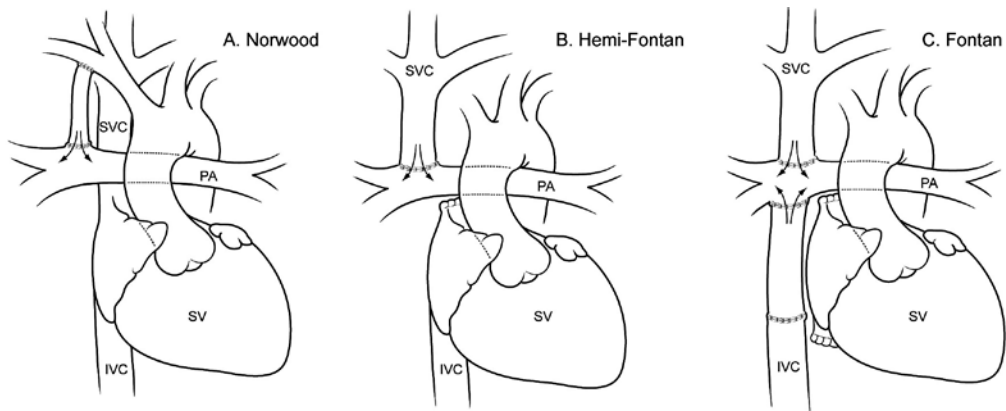
Figure 1.2: Staged surgical repair of functional single ventricle. A) Stage-1 Norwood repair. B) Stage-2 Hemi-Fontan repair. C) Stage-3 Fontan completion. SV, single ventricle; PA, pulmonary artery; SVC, superior vena cava; IVC, inferior vena cava [5, 10, 11]

As shown in **Figure 1.2 (C)**, the culmination of these surgeries is typically the last step, the Fontan procedure. The inferior vena cava is attached to the pulmonary artery, which separates the pulmonary circulation from the systemic circulation. This surgery usually occurs between 3 and 5 years of age but may occur as late as 12 years of age depending upon the hemodynamic stability of the Glenn procedure. The Fontan procedure is the final stage in the cardiac reconstruction, with a complete right heart bypass, which completely separates the systemic and pulmonary circulations [9].

The immediate effects of the surgery are decreased single ventricular loading, increased pulmonary perfusion and increased exercise tolerances.. The pulmonary and systemic circulations are interdependent and very sensitive to perturbations in either circulation. The compliant venous circulation remodels to adapt to this altered circulation, resulting in a chronic state of systemic venous hypertension and pulmonary hypotension, a state known as the Fontan paradox [6].

Unfortunately, the Fontan procedure is an imperfect solution for complex cardiac defects with late stage mortality and morbidity occurring months to decades after the surgery. A study of

405 patients conducted by Ohuchi *et al.* [12] reviewed the survivorship of patients who had received the Fontan procedure at the National Cerebral and Cardiovascular Center in Osaka, Japan between 1979 and 2010. It was noted that the complication-free patient survival rates at 1, 5, 10, and 15 years were 87.1%, 84.6%, 83.4%, and 81.6%, respectively. There are numerous complications, which include and are not limited to: reduced exercise tolerance, arrhythmias, atrial fibrillation, increased venous and pulmonary pressures, and low cardiac output [12]. There is a gradual decline in the effectiveness of the surgery with time due to mounting complications and long-term effects, leading to congestive heart failure [13].

Congestive heart failure typically ensues in the adolescent years, resulting from a breakdown in the efficiency of the surgical corrections, primarily caused by an increase in body surface area. Surgical reconstruction to restore hemodynamic stability is possible, but may be complicated due to the presence of scar tissue from previous surgeries and the rapid onset of heart failure. The only sure solution for these patients is a heart transplant for which a limit number of donor organs are available. Additional therapeutic treatment options are severely limited.

Over the years, several modifications have been made to the Fontan procedure in order to improve surgical outcomes of patients. Most recently, the formation of the total cavopulmonary connection (TCPC) has evolved as a more efficient surgical approach in contrast to the original intra-atrial connection. The TCPC is composed of the SVC and IVC connected to pulmonary artery, splitting it at or near the branch point to create the left- and right-sided pulmonary arteries, which perfuse the pulmonary beds of the left and right lungs. In order to minimize the stress that is placed upon the single ventricle, as a result of increased systemic resistance in the

venous system, it is necessary to conserve energy in the flow that passes through the TCPC junction [14, 15].

Since its inception in 1988 by de Leval, *et al.* [15] several improvements have been proposed to decrease the energy losses in the TCPC. These improvements involve changes in geometry such as off-setting the vena cava (caval offset), curvature of the inlets, flaring of the vena cava anastomoses, and enlargement of the IVC inlet connection [16, 17]. Advances in pharmacologic or novel surgical treatments have reached a plateau with little forward progress, resulting in the need for alternative therapeutic options for these patients. Thus, there is now a growing interest in the implementation of mechanical circulatory assistance in the cavopulmonary connection to boost pressure and thereby flow through the pulmonary vasculature [18].

1.4.   The Basis of Cavopulmonary Assist

While many heart pumps or ventricular assist devices (VADs) are being developed and are in various stages of clinical trials or use, all of the pulsatile and continuous flow pumps generate pressures in far excess of the desired range for right-sided cavopulmonary support. Progress in the development of pediatric VADs continues to achieve new milestones; a majority of these more compact, pediatric VADs, however, have been designed to support the systemic circulation in a normal biventricular physiology, not to support a cavopulmonary circulation. All of these mechanical blood pumps were designed and developed for adult or pediatric patients with normal biventricular circulations exhibiting congestive heart failure (CHF) and to support the systemic circulation, not the unique anatomic physiology of the cavopulmonary connection. Researchers have theorized that a pressure boost of as small as 2 to 5 *mmHg* may be sufficient to

unload the cavopulmonary circulation in adolescent and adult Fontan patients who have dysfunctional single ventricle [19].

Research teams are pursuing the design and development of cavopulmonary assist devices. Rodefeld and colleagues [18] have successfully demonstrated the use of the axial flow Hemopump to assist cavopulmonary flow in animals. This research group is also developing an innovative percutaneously-implantable, expandable propeller blood pump as a cavopulmonary assist device [20]. Limitations of this design include a wide distance between the rotor and blade-tip, increasing shear stresses, and an extremely short contact time with the thin propeller blades, preventing flow control downstream. Additionally, Rodefeld *et al*. [18] is currently developing an alternative pump design for a cavopulmonary assist device using a Von Kármán viscous pump to augment pulmonary flows. This catheter-based, collapsible/expandable viscous impeller pump takes on the form of a double-side conical disk [21, 22]. There are notable limitations present with the use of this device. The device would only function inside of an idealized TCPC or perhaps a TCPC without a caval offset since a stationary spindle would have to extend into the SVC in order to stabilize the spinning rotor. The device would be positioned in the center of the TCPC junction which is known to exhibit a complex three-dimensional flow structure including a vortex. The device could increase the mixing present leading to high shear stresses and hemolysis. Moreover, the device offers limited protection of the rotating disk from the vessel walls and must use them for support. Given the often complex geometry and morphology of the TCPC, it is unlikely that this device is clinically viable [23, 24].

Riemer *et al*. [25] at Stanford University have used a sheep model of the TCPC to test the response to the Thoratec HeartMate II axial flow blood pump (Thoratec Corporation, Pleasanton, CA). These studies demonstrated a return to baseline cardiac output, IVC flow, and arterial

pressures. They have had some success with both short and long term surgical implantation of the device [24, 26]. Similarly, the research team at the University of Colorado has made steady progress through numerical and *in vitro* studies on the development of an axial flow pump for proposed use in the IVC only [27]. The blood pump design, however, may be obstructive to flow in the event of catastrophic failure, and implantation requires invasive surgery.

1.5. Intravascular Cavopulmonary Assist

The increasing need for alternative therapeutic options for Fontan patients serves as the motivation for the development of an intravascular cavopulmonary assist device. To address this need, the VCU BioCirc Research Laboratory is developing a novel intravacular blood pump with the following new features to overcome the existing limitations of current technologies and to provide a much needed therapeutic option for Fontan patients:

1. **Cavopulmonary Assist**. No blood pump to date has been designed to function in the unique physiology of the Fontan circulation. By designing the device to be percutaneously-inserted, this overcomes the problems of implanting a device and subsequently explanting a device. Surgical implantation of VADs in Fontan patient remains a risky venture since the thoracic cavity has developed scar tissue from the three or more operations to construct the Fontan configuration.

2. **Minimal pathway obstruction in the event of device catastrophic failure.** An obstruction of any kind in the vena cavae flow could lead to a potentially life-threatening situation for the patient. The novel cavopulmonary pump is designed to allow for fluid volume flow through in the event of failure. This strongly differs to commercial pumps which must utilize occluders and cannulae in the pump placement.

3. **An efficient protective structural cage**. The cage around the pump provides support for the impeller and contains an optimized form of critical components of traditional axial-flow pumps, the inducer and the diffuser regions. The inducer and diffuser are seamlessly integrated into the cage design such that the cage filaments provide hydraulic energy transfer.

1.6.   Cavopulmonary Assist Device

In support of this effort to develop alternative therapeutic options for Fontan patients, the VCU BioCirc Lab is developing an intravascular, axial flow blood pump having a uniquely shaped protective cage. **Figure 1.3** illustrates the conceptual design of the blood pump. The intravascular axial flow pump is designed for percutaneous positioning in the inferior vena cava (IVC). The outer protective cage has radially arranged filaments that serve as touchdown surfaces to protect the vessel wall from the rotating impeller. Each filament is hydrodynamically designed to reduce drag and to maximize energy production from the rotating, engineered impeller blades. Currently the rotating pump consists of an impeller with three uniquely designed and helically wrapped blades to maximize energy transfer. Pump rotation is induced through a catheter-based drive cable configuration. The catheter lubrication system will allow for any blood elements to be flushed from the fluid seal location using a 5% dextrose solution.
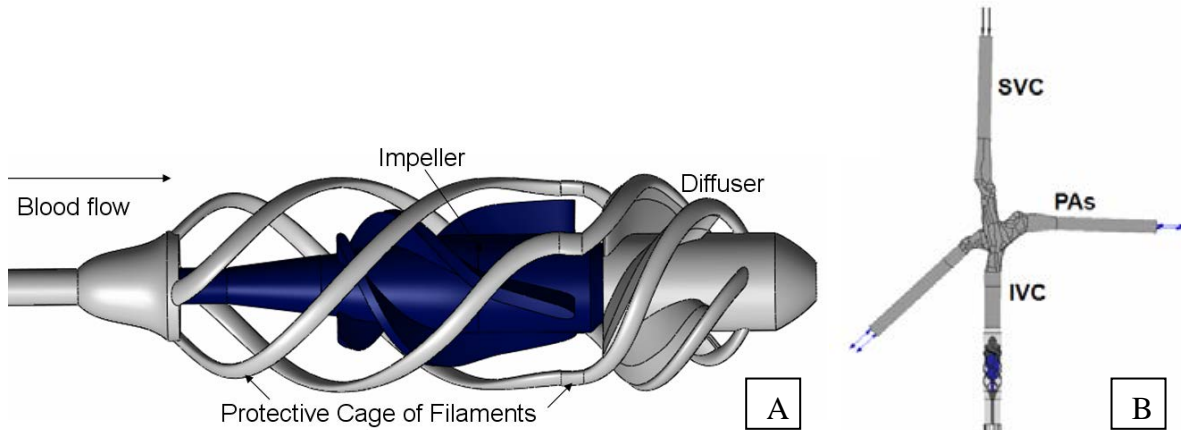
Figure 1.3: Percutaneously-Inserted Axial Flow Blood Pump for Single Ventricle Patients. Design consists of a catheter, protective cage of twisted filaments, impeller blade set, and diffuser blade set: A) The device consists of a protective sheath with cage filaments, a rotating shaft and catheter, an impeller blades, diffuser region, and inlet and outlet sections. B) Position of the cavopulmonary assist device in the IVC of the TCPC for Fontan patients. It is designed to augment pressure and thus flow in IVC and subsequently drive blood into the left and right pulmonary arteries (LPA and RPA) while supporting the incoming flow from the superior vena cava (SVC) [28].

The blade tip-to-tip diameter of the first generation design is 14 *mm* in the fully open configuration. In this study, for the purposes of measuring hydraulic performance, the pump prototype was mounted to a drive-shaft that was supported by mechanical bearings. The target design for the intravascular pump is to generate flow rates of 0.5 to 4 *L/min* with pressure rises of 2 to 25 *mmHg* for rotational speeds of 1500 to 9000 RPM. The target cage diameter is currently designed for vessel diameters of 18-25 *mm*. The device is intended for short-term use only as a bridge-to-transplant, bridge-to-hemodynamic stability, or bridge-to-Fontan surgical reconstruction.

The methodology for developing such a blood pump involves a high degree of interplay between numerical modeling and experimental testing. **Figure 1.4** presents an overview of our proposed methodology. The proposed methodology having a combination of computational modeling along with experimental validation offers a powerful approach to address our scientific questions in terms of hydraulic efficiency, ideal fluid dynamic conditions, and applicability of

mechanical circulatory assist. We expect to gain significant knowledge and insight into a relatively new class of blood pumps, which may offer clinical advantages over existing designs, and into how these devices interact with the cavopulmonary circulation in single ventricle patients.
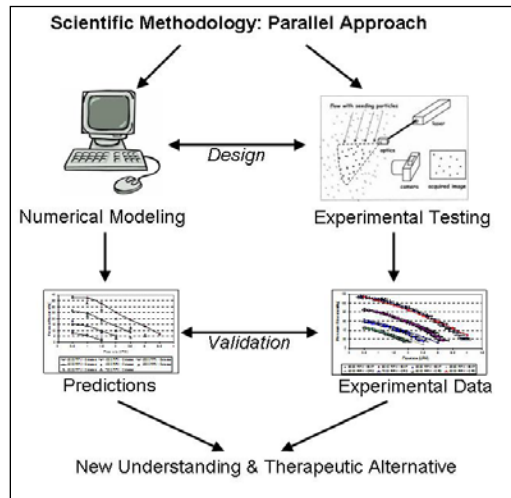
Figure 1.4: Development Methodology [5]

In addition to strategic coupling of computational fluid dynamics (CFD) modeling and hydraulic testing of pump prototypes, a common experimental technique for measuring the internal flow dynamics within the intravascular device is particle image velocimetry (PIV). While the pump design is a critical component, the fluid domain must also be free of irregular flow patterns, vortices, retrograde fluid layers, and stagnant flow. Irregular flow patterns can lead to conditions of high fluid shear stresses, risking damage to red blood cells and the generating a thrombus because of platelet activation. Irregular flow patterns can also lead conditions of low shear stresses, risking initiation of clotting cascades and generating a thrombus because of fluid stasis [29]. The application of PIV allows medical device developers to experimentally investigate flow conditions in blood pumps at various locations in the fluid domain and to assist in the overall design effort.

1.7. Numerical Modeling

Computational fluid dynamics (CFD) is a predictive tool that is utilized to provide detailed information about the hemodynamics of the TCPC and the performance of the cavopulmonary assist device. Previous numerical work has been used in the development of the pump impeller, the diffuser blades, and the protective cage filaments for design optimization and improvement. Numerically modeling the hemodynamics of the cavopulmonary connection provides a basis for comparison of the experimental results that are be obtained from the PIV experiments [30-33].

CFD provides information that cannot be readily obtained through physical experiments and provide data for other analyses. Such instances include determining the instantaneous velocities of the fluid flow surrounding the rotating impeller in the pump, or generating three-dimensional plots of fluid shear stresses. Blood damage analyses examine the potential for hemolysis and thrombosis as a result of the cavopulmonary assist device. Further numerical studies can examine factors such as irregular flow patterns, vortices or regions of stasis that are generated by the pump impeller.

The changes in pressure and flow through a TCPC provide quantitative information about the energy efficiency with regard to the power loss in the cavopulmonary circulation. Numerical simulations of the total cavopulmonary connection are common in the literature with researchers applying computational fluid dynamics to examine the fluid flow field and to assess power loss predictions of both idealized and patient-specific TCPC models [34-41]. Power loss refers to the amount of energy that is expended within a TCPC model due to unsteady flows and mixing. The addition of a pump into the TCPC will decrease the power loss and increase the flow energetics since the pump inherently adds energy and rotational force to the fluid flow as

balanced with resistance. The term power efficiency is used to describe the energy gains in the TCPC with pump support. CFD is able to provide estimates of the power efficiency in a TCPC.

1.8. Particle Image Velocimetry

Particle image velocimetry (PIV) has earned its place among flow measurement techniques because of its ability to collect quantitative data on the instantaneous velocity field for a given flow field [42, 43]. The premise of PIV is rooted deep in physics by drawing upon the key areas of optics, kinematics, and fluid mechanics. The average velocity for the movement of a particle in space can be simply calculated as the distance that the particle traverses divided by the time necessary to do so. This simple principle is applied to flows by capturing the movement of particles with in a two dimensional fluid field at two successive instances in time. If the amount of time is extremely small relative to the time necessary to move through the measurement region, then it is possible to approximate the local velocity of the particle as an instantaneous velocity of the flow field for that region by comparing the particle displacement in space between the two image captures. The technique is illustrated in **Figure 1.5**.

PIV uses a high energy laser sheet to illuminate a plane within a fluid flow that is seeded with minute particles. Two laser pulses are triggered at a known amount of time apart and synchronized with a high speed camera to capture two successive images of the seeded flow. The two images are compared to each other to determine the particle displacement over the time interval. A special algorithm divides the images into regions and computes the velocity vectors for each individual region of flow. The velocity vectors allow for the formation of velocity plots to visualize the fluid dynamics within the image plane of interest. Such velocity mapping is also critically important in the design of a blood pump by providing essential information about the localized fluid velocities, such as velocity gradients, flow directionality, and identification of

14

flow vortices, irregular flow patterns and flow stagnation. High shear stresses, irregular flow patterns, and vortices are well known to lead to platelet activation or destruction of red blood cells based on the magnitude of the shear and the exposure time. Alternatively, low shear levels are evident in regions of flow stasis, which provide conditions for thrombus formation through red blood cell aggregation [28, 44, 45].
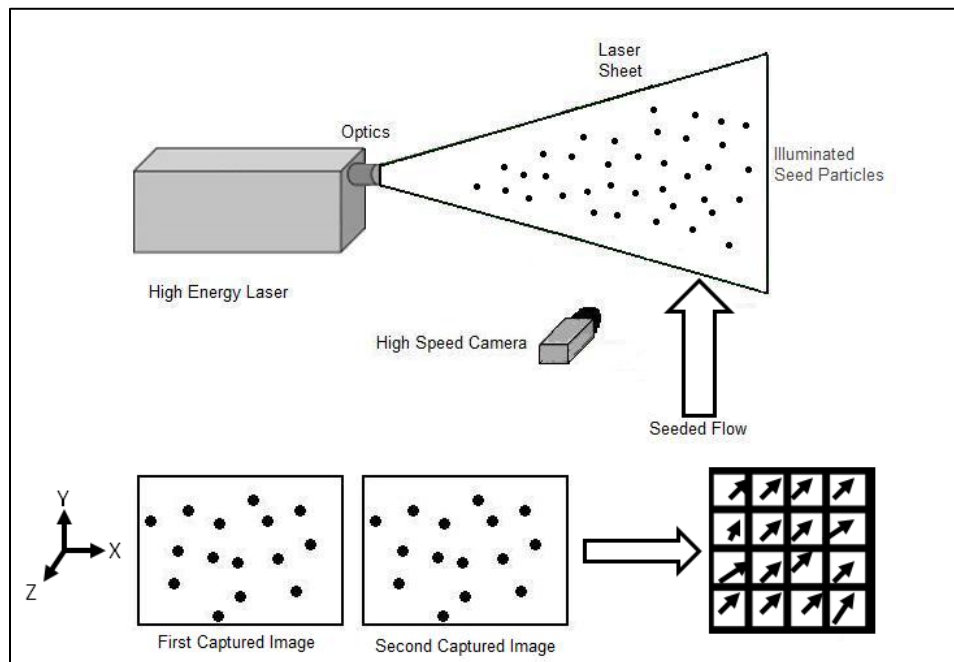
Figure 1.5: Particle Image Velocimetry

Particle image velocimetry is an accepted evaluation technique for blood pumps for researchers in the artificial organ community. Particle image velocimetry has also been used extensively to examine the internal fluid dynamics in patient-specific cardiovascular models [46-48]. Previous research studies have used particle image velocimetry to investigate the internal fluid dynamics of the total cavopulmonary connection. Idealized models of the total cavopulmonary connection have been investigated rigorously investigated by researchers [14, 16, 34, 49, 50]. Patient-specific models of the TCPC have been studied more recently by de Zelicourt *et al.* [41, 47] and Kitajima *et al.* [51]. The patient-specific models have revealed that the flow field of the TCPC is

highly three-dimensional with rapid mixing from the colliding vena cavae flows, which then split off into the pulmonary arteries.

Particle image velocimetry provides a unique opportunity to examine the interactive fluid dynamics which can occur when a prototype axial flow pump is implanted into the inferior vena cava of a patient-specific total cavopulmonary connection to provide mechanical cavopulmonary assistance. The PIV data provides quantitative data about the nature of the fluid flow field which allows for a clear determination of the benefits of cavopulmonary assist. The implementation of particle image velocimetry studies was the central focus of this dissertation project, in addition to computational modeling [52].

1.9. Dissertation Overview

This section provides an overview of the chapters to follow in this dissertation. As previously discussed **Chapter 1** provides an introduction to relay the revelant information for the motivation and significance behind the development of the cavopulmonary assist device. **Chapter 2** lays out the specific aims which will be accomplished through this dissertation research. **Chapter 3** provides the theoretical background for the numerical methods. **Chapter 4** discusses the theoretical background for particle image velocimetry experiments. **Chapter 5** relates the necessary methods and materials that were required to execute the numerical methods. **Chapter 6** discusses the necessary methods and materials to accomplish the particle image velocimetry experiments as well as hydraulic testing to assess the overall pump performance. **Chapter 7** presents the results for the numerical methods previously discussed in **Chapter 5**. **Chapter 8** presents the results from the hydraulic testing and the particle image velocimetry experiments. This chapter concludes with a comparison between the numerical and the experimental results. **Chapter 9** discusses the results and the scientific impact as well as

16

recommendations for future work. Finally, **Chapter 10** contains gives concluding remarks about

the scientific merit of this dissertation research.

CHAPTER 2: Specific Aims

The treatment of single ventricle anomalies is a formidable and costly challenge for clinical teams caring for patients with congenital heart disease. Despite having an incidence of only 2 per 1000 births, these patients utilize healthcare resources disproportionate to their numbers, thus constituting an emerging public health concern [1]. Those patients fortunate to survive surgical palliation contend with morbidity and lifelong physical limitations. During the final surgical palliative procedure, the right heart is completely bypassed by connecting the inferior vena cava to the pulmonary artery, forming the total cavopulmonary connection. The end result is a 'man-made' physiology in which a single ventricle drives blood flow through the systemic and pulmonary circulations without a subpulmonary pressure source. The systemic and pulmonary circulations are interdependent and very sensitive to perturbations in either circulation. The compliant venous circulation remodels to adapt to this altered circulation, resulting in a chronic state of systemic venous hypertension and pulmonary hypotension, a state known as the Fontan paradox. This significant alteration of venous return contributes to early and late pathophysiology and comorbidities [6].

A mechanical blood pump specifically designed to increase pressure in the great veins would augment flow through the lungs and reverse the Fontan paradox in adolescent and adult patients with failing single ventricles. During bridge-to-transplant, this pump would provide hemodynamic stability until a donor organ is located. Alternatively, the application of this pump as a bridge-to-recovery would potentially prevent the onset of many of the late comorbidities, such as congestive heart failure. The functional parameters for a pump to operate in the anatomic and physiologic conditions of a cavopulmonary connection are distinctive and unlike standard requirements for systemic left ventricular assist [11, 53, 54]. It has been postulated that a pressure

adjustment of only 2-5 *mmHg* would be sufficient to improve stability [19]. Having a proven track record of success in this field, we have generated preliminary data through numerical modeling and particle image velocimetry flow measurements to demonstrate the feasibility of this approach. The pump prototypes delivered 2-25 *mmHg* for flow rates of 0.5-4 *L/min* at 1500-9000 RPM [28, 54, 55].

Building upon the preliminary data, this dissertation research seeks to continue this technology-driven research by characterizing the interaction of mechanical assistance in a simulated total cavopulmonary connection and by performing particle image velocimetry studies of the pump within a patient-specific *in vitro* model. The following supporting objectives will be achieved through simulation and laser flow experiments:

1. Numerically simulate mechanical cavopulmonary assistance of a 3-D reconstructed patient-specific model.

2. Design and construct a new experimental configuration to perform 3-D measurements of the flow fields in the patient-specific cavopulmonary model.

3. Conduct stereo-particle image velocimetry to capture the fluid dynamics of a control case having no pump support and mechanical cavopulmonary assistance in the inferior vena cava.

4. Investigate the impact of 3 uniquely designed cardiovascular stents around the pump on the flow field in the patient-specific model.

5. Evaluate power loss and efficiency of the patient-specific model with and without mechanical cavopulmonary assistance.

6. Compare the numerical simulation findings to the experimental measurements.

This research project will further develop a new therapeutic tool that will provide mechanical assistance to patients with failing single ventricle physiology. It will serve as a bridge-to-recovery, bridge-to-transplant, bridge-to-surgical reconstruction, or bridge-to-hemodynamic stability for Fontan patients. We expect to gain significant knowledge and insight into a new class of intravascular blood pumps, which will offer clinical advantages over existing devices, and into how these pumps will interact with the cavopulmonary circulation in single ventricle patients.

CHAPTER 3: Computational Fluid Dynamics Theoretical Background

3.1   Introduction to Numerical Methods

Modern computer systems support the completion of fluid dynamic-based simulations, which provide valuable insight to developers and lead to design optimization. Computational fluid dynamics (CFD) is the process of using such computer systems to obtain a numerical solution for various flow phenomena. The physics of fluid flow is described by the continuity and Navier-Stokes equations [56-58]. Since exact solutions are available for only a few physical flows, application of these governing equations in practice is mainly accomplished via numerical methods. Numerical or CFD methods replace the governing equations with a set of algebraic equations, a process known as discretization, providing solutions at discrete points in the flow domain [56]. The CFD analysis yields an approximate solution to characterize the flow field. Commonly used discretization methods include: Finite Difference Methods (FDM), Finite Element Methods (FEM), and Finite Volume Methods (FVM), which are all fundamental approaches to solving partial differential equations describing fluid flow [56-59].

FDM replace the partial derivatives appearing in the Navier-Stokes equations of fluid motion with algebraic difference quotients or translation operators [57, 58]. This technique produces a set of linear operator combinations and yields a system of equations that can be solved at discrete points throughout the flow field [57]. The derivatives are represented based on Taylor's series expansions with truncation typically at a second order accuracy.

FEM are based on finite dimensional spaces with descriptive functions in an integral formulation. This application allows the differentiations to be transferred to interpolation polynomials [58]. The continuum field is subdivided into cells or elements where an algebraic

equation can be derived. The equations are then solved for an approximate solution. Applications of FEM include structural design, vibration analysis, and heat transfer.

In contrast to FDM, FVM uses integral formulations to express the conservation laws, allowing computation of discontinuous functions [58]. It involves dividing the physical flow domain into cells or elements with certain flux characteristics. FVM discretizes the integral form of the governing equations and applies variables to discrete points of cells, called nodes, in the flow domain [57]. This integral formulation is prone to instabilities, therefore FVM methods normally introduce artificial viscosities for stabilization [58]. This technique gives users the geometric flexibility of grid generation and flexibility in defining the discrete flow variables [57]. FVM enables the geometric flexibility gained by FEM with discretization of the flow field per FDM techniques.

3.2   Laminar or Turbulent Flow Conditions

Fluid dynamic conditions in a flow field are divided into three primary regions and are often defined by the non-dimensional number, called the Reynolds number. Flow conditions are expected to be laminar, transitional, or turbulent. **Equation 3.1** shows the algebraic form of the Reynolds number (Re) as the ratio of inertial forces to viscous forces, where L is the characteristic length, V is the velocity, ρ is the fluid density and μ is the dynamic viscosity.

$$R_e = \frac{LV\rho}{\mu} \qquad\qquad 3.1$$

Table 3.1 provides a display of the fluid flow behavior in pipe flow for set ranges of Reynolds numbers. It is important to note that the ranges for the Reynolds numbers are arbitrary such that laminar flow and turbulent flow are well established within a range of Reynolds numbers less than 2000 or greater than 4000, respectively. Transition to turbulence occurs at arbitrary values

in between 2000 and 4000, but can be delayed or promoted based on other factors affecting the fluid flow, such as surface roughness [60].

Table 3.1: Reynolds Number Ranges [60]

0<Re<1; Highly viscous creeping flow (Stokes flow)
1<Re<100; laminar, strong Reynolds number dependence
100<Re<2x10^3; laminar
2x10^3<Re<4x10^3: transition to turbulence
4x10^3<Re<10^6; turbulent, moderate Reynolds number dependence
10^6<Re<Really large; turbulent, slight Reynolds number dependence

When evaluating flow conditions in a rotating domain, a second non-dimensional number to be considered is the Taylor number (Ta), which characterizes the flow between two long rotating, concentric cylinders [60]. When only the inner cylinder is rotating a narrow gap of fluid exists between the cylinders, forming Couette flow. An exact solution to the Navier-Stokes equations represented in cylindrical coordinates exists for the more general case of two rotating cylinders and forms a linear second-order ordinary differential equation. The solution for the velocity distribution, for the case of only the inner cylinder rotating is shown in **Equation 3.2**. The velocity is given by V_θ, Ω_i is the rotation speed of the inner cylinder, r_o and r_i are the radii of the outer and inner cylinders.

$$V_\theta = \Omega_i r_i \frac{\dfrac{r_o}{r} - \dfrac{r}{r_o}}{\dfrac{r_o}{r_i} - \dfrac{r_i}{r_o}}$$

3.2

23

The Taylor number is derived by substituting the velocity distribution back into the N-S equation for the θ-direction and simplifying. It forms the expression in **Equation 3.3** showing the ratio of centrifugal to viscous forces [60].

$$Ta = \frac{r_i \left(r_o - r_i\right)^3 \Omega_i^2}{v^2}$$

3.3

Turbulent flow conditions have been experimentally measured and are known to exist for Taylor numbers above 400 [61]. Preliminary calculations were performed in order to estimate these non-dimensional values. The Reynolds number was predicted using the diameter of the impeller hub to be the characteristic length L, and the velocity V was defined to be the rotor diameter multiplied by the angular speed for the pump speed of 4000 RPM. This calculation yields a Reynolds number of 19,000. For the Taylor number, r_i is defined to be the diameter of the impeller hub and r_o is defined to be the tube internal diameter. This calculation gives a Taylor number of 580. These preliminary calculations have demonstrated that the Reynolds and Taylor numbers are above 5000 and 450, respectively, thereby indicating that turbulent flow conditions will dominate in the pump region.

3.3   Treatment of Turbulence

Turbulence is a random flow phenomenon having complex structural swirling eddies and is characterized by the presence of high Reynolds numbers in a flow field. It has strong diffusive properties due to rapid mixing flow conditions and high rates of mass and momentum transfer [62]. The time and length scales of the smallest turbulent eddies are several orders of magnitude greater than the time and length scales of molecular motion. Turbulence is also dissipative with connecting large scale eddies to smaller scale eddies, where fluid viscosity controls flow

behavior [56]. The nonlinear convective components in the Navier-Stokes equations capture the spatial and temporal turbulent scales [56]. The largest turbulence scales carry kinetic energy while the smallest scales involve the dissipation of energy. Turbulence is characterized by high Reynolds numbers throughout a three-dimensional fluid domain. Unsteady flow will occur as a result of the rotating impeller in the pump domain. Unsteady flow also occurs in the TCPC as a result of the colliding vena cavae flows which then split off toward the pulmonary arteries. Turbulence flow conditions are expected to dominate the flow field within the cavopulmonary assist device and the TCPC junction. The three most common approaches that are used to model turbulent flows are direct numerical simulation (DNS), large eddy simulation (LES), and Reynolds-Averaged Navier Stokes (RANS).

The modeling of complex flow fields by deterministic methods is computationally intensive, especially if the smallest of flow scales must be resolved. DNS is able to model simple flow phenomena and geometries very well [58]. In contrast, however, DNS is unable to resolve all component scales within the complex turbulent flow conditions. The LES approach to turbulence modeling addresses large scales of turbulence only and simulates the smaller scale effects by using subgrid models [58]. This approach provides a full 3-D, time-dependent solution of the fluctuating turbulent flow field, but only at large flow scales [58]. LES has a track record of success for modeling flow conditions with very high Reynolds numbers, which are not expected in the cavopulmonary pump.

3.4   Reynolds-Averaged Navier-Stokes (RANS)

As an alternative to DNS and LES, the RANS approach simulates the entire flow field by using averaged quantities for the mean velocities and turbulent motion. Reynolds-averaging involves the decomposition of the flow variables into mean and fluctuating components [58, 59]. A

drawback to implementing Reynolds-averaging is the appearance of higher order correlations in the mean and turbulent flow equations. These correlations or unknown turbulent fluid stresses require modeling, which gives rise to the conventional 'closure problem' associated with the RANS approach. The RANS approach solves for the mean turbulent motion in conjunction with a closure scheme for the correlations or unknown turbulent stresses. Numerous closure models exist, such as the Reynolds stress scheme, turbulent diffusion model, and two equation models, to characterize the additional unknown turbulent stresses as a result of the averaging procedure. The two-equation models account for the effect of turbulence on the mean flow components by introducing an eddy viscosity term. The viscosity term is given by the product of the turbulent velocity scale and the turbulent length scale. This dissertation research utilized CFD that is based on a FVM and RANS approach for turbulence characterization. The subsequent sections discuss the use of CFD in assessment of performance and fluid conditions through blood pumps and the software employed to achieve the numerical design objectives of this dissertation.

3.5   The Use of CFD in Blood Pump Design

CFD has been widely used in the design and optimization of ventricular assist devices (VADs) and blood pumps. In 2008, and similar to our ongoing research effort, Zhang *et al*. [63] presented a detailed study of the design optimization of an axial blood pump using CFD, which included performance modeling of the pump itself and the levels of blood trauma. Last year, a CFD study for blood flow in the aortic arch and the resulting hemodynamics due to the influence of a VAD was published by Xuan *et al*. [64]. Karmonik *et al*. [65] also used ANSYS CFD software to computationally investigate the positioning of the outflow cannula on blood flow conditions using patient-specific models. Additionally, Toptop *et al*. [66] described in detail their recent effort in Turkey to design and numerically evaluate a new magnetically levitated axial flow pump for

left ventricular support. All of these previous research groups used software available from ANSYS Incorporated to complete the CFD analyses. Over several years, the VCU BioCirc Lab has successfully employed ANSYS CFD software to design and optimize the cavopulmonary assist device for Fontan patients. This chapter details the underlying theory of each software program.

3.6   Software Theory of Operation

3.6.1 ANSYS CFX-Mesh

CFX-Mesh is a mesh generating program in the ANSYS software suite. It has the capabilities to resolve reasonably complex boundary layer phenomena using a hybrid approach to mesh generation. The available mesh structures include tetrahedral, prisms, and pyramid element structures. The program has advanced surface and volume controls, such as the ability to create inflation layers (used for resolving mesh in the near walls region), edge and surface proximity controls, and parallel volume meshing. CFX-Mesh allows the user to import a solid body from a CAD program or the ANSYS Design modeler software, design the regions of interest in fluid or solid domain, specify the mesh attributes, produce a surface mesh, and finally generate a volume mesh. This dissertation project utilized ANSYS CFX-Mesh in the mesh construction for its model analysis.

3.6.2 Theory for CFX-Solver

ANSYS 12.1 CFX-Solver is a program capable of numerically solving complex, multidimensional flows for incompressible or compressible, steady-state or transient, and laminar or turbulent fluid dynamics. This solver models the equations for the conservation of

mass, momentum, and energy in terms of dependent variables (pressure, velocity, etc.). Based on the geometrical design and mesh generation from ANSYS CFX-Mesh, CFX-Solver implements a finite volume approach toward solving the equations for conservation of mass and momentum. The program allows the user to apply turbulence modeling for turbulent flow conditions. This research employed CFX-Solver to complete steady-state CFD simulations of the flow field through the cavopulmonary assist device and TCPC junction.

CFX-Solver utilizes the equations for conservation of mass and momentum in terms of the dependent variables velocity and pressure [67]. Under turbulent flow conditions, the instantaneous value of these dependent variables fluctuates about their mean value. Reynolds-averaged equations for turbulent flow include the superposition of the mean flow and fluctuating flow contributions. The following sections discuss the continuity equation, equations of motion, and Reynolds-Averaging procedure [67].

3.6.3 Conservation of Mass

The conversation of mass equation or the continuity equation is derived by analyzing the mass flow into and out of an infinitesimal control volume, as follows in Einstein summation convention [56, 67]:

$$\frac{\partial \rho}{\partial t} + \frac{\partial}{\partial x_i}\left(\rho U_i\right) = 0 \qquad\qquad 3.4$$

where U_i represents the three-dimensional velocity vector components of flow, t signifies time, ρ is the fluid density, and x_i is the summation of spatial variables. Einstein summation convention provides a compact method of keeping track of spatial variables that are related to vector or tensor terms. The index 'i' signifies the summation across three spatial directions within a 3-D coordinate system [68].

3.6.4 Navier-Stokes Equations of Motion

The application of Newton's Second Law of Motion to an infinitesimal control volume yields the Law of Conservation of Momentum, which is shown in **Equation 3.5**, where P is the

$$\frac{\partial}{\partial t}\left(\rho U_i\right)+\frac{\partial}{\partial x_j}\left(\rho U_i U_j\right)=\frac{\partial P}{\partial x_i}-\frac{\partial \tau_{ij}}{\partial x_j}+\rho f_i \qquad 3.5$$

pressure gradient that drives flow, τ_{ij} is the stress tensor, x_i is the summation of spatial variables and f_i is the body force vector. This is the condensed form of the Navier-Stokes Equations for Cartesian coordinates. Other coordinate systems, such as cylindrical coordinates, may be applied as needed. The body force contribution due to gravity can be neglected because the effect of gravity is negligible compared to the centrifugal acceleration [60, 68]. For flow fields with a rotating frame of reference, CFX-Solver models the body force by incorporating the effects of the Coriolis and centripetal forces:

$$\vec{f}_i=-\rho\left(2\vec{\Omega}\times\vec{\Omega}+\vec{\Omega}\times\left(\vec{\Omega}\times\vec{r}\right)\right) \qquad 3.6$$

where '×' is the vector cross-product operator, Ω is the rotational speed, r is the vector representing spatial location, and '→' indicates vector notation. The remaining derivations neglect the contribution of the body force. For a Newtonian fluid, the stress tensor can be formulated as follows:

$$\tau_{ij}=-\mu_b\delta_{ij}\frac{\partial U_k}{\partial x_k}-\mu_v\left\{\frac{\partial U_i}{\partial x_j}+\frac{\partial U_j}{\partial x_i}\right\} \qquad 3.7$$

where $\mu_b = (2/3)\mu_v$ is the bulk viscosity, μ_v represents the dynamic viscosity, and δ_{ij} is the Kronecker delta (when i=j, then $\delta_{ij}=1$, and $\delta_{ij}=0$ for i≠j).

3.6.5 Reynolds-Averaging Procedure

In turbulent flow conditions, the value of scalar flow variables can fluctuate dramatically. Instantaneous scalar quantities are interpreted as the superposition of a mean and fluctuating component. Any arbitrary flow quantity can be represented in **Equation 3.8** by the symbol θ, with $\bar{\theta}$ representing the time-average of the mean component of the scalar and φ' representing the time-average of the fluctuating components. These quantities are expanded to form **Equations 3.9** and **3.10**. **Equation 3.9** is the time-averaged mean component of the flow. **Equation 3.10** shows that the mean of the individual fluctuating components has a net value of zero, but the individual components are each finite, non-zero values [62].

$$\theta = \bar{\theta} + \varphi'$$

3.8

Equation 3.8 links the steady and fluctuating components together. We will encounter this equation again in slightly different form in the next chapter as a statistical description of the mean and standard deviation of the instantaneous velocity.

$$\bar{\theta} = \lim_{\Delta t \to \infty} \frac{1}{\Delta t} \int_{t}^{t+\Delta t} \theta \, dt$$

3.9

$$\overline{\varphi'} = \lim_{\Delta t \to \infty} \frac{1}{\Delta t} \int_{t}^{t+\Delta t} \left[\theta - \bar{\theta} \right] dt = 0$$

3.10

For incompressible flows, the conservation of mean momentum can be derived from the above equations as the Reynolds-Averaged Navier-Stokes equation as is seen in **Equation 3.11**.

$$\frac{\partial}{\partial t} \left(\rho \bar{U}_i \right) + \frac{\partial}{\partial x_j} \left(\rho \overline{U_i U_j} \right) = \frac{\partial \bar{P}}{\partial x_i} - \frac{\partial}{\partial x_j} \left(\overline{\tau_{ij}} + \rho \overline{u_i' u_j'} \right)$$

3.11

The Reynolds stress tensor term $\rho\overline{u_i'u_j'}$ arises as a result of the Reynolds Averaging of the convection term on the left hand side of **Equation 3.11**. This term is not easily calculated and must be estimated using turbulence models. Eddy viscosity approximations are used to relate Reynolds stress and turbulent fluctuating terms to mean flow variables, as shown in **Equation 3.12.** The symbol μ_t is the turbulent viscosity, and k is the turbulent kinetic energy term.

$$\rho\overline{u_i'u_j'} = -\mu_t\left\{\frac{\partial\overline{U}_i}{\partial x_j} + \frac{\partial\overline{U}_j}{\partial x_i}\right\} + \frac{2}{3}\rho\delta_{ij}k \qquad 3.12$$

For an incompressible, Newtonian fluid, the Reynolds-Averaged viscous stress tensor is defined as:

$$\overline{\tau}_{ij} = -\mu_v\left\{\frac{\partial\overline{U}_i}{\partial x_j} + \frac{\partial\overline{U}_j}{\partial x_i}\right\} \qquad 3.13$$

The turbulent viscosity and the turbulence kinetic energy term are estimated by selecting the appropriate turbulence model for the physics.

3.6.6 Turbulence Closure Modeling

Turbulence models in CFD codes solve for terms in the nonlinear Reynolds stress tensor in the Navier-Stokes equation by approximating turbulent flow conditions for viscous dissipation and kinetic energy transfer [56]. The determination of the nonlinear terms in the momentum and mass equations requires statistical averages of the unknown quantities. In general, one and two-equation based turbulence models are used. CFX-Solver incorporates three of the more popular

and widely used closure models: k-ε model of Jones and Launder, k-ω model of Wilcox, and the Shear Stress Transport (SST) model of Menter, which combines the k-ε model in the outer region and k-ω model in near wall region [59].

3.6.6.1   k-ε Turbulence Model

The *k*-ε turbulence model solves the equations for *k*, the turbulent kinetic energy, and ε, the dissipation rate of *k* [56]. The dissipation rate of *k* is defined as the amount of *k* per unit mass and time converted to internal fluid energy by viscous motion. The turbulent viscosity (μ_t) is modeled as the product of a turbulent velocity scale (V_t) and a turbulent length scale (l_t), based on Prandtl and Kolmogorov, with a proportionality constant:

$$\mu_t = \rho c_\mu l_t V_t \qquad\qquad 3.14$$

This model assumes the velocity scale to be the square root of the turbulent kinetic energy or $V_t = \sqrt{k}$. In the standard k-ε two equation model, the length scale is considered to be the same as the dissipation length scale:

$$\varepsilon = \frac{k^{3/2}}{l_t} \qquad\qquad 3.15$$

Equation 3.16 and **Equation 3.17** are the semi-empirical transport equations *k* and ε, respectively:

$$\frac{\partial(\rho k)}{\partial t} + \frac{\partial(\rho \overline{U}_j k)}{\partial x_j} = \frac{\partial}{\partial x_j}\left(\Gamma_k \frac{\partial k}{\partial x_j}\right) + P_k - \rho\varepsilon \qquad\qquad 3.16$$

$$\frac{\partial(\rho\varepsilon)}{\partial t}+\frac{\partial(\rho\overline{U}_j\varepsilon)}{\partial x_j}=\frac{\partial}{\partial x_j}\left(\Gamma_\varepsilon\frac{\partial\varepsilon}{\partial x_j}\right)+\frac{\varepsilon}{k}\left(c_{\varepsilon1}P_k-\rho c_{\varepsilon2}\varepsilon\right) \qquad 3.17$$

where Γ_k and Γ_ε are diffusion coefficients defined below in **Equations 3.18** and **3.19** while $c_{\varepsilon1}$

and $c_{\varepsilon2}$ are model constants illustrated in **Table 3.2** with model constants σ_k and σ_ε.

$$\Gamma_k=\mu+\frac{\mu_t}{\sigma_k} \qquad 3.18$$

$$\Gamma_\varepsilon=\mu+\frac{\mu_t}{\sigma_\varepsilon} \qquad 3.19$$

The turbulent kinetic energy term, P_k, for incompressible flow is given by:

$$P_k=\mu+\left(\frac{\partial\overline{U}_i}{\partial x_j}+\frac{\partial\overline{U}_j}{\partial x_i}\right)\frac{\partial\overline{U}_i}{\partial x_j} \qquad 3.20$$

Once the values of k and ε are known, the turbulent viscosity can be calculated as follows:

$$\mu_t=\rho c_\mu\frac{k^2}{\varepsilon} \qquad 3.21$$

where μ_t is the turbulent viscosity and c_μ is a model constant shown in **Table 3.2** [62].

Table 3.2: k-ε Turbulence Model Constant Values [62]

Variable	Default Value
c_μ	0.09
$c_{\varepsilon1}$	1.44
$c_{\varepsilon2}$	1.92
σ_k	1.0
σ_ε	1.3

Turbulence models approximate the physics of the fluid flow and are dependent on empirical

data constants, which give rise to inaccuracies [57].

3.6.6.2 k-ω Turbulence Model

Standard turbulence models based on the k-ε equations have limitations. They usually predict the onset of flow separation too late and under estimate the amount of flow separation [67]. The other two-equation closure models, such as the k-ω model, demonstrate more accurate predictions of flow separation. This model does not have complex non-linear damping functions in its calculations, as is found in the k-ε model. Thus, the k-ω model is thought to be more robust for solutions along boundaries. It solves two transport equations, one for the turbulent kinetic energy and a second for the turbulent frequency (ω) [69].

k-equation:

$$\frac{\partial(\rho k)}{\partial t}+\frac{\partial(\rho U_j k)}{\partial x_j}=P_k-\beta^*\rho k\omega+\frac{\partial}{\partial x_j}\left\{\left(\mu+\frac{\mu_t}{\sigma_k}\right)\frac{\partial k}{\partial x_j}\right\} \qquad 3.22$$

ω-equation:

$$\frac{\partial(\rho\omega)}{\partial t}+\frac{\partial(\rho U_j\omega)}{\partial x_j}=\alpha\frac{\omega}{k}P_k-\beta\rho\omega^2+\frac{\partial}{\partial x_j}\left\{\left(\mu+\frac{\mu_t}{\sigma_\omega}\right)\frac{\partial\omega}{\partial x_j}\right\} \qquad 3.23$$

P_k is the production rate of turbulence, and S_{ij} is the strain rate tensor:

$$P_k=\mu_t 2S_{ij}\frac{\partial U_i}{\partial x_j};\qquad S_{ij}=\frac{1}{2}\left(\frac{\partial U_i}{\partial x_j}+\frac{\partial U_j}{\partial x_i}\right) \qquad 3.24$$

Table 3.3: *k*-ω Turbulence Model Constant Values [69]

Variable	Default Value
β*	0.09
α	0.555
β	0.075
σ_k	2.0
σ_ω	2.0

The k-ω Wilcox model, however, does not adequately treat turbulence in the bulk or wake flow regions [69]. In the free shear regions or wake, the standard k-ε model approximates the eddy viscosity more accurately and simulates the free stream conditions far better [69]. Therefore, a blend or mixture of the two models may generate an optimal closure model for certain flow conditions. The Shear Stress Transport (SST) closure model is a combination of the k-ε and k-ω turbulence models.

3.6.6.3   Shear Stress Transport (SST) model

Two equation models, such as the k-ε and k-ω alone, tend to under predict flow separation in the boundary layer due to pressure gradients [59]. The SST model attempts to correct this limitation of the two-equation models by combining the desirable aspects of the k-ε and k-ω models. This approach applies the k-ω Wilcox model near the solid walls and the k-ε model attributes in the free shear flows [59]. The switching or transition from one model to another occurs using a unique blending function. This blending function modifies the eddy viscosity accordingly by bounding the turbulent stresses inside of the boundary layer [59, 69].

The k-ε model is transformed into the k-ω model into a similar approach as represented previously by the k-ω model. The k-ε model is multiplied by a blending function $(1-F_1)$ and then subsequently added to the original k-ω times F_1. The blending function (F_1) was designed to equal one in the sublayer / logarithmic regions and approach a value of zero in the free shear flow domain [69]. Thus, this arrangement allows for the Wilcox model to dominate near the walls and the k-ε model to dominate flow conditions in the free shear regions. The transformation of the k-ε model to the SST model is reflected in the following equations [69]:

$$\frac{D\rho k}{Dt} = \tau_{ij}\frac{\partial u_i}{\partial x_j} - \beta^*\rho\omega k + \frac{\partial}{\partial x_j}\left\{\left(\mu + \sigma_{k2}\mu_t\right)\frac{\partial k}{\partial x_j}\right\}$$

<div align="right">3.25</div>

$$\frac{D\rho\omega}{Dt} = \frac{\gamma_2}{\nu_t}\tau_{ij}\frac{\partial u_i}{\partial x_j} - \beta_2\rho\omega^2 + \frac{\partial}{\partial x_j}\left\{\left(\mu + \sigma_{\omega2}\mu_t\right)\frac{\partial\omega}{\partial x_j}\right\} + 2\rho\sigma_{\omega2}\frac{1}{\omega}\frac{\partial k}{\partial x_j}\frac{\partial\omega}{\partial x_j}$$

<div align="right">3.26</div>

In this transformation, the original k-ε equations, as presented earlier in **Equation 3.16** and **3.17**, are multiplied by F_1, and then these equations are then multiplied by (1-F_1). Each set of equations are added together to give the new SST model:

$$\frac{D\rho k}{Dt} = \tau_{ij}\frac{\partial u_i}{\partial x_j} - \beta^*\rho\omega k + \frac{\partial}{\partial x_j}\left\{\left(\mu + \sigma_{k1}\mu_t\right)\frac{\partial k}{\partial x_j}\right\}$$

<div align="right">3.27</div>

$$\frac{D\rho\omega}{Dt} = \frac{\gamma}{\nu_t}\tau_{ij}\frac{\partial u_i}{\partial x_j} - \beta\rho\omega^2 + \frac{\partial}{\partial x_j}\left\{\left(\mu + \sigma_{\omega}\mu_t\right)\frac{\partial\omega}{\partial x_j}\right\} + 2\rho(1-F_1)\sigma_{\omega2}\frac{1}{\omega}\frac{\partial k}{\partial x_j}\frac{\partial\omega}{\partial x_j}$$

<div align="right">3.28</div>

where the blending function F_1 can be derived relating the energy production and dissipation to the boundary wall distance [69].

3.6.6.4   Near-Wall Modeling

Near a boundary wall, strong gradients may exist in dependent flow variables due to the viscous flow effects. The turbulence closure models apply wall functions to resolve gradients along a near-wall boundary. These functions link flow conditions in the sublayer region to empirical formulas in order to provide near-wall boundary conditions for the mean flow and turbulent equations. A substantial number of nodes is typically required to resolve the solution in these boundary, near wall regions. Applying wall functions decreases the required nodes and thus reduces the convergence time. **Figure 3.1** displays a diagram of the near wall region [56].

The presence of the turbulent boundary layer arises from shear and pressure gradients in the fluid flow near the wall [59]. In the innermost region or the viscous sublayer, the flow is laminar with the molecular viscosity dominating the flow conditions and momentum. Along the boundary or wall, the production of the kinetic energy is due to turbulence through the Reynolds stresses and dissipation of energy due to viscosity [59]. The transition layer or region between the viscous and turbulent layers has both viscosity and turbulence driving the flow conditions. In this transition region, energy exchange is virtually in equilibrium as the local production of energy and local dissipation of energy compensate each other [59]. In the outer layer or fully turbulent region, turbulence dominates the flow conditions with convection and dissipation driving energy exchange[59].
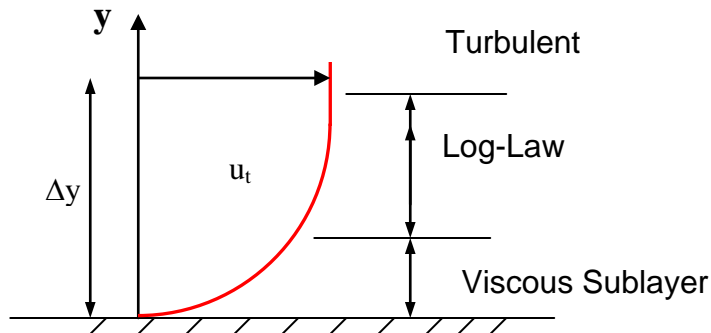
Figure 3.1: Near-wall region (derived from:[67])

For a standard log-law wall function approach, the near wall tangential velocity (u+) is related to the wall shear stress as given by [56]:

$$u^+ = \frac{1}{\kappa}\ln(y^+) + C \qquad\qquad 3.29$$

where

$$u^+ = \frac{u_t}{u_\tau} \qquad\qquad 3.30$$

$$y^+ = \frac{\rho(\Delta y)u_\tau}{\mu}$$
　　　3.31

$$u_\tau = \left(\frac{\tau_w}{\rho}\right)^{1/2}$$
　　　3.32

τ_w represents the wall shear stress, u_t is the tangential velocity to the wall at a distance of Δy, κ denotes the Von Karman constant for smooth walls, and C is a constant that depends on the wall roughness.

The use of logarithmic functions, as in ANSYS CFX-Solver, has risk since equations could become singular when the tangential velocity approaches zero. Therefore, u^+ can be approximated based on the following relationship: [62, 67]

$$u^+ = c_\mu^{1/4}\sqrt{k}$$
　　　3.33

where

$$\tau_w = \tau_{visc}\frac{y^*}{u^+}$$
　　　3.34

$$y^* = \rho u^+ \Delta y / \mu$$
　　　3.35

$$u^+ = \frac{1}{\kappa}\ln(y^*) + C$$
　　　3.36

3.7　Chapter Summary

This chapter discussed the theory of CFD in the context of this dissertation work. It detailed the background and theoretical framework of the software for ease of understanding. Using these software programs, the next chapter presents the theoretical background of the experiments for this dissertation. In order to validate the numerical methods discussed in this chapter, physical experiments are conducted.

CHAPTER 4: Experiment Theoretical Background

4.1   Introduction

Particle image velocimetry (PIV) is a flow measurement technique that is utilized to measure the instantaneous fluid velocity within a fixed geometry. It is related to other flow measurement techniques, such as laser doppler anemometry and particle tracking velocimetry [42]. Light-based measurement methods have the distinct advantage over other velocity measurement techniques. Light is capable of passively measuring the fluid flow field and does not cause an obstruction or a disturbance to the flow which occurs using Pitot tubes or hot wire anemometry. Light can also span a wider area and move into regions with tight spaces and complex geometries, where a physical probe cannot go.

PIV, as shown in **Figure 4.1**, in 2-D space is performed by taking a high energy laser pulse and forming it into a wide sheet using a set of optics. This laser sheet is used to illuminate a two-dimensional plane within the fluid model. The fluid flow field is uniformly seeded with neutrally buoyant particles. Light from two successive laser pulses, a known amount of time apart, is reflected from the particles and is captured by a high speed camera. The camera uses an electronic chip for digital image recording located behind the camera lens. The chip collects and transfers the image data to the computer. Two successive images are taken and are timed to coincide with the laser pulses.
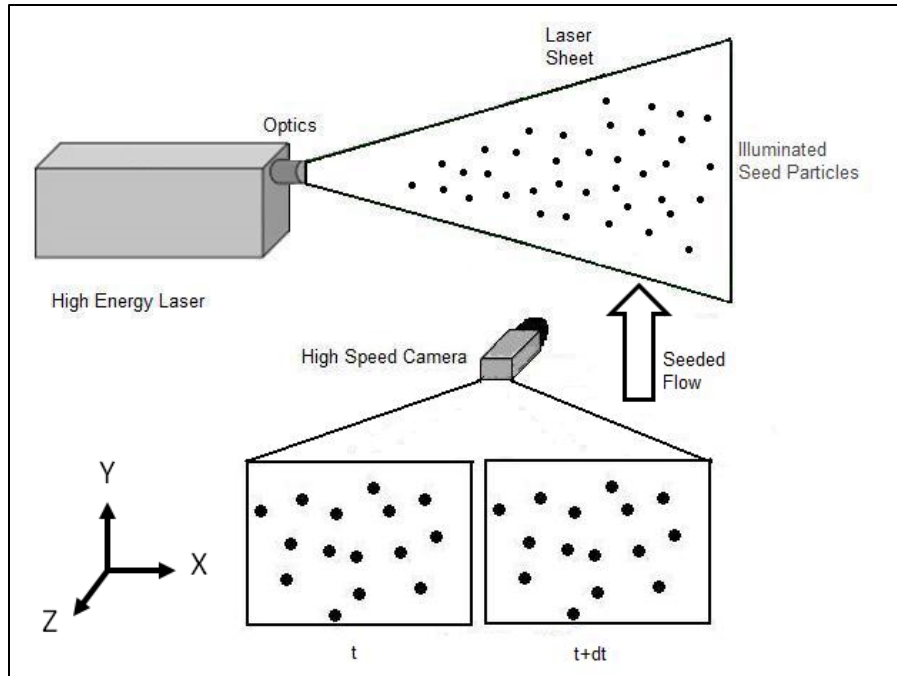
Figure 4.1: 2-D Particle Image Velocimetry

The basic data processing scheme is illustrated in **Figure 4.2** and is as follows. The image data is divided into squares on a grid called interrogations regions and the two images are compared using a using Fast Fourier Transforms (FFT) to perform a cross-correlation algorithm. The size of these regions determines the spatial resolution of the measurement. The cross-correlation algorithm produces a peak within each region, the peak is located using a Gaussian curve. An inversion of the FFT combined with a spatial calibration produces the local velocity field. It is important to remember that each interrogation region has exactly one velocity vector based on the seed particle displacement and time elapsed between the two successive images. The velocity data can then be used to create velocity vector plots and streamline plots in order to assess the fluid dynamics in the region of interest (ROI).

In the following sections, the above description of PIV will be laid out in more detail in order to assess how each component of the testing apparatus functions and interacts with each

other. The discussion will be compounded doubly in complexity with an ascension to 3-D techniques in **Section 4.9** and finally to volumetric PIV techniques in **Section 4.11**. In essence, we will be building from the 2-D approach increasing in complexity to 3-D and volumetric analyses in this chapter. The following section, **Section 4.2,** will give a brief review of the use of PIV in the design of blood pumps.
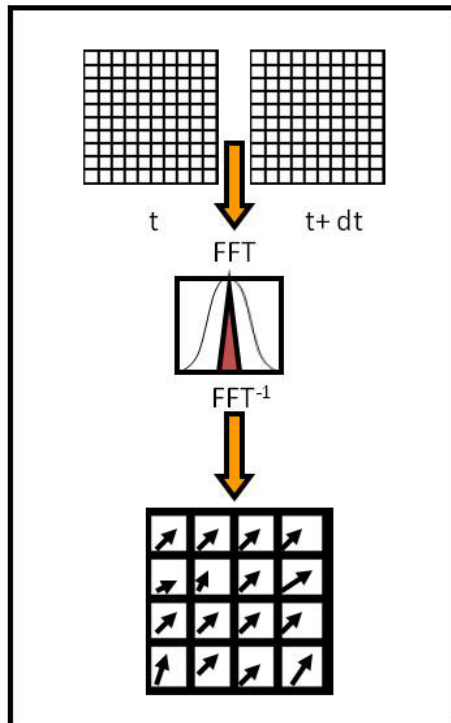
Figure 4.2: Particle Image Velocimetry Vector Processing: The images are broken up into interrogation windows and then a cross-correlation algorithm combined with Fast Fourier Transforms is used to determine the particle displacement. Velocity vectors are determined through an inverse transform and a spatial calibration.

4.2   The Use of PIV in Blood Pump Design

Particle image velocimetry measures the instantaneous velocity of fluid flow within a given region of interest and allows for the visualization of the fluid dynamics through plots of the velocity vector field. Visual inspection of a vector plot allows for the display of the local fluid

velocity gradients which allow for the identification of vortices, flow stagnation regions, and irregular flow patterns. Fluid flow structures are important in the design of blood pumps because irregular flow patterns and stagnation regions can lead to hemolysis and thrombus formation [44, 45].

Particle image velocimetry has a proven track record for testing of blood pumps including both axial flow and centrifugal pumps. Day *et al.* [52, 70] used PIV to examine different regions of the HeartQuest centrifugal ventricular assist device. Su *et al.* [71] studied the internal flow patterns of an axial flow pump and performed PIV studies in order to validate computational fluid dynamics simulations. Liu *et al.* [72] used PIV to examine the exiting flow into a cannula for a prototype LVAD. All of these research groups used commercial PIV software for their PIV studies. Over several years, the VCU BioCirc Lab has successfully used PIV to evaluate impeller prototypes for our axial flow pump designs. The data gathered from the PIV studies provides guidance for future design iterations of the cavopulmonary assist device.

4.3   The Measurement Plane

The measurement plane corresponds to the region in the fluid flow field where the PIV measurement is taken. It is restricted to the width of the laser light sheet and the available field of view of the camera. 2-D PIV provides information about the planar fluid flow field in the in-plane directions, which is denoted by x and y on a Cartesian coordinate system. It provides 2 components of the velocity, with u denoting the velocity component in the x-direction and v denoting the velocity component in the y-direction. 2-D PIV measures a projection of a 3-D velocity vector in a 3-D fluid volume within the 2-D plane of the laser light sheet. Information

about the motion of the particles and their velocity perpendicular to the laser light sheet in the "out-of-plane" z-direction are not measured.

4.3.1 Important Terminology

Some basic terminology will help with the ensuing discussing of 2-D PIV in the coming sections. The *light plane* is the volume of fluid that is illuminated by the laser light sheet. The *object plane* is the volume of volume of fluid within the light sheet that the velocity measurement is performed on. The *image plane* is the image from the light plane captured on the CCD chip. It is a reproduction of the object plane. The light plane is a 3-D volume while the object plane is interpreted solely as a 2-D surface. The volume that is selected from the light plane for cross-correlation is called the *interrogation volume*. *Particles* refers to seed particles while *particle image* refers to the image of each particle on the image plane. The two captured images used for determining the particle displacement are referred to as a *particle image pair*.

The corresponding location of the volume captured on a 2-D plane is the *interrogation area* or *interrogation region*. Displacement vectors in an interrogation volume are 3-D, while displacement in an interrogation area yields only 2-D vectors. The *spatial resolution* for a velocity vector is the size of the interrogation window. This relates to the spatial resolution within the fluid flow field so that the velocity vector field will have one and only one vector per an interrogation area so that it is the distance between two vectors.

The main idea is that velocity data from a 3-D volume must be recorded onto a 2-D CCD chip inside of the camera. It is only possible to collect information about the fluid dynamics in this manner. Some information about the three-dimensionality of the fluid domain is inherent to the particle image pairs. The photography term *depth of field* is used to define the spatial reference of the image focus which is controlled by the lens aperture f-stop value and the lens

magnification. It is twice the distance from the object plane in which the particle is considered to be unfocused and contributes to background noise. Also of use is *depth of correlation*, which is defined as twice the distance that a particle can be positioned from the object plane so that the light intensity can be considered to be a fraction of its focused intensity. Beyond this value, the light intensity of the particle cannot contribute to the velocity measurement and instead contributes to the background noise. Depth of field and depth of correlation become important when dealing with highly 3-D flows that can cause particles to move rapidly through or across the light sheet. This out of plane motion can cause erroneous velocity vectors in the velocity measurement data. We are reminded of PIV's roots in statistics by the use of correlations in data processing. Correlation is the measure of the similarity between two or more groups of arranged points or variables. The term *cross-correlation* is a reference to a particular type of correlation. Cross-correlation is a measure of the similarity between two signals. If the two signals are functions of two independent variables, then a displacement or shift can be inferred between the two signals [42]. With regard to PIV theory, the two signals are the 2-D light intensity fields from two separate images. We will expand upon the concept of cross-correlation further in **Section 4.5** as part of an in-depth discussion on the specifics of vector processing. The *signal to noise ratio* (SNR) refers to the ratio of the signal amplitude or signal power with regard to the background noise. SNR is an important factor in PIV since light that is reflected or emitted from particles must be sufficient to override the background noise in a particle image. This will have a direct effect on the cross-correlation of the two images and the resulting error in the measurement. An in-depth discussion of 2-D PIV error will occur in **Section 4.7**.

4.3.2 Particle-Fluid Interaction

Since PIV provides an indirect measurement of the velocity of seed particles in the fluid flow field, the equivalent relative velocity between the particle and the fluid velocity must be quantified in order to determine possible sources of error. It is generally assumed that seed particles track the fluid streamlines of the flow in order to give an accurate measurement of velocity. Particle tracking velocimetry (PTV) is an alternative measurement technique which uses the Lagrangian point of view and incorporates special tracking algorithms to follow the three-dimensional motion of particles [42]. All particles move in 3-D space, however, the defining difference between PIV and PTV other than point of view is that PIV has information on the particle motion within the two images of fluid flow. There is no information on the particle motion during the time delay between the two images (Eulerian point of view). For this reason, the time delay or delta t value (δt) will be a topic of further discussion, since it is just as important as the particles in determining the local velocity magnitude.

Ideally, tracer particles should be matched to the fluid density. However, there is often a small, but frequently negligible density mismatch (<5%) that inevitably occurs. The diameter of the particles should be very small to ensure good tracking of the fluid motion, but not too small since this would affect the ability of the particles to effectively scatter light and in turn affect the image light intensity. A trade off exists between the particle size and the density. Particle density is a primary factor in particle selection since the material should have density that is close to that of the fluid medium. Particles that have densities that are greater than or less than the fluid density will tend to sink or rise in the fluid and have limited tracking capabilities [73].

The two main influences on particle motion are inertia and gravity. The effect of inertia determines the ability of the particle to suddenly change direction, while the gravitational effect

acts on the difference in the relative densities of the tracer particles and the fluid medium. It is possible to estimate the effects of both components by estimating the amount of drag acting on a particle and comparing it to the resultant force. A single particle can be reasonably assumed to be a solid sphere. An appropriate model that is used is that of Stokes' Law, which is applied to a sphere in a viscous flow with a Reynolds number less than one. Stokes' Law tends to give a conservative estimate of the particle tracking abilities since the actual drag tends to be somewhat higher [73]. A viscous flow at a higher Reynolds number will have much higher drag than Stokes drag and serves to underestimate the amount of drag force on a particle and its ability to track the flow. In the Stokes flow regime, provided the object is a sphere, the Stokes drag force, D_f is provided by **Equation 4.1**, where μ is the dynamic viscosity, U is the fluid velocity and U_p is particle velocity.

$$D_f = 3*\Pi*\mu*d_p\left(U - U_p\right)$$

4.1

The settling velocity of a particle U_g shown in **Equation 4.4** can then be defined by equating the gravitational force in **Equation 4.2** with the Stoke drag of **Equation 4.1** to produce the intermediate equation, **Equation 4.3**. Physically, this signifies that the particle is at equilibrium such that the acceleration does not change and that the weight of the sphere is balanced by the viscous drag acting on it [42, 68].

$$F_g = \frac{1}{6}*\Pi*d_p^{3}*\left(\rho_p - \rho_o\right)*g$$

4.2

$$F_g = D_f = 3*\Pi*\mu*d_p\left(U - U_p\right) = \frac{1}{6}*\Pi*d_p^{3}*\left(\rho_p - \rho_o\right)*g$$

4.3

$$U_g = d_p^{2}*\frac{\left(\rho_p - \rho\right)}{\left(18*\mu\right)}*g$$

4.4

46

The drag force can be compared to an acceleration force 'a', experienced by a particle to determine the ability of a particle to respond to changes in fluid velocity. The difference between the particle velocity U_P and the fluid velocity U is the particle lag velocity denoted U_s, that is shown in **Equation 4.5**.

$$U_s = U_P - U = d_p^2 * \frac{(\rho_p - \rho)}{(18 * \mu)} * a$$

4.5

The transient response of a particle velocity $U_P(t)$ to a step function input in fluid velocity is an effective measure of its ability to track the flow. An equation for the time response to a step change in fluid velocity is given when the particle density is much greater than that of the fluid such that the fluid density is ignored altogether [42, 73].

$$U_P(t) = U\left[1 - e^{\frac{-t}{t_s}}\right]$$

4.6

Further analysis of the particles is gained by rearranging the expression to form the non-dimensional Stokes number. The particle relaxation time, t_s is defined by **Equation 4.7**.

$$t_s = d_p^2 \frac{\rho_p}{18\mu}$$

4.7

If the fluid acceleration is not constant or Stokes drag around a simple sphere does not apply, the equations of particle motion become more difficult to solve. Such solutions are available in Mie, *et al.* [74]

4.3.3 Seed Particles

If the fluid and particle properties are known values then the above equations can be utilized to model the ability of the seed particles to track the fluid flow. The working fluid for the intended PIV experiments is a solution of 94% diethyl phthalate and 6% ethanol with a density of 1105 kg/m^3, a dynamic viscosity of 3.5 cP, and a kinematic viscosity of 3.2 cSt. The seed particles are rhodamine B fluorescent spheres (Fluostar, EBM Incorporated, Model No. FF1015-01) with a nominal diameter of 13 $microns$ and a density of 1,100 kg/m^3. These particles able absorb the laser light and emit light at of a specific wavelength of 622 nm (orange light) which serves to increase the signal to noise ratio of the PIV measurement.

Given the close proximities of the particle and fluid densities, we are able to state that the particles are effectively neutrally buoyant. The settling velocity is $12x10^{-9}$ m/s. Further analysis reveals that the relaxation time is negligible at about $0.9x10^{-6}$ s. The inertial and gravitational effects on the particle are negligible so the particles will provide effective tracking of the fluid flow patterns. This is fact is important when identifying stagnation or recirculation regions within the fluid flow field.

Since the working fluid is a clear, viscous fluid that is meant to approximate the properties of whole blood, the seed particles can be used to an extent, to simulate blood cells. A white blood cell is on the order of 10-12 $micron$ in diameter, while a red blood cell is on the order of 6-8 $micron$ in diameter, both of which are close to the 13 $micron$ diameter particles used. A limitation is present in the shape in that the particles are spheres, while a red blood cell is a biconcave disc. Despite this fact, a parallel can be drawn between the particles and the blood cells such that a recirculation region in the fluid flow field would be indicative of a similar flow structure that could promote thrombus formation.

4.4   Commercial PIV System: Hardware

The particle image velocimetry system used for this dissertation work was a commercial PIV system sold by TSI, Inc. (TSI, Inc. Minneapolis, MN). In this section, the main hardware components of the PIV system will be discussed in detail.

The laser in the PIV system is a double pulsed Nd:YAG laser (New Wave Research, Inc., Fremont, CA) with a maximum laser pulse intensity of 50 *mJ/pulse* and firing rate of 15 *Hz.* There are two key parts of the laser, which are electronically controlled. These are the flashlamp and the Q-switch on each of the two lasers. The flashlamp generates the energy that is converted into the laser pulse. The Q-switch acts as a shutter to release the laser pulse. Nd:YAG lasers emit at 532 *nm* wavelength corresponding to the color green in the visible spectrum.

Before using the laser for an experiment, it is necessary to make sure that both lasers are on the fixed alignment path, and that the laser pulses emitted from the two lasers are: 1) Gaussian, such that the laser pulse will have a Gaussian distribution of light intensity, and 2) the laser pulses have similar light intensities associated with them. If the laser light intensity is not consistent between the two lasers then the two captured images will have different light intensities associated with the illuminated plane, which will affect the estimate of the velocity. The laser pulse intensities were verified to match between the two lasers before the PIV system is used for an experiment.

The laser sheet is created using a lens array. The cylindrical lens controls the light sheet divergence angle, broadening the pulse so that it fans out to form the laser sheet. The spherical lens limits the divergence of the laser sheet and sets the light sheet thickness. The lens and the lens holders were manufactured by TSI. The lens array hardware is produced by Thorlabs, Inc. (Thorlabs, Inc., Newton, NJ). In order to minimize particle motion inside of the laser sheet and to maintain a reasonable spatial resolution, it was determine that the laser sheet would need to be

a thickness of 1 *mm*. Two 25 *mm* diameter lenses were selected to meet this criterion. The cylindrical lens had a focal length of -15 *mm* (TSI Model No. 610081) and the spherical lens had a focal length of +500 *mm* (TSI Model No. 610062). This corresponded to a laser sheet with a 1 *mm* waist and a width of 250 *mm*. The lenses were attached to the lens holders on the lens array. The fluid model would therefore need to be positioned at a distance of 500 *mm* such that the model will be at the focal length of the spherical lens and the thinnest part of the laser sheet. This arrangement has been shown to minimized errors associated with laser light propagation since the waist of the laser sheet falls directly in the center of the region of interest.

The PIV system has two high speed cameras (TSI Model No. 630066, PowerView 1.4MP). The cameras are able to capture 12-bit images with a minimum time delay between of 200 *ns* between image captures. The cameras use a Charge Coupled Device (CCD) chip, which is a referenced to the photo-reactive chip that is located behind the camera lens. The CCD chip in each camera had an available resolution of 1376 x 1040 pixels. It is important to note that the high speed camera only captures gray-scale images. This is to increase the spatial resolution of the camera and to speed up the data transfer by having to transfer only one channel of data as opposed to three channels for color images. The CCD chip in the camera captures the raw data images, such that its function can be approximated to be a light intensity meter [75, 76]. Each camera is equipped with a short range lens (AF Micro Nikkor 60mm lens, Nikon Camera Co., Melville, NY).

The laser is used on higher power such that it was able to deliver the maximum energy of 50 *mJ* per pulse. This is to compensate for the dissipation of laser pulse energy that occurs as the pulse travels through the lens array, then through open space and finally through the side wall of the model to illuminate the measurement plane. Too much high intensity light can damage or

destroy the CCD chip. The lens aperture for the camera lens has to be adjusted to limit the amount of light that can enter camera. The light intensity can also be limited by the use of an optical filter which limits the background noise and promotes the SNR for the particle images. The f-stop value will also affect the depth of field of the captured image by limiting the portion of the image that is in focus. An f-stop value of 32 is applied to the lens aperture. A narrow band color filter with a wavelength cut-off of 545 *nm* (TSI Model No. 610072) was utilized to collect the light emitted from the seed particles and block noise created from light being reflected and scattered from the model and nearby surfaces.

A computer controlled synchronizer (TSI Model No. 610035) is employed to set the timing for the data acquisition and to interface the cameras and the laser with the computer. The synchronizer is used to control the timing between the laser pulses and image capture of the camera. Without the synchronizer, there would be no way to keep the laser and cameras in the proper sequence [76].

4.5   Parameters for Data Acquisition

4.5.1 Frame Straddling Technique

In an effort to address both the temporal and hardware constraints of the PIV system, a technique called frame straddling was used. The Nd:YAG laser is limited by the recharging time for the flashlamp, which creates the laser pulse. Similarly, the camera is limited by the frame capture rate and its data transfer rate to the computer hard drive, which are both fixed values. These factors severely limit the time, the delta t value (δt), between image captures. The typical PIV measurement is as follows: the laser is fired and a region of the flow is illuminated, which is simultaneously captured by the camera creating the first image. The laser shuts down briefly in

order for the flashlamp to recharge and then fires a second time, with the camera capturing the second image. Using two lasers, the frame straddling approach is able to reduce the time between frames significantly. Firing two separate lasers eliminates the problem of waiting for the flashlamp to recharge between pulses and the camera is able to continuously read out the image data by controlling the opening and closing of the shutter. The diagram in **Figure 4.3** illustrates the frame-straddling technique where the first laser pulse is fired at the end of the first frame of the CCD camera, the second laser pulse is delayed by the δt value, and then it is fired near the beginning of the second frame. The camera camera stops recording only briefly during the time delay for the δt value. The exposure time for each frame is regulated by camera hardware and the PIV software and a specifically timed to be in sequence with the laser pulses.
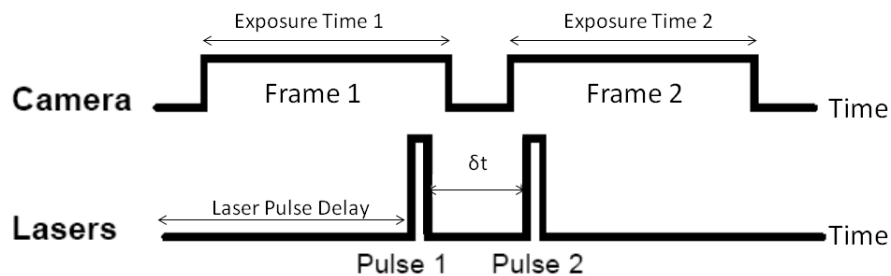
Figure 4.3: Frame Straddling Technique (derived from [5, 42])

4.5.2 Hardware Timing for Data Acquisition

Additional temporal settings that are used as part of the frame straddling technique shown in **Figure 4.3** are further described in this section. There are three main temporal settings that are controlled during the PIV measurement. These are the delta t value, the laser pulse delay, and the frame exposure time. Each PIV measurement occurs by taking two successive images at a known value of time apart. This value of time is called the delta t value (δt) which is chosen based upon the estimated velocity magnitude of the flow being measured. For the PIV measurements, the δt

value has to be determined experimentally and is critical to the image processing and analysis that occurs after the measurement. Since two lasers are used during the measurement, and since the image is only visible during the duration of the laser pulse, the δt value becomes the distance between images and the set amount of time available for particle displacement. The δt value must be optimized for the experiment. If this value is too large or too small than the particle motion and the underlying fluid dynamics may not be adequately resolved, limiting the spatial resolution of the data and adding to the measurement error.

The second temporal setting is the laser pulse delay. This parameter is used to specify an amount of time to wait before activating the first laser in a firing sequence. This allows for the first laser pulse to be fired toward the end of the first frame. This value of time is set to 250 microseconds. The third temporal setting is the frame exposure time. This parameter is used to set the amount of time that the camera shutter is open for the first frame that was captured. The value of time is set to 500 microseconds. The second frame exposure time shown in **Figure 4.3** is a fixed value that is hardware dependent for the camera being used.

With the exception of the δt value, the remaining parameters remain fixed for the duration of an experiment. The δt value is usually determined at the beginning of an experiment using a procedure that will be described in detail in the next section. This value may be changed during the experiment in order to compensate for changes in flow conditions since physical velocity distribution will vary based on location in a physical model.

4.5.3 The Rules of Keane and Adrian

In PIV experimentation, the interrogation region size must be determined at the beginning of the experiment. This approach attempts to prevent the disappointment that can occur during data processing when it is discovered that the experiment did not yield viable data.

The interrogation region size is determined through an iterative approach using the method of guess-and-check to systematically adjust the δt value to an optimum value that will yield inaccurate vector data. Recall from the previous section that the δt value directly affects the available image spatial resolution and the measurement error. The available image spatial resolution is used to set the interrogation region size that will be used during vector processing. If there is insufficient seeding, or there is insufficient particle motion between the particle image pair, then it is necessary to use a large interrogation region during vector processing to obtain valid velocity vectors.

Guidance in optimizing the interrogation window size and the δt value is provided by the criteria developed by Keane and Adrian [77]. The rules specified in this article were used to select the appropriate region size for multi-pass cross-correlation. The rules state that for an image pair the following must be true:

1) The final interrogation window should be the smallest possible to resolve small flow structures and to ensure that the average velocity in each window properly represents the motion of the particles throughout the entire interrogation region.

2) There should be more than ten particle image pairs per interrogation region.

3) The maximum in plane displacement should be less than ¼ of the interrogation region size.

4) The maximum out of plane displacement should be less than ¼ of the light sheet thickness.

5) The minimum in-plane displacement should be two particle image diameters.

Some knowledge about the relative velocity and the Reynolds number of the fluid flow within the fluid domain of the model to be measured is important since it will provide a reasonable starting point for the δt value. To apply the rules, a set of test images is acquired at an arbitrary δt value. Then, an initial guess of a 16 x 16 region size is made and an equally sized

grid is applied to the image pair using the data acquisition software. With the grid in place it is noted, by visual inspection, whether the particle motion between the two successive images satisfies the rules. The number of particles in a group moving across an interrogation region is compared between the two successive images. If seeding was deemed to be insufficient, then particles need to be added to the flow and the process repeated. If the relative motion of the particles is outside of the estimate interrogation region on the grid, then the δt value is reduced. Eventually, an optimum value for the δt value will be reached [78].

An interrogation region size of 16x16 pixels is standard practice in PIV experiments. It will be discussed in further detail in **Section 4.6.3** that the smallest possible interrogation region size is 4x4 pixels. A smaller interrogation region is not necessarily possible, nor desirable, due to the increase in background noise that occurs at every decrease in interrogation region size.

4.6   Image Processing and Analysis

4.6.1 Introduction

As in shown in **Figure 4.4**, the processing of the PIV measurement data is performed in 3 separate distinct stages. Vector preprocessing prepares the velocity data for the vector processor. The vector processor determines the average velocity for an interrogation window by computing the cross-correlation function on the motion of the particles in two successive images with a known temporal delay. The post-processor eliminates any erroneous vectors, which may have been created during the processing stage. The data acquisition and processing package that was used in the PIV experiments is INSIGHT3G, version 9.1, which is provided by TSI, Inc.
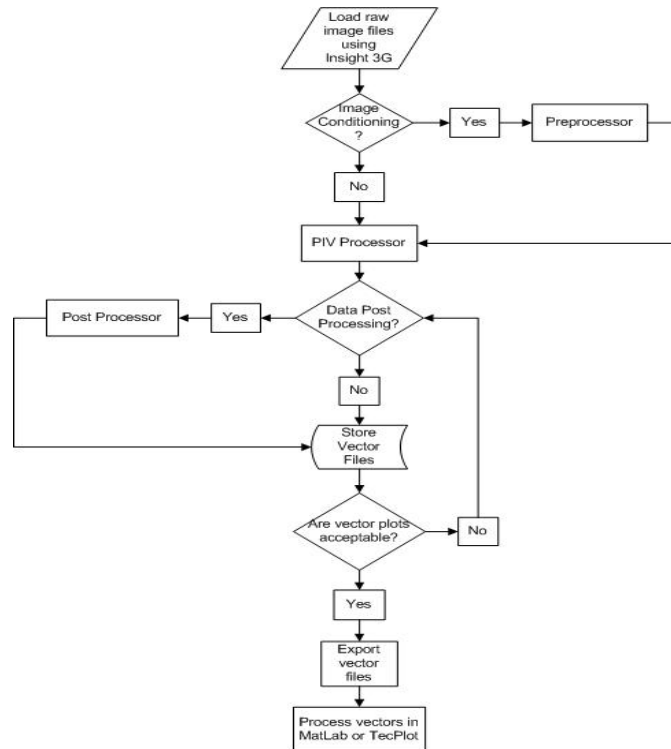
Figure 4.4: PIV processing methods flowchart [5]

4.6.2 Preprocessing

Image preprocessing provides support for the vector processor in INSIGHT3G by
manipulating or filtering the image data prior to the velocity data extraction. The image
preprocessor provides features for creating a mask for the raw image, filtering the raw image, or
rotating and translating the raw image [76].

The masking capability allows for the creation of a mask around the ROI in the captured
image to eliminate the noisy areas outside of the model or the fluid domain. Everything outside
of the mask is ignored by the computer during vector processing and analysis. The mask is not a
necessary step, but it adds aesthetic value by giving a clean image and helps to limit the data
processing load on the computer by allowing the vector processor to ignore areas of the model
that will not yield useful information. The mask helps to prevent spurious vectors outside of the
measurement area which can occur during vector processing. A mask corresponding to the

relative solid boundaries (model walls) is defined and applied to all of the images before vector processing. Further clean-up of erroneous vectors occurs in the post-processing stage as well [5].

The image calibration which relates the physical world in units of *mm* to the digital realm inside of the computer in units of *pixels* occurs as part of the image preprocessor. For 2-D PIV, an image of a ruler or an object of known dimensions can be used to provide a calibration factor for distance. Additional information on 2-D PIV calibration is provided in **Section 4.9.2.1**. Stereo-PIV which measures 3-D velocities requires a more complex calibration technique and is thoroughly discussed in **Section 4.9.2.2**.

4.6.3 Vector Processing

4.6.3.1   Raw Image Data

It is necessary to pause for a second to assess the necessity of the two successive images that were addressed in the **Section 4.5.3**. Two test images appear in **Figure 4.5** showing adequate seeding in order to accurately measure the average velocity in the ROI. In order to understand how the vector processor functions, it is first necessary to understand the nature of the raw PIV particle image pair. Recall that the high speed camera that is used to capture the images is in the larger sense a light intensity meter. The camera effectively measures the light intensity that is reflected or emitted from the seed particles. The light intensity distribution is defined by the presence of light everywhere there is a particle and dark where no particles are located. This allows for the use of a special comparison or cross-correlation method.
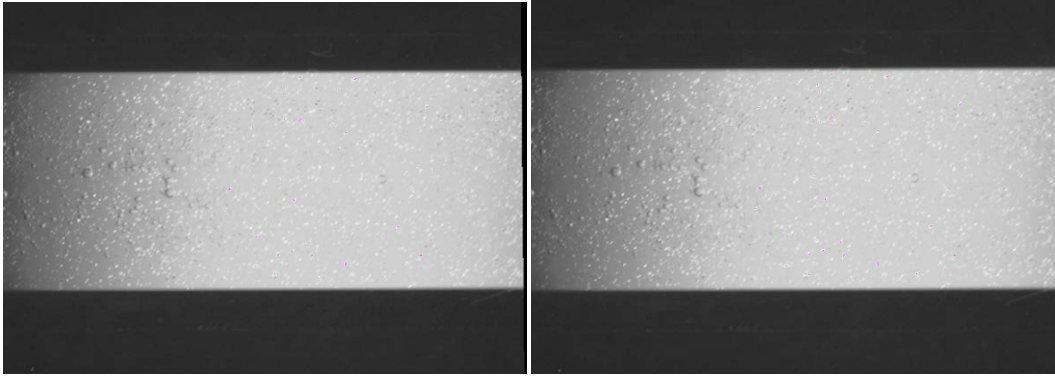
Figure 4.5 Raw PIV Data Images

4.6.3.2 Cross-Correlation Method

The velocity vector data can be extracted from the image data using a statistical approach called double frame cross-correlation processing. Initially, the image pairs are split into interrogation regions corresponding to squares on a grid. The choice of the size of the interrogation regions and the distribution of the measurement grid has already been discussed in great detail in **Section 4.5.3**. Each interrogation region will contain one and only one velocity vector after processing is completed.

When computing the particle displacement on an interrogation region, it is assumed that the particles move uniformly, that is, that all of the particles move at similar velocities and move a similar distance during the frame exposure time. The mean particle displacement cannot be directly measured from the images. In order to calculate the mean particle displacement a statistical technique call cross-correlation is used [42, 79].

Cross-correlation works on the principle of pattern recognition and comparison. It operates not only on the interrogation region but on the interrogation volume. Recall that the interrogation region will be 2-D but the interrogation volume will be 3-D due to the depth of field in the image. The local particle distribution pattern in each frame will be similar, but a group of local particles will be shifted somewhat between frames. The cross-correlation

algorithm must recognize the pattern between the two images to determine the particle displacement. The equation for the cross-correlation of image intensities of two images is shown in **Equation 4.8**. The cross-correlation function exists in the X-Y plane with the light intensity varying in the Z direction. Therefore, the cross-correlation peak that that is calculated from the cross-correlation function corresponds to the maximum light intensity. The location of the maximum value of the cross-correlation function represents the mean particle displacement between the two images [42, 80].

$$R_{II}\left(s, \Gamma, D\right) = I\left(x, \Gamma\right) I'\left(x + s, \Gamma\right) \qquad \text{4.8}$$

The variables are defined as follows: s is the separation vector that details the information for the shifting of the second interrogation window, Γ is a series of location vectors for each particle in the interrogation volume, D is the displacement vector for each particle, x is the spatial domain vector within the interrogation region, I and I' are the light intensity matrices for the interrogation area in the first and second images [42].

        Equation 4.8 is not in a usable form since the digital images collected by the CCD camera are matrices of discrete points. Therefore, **Equation 4.8** can be algebraically manipulated to produce **Equation 4.9** which is the discrete form of the cross-correlation function.

$$R_{II}\left(s_x, s_y\right) = \sum_{i=-K}^{K} \sum_{j=-L}^{L} I\left(i, j\right) I'\left(i + s_x, j + s_y\right) \qquad \text{4.9}$$

K and L are the size of the interrogation region in pixels, i and j are the indices from i=1, j=1 to the length of the region, while S_x and S_y are the sample shift values. The variables I and I' are the data samples or the light intensity values for each pixel in the first and second image for a particular interrogation region. The image I is linearly shifted over the image I' without going over the edge. For each shift position (S_x, S_y), the sum of the products of all the overlapping

pixel intensities produces one correlation value. The shift position value at which the particle images align with each other will form a maximum or peak. This peak is called the cross-correlation peak [42, 79].

The cross-correlation function statistically measures the degree of match between the two data samples for a given image shift. The cross-correlation peak can be used as a discrete estimate of the mean particle displacement. In order to provide for a more efficient procedure for cross-correlation, the use of discrete Fast Fourier Transforms (FFTs) can significantly speed up the processing and reduce the computational load as opposed to directly calculating the cross-correlation for each interrogation region. Correlation theorem states that the cross-correlation of two functions is equivalent to a complex conjugate multiplication of their Fourier transforms. The use of discrete FFTs reduces the computational load from $O[N^4]$ operations for direct computation to $O[N \log_2 N]$ operations. N is the square size of the interrogation region (K=L). This greatly simplifies things such that two 2-D FFTs can be computed on equal sized samples of the images followed by a complex-conjugate multiplication of the resulting Fourier coefficients. The inverse Fourier transform that is performed to produce the cross-correlation data for the mean particle displacement with an interrogation region is displayed in **Equation 4.10**.

$$R_{II}(x, y) = F^{-1}\left[F(I) \bullet F^*(I') \right]$$ 4.10

F is the Fourier transform, F^{-1} is the inverse Fourier transform, and F* is the complex conjugate of the Fourier transform. The interrogation region must be a square (i.e. K=L) [42, 79, 80].

FFTs work well for cross-correlation if they are used within their limits. The particle displacement should be less than N/2 or half the interrogation region to meet the Nyquist sampling criteria and to avoid aliasing. The data set is inherently assumed to be periodic in nature. If the data length N exceeds the length of N/2, then there is the potential for the

correlation peak to fold back into the correlation plane and appear on the opposing side. The interrogation region must be a square. Non-square interrogation regions have to be made square by using zero-padding which can add noise to the FFT. Some of these criteria will be familiar from the discussion in **Section 4.5.3** of the Rules of Keane and Adrian for good PIV data collection practices [43, 77, 79].

4.6.3.3 Discrete Window Offset

Offsetting the interrogation window, according to the mean particle displacement, increases the number of matched particle images to unmatched particle images and increasing the SNR of the correlation peak. The associated uncertainty in the location of the cross-correlation peak is a positive integer value that increases the allowable particle displacement, and decreases the relative uncertainty in the measurement. In order to optimize the location, a trade-off is apparent between allowing more time for the particle to displace and increasing the δt value associated with this displacement. The maximum allowable displacement of particles in an interrogation region is limited by the restriction that the majority of the particles must be present in both images, that is, they have not moved beyond the boundaries of the interrogation region. Typically, a single particle should not move more than ¼ of the initial interrogation window [81].

Creating an overlap between the interrogation regions of the first and second images has the effect of moving the correlation peak closer to the origin which reduces the measurement uncertainty. More particles are able to contribute to calculation of the correlation function, which has the added effect of increasing the signal to noise ratio and decreasing the bias error. Large displacements relative to the interrogation region size may be used, since the particle pairs in both images overlap from the interrogation region translation. Larger particle displacements increases the accuracy of the velocity measurements [81].

4.6.3.4   Multi-pass Cross-Correlation Method

Grid refinement has the advantage of refining the sampling grid, while simultaneously reducing the interrogation region size. This allows for the ability to utilize interrogation region sizes that are smaller than the particle image displacement. The choice for the final interrogation region size depends heavily on the particle image density. Noise increases with each reduction in interrogation region size such that the number of matched particle pairs decreases rapidly at small interrogation region sizes [78, 82]. Additionally, uncertainty in the particle displacement is reduced significantly when the particle image displacement is less than ½ a pixel, such that it scales proportionally to the displacement [81, 82]. The multi-pass cross-correlation method functions in the following manner:

1) Begin with a sufficiently large interrogation window that obeys the one quarter displacement rule for the particles. Recall this rule from the rules of Keane and Adrian [77].

2) Perform standard cross correlation method for the entire image using the initial interrogation window size with no image overlap in order to obtain estimates of the particle displacement

3) Scan the measurement grid for outliers using preset validation criteria and replace outliers with interpolated values. The velocities are estimates for the next highest resolution level to be achieved.

4) Recall that interrogation windows are offset by an integer value based on the estimates of the local displacements. Repeat the interrogation procedure with a smaller interrogation window size.

5) Downsize the IA to the next resolution level and repeat above steps (2-4) until the final interrogation window size is reached.

6) Perform interrogation of the measurement region using the final window size and overlap of the final measurement.

7) Validate the data.

In effect, the down sampling of multi-pass cross-correlation is able to continue down to a 4 x 4 interrogation window size. The resolution limit is set by the apparent background noise in the captured images. Background noise occurs as a result of reflection and refraction of the laser light inside of the test model as well as from particles that move perpendicular to the image plane [78, 79]. This phenomenon is unavoidable and increases the number of erroneous vectors that are present in the measurement as well as the need for data validation techniques. Some image processing techniques, such as thresholding or background subtraction, can aid in the reduction of background noise but cannot target imbedded noise in the particle images [80]. There is a trade-off between the available resolution and the background noise in the image. A smaller interrogation region is possible but at the expense of noise amplification, which would require additional methods to increase the signal to noise ratio significantly. Therefore, it is common practice to apply a 64 x 64 or a 32 x 32 pixels starting interrogation window size and a final interrogation window size of 16 x 16 pixels. An 8 x 8 interrogation window is seldom seen in macro scale PIV studies as it would require a significant noise reduction in the measurement image coupled with rigorously optimized δt value [42, 78, 82, 83].

4.6.3.5   Peak Selection

After cross-correlation is performed on the particle image pair, it is necessary to locate the correlation peak. Cross-correlation peaks can be located to within subpixel accuracy. An 8-bit digital image is capable of providing an accuracy of 1/10th to 1/20th of a pixel accuracy for 32 x 32 interrogation regions. There are three possible methods for locating the correlation peak. Each method requires fitting the correlation peak to some type of function. The possible fit methods are: Gaussian, Parabolic and Centroid. The Gaussian curve is the most common

function used because the cross-correlation of two Gaussian functions will yield a Gaussian function. If the laser light intensity reflected from the individual particles is Gaussian because of the Gaussian laser light intensity, then the correlation function can be considered to be Gaussian as well. The parabolic peak method uses a parabola to locate the correlation peak, but is not as accurate or robust as the Gaussian peak method. The peak centroid method is used when the cross-correlation peak is broad in shape. This occurs for large particle displacements or for low SNR where it is difficult to detect the light intensity reflected from the particles. A threshold is used to separate the cross-correlation peak from the background noise.
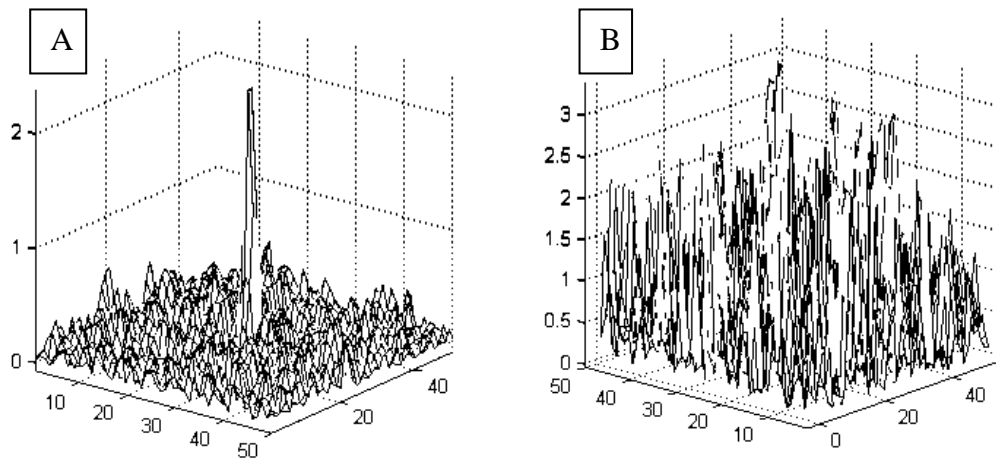
Figure 4.6: Cross-correlation peaks: A) Strong peak and B) weak peak embedded in background noise [84]

4.6.3.6   Velocity Values

The displacement of the particles is calculated by tracking the movement of the particles from one frame to the other. The particle displacement within each interrogation region is calculated using discrete correlation algorithms utilizing Fast Fourier Transforms (FFTs). After the cross-correlation function is calculated, the particle displacement distance is known in pixels. The physical distance in space is related to the measured displacement field in pixels through a spatial calibration image which provides a conversion from pixels to millimeters. Using the δt

value, it is possible to calculate the local velocity within each interrogation region. It is noted that each local velocity is independent of the others, yet all are simultaneous velocities to velocity vector field.

4.6.3.7   INSIGHT3G Vector Processor

The INSIGHT3G vector processor uses all of the previously described theory in order to determine the displacement of the seed particles within two images. An overview of the PIV processing scheme is shown in **Figure 4.7.** There are several stages to determining the velocity vectors from the interrogation windows. The Grid Engine sets up the type of the grid for the interrogation windows over both of the images and shifts the images to overlap each other. The Recursive Nyquist scheme is selected to process the vectors using the multi-pass cross-correlation method with a 50% image overlap. An initial grid of 32 x 32 pixels interrogation windows was setup with a final interrogation window size of 16 x 16 pixels over each image. The grids aligned the images with a 50% overlap to satisfy the Nyquist sampling criteria for cross-correlation. The Spot engine identifies the particle pairs within each image. It is set to 'No Mask' to prevent filtering of the pixels in the interrogation windows [76]. The Cross-Correlation engine computes the correlation function between the images. The cross-correlation engine is set to perform the correlation function using Fast Fourier Transforms. In order to prevent erroneous vectors from being used in the calculation for the next iteration of multi-pass cross-correlation, a validation scheme is put into place. The local vector validation option utilizing the universal median test for vector validation is set to calculate the mean and the standard deviation of the x and y components of velocity in a 3 x 3 perimeter around each interrogation region. The tolerance limits for the standard deviation of velocity is specified to be 2 standard deviations from the mean value. Bad vectors are removed and no data replacement is performed. The Peak

Engine identifies the peak that is generated by the FFT correlation. The Peak Engine was set to identify the correlation peak by comparing it to a Gaussian peak. In addition, a secondary peak is identified in the cross-correlation calculations and is stored in memory for use in the data replacement during post-processing [76].
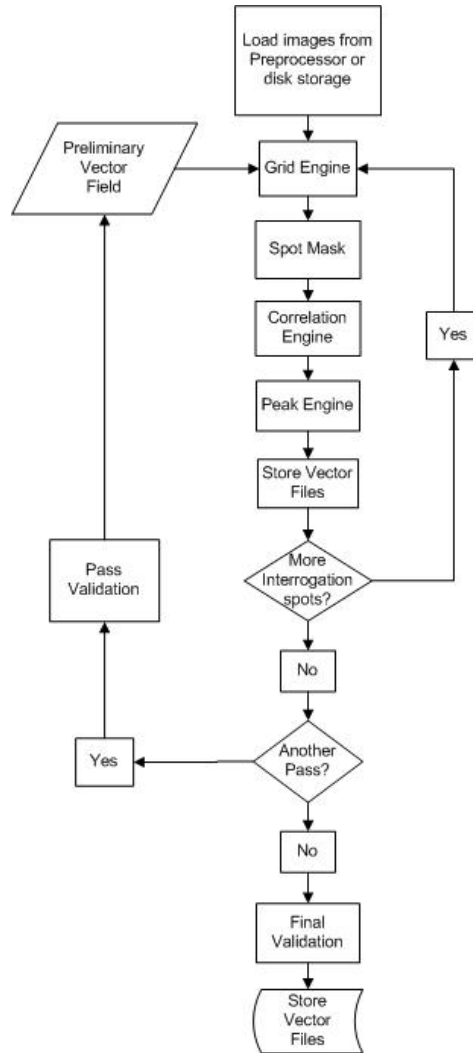
Figure 4.7: PIV Processing Flowchart [5]

4.6.4 Vector Post-Processing

Validation of vectors as well as removal of erroneous vectors is performed on the final vector field. Cross-correlation has the potential for self-propagating error due to incorrect correlation of particles. Validation schemes that are applied during cross-correlation have the ability to identify and then remove and replace erroneous vectors but may not eliminate all of those present. Unphysical vectors may be generated from light refractions in the model or by vectors that moved outside of the acquisition plane in between the two captured images and were misinterpreted by the computer. A given velocity vector field may contain 5-10% erroneous vectors although this range may be as high as 20% for flows with increased mixing [85].

There are several schemes that can be used to validate PIV data with no one standard method that is applicable to all cases. Global methods look at the velocity magnitude of all of the vectors and set a threshold based off of either mean or standard deviation of the numbers. Local mean and local median tests have a fixed threshold based off of a statistic quantity in a region of surrounding vectors. Both techniques test a selected vector against the surrounding neighbors by comparing its value with the mean or median value of all of the members in a selected area, typically 3 x 3 or in some cases 5 x 5. Local methods are better suited to regions of high velocity than global methods [86]. The universal median test tends to be more robust than the local median test.

Additional processing is performed to replace bad vectors and to fill in holes in the vector plots. Vector replacement is performed using either direct replacement or an interpolation scheme. With direct replacement either the mean or the median value of the surrounding valid vectors is calculated and used to create a valid vector to fill the hole. With data interpolation,

typically bilinear interpolation is applied to the surrounding vectors and a vector is calculated to fill the hole[42, 85].

4.6.4.1   Vector Post-Processor

The vector post-processing filter is configured in the Insight 3G vector post-processor in the following manner. The local vector validation option utilizing the universal median test for vector validation is set to calculate the mean and the standard deviation of the x and y components of velocity in a 3 x 3 perimeter around each interrogation region. This is the same criteria that are used for data validation in the grid engine of the vector processor. The tolerance limits for the standard deviation of velocity is specified to be 2 standard deviations from the mean value. The vector conditioning option is set to fill in holes in a 3 x 3 region with a valid secondary peak, or the local median.

The post-processor validates the data in four separate passes. A flow chart of the vector filter scheme is provided in **Figure 4.8**. First, the average and standard deviation of the 8 nearest neighbors to each vector were calculated for every vector in the flow field. If the vector was found to have a value that is outside the allowable standard deviation from the mean, it was removed as an outlier. A second pass removed vectors that did not have enough neighboring vectors for validation. A third pass attempted to fill in the spaces where vectors were removed. If all of the unphysical vectors are removed, then the standard deviation of the remaining vectors should be less than those of the first pass. The vector insertion criterion was set to be two standard deviations. Since one of the correlation peaks that were generated during the vector processing was stored in memory from the calculations, it can be used for the vector insertion. The fourth and final pass removed any group with less than 3 or 4 vectors and eliminated any remaining erroneous vectors. The vector conditioning function was then used to fill in the

remaining empty spaces with the median value of the remaining vectors or using a valid secondary peak. After all the PIV results are processed then the files are loaded into TecPlot 2009 (TecPlot, Inc., Bellevue, WA) to allow for quality assurance of the data [76].
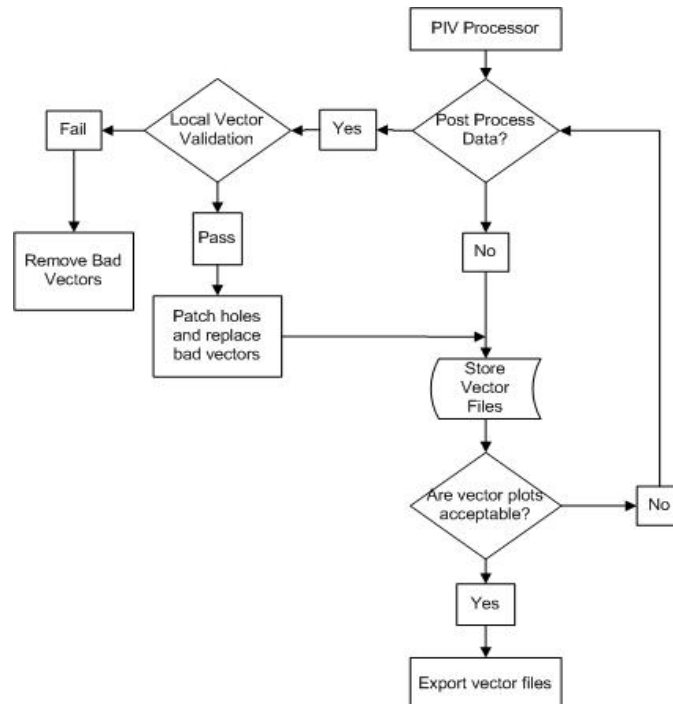
Figure 4.8: Post-processing Flowchart [5]

4.7   Sources of Measurement Error of 2-D PIV

Two-dimensional PIV has sources of measurement error, which are specific to both the data collection as well as the data processing that occurs on it. A very strong source of processing error occurs when the size of the particle images is small compared to the size of a single pixel. This adversely affects the sub-pixel interpolation that is used to locate the cross-correlation peak resulting in a phenomenon known as "pixel locking". The particle displacements are interpreted as fractions of an integer pixel which tend to be biased toward the integer value of displacement. This phenomenon can be avoided by ensuring that the particle

image is in the range of 1-2 pixels in diameter. Further limitations are caused due to using large particles and magnification from the use of lens optics [42, 81, 87].

Velocity bias can also contribute to the measurement error. If in a particular interrogation region, the particles do not have identical velocities due to irregular flows and velocity gradients, then the correlation function will be slightly wider and have a lower absolute maximum value. The location of the interrogation peak or its absolute maximum value is still a determination of the mean particle displacement. However, particle image pairs do not necessarily contribute equally to the correlation function. Statistical errors in particles will cause some particle pairs to contribute more to the correlation function than others.

The first source of correlation bias is a loss of particles between the first and second captured images. This is apparent in flows with high velocities since faster moving particles have a higher probability of moving outside of the interrogation region and not contributing to the correlation function. Recall from earlier that the correlation peak is located using a continuous function that is fitted to the correlation function. When particles are only present in one image of a two image pair, then these particles do not contribute. Slower particles are more likely to be in both images and therefore will contribute. This skews the correlation function towards lower velocities and causes the interpolation function to choose a lower value. A window offset between the two images aids in removing the bias.

Moreover, the correlation function may be biased due to light intensity from particles. Brighter particle images will contribute more than darker particle images. This may be due to the nature of particles which are manufactured to a mean diameter. Therefore, slightly larger particles will scatter more light. Similar errors can occur with non-uniformity of seeding as well

as a non-uniform laser intensity. Densely seeded flow fields will be biased to areas with higher particle density and more laser light energy.

Random errors due to particle displacement are another source of bias. These errors arise as a result of the uncertainty in locating the maximum cross-correlation peak. The error is influenced by the number of particles present inside of an interrogation region, as well as the number of particles that are present in only one of the two captured images due to fluid motion, i.e. vorticity and particle motion out of the plane of the laser light sheet.

4.8   Ensemble Averaging

In order to compensate for errors in the PIV measurement, a mean value for the velocity is obtained using a process called ensemble averaging which is that is perform in three possible methods. These are:

1) The ensemble averaging of individual instantaneous vectors to obtain a mean value is performed by vector processing a large set of vectors files to create individual vector files and then averaging the velocities together.

2) The ensemble averaging functions by averaging a set of particle image pairs to obtain an averaged image. This normalizes the light intensity in the image and strengths the cross-correlation peak during vector processing.

3) The ensemble averaging of cross-correlation peaks occurs during vector processing. The individual cross-correlation peaks of set of instantaneous velocity measurement are simultaneously averaged.

Ensemble averaging of cross-correlation peaks gives the most accurate representation of the mean velocity of fluid flow field [82]. This method was selected to be used in PIV experiments. The vector processor was set to create an ensemble average of the cross-correlation peaks from a set of 300 particle image pairs. The method yielded one averaged correlation peak which was used to determine the average velocity for a particular measurement plane.
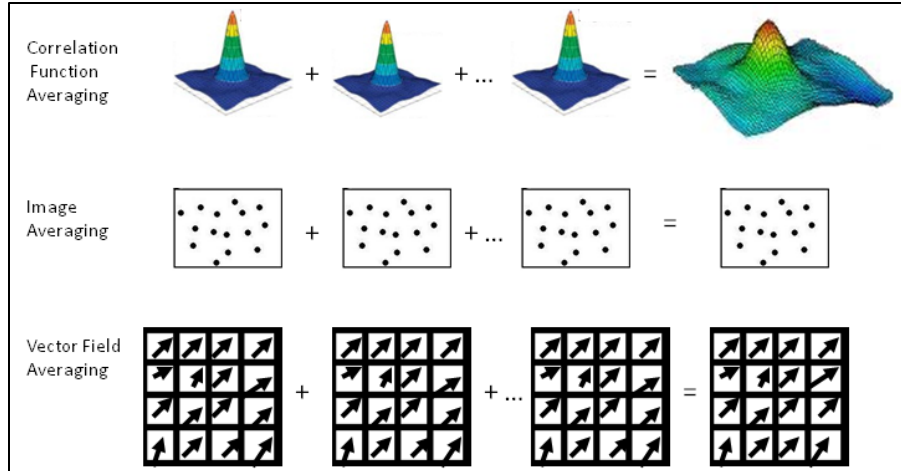
Figure 4.9: Ensemble Averaging Techniques.

B. Three-Dimensional Particle Image Velocimetry

4.9   Introduction to Stereo Particle Image Velocimetry

4.9.1 Stereoscopic Reconstruction of the Third Component of Velocity

A limitation of 2-D PIV is that it yields velocity data only within the light sheet plane and the velocity component that is perpendicular to the light sheet plane is not resolved. The out of plane velocity is important particularly in instances where there is unsteady flow and increased vorticity. These instances can cause excessive particle motion out of the 2-D measurement plane due to the inherent three-dimensionality of the flow field and can increase the relative error in the measurement. When measuring flow conditions inside of a model of an anatomic structure, such as the total cavopulmonary connection or in the downstream flow of a blood pump, the importance of the 3rd component of velocity cannot be overstressed.

Stereoscopic particle image velocimetry or Stereo-PIV is a direct extension of the principles of 2-D PIV with two or more cameras being used to collect multiple instantaneous measurements of the fluid flow field. The stereo-PIV system that is used in this dissertation work has two cameras. When stereo-PIV is performed with two cameras, two particle-image pairs are

collected. The three-dimensional flow field will be concurrent to both image pairs, but the out of plane component of velocity will result in small differences which can be determined using a stereoscopic reconstruction method. It is important to remember that the discussion of 2-D PIV in the previous sections still apply to each camera used in the stereoscopic configuration.

4.9.2 Stereo-PIV Calibration

In stereo-PIV, the high-speed cameras must be aligned to the laser light sheet at an oblique angle. Two issues arise: blurring of the image caused by the plane and the lens focal plane being rotated relative to one another and perspective distortion. The perspective distortion complicates the issue of matching the corresponding vectors between the two fields of view, since the magnification is no longer constant across the field of view. In order to compensate for these problems, the image plane, the camera lens and the laser light sheet must be brought into a common plane as viewed from the cameras and be in clear focus across the field of view. This alignment is called the Scheimpflug criterion. The camera lens is tilted relative to the camera body using a special connector and independent rotational axes. In order to compensate for the image distortion that is inherent to the viewing angle, image preprocessing must be performed prior to vector analysis. If two reconstructed vectors were not obtained from the same physical location in the physical space, then the reconstructed vectors will produce meaningless information and add to the measurement error [42, 88].

The system calibration has an additional function in stereo-PIV. First, it provides a means to convert the image between the physical space and the computer space. This is the distance calibration, which provides an mm/pixel calibration factor. Second, the system calibration provides a means to correct for the perspective distortion introduced into the measurement by the introduction of the Scheimpflug criterion. The perspective distortion is removed by introducing a

mapping function that allows for the distorted raw image data to be related to a regularly space grid to be undistorted.

Figure 4.10 provides a great deal of information about the setup of the stereo-PIV. The angles θ and α represent the Scheimpflug angle of the lens and the camera angle or the image plane angle in the Z-X plane with Y going into the page. The dash lines represent the intersection of the planes of view of the cameras at point Q. The term h represents the distance from the measurement plane or the object plane. The image plane represents the plane of view of the CCD chip.
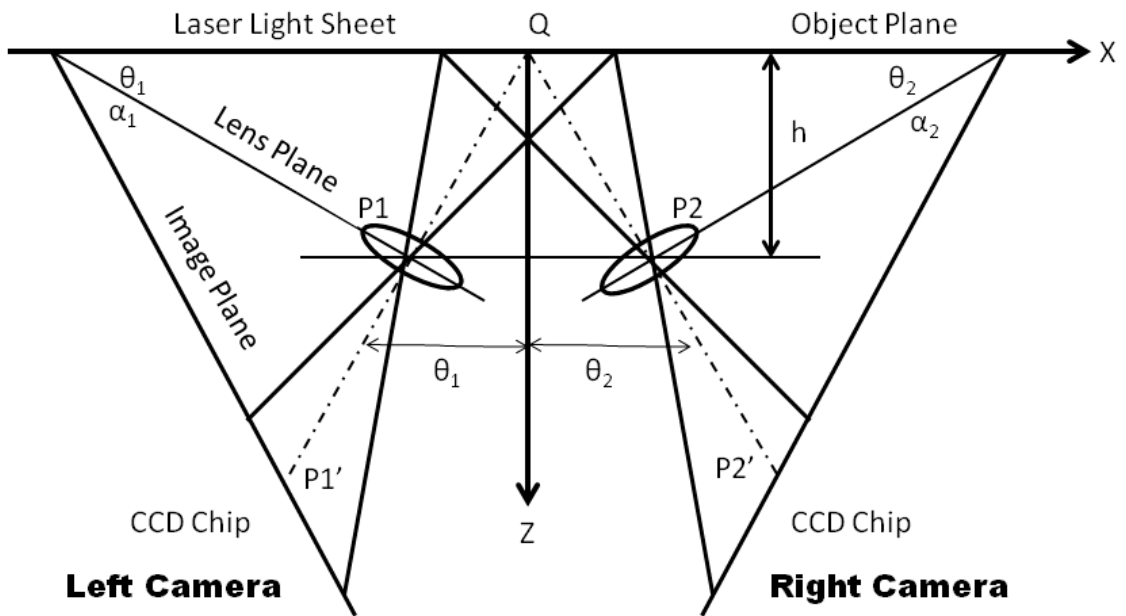
Figure 4.10: Stereoscopic Viewing Angles for the Angular Displacement Method (derived from [42, 88])

With regard to the axes, the cameras are positioned in 3-D space and are acted upon by motion in the x, y, and z axes as well as rotational angles α, β, and γ corresponding to the y, x, and z axes, respectively. The term β represents the camera angle with regard to the image plane. In order to provide an accurate and precise stereo-PIV measurement, the image plane, the camera lens of

both cameras and the laser light sheet must be brought into a common alignment as viewed through the CCD chips in the cameras and the images must be in clear focus across the field of view.

Using **Figure 4.10**, it is possible to derive expressions for the motion of a particle located at point Q and its perspective motion recorded by the two high-speed cameras at points P1' and P2'. **Equations 4.11-4.13** represent the motion of a particle on the object plane in 3-D space represented by the terms x_1 x_2 and x_3 to represent the x, y, z displacements with regard to the displacements X^1 and X^2 to represent X and Y motion on the image plane of the CCD chip. The attached subscripts represent the respective cameras.

$$x_1 = \frac{X_1^{(1)} \tan(\alpha_2) - X_1^{(2)} \tan(\alpha_1)}{\tan(\alpha_2) - \tan(\alpha_1)} \qquad 4.11$$

$$x_2 = \frac{X_2^{(1)} \tan(\beta_2) - X_2^{(2)} \tan(\beta_1)}{\tan(\beta_1) - \tan(\beta_2)} \qquad 4.12$$

$$x_3 = \frac{X_1^{(1)} - X_2^{(1)}}{\tan(\alpha_1) + \tan(\alpha_2)} = \frac{X_2^{(1)} - X_2^{(2)}}{\tan(\beta_1) + \tan(\beta_2)} \qquad 4.13$$

The above equations are over-defined with four known and three unknown values. A further simplification can be made. If the camera tilt angle β is very small representing cameras located on a common plane then the x_2 equation can be modified to form **Equation 4.15** which forms an averaged value of Y displacement. Typically this equation is used to improve the accuracy of the x_2 term, however this only occurs in an ideal case [89, 90].

$$x_2 = \frac{X_2^{(1)} \tan(\beta_2) - X_2^{(2)} \tan(\beta_1)}{\tan(\beta_1) - \tan(\beta_2)} = \frac{X_2^{(1)} + X_2^{(2)}}{2} + \frac{w}{2} * (\tan(\beta_2) + \tan(\beta_1)) \qquad 4.14$$

$$x_2 = \frac{X_2^{(1)} + X_2^{(2)}}{2}$$ 4.15

Figure 4.11 further illustrates **Figure 4.10** to show the image planes that would be captured by the camera configuration. It is important to note that the images must intersect in a common area. If the image pairs for both the left and the right camera are dewarped and cross-correlated, the reconstruction of the out-of-plane velocity will only occur in regions where the two images overlap. Areas of the image that are outside of this region are ignored and are not used as part of the stereoscopic reconstruction.
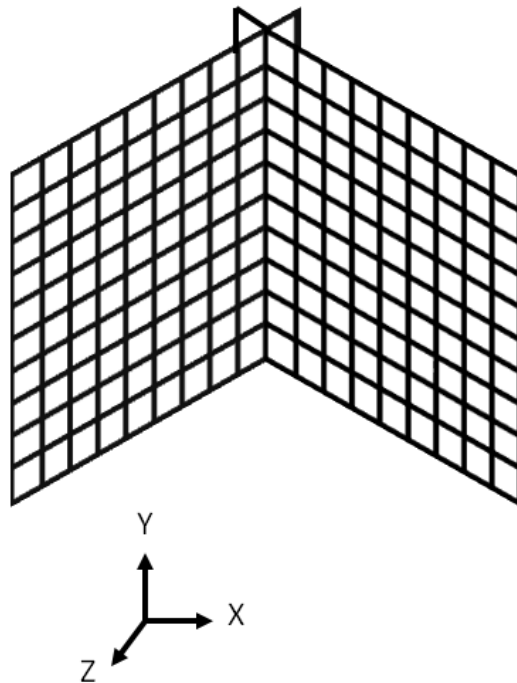
Figure 4.11: Stereoscopic Image Reconstruction (derived from [42, 88])

There are three possible approaches used for calibrating the image data and then performing the 3-D velocity field reconstruction from the two images. The primary difference between them is the method used for dewarping the images by fitting them to a regular grid and

the requirement for knowledge about the camera recording system configuration such as camera angles and distances to the object plane.

All of these approaches require the use of a square target with regularly spaced dots 10 *mm* apart that is placed on the measurement plane in the path of the laser light sheet. The center of the grid is marked with a cross. This is used to align the centers of the CCD chips and subsequently the high speed cameras to meet the Scheimpflug criterion. Once this condition is met, the camera configuration is locked into place so that the calibration procedure can be performed. There are two possible calibration targets that exist. The use of a dual-plane 3-D calibration target has two separate levels that are separated by indented diagonal grooves. A single image captured by each camera is sufficient for use in calibration. Alternatively, a planar target with a translation stage can be used with multiple recordings of the target at different distances from the cameras. Either way, the outcome of the calibration will be a mapping function from physical space in x, y, and z coordinates to camera pixels in X and Y coordinates for each camera [91].

The first approach is called geometric reconstruction and is not commonly used due to large errors resulting from the reconstruction of the 3-D velocity field using only knowledge of the camera configuration. The basic layout of the remaining two methods that are used for stereoscopic reconstruction is as follows. A calibration image of the calibration target is required for each camera to be used, so two images captured. A mapping function is then applied to transform the object coordinates in x, y, and z to the image coordinates of the cameras in X and Y. Misalignment between the calibration and the measurement planes is evaluated and the displacement field is reconstructed. The two methods used for stereoscopic reconstruction are

discussed in the next section. These methods are referred to as the two-dimension-based calibration method and the three-dimension-based calibration method.

4.9.2.1   Two-Dimension-based Calibration

The two-dimension-based calibration method (Willert method [92]) is performed as follows: A calibration target is aligned to the laser light sheet and each camera records a warped image of the target. A polynomial mapping function is numerically determined between the image and 2-D physical space for each camera. **Equation 4.16** represents the particle motion on both the object and the image planes,

$$x_i = f\left(X_i\right)$$
4.16

with the variables x_i and X_i, where 'i' is a counting variable (1,2,…,n) for the corresponding matching grid points on the calibration target and 'f' is the mapping function between the planes. Second order mapping functions are employed and are displayed in **Equations 4.17** and **4.18**. The coefficients a_{ij} are determined using a nonlinear least squares method to compensate for complex distortion [92].

$$x = \frac{a_{11}X + a_{12}Y + a_{13} + a_{14}X^2 + a_{15}Y^2 + a_{16}XY}{a_{31}X + a_{32}Y + a_{33} + a_{34}X^2 + a_{35}Y^2 + a_{36}XY}$$
4.17

$$y = \frac{a_{21}X + a_{22}Y + a_{23} + a_{24}X^2 + a_{25}Y^2 + a_{26}XY}{a_{31}X + a_{32}Y + a_{33} + a_{34}X^2 + a_{35}Y^2 + a_{36}XY}$$
4.18

$$a_{33} = 1$$
4.19

Recorded PIV images from each camera are interrogated independently onto a Cartesian grid. The mapping function is used to project the interrogation spot positions and displacements onto the object plane or into physical space. A common intersecting area is determined between the two images and a new Cartesian grid is inscribed inside of it. The projected data from each

camera is interpolated on to the final Cartesian grid using a special interpolation scheme to move from a non-square to a square grid. The 3-D reconstruction is performed using a system of equations displayed in **Equations 4.11** to **4.13** to reconstruct the object plane based on knowledge of the recording system configuration [88, 92]. Additional equations allowing for the calculation of the distance to the object plane, lens separation angles and camera angles are available in Scarano *et al.* [93]

Two approaches can be used with this method, these are the mapping approach and the warping approach. Using the mapping approach, the raw PIV images from both cameras are first dewarped using the derived mapping function from the camera calibration. Cross-correlation is then performed on the individual images and the vector sets are applied to a common grid to reconstruct the 3rd velocity component. The warping approaches applied the cross-correlation to the warped images. The stereoscopic reconstruction occurs as the final stage in the vector processing by applying the mapping function to the two vector fields to project the vectors on to the object plane. The vectors are then interpolated onto a common grid[42, 89].

4.9.2.2   Three-Dimension-based Calibration

The three-dimension-based calibration method (Soloff method [94]) is performed as follows: A calibration target is aligned to the laser light sheet and each camera records a warped image of the target. The target is moved in the out-of-plane direction to 3-5 positions both above and below the object plane where additional images are recorded. A mapping function is determined between the image planes and 3-D space. Recorded PIV images from each camera are interrogated independently onto a Cartesian grid. The 3-D reconstruction is performed by inverting the mapping function and using a system of equations to reconstruct the object plane[88, 94]. This method functions as a more efficient extension of two-dimension-based calibration.

The relationship between the 3-D object field position 'x' and the 2-D image field for each camera 'X' is given by **Equation 4.20**. The term 'Δx' signifies a change in position of a particle within the object field [88, 94]. The term X_i, where i=1,2 represents the particle displacement on the image plane and the term x_j, where j=1,2,3 represents the particle displacement on the object plane.

$$X = F(x) \qquad\qquad 4.20$$

The mapping function 'F' which transforms the three-dimensional object field and the two-dimensional image plane for each camera is given by **Equation 4.21**, where a_i are the vector-valued coefficients that are determined through a least-squares technique[88, 94].

$$\begin{aligned}
\overline{F(\mathrm{x})} &= a_0 + a_1 x_1 + a_2 x_2 + a_3 x_3 + a_4 x_1^2 + a_5 x_1 x_2 + a_6 x_2^2 + a_7 x_1 x_3 \\
&+ a_8 x_2 x_3 + a_9 x_3^2 + a_{10} x_1^3 + a_{11} x_1^2 x_2 + a_{12} x_1 x_2^2 + a_{13} x_2^3 + a_{14} x_1^2 x_3 \\
&+ a_{15} x_1 x_2 x_3 + a_{16} x_2^2 x_3 + a_{17} x_1 x_3^2 + a_{18} x_2 x_3^2
\end{aligned} \qquad 4.21$$

Particle displacement within the field of view of the cameras is given by **Equation 4.22**,

$$\Delta X = F(x + \Delta x) - F(x) \qquad\qquad 4.22$$

which can be approximated to be:

$$\Delta X \approx \nabla F(x) \Delta x \qquad\qquad 4.23$$

where $\nabla F(\mathrm{x})$ is the gradient operator operating on the warped displacement 'x' to give:

$$\left(\nabla F \right)_{i,j} = \frac{\partial F_i}{\partial x_j} = F_{i,j} \qquad\qquad 4.24$$

where, i=1,2, and j=1,2,3. Then a matrix of the x, y displacements between the two cameras can be constructed and solved by the least squares method. **Equation 4.25** is the local gradient matrix that transforms the particle motion on the object plane into a physical displacement on the

image plane. **Equation 4.25** forms a redundant set of equations owing to its basis from

Equations 4.11 to **4.13**,

$$
\begin{bmatrix} \Delta X_1^{(1)} \\ \Delta X_2^{(1)} \\ \Delta X_1^{(2)} \\ \Delta X_2^{(2)} \end{bmatrix} = \begin{bmatrix} F_{1,1}^{(1)} & F_{1,2}^{(1)} & F_{1,3}^{(1)} \\ F_{2,1}^{(1)} & F_{2,2}^{(1)} & F_{2,3}^{(1)} \\ F_{1,1}^{(2)} & F_{1,2}^{(2)} & F_{1,3}^{(2)} \\ F_{2,1}^{(2)} & F_{2,2}^{(2)} & F_{2,3}^{(2)} \end{bmatrix} * \begin{bmatrix} \Delta x_1 \\ \Delta x_2 \\ \Delta x_3 \end{bmatrix}
\qquad 4.25
$$

where ΔX_1 and ΔX_2 are the apparent particle displacements in the x and y directions for cameras

1 and 2 and Δx_1 is the physical displacement in the x-direction of the object plane, Δx_2 is the

physical displacement in the y-direction of the object plane, and Δx_3 is the physical out of plane

displacement in the z-direction [88, 94]. The second and fourth equations are redundant only under

an ideal measurement. Stereo-PIV measurements can contain random errors that are incurred

from the individual cameras, so the second and fourth equations will vary slightly. In this case,

the equations are used to minimize the residual of the least squares solution of the matrix.

Residual values of .1-.5 pixels are common with larger residuals occurring with larger

misalignment between the cameras and the object plane [42, 89, 94]. **Figure 4.12** visually displays

how the two vector fields are combined to reconstruct the out-of-plane velocity.
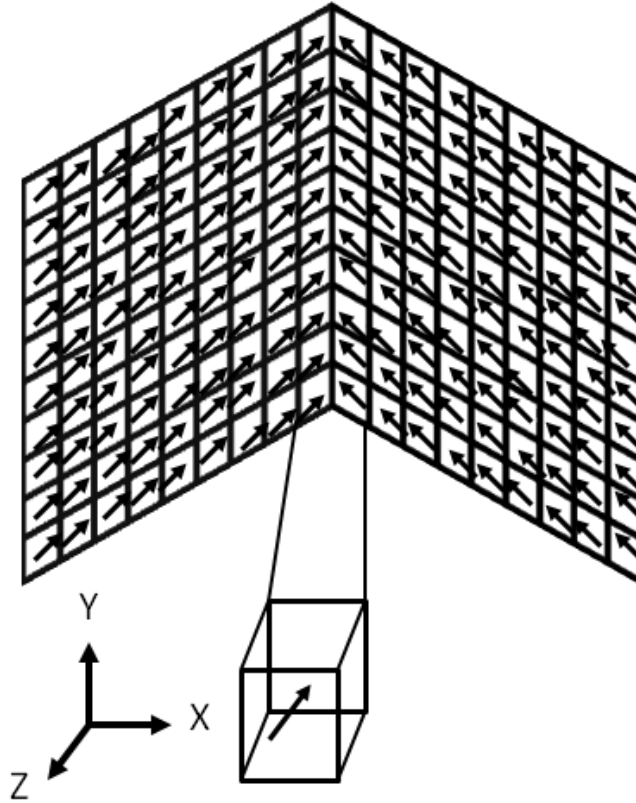
Figure 4.12: Stereoscopic Vector Reconstruction (derived from [42, 88])

4.9.2.3 Stereo-PIV System Calibration

The INSIGHT3G software that operates the PIV system uses a hybrid method of calibration. It primarily uses the three-dimension-based calibration method however it integrates some aspects of the three-dimension-based calibration method in that the dewarping of the images can be performed either before or after the vector processing is performed. Three-dimension-based calibration normally only occurs after the vector processing stage.

A square calibration target is used to align the camera angles and set the distance between them for the proper viewing of the image plane. The camera lens is then rotated relative to the camera body to meet the Scheimpflug criterion. In interrogation regions, the overall light intensity patterns are compared for window offset than matching individual particles from

independent subsequent exposures [42, 88, 95]. The calibration image must be dewarped prior to cross-correlation. A dewarping algorithm calculates a 2nd or 3rd order polynomial function that maps the locations of the dots on the calibration target in the distorted image to a regularly spaced non-distorted grid. The two component cross-correlation for each view is computed on the same regular grid as the dewarped images. The 3-D reconstruction is performed by projecting the vector maps onto a common grid using bicubic spline interpolation [42]. INSIGHT3G automatically reconstructs the image at the conclusion of the vector post-processing stage. The image dewarping can occur at either this stage or in the vector preprocessing stage. Allowing the dewarping to occur during the post-processing stage is not necessary more efficient nor would preprocessing the raw images to dewarp them provide any significant benefit to the vector processor. Hard drive space comes into play since preprocessing the images to dewarp them would cause the software to create separated files for the dewarped images which would strain the limited storage resources.

4.10   Errors of Stereo-PIV

Stereo-PIV errors include errors previously discussed in the 2-D PIV section; these are errors due to biasing and random errors which can now be applied to two cameras. To these errors, stereo-PIV adds a perspective error called disparity. This typically results from errors which occur during the system calibration stage. Particles moving out of the plane of the laser light sheet can be problematic as well due to lost particle pairs leading to erroneous vectors. Errors regarding the velocity field reconstruction are important since the out-of-plane velocity can be influenced by the out-of-plane motion of particles.

4.10.1   Disparity

Disparity occurs as the result of being unable to set the calibration target at precisely at the position z=0 relative to the center of the laser light sheet. In effect, this criterion is impossible because there will always be some rotation or translation of the calibration target relative to the laser sheet or the cameras leading to a misalignment. Failure to meet this ideal case will result in two sets of errors: position error and velocity field reconstruction. Small misalignments can be corrected during the calibration of the cameras to the field of view however large misalignments require further perspective adjustments which are discussed in the following section [42, 76, 89].

4.10.1.1   Position and Velocity Field Reconstruction Errors

Position error results in the 2-D calculation of the individual vector fields using two different positions because the physical point is viewed by two different positions by the two cameras. Reconstruction error occurs from a propagation of error from the position error so that a displacement vector is computed at the wrong point [89]. Errors in the mapping function arise from position error due to an inaccurate plate movement, inaccurate calibration points, and additional unaccounted for optical distortion. A 2-D measurement will be mapped correctly but a 3-D reconstruction will be inaccurate since the individual displacements between the cameras will not match up physically. A typical error is between 0.5-2 pixels [91].

Translational or rotational misalignment of the calibration target position compared to the actual position of the laser light sheet is another known source of error. This is often referred to as the disparity problem with fairly large errors on the order of 5-20 pixels. A disparity correction is often performed to correct for the misalignment of the light sheet. Several images of the particle flow field are taken (typically 10 images) and dewarped and processed using cross-correlation. The resulting 2-D disparity vector field should technically be zero. Any non-zero

vectors can be used to discern a correction to rotate or shift the coordinate system so that the new coordinate system corresponds to the actual light sheet plane [91]. Due to the finite thickness of the light sheet, the images of the particles will never fully coincide with each other, even if a perfect alignment were obtained. The cross-correlation peak that occurs in the disparity correction is an extended streak with a base that is proportional to the light sheet thickness. Disparity correction works well for thin lightsheets (*µm -mm*) but fails for thick lightsheets (several *mm*) [42, 91]. More recent attempts at camera self-calibration have sought to improve disparity corrections [96]. Further discussions of errors specific to Stereo-PIV can be found in Giordano *et al*. [89]

INSIGHT3G performs a disparity correction automatically as part of the dewarping algorithm. This corrects for any minor misalignments of fractions of a degree or millimeter. A disparity correction tool is available as part of the preprocessor but it is meant for gross misalignments of the calibration target, the laser light sheet and the cameras through translation of a few millimeters or rotation of a few degrees. Simply leveling the model properly with a quality leveling device corrects any gross misalignments that might otherwise occur.

C. Volumetric Reconstruction of the Measurement Field

4.11   Introduction to Volumetric Reconstruction

Reconstruction of a measurement volume allows for the ability to combine 3-D data sets to get a larger 3-D data. Three-dimensional data is the primary benefit of the previous discussion on stereo-PIV. However, although stereo-PIV allows for the reconstruction of the third component of velocity, typically W in the out-of-plane, z-direction on an x, y coordinate system, it provides limited resolution of the full 3-D velocity profile of the fluid domain of the model.

The following discussion deals with the challenges of reconstructing the full 3-D data volume of the measured fluid domain of a model using multiple stereo-PIV measurements.

Full reconstruction of an entire fluid domain is not new. Researchers have been attempting volumetric reconstruction from individual slices of data since the early days of PIV. Original reconstructions were attempted using only 2-D slices of data sliced directly on top of each other. This would theoretically reconstruct the volumetric velocity field except that the out-of-plane velocity is being ignored since it cannot be measured. In highly three-dimensional flows, this can increase the in-plane measurement error by as much as 15% of mean fluid flow velocity. Researchers compensated for this error by using small δt values to limit the out of plane motion as well as very thin laser light sheets on the order of a hundred microns [42].

Prasad *et al.* [97] first attempted to stack slices of stereoPIV data in order form a 3-D representation of the volumetric fluid flow field. They recognized the limitations of the stereo-PIV technique in that although a volume is measured, it is a plane that is reconstructed. This lead to the development of point-based volumetric reconstruction such that the velocity magnitudes of the individual vectors in a given slice form a point cloud in 3-D space that can be visualized by several methods but requires a small amount of further data processing [98].

Direct visualization is a common 3-D visualization in PIV. The velocity vectors are plotted as data points on a grid to form a three-dimensional velocity distribution [99]. Geometric visualization requires the use of a mesh to connect the points to form an isosurface. This allows for the ability to extract 2-D slices from the overall volume to observe the local fluid flow structures. Slicing the volume reduces 3-D information to 2-D information and allows for streamlines to better illustrated the flow path [98, 100].

Equation 4.26 shows the deformation tensor for a particle suspended in a 3-D volume. It is known from **Section 4.3** that 2-D PIV will resolve only the four terms in the upper left corner, since a single camera can measure U and V velocities in x and y components. Stereo-PIV is capable of measuring 6 of the 9 components of the deformation tensor. In order to have the full displacement tensor, the remaining three terms of dU/dz, dV/dz, and dW/dz have to be determined by other means. In some cases, they can be determined using the continuity equation, **Equation 3.4** under a steady-state condition [48].

$$\begin{bmatrix} \dfrac{dU}{dx} & \dfrac{dU}{dy} & \dfrac{dU}{dz} \\[2ex] \dfrac{dV}{dx} & \dfrac{dV}{dy} & \dfrac{dV}{dz} \\[2ex] \dfrac{dW}{dx} & \dfrac{dW}{dy} & \dfrac{dW}{dz} \end{bmatrix} \qquad 4.26$$

For the case of a volumetric representation of velocity, the remaining three terms can be interpolated based off of the measurements of two separate planes of measured 3-D data, provided that the separate distance between the planes is small. The data interpolation is a necessary step to reforming a continuous volume [101, 102]. Several methods of data interpolation are available including using a kriging algorithm, linear interpolation, or bicubic spline interpolation [42].

4.12   Errors of Volumetric Reconstruction

Errors in volumetric reconstruction typically can occur from two sources. Errors in the stereo-PIV measurement can be compounded by the volumetric reconstruction. Therefore, it is necessary to carefully validate the velocity data so that only true vectors are reconstruction from the stereo-PIV measurements and that missing vectors are interpolated from the surrounding

vectors to prevent a hole from forming in the continuous volume. Further errors occur due to mesh generation of the measurement volume. The mesh generator attempts to provide connectivity of all the velocity data points in the measurement volume. If velocity data points are missing, or if noise is eliminated then the mesh generator can improperly construction tetrahedral elements that cannot easily be repaired. Moreover, noise is additive and may interfere with the data interpolation scheme that is integrated into the mesh generator to provide connective points between the slices of data [98].

D. Calculated Quantities

4.13   Turbulence Statistics and Other Relevant Quantities

4.13.1 Introduction

The Stereo-PIV data that is extract from INSIGHT3G can be used to extract additional information about the three-dimensional nature of the fluid flow field. The following paragraphs discuss the fundamental equations that are able to further characterize the fluid dynamics. A list is provided in **Table 4.1**. These quantities were calculated using the following equations which are broken down to describe the individual components.

Table 4.1: Velocity Field Calculated Quantities

Velocity Magnitude
Standard Deviation of Velocity Magnitude
2-D Vorticity

The velocity magnitude can be readily calculated from the u, v, and w velocities of the vector files. This calculation is shown in **Equation 4.27** and will produce a 3-D vector plot when plotted in 3-D space with the x, y, z spatial information.

$$\bar{V} = \sqrt[2]{u^2 + v^2 + w^2}$$

4.27

4.13.2   Reynolds Decomposition

The nature of the instantaneous velocity data can be noted in **Equation 4.28**. This equation states that the instantaneous velocity at any given instant in time is composed of a mean velocity U and an unsteady velocity ũ. The magnitude and the standard deviation of the instantaneous velocity are statistical descriptions of the flow and can be found from a continuous function of the instantaneous velocity ũ. Therefore, u' becomes the standard deviation of the instantaneous velocity. U' is also equal to the standard deviation of u and the RMS of u because the time averaged mean of u is close to zero. Using this relationship, the estimates of the mean and fluctuating components of velocity using time series measurements of the instantaneous velocity field are determined in **Equation 4.30**.

$$\tilde{u} = U + u$$

4.28

$$U = \frac{1}{T}\int_0^T \tilde{u}(t)\,dt$$

4.29

$$u = \sqrt[2]{\frac{1}{T}\int_0^T (\tilde{u}(t) - \mathrm{U}dt)^2\,dt} = \sqrt[2]{\frac{1}{T}\int_0^T u^2\,dt}$$

4.30

In order to form the above equations into a usable format for computational methods, they must be place into a discretized form so that they can act on the discrete points that are provided from the velocity data. The velocity data used for the statistics uses a process called ensemble averaging. Recall from **Section 4.8** that ensemble averaging has three possible methods. The method that is used here is the singular cross-correlation of raw PIV data to create 200 individual vector files from a single measurement plane. This method has been used

successfully by other researchers to determine statistically quantities about the fluid flow [103]. The remaining two methods are unsuitable for statistical analysis. The ensemble average of cross-correlation peaks is unsuitable because although a more accurate representation of the mean velocity is obtained, the fluctuating component is lost in the cross-correlation calculation. Only recently have attempts have been made to use the correlation data but this requires prohibitively high spatial resolution [104]. Image averaging is unsuitable as well because like ensemble averaging of the correlation peaks, it will increase accuracy by increasing the signal to noise ratio, but the fluctuating component of velocity is lost. For this reason, vector field ensemble averaging is the current approach that is used. The use of the term ensemble averaging is used to refer to this method for the duration of this section.

Ensemble averaging make it possible to stack the i,j vector matrices to form an i,j,k dimensional array, where i and j are the dimensions of the vector matrix and k is the number of matrices in the stack. This is displayed graphically in **Figure 4.13**. Using this approach, it is possible to estimate the mean velocity using the i,j components of the instantaneous velocity vector field as in **Equation 4.31**. U(i,j) is the mean velocity, N is the vector field in the stack, and ũ(i,j,n) is the instantaneous measure of velocity within the stack.

$$U_{i,j} = \lim_{N \to \infty} \frac{1}{N} \sum_{n=1}^{N} \tilde{u}_{i,j,n} \qquad \qquad 4.31$$

The standard deviation of velocity is calculated from **Equation 4.32**.

$$u'_{i,j} = s'_{i,j} = \lim_{N \to \infty} \frac{1}{N} \sum_{n=1}^{N} [\tilde{u}_{i,j,n} - U_{i,j}]^2 \qquad \qquad 4.32$$

Substituting in **Equation 4.31** and applying the rules of summation, the equation can be simplified to **Equation 4.33.**

$$u'_{i,j} = \lim_{N \to \infty} \frac{1}{N} \sum_{n=1}^{N} u^2_{i,j,n}$$ 4.33

Given the arrangement of the vector, it is possible to simultaneously calculate the mean velocity components of u, v and w for the given set of vector fields. A definitive estimate of the fluctuating component $\tilde{u}_{i,j,n}$ was also obtained through these calculations [105].
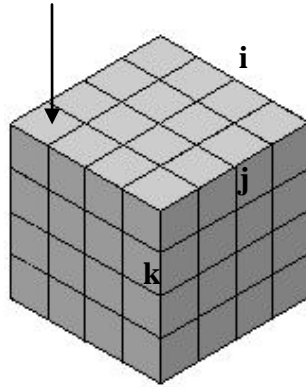
Figure 4.13: Ensemble averaging [5]

4.13.3   Vorticity

Among the other quantities, which may be derived from the 2-D velocity data, are the viscous shear stresses and the vorticity of the flow. The viscous shear stresses can be found by taking the spatial derivatives of either the mean or the instantaneous flow field. These derivatives are approximated using **Equations 4.53** and **4.54** which uses a central difference scheme [42].

$$\left(\frac{\partial U}{\partial y} \right)_{i,j} \approx \frac{U_{i,j+1} - U_{i,j-1}}{2\Delta y}$$ 4.34

$$\left(\frac{\partial U}{\partial x} \right)_{i,j} \approx \frac{U_{i,j+1} - U_{i,j-1}}{2\Delta x}$$ 4.35

Although viscous shear stresses are not a calculated quantity that is of particular importance, the calculated derivatives show that is possible to compute individual terms of the deformation tensor.

Vorticity is defined as the curl of the velocity vector. It provides information about the fluid motion that is perpendicular to the measurement plane, particularly the out of plane fluid motion. Since the resultant data set does not describe the full deformation tensor, the three dimensional vorticity cannot be calculated. Instead the vorticity is calculated only in two dimensions to describe the planar measurement of velocity, which calculates only the out-of-plane component of vorticity. This done by using the trapezoid rule to integrate around a point located at particular (i,j) location. This requires 8 points forming a square with one point in the center. The integrand is then divided by the enclosed area to give an average vorticity for the area [42].

$$\Omega_{i,j} = \frac{1}{4\Delta x \Delta y} \left[\begin{array}{l} \dfrac{\Delta x}{2}(U_{i-1,j-1} + 2U_{i,j-1} + U_{i+1,j-1}) \\ + \dfrac{\Delta y}{2}(V_{i+1,j-1} + 2V_{i+1,j} + V_{i+1,j+1}) \\ - \dfrac{\Delta x}{2}(U_{i+1,j+1} + 2U_{i,j+1} + U_{i-1,j+1}) \\ - \dfrac{\Delta y}{2}(V_{i-1,j+1} + 2V_{i-1,j} + V_{i-1,j-1}) \end{array} \right] \qquad 4.36$$

All of the above quantities can be calculated from the stereo-PIV data and can be interpreted by plotting the relevant quantity.

4.14 Chapter Summary

This chapter reviewed the relevant theory for the experimental methods. The specific experimental methods that are executed for this dissertation research will be discussed in

Chapter 6. Stereo-PIV is an extension of 2-D PIV by applying two cameras in an angular displacement configuration in order to measure the out-of-plane component of velocity. The 3-D data that is collected can be interpolated to reform a volume representation of velocity.

CHAPTER 5: Computational Methods and Materials

The CFD software from ANSYS Inc. (ANSYS Incorporated, Canonsburg, PA) was employed to simulate flow through the computational model of the TCPC and intravascular blood pump (**Figure 5.1**). ANSYS-*Bladegen* was used to create the impeller, and *Solidworks* (SolidWorks Corporation, Concord, MA), a computer-aided design (CAD) program, was utilized to generate the protective cage geometry. CFX-Mesh, an ANSYS mesh generation software, was used to build the tetrahedral element-based mesh for the CFD analysis.
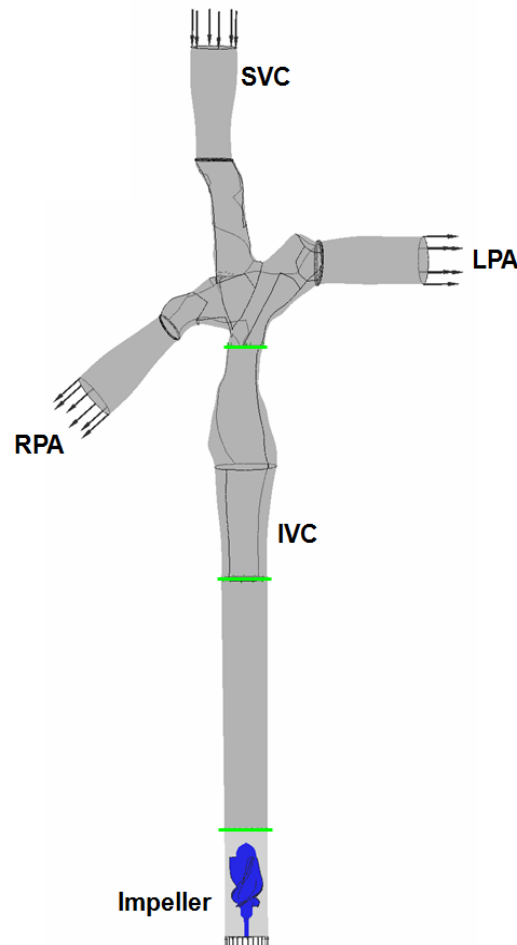
Figure 5.1: Computational Model of TCPC and Pump

5.1. Turbulence and Mesh Generation

Turbulent-to-transitional flow conditions are expected to dominate in the region surrounding the pump impeller with Reynolds (Re) numbers on the order of 10^3 to 10^4. The global Re number can be approximated by using the impeller diameter (D) as a characteristic length as per the expression: $Re = \rho\omega D^2/\mu$, for pump design. Values for the Re will vary throughout the pump depending on the section being examined. ANSYS-CFX estimates the Re number according to the conventional expression: $Re = \rho VL/\mu$, where L is the characteristic length, which is calculated by the cube root of the total volume available to the fluid in the computational domain. The velocity (V) is determined as an RMS average of the fluid domain. This global Re by ANSYS does not accurately indicate the Re numbers in all regions of the flow domain. Thus, the turbulent viscosity throughout the computational field will be normalized with respect to the molecular viscosity to demonstrate the dominance of turbulence and transitional flow conditions [106].

The choice of a turbulence model is critical to the accuracy of the CFD simulations. There is, however, no definitive determination as to which turbulence model is appropriate for miniature blood pumps. The primary two-equation turbulence models are the k-ε model and k-ω model, where ω is the turbulent frequency. The k-ε turbulence model has been used in the VCU BioCirc Lab for several years in designing other pump prototypes and has been used successfully by other researchers designing and optimizing numerous other blood pumps with experimental validation [11, 107-111]. The k-ω and SST turbulence models have also been employed in the development of other rotary blood pumps [33, 107, 110]. The CFD analysis for this dissertation research applied the k-ε and SST turbulence models for comparison with PIV and power efficiency experiments.

5.1.1. Grid Convergence Studies

The accuracy of the computational model and its numerical solution are directly proportional to the grid quality and density. A grid density and convergence study were completed for grid quality assurance to ensure density independence from the flow physics. This process included incremental adjustments to grid size until the performance results deviate less than 3%, thereby ensuring grid size independence. A maximum convergence study was executed to determine the optimal cutoff level for each computational model. For each simulation, the incremental time step, or the relaxation factor in the steady state simulations, was specified as 0.0003 to 0.005 with a maximum normalized convergence residual of $1x10^{-3}$ in accordance with prior work and dozens of blood pump designs [33, 112].

5.2. Mesh Generation

The computational studies of this dissertation included the use of the ANSYS RANS solver and the closure necessity of turbulence models. As previously highlighted in **Chapter 3**, two main turbulence models were used: k-ε and shear stress transport (SST) models. The k-ε model predicts bulk flow conditions well where large gradients and flow separation do not exist. In contrast, the k-ω model is able to predict flow separation more accurately along the boundaries. The SST takes advantage of both the k-ε and k-ω models and applies the k-ω model near the solid walls and the k-ε model attributes in the free shear flows. Each model has specific requirements for mesh generation revolving around the first nodal location or y+ value, thereby necessitating different mesh structures. Two meshes were generated for this dissertation research to satisfy both primary turbulence models with particular focus on mesh quality.

5.3. Execution of Simulations

After successful mesh generation, the computational flow model was then implemented in the 2nd order accurate fluid solver, ANSYS-CFX. Blood flow through the impeller and TCPC was defined to be steady-state with constant boundary conditions and velocities for these simulations. The no-slip boundary condition was assigned to the stationary walls such that the fluid velocity values along the boundary would equal zero. A stationary wall boundary was applied to the internal housing regions of the impeller. The impeller blades and hub were specified as rotating walls in the counterclockwise direction in accordance with the blade orientation. The frozen rotor interface linked regions of differing reference frames between the impeller domain and protective cage [33, 67]. A uniform mass inflow rate (i.e. cardiac output of 3 L/min) and rotational speed (i.e. 3000 RPM) were specified for each simulation. A constant fluid density of 1,050 kg/m^3 and physiologic viscosity of 3.5cP (hematocrit of 33%) were also applied for each simulation assuming a Newtonian fluid behavior [113]. The outlet boundary surface was specified as an opening to capture any possible irregular flow conditions at the outflow. The outlet boundary conditions, such as the left and right pulmonary arteries (LPA and RPA), were defined to have static pressures of 8, 12, 16, and 20$mmHg$. All of the vessel walls for the IVC, SVC, and pulmonary arteries were modeled as rigid tubes in line with the physical TCPC prototype.

5.4. Blood Damage Analysis

A blood damage analysis was performed to consider the potential for hemolysis and thrombosis for this blood-contacting intravascular blood pump. The blood damage model developed by Bludzuweit *et al.* [106, 114] has been widely employed as a predictive tool in the

development of several rotary blood pumps [33, 54, 112]. A blood damage technique was employed that considers the three-dimensional flow field and calculates a scalar stress (σ), which includes the six components of the stress tensor and represents the level of stress experienced by the blood [114]:

$$\sigma = \left(\frac{1}{6} \sum \left(\sigma_{ii} - \sigma_{jj} \right)^2 + \sum \sigma_{ij}^2 \right)^{1/2} \qquad 5.1$$

The design criterion in the development of axial flow VADs has been a maximum stress value of 425 *Pa* for 600 milliseconds [33, 54, 112]. We also examined fluid streamlines as indicative of numerically predicted fluid residence times within this intravascular blood pump. Using a power law relationship between the scalar stress level and the exposure time, a blood damage index was estimated for the selected models [115], according to:

$$dHb/Hb = C \cdot \sigma^{\alpha} \cdot T^{\beta} \qquad 5.2$$

where Hb is the hemoglobin content, dHb signifies the change in hemoglobin content due to blood trauma, σ corresponds to the scalar stress, T is the exposure time to the scalar stress levels, and C, α, and β reflect proportionality constants that are obtained by regressing experimental data. The accumulation of stress and exposure time was summed along the streamlines. This approach provided a statistical estimate of damage to blood cells traveling through this blood pump, according to the following power law equation:

$$D = \sum_{inlet}^{outlet} 1.8x10^{-6} \cdot \sigma^{1.991} \cdot \Delta t^{0.765} \qquad 5.3$$

where *D* represents the blood damage index and indicates a 'probability' of damage to red blood cells; *t* corresponds to the stress exposure time; and *inlet* and *outlet* symbolize the entrance and exit faces in the CFD model, respectively. This model only examined the relationship between

scalar stress and exposure time to the level of stress for each particle; the analysis incorporated adiabatic and isothermal conditions. The numerical constants in **Equation 5.3,** relating the stress to the exposure time, were obtained by regression of experimental data in a Couette viscometer with an exposure time of 0.0034 to 0.6 seconds for fluid stresses of 40 to 700 *Pa* [115, 116]. This range of investigation is comparable to the flow conditions and stress levels found in blood pumps [115, 116]. We seek a blood damage index below 2% for our target design [117, 118].

5.5.   Hydraulic Power Calculations for the TCPC

To assess the impact of the impeller in the IVC on the total energy of the cavopulmonary flow conditions, we used a simplified control volume approach to calculate the rate of energy change through TCPC configuration with and without the impeller [33, 40]. As a common approach used when considering surgical optimization of the TCPC, this analysis allowed for the estimation of the rate of energy loss or gain in the cavopulmonary configuration, according to the following equations:

$$E_{loss} = -\sum (P_{static} + 0.5\rho u_k u_k) u_i n_i A_i = \sum \left(P_{total\_in} \right) Q_{inlet} - \sum \left(P_{total\_out} \right) Q_{outlet} \quad 5.4$$

$$P_{total} = \overline{P}_{static} + 0.5\rho \overline{u_i u_i} \quad 5.5$$

where

$$Q_i = u_i A_i \quad 5.6$$

In the aforementioned equations, ρ corresponds to the fluid density, P_{static} is the static fluid pressure, u_i symbolizes the components of the velocity vector, n_i is the components of the outward surface normal vector of the control surfaces, E_{loss} represents the rate of energy consumption within the control volume, P_{total} is the total pressure including the static pressure component in addition to the kinetic energy component, and Q_i is the flow rate at an inlet or

outlet. Comparisons of these computational estimations were made to the experimental measurements.

5.6.   Chapter Summary

In this chapter, the computational methods to numerically predict the interaction between an axial flow pump and a patient-specific Fontan configuration were outlined. The following chapter, **Chapter 6** will outline the experimental methods which will provide validation for the numerical estimations. The results of the numerical simulations will be present in **Chapter 7** with a comparison between the numerical and the experimental results to follow in **Chapter 8**.

CHAPTER 6: Experimental Methods and Materials

This chapter addresses the experimental methods that were employed to accomplish the specific aims of this dissertation research. A detailed description of each step in preparation for the experiments is provided, including the design and construction of the experimental patient-specific TCPC model, the pump test rig, the particle image velocimetry experimental setup, and the power efficiency experimental setup. A description of the experimental methodology is also provided.

6.1. Patient-Specific TCPC models

6.1.1. Patient-Specific TCPC Model

Following investigational review board approval (IRB #HM11360), a retrospective study of patient data was conducted and 2-D magnetic resonance images (MRI) of a Fontan circulation were harvested. The patient-specific anatomical model was created by transforming the 2-D magnetic resonance images (MRI) into a 3-D CAD solid body. The software package *MIMICS* (Materialise, Leuven, Belgium) was employed to generate a 3-D point cloud mesh from the patient's MRI images and to produce the solid body model in the computer-aided-design software SolidWorks (SolidWorks, Concord, MA). **Figure 6.1** illustrates the patient specific TCPC model generation. Connecting vessel sections of the TCPC were extended for CFD analysis with tapering of vessels to ellipse forms [31, 119]. A separate solid body model was created to be implemented as a physical model of the TCPC vessel configuration.
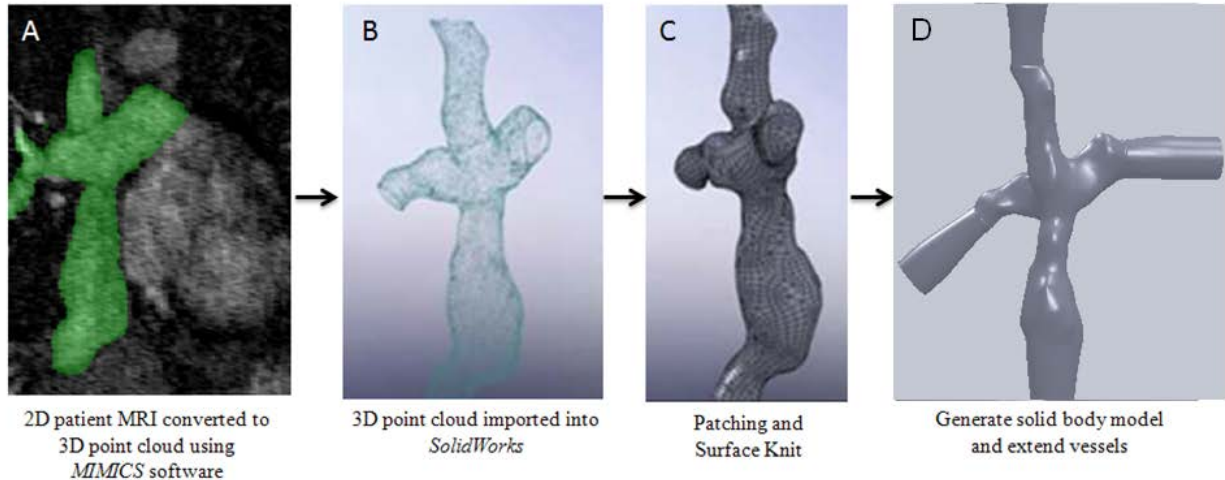
Figure 6.1: Generation of the Patient-specific TCPC Model. A) 2-D patient MRI converted to 3-D point cloud in MIMICS, B) Smooth point cloud mesh imported into SolidWorks; C) Surface knit to solid body; D) Vascular extensions to the solid body TCPC (derived from [31, 54]).

6.1.1.1. Physical Model

The creation of the patient-specific anatomical model was previously described. The TCPC vascular lumen was imbedded into a solid block of material with extended tubes. Model construction for stereolithography replica manufacturing was performed in accordance with the methods prescribed in de Zelicourt, *et al.* [41] The lumen enclosure had its top and bottom referenced to the patient anterior and posterior directions, such that the vessels travel through the sides. At least one side between the vessels was wide enough for a laser sheet to illuminate the entire TCPC interior. The minimum thickness for all surfaces was 4 *mm* to avoid creating an excessively fragile model prone to fracture. The model was manufactured in two halves split along a coronal plane. A clear SLA resin with chemical resistant properties was selected. Clear urethane resin (WC-792, BJB Enterprises, Inc., Tustin, CA) was use since it has refractive index of 1.49 and an industrial partner executed the SLA manufacturing (Applied Rapid Technologies, Fredericksburg, VA). **Figure 6.2** shows the anterior and posterior halves of the model after manufacturing.
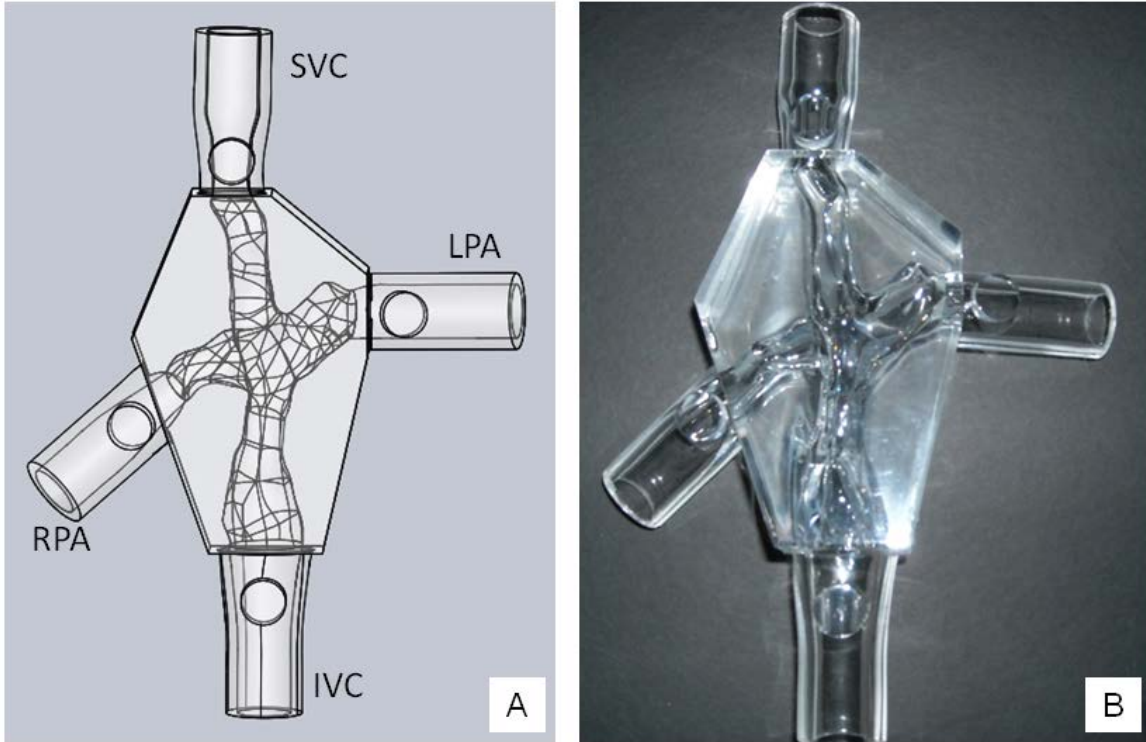
Figure 6.2: Anatomic Prototype Design. A) CAD Model B) Rapid-Prototype Model
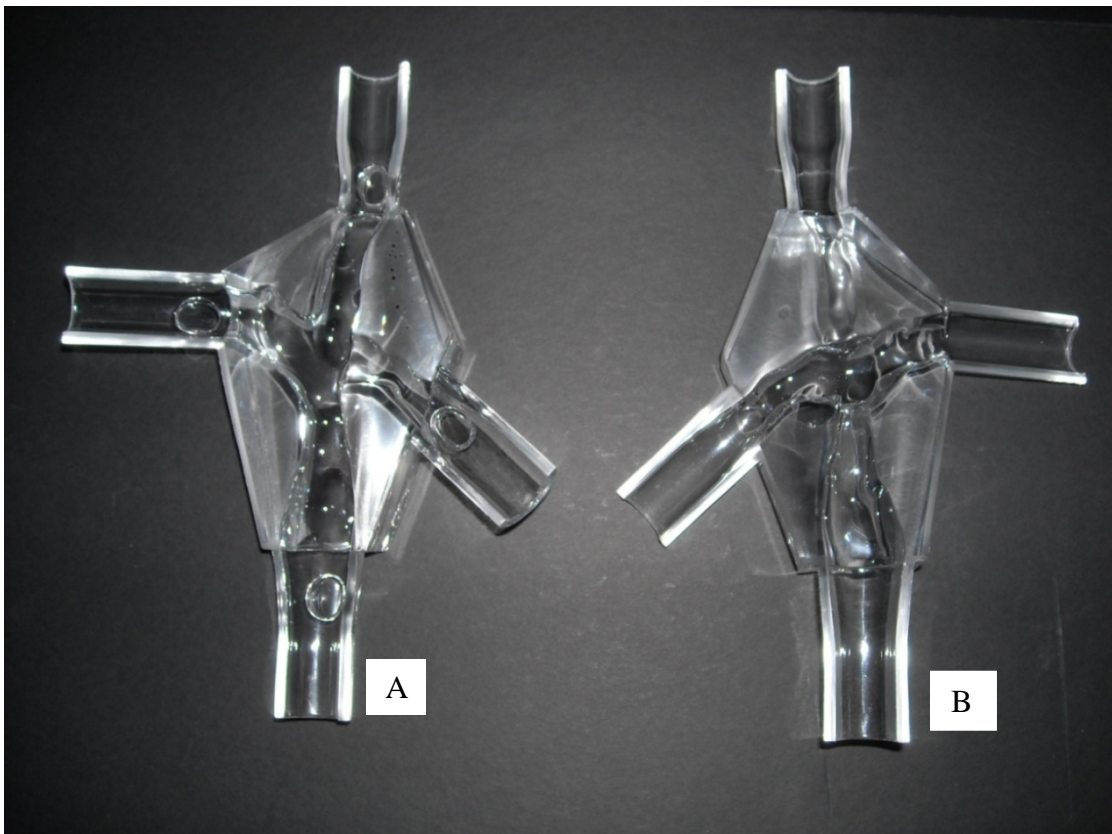
Figure 6.3: Rapid-Prototype Model. A) Anterior B) Posterior Halves

Clear urethane resin was selected for the anatomic model in order to facilitate particle image velocimetry studies by matching the refractive indices of the model to the working fluid. Refractive index matching increases the accuracy of the measurement by eliminating distortion of the particle images and preventing reflections of the laser light that can occur from the curvature of the internal vasculature of the anatomic model. Other SLA manufactured components that are used in the experimental setup are manufactured from a different SLA resin since these components do not require refractive index as a material property.

6.1.2. Axial Flow Pump Design

The design of the prototype impeller used in this study follows the same method outlined by Kapadia *et al*. [32] and Throckmorton *et al*. [11]. The design of the impeller is outside of the scope of this dissertation, and was performed by other personnel in the lab. Several impeller designs have been completed through an iterative optimization process using pump design equations and computation fluid dynamics (CFD) analysis. For this dissertation project, a three bladed-impeller prototype was selected. A clear SLA resin with chemical resistant properties (Watershed XC11122, DSM Somos, Elgin, IL) was selected. Prototype manufacturing was done using SLA rapid prototyping through a commercial manufacturer (Applied Rapid Technologies, Fredericksburg, VA). **Figure 6.3 (A)** shows the prototype impeller mounted to the driveshaft of the pump testing apparatus that is located in the IVC section the hydraulic test loop. The inlet to IVC of the patient-specific model is located a short distance away. **Figure 6.3 (B)** shows the prototype impeller used in these experiments. The pump prototype had three helically wrapped blades around the rotor hub with no diffuser blade set or protective cage of filaments [5, 11, 28].
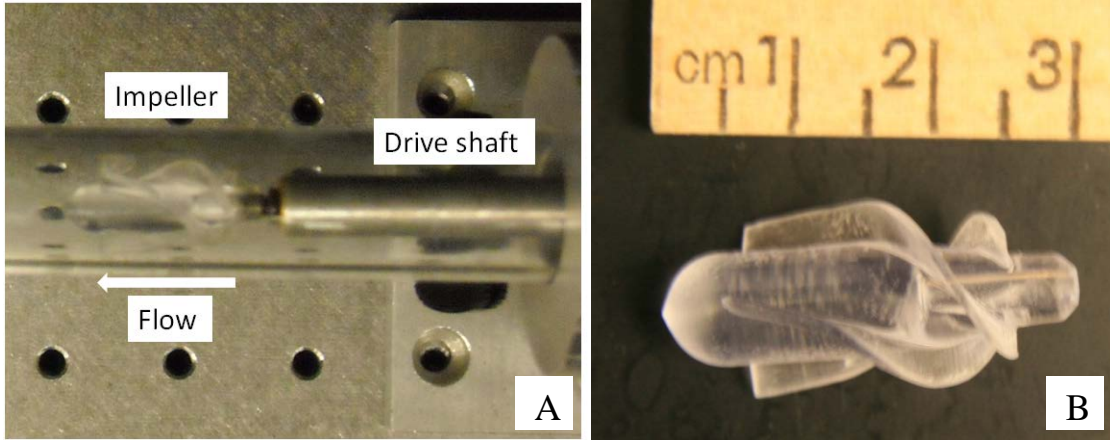
Figure 6.4: Blood Pump Prototype. A) Prototype mounted to the driveshaft and located within the IVC of the hydraulic loop; flow moves from right to left across the pump. B) Pump prototype with three helically wrapped blades around the rotor hub [5].

Table 6.1: Design Characteristics of the Impeller Prototype

Characteristics	Impeller
Number of Blades	3
Hub Diameter (Leading edge) (mm)	4.75
Hub Diameter (Trailing edge) (mm)	9.00
Blade Height (mm)	3.00
Blade Thickness (mm)	1.00
Impeller Tip Clearance (mm)	2.00
Hub Length (mm)	30.0

6.1.3. Prototype cages

The blood pump has a uniquely designed set of protective cage of filaments that surrounds the rotating impeller blades and has two purposes: 1) to protect the vessel wall from the rotating blades, and 2) to enhance energy transfer across the pump. Prior computational and experimental studies have evaluated pressure generation across the pump for three impeller cases having: 1) no protective cage; 2) a protective cage with axially straight filaments and a set of diffuser blades (super-diffuser cage); and 3) a protective cage having filaments twisted in the opposite direction of the impeller blades and in the same direction as the diffuser blades (against-with cage) [32, 54, 120, 121]. **Figures 6.5 (A)** and **(B)** illustrate the two protective cage geometries that will be investigated in this dissertation work. The against-with design demonstrated superior

105

pressure generation as compared to the super diffuser cage in previous studies [120, 121].

Nevertheless, in the design of blood pumps, pressure generation is only one aspect to consider; streamlined flow conditions with minimal turbulent vortices and lower shear stresses are highly desired to reduce the risk of hemolysis and thrombosis [122].
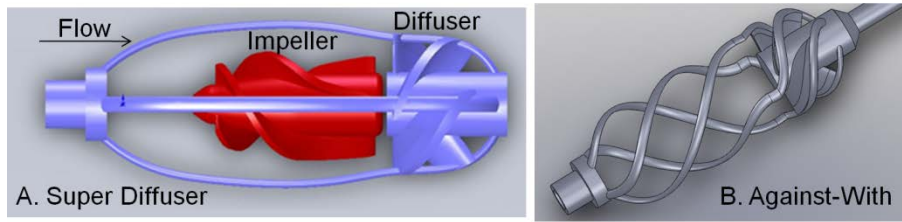
Figure 6.5: Axial flow blood pump and the 2 cage configurations: A) Straight filaments with diffuser blades on the cage (super diffuser); B) Partially twisted filaments in the opposite direction of the impeller blades and partially twisted filaments in the same direction of the diffuser blades (against-with) [120].
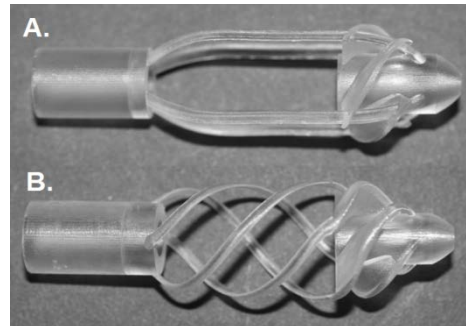
Figure 6.6: SLA manufactured cages: A) Super diffuser cage, B) Against-with cage [122]

Table 6.2: Design Characteristics of the Cage Prototypes [122]

Characteristics	Super-Diffuser	Against-With
Number of Blades	4	4
Hub Diameter (Leading edge) (mm)	10.00	8.00
Hub Diameter (Trailing edge) (mm)	3.00	3.00
Blade Height (mm)	5.00	4.50
Blade Thickness (mm)	1.00	1.00
Impeller Tail Clearance (mm)	1.00	1.00
Hub Length (mm)	19.00	18.00
Filament number	4	4
Filament Height(mm)	2.50	2.00
Filament Width (mm)	1.50	1.00
Filament Length (mm)	42.00	40.00
Overall Cage Length (mm)	48.00	45.00
Outer Diameter (mm)	20.00	20.00

6.2. Pump Assembly

The pump assembly was designed and constructed by an industrial partner (3D Design and Manufacturing, Powhatan, VA). The design for the housing was based upon previous testing configurations and included a sleeve to cover the rotating driveshaft and thus eliminate any added vorticity that could be caused by the rotating shaft. The shaft was connected to the motor using a split shaft coupling and aligned using ball bearings. A high speed, brushless DC motor (MicroMo Electronics, Inc. Clearwater, FL) was employed to drive the shaft at varying speeds. The pump was mounted on the end of the shaft utilizing left handed threads to complement the clockwise rotation of the shaft, thereby preventing the impeller from unscrewing itself at high rotational speeds. A clear acrylic tube *100mm* in length was then slid over the impeller prototype and locked into place using a mounting ring. The opposite end was sealed to the connection of the IVC using a commercial sealant. **Figure 6.7** demonstrates a top-view of the pump mounted to the drive shaft and the motor-drive configuration for the prototype.
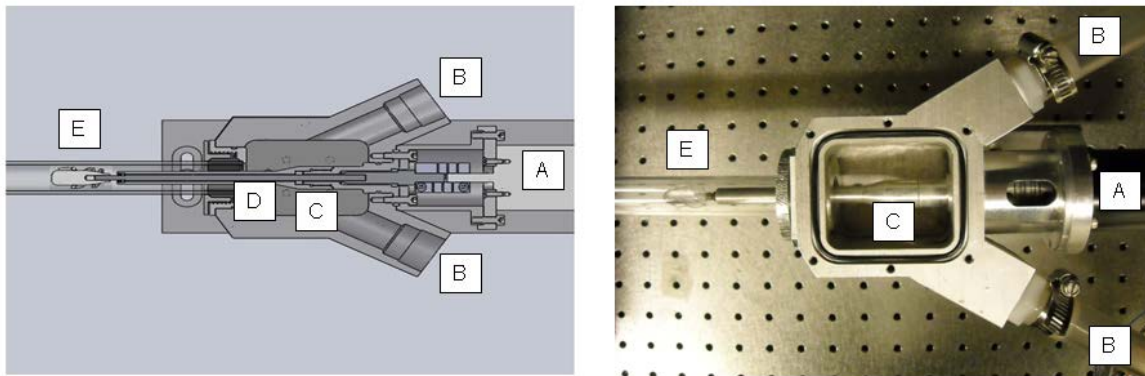
Figure 6.7: Pump housing: Left: Solidworks CAD model; Right: Constructed Piece; Components are: A) motor, B) inlet connection, C) shaft sleeve, D) shaft, E) impeller

6.3. Steady Fluid Flow Loop

To evaluate the flow in this anatomic prototype, a hydraulic flow loop was designed and constructed to circulate the experimental fluid through the model at the pre-determined flow rates. The system was powered by a constant flow pump (Model BC-3C-MD, March Mfg., Chicago, Ill). Four constant pressure head tanks were used to control internal pressures in the system and to ensure a constant pressure gradient to control flow rates and mimic physiologic conditions. The flow rates were measured using an ultrasonic flowmeter (Model TS610, Transonic Systems, Ithaca, NY) and two probes (PXL-16, Transonic Systems, Ithaca, NY) located on the SVC and IVC of the model. Once the flow rates in the SVC and IVC connections were set to the correct inflows, the flow probes were shifted to the RPA and LPA to measure the outgoing flow from the model. All experiments for the purposes of this dissertation were conducted on the flow loop shown in **Figure 6.8**.
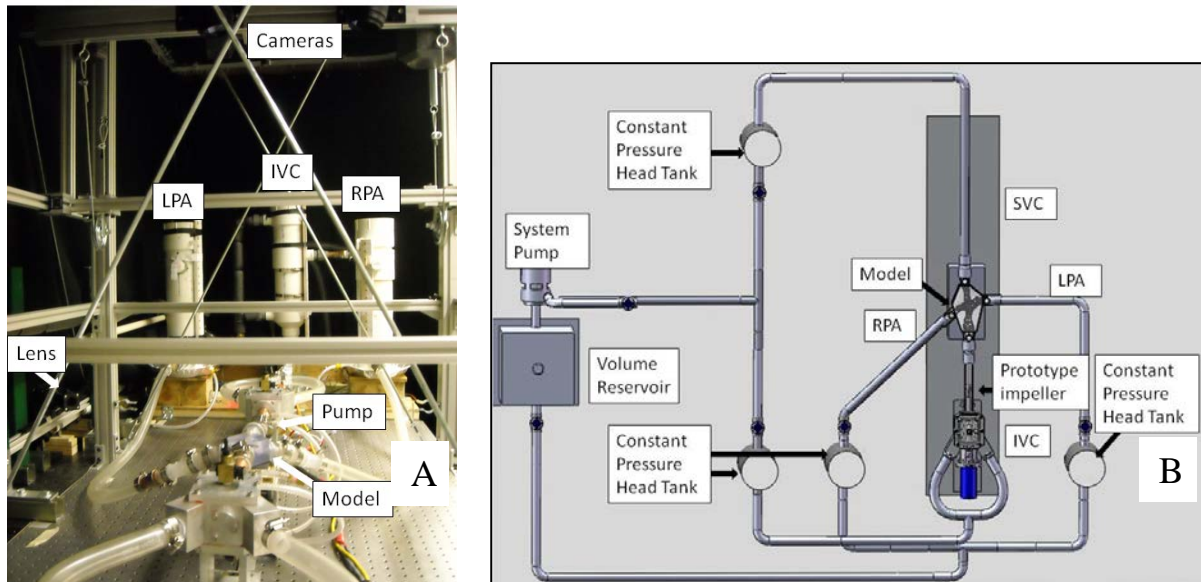
Figure 6.8: Experimental Flow System for PIV Studies: A) Photograph of the experimental setup, B) Fluid system layout

The constant pressure head tanks regulate fluid using a standpipe to remove excess fluid and to maintain the fluid volume at a constant level for the desired pressure. The constant pressure head tanks can provide a range of physiologic pressures between 8 and 26 *mmHg* for cardiac outputs of 2-6 *L/min*. A constant pressure gradient is important to adequately drive fluid flow through the system and to experimentally mimic the Fontan physiology. Ball valves were used in the system to create the required physiologic flow splits within the anatomic model. The fluid system has the capacity for different working fluids to be used depending upon the application.

6.3.1. Working Fluid for Power Efficiency Experiments

For the case of pump performance experiments, a water/glycerin mixture (60% / 40% by weight) was used as the fluid medium and blood analog solution. The working fluid approximates blood as a Newtonian fluid, which is true of blood in large blood vessels. The working fluid has a kinematic viscosity of 3.2 *cSt* (+/-.1cSt). The fluid density was 1098 *kg/m^3* (+/-2) with a dynamic viscosity of 3.5 *cP*. The viscosity of the working fluid was measured using a Canon-Fenske viscometer (Model 25, Fisher Scientific, Pittsburgh, Pa).

6.3.2. Working Fluid for PIV Experiments

Refractive index matching is necessary for complex geometries in which there are multiple curvatures, and uneven surfaces, such as in an anatomical model. These irregularities in the surface area allow the light to refract uncontrollably creating noise, and thus it is therefore necessary to match the fluid as closely as possible to the model substrate to raise the signal to

noise ratio and increase accuracy [123, 124]. At the beginning, an aqueous sodium iodide solution was considered, but it was deemed unnecessary.

The working fluid for the PIV experiments was a solution of diethyl phthalate and ethanol. The constitutive theory for the behavior of the solution is described in Nguyen, *et al.*[125], and is outlined in **Appendix A.** The fluid properties were predicted by applying the equations using Microsoft EXCEL (Microsoft, Corp., Redmond, WA). The working fluid is an "engineered" fluid such that changing the concentrations of the components will change the fluid properties. Diethyl phthalate can be closely tuned to match the refractive index of the model through altering both the ethanol concentration and the temperature of the solution. For a refractive index of 1.49, a solution of 94% diethyl phthalate and 6% ethanol at a temperature of 50 *degrees* Centigrade $(+/-2^o)$ was used [125]. The fluid was heated using a copper coil heat exchanger located in the fluid reservoir. The working fluid matches the kinematic viscosity of blood in large vessels at a viscosity of 3.2 *cSt* (+/-.1 *cSt*). Additionally, the density and the dynamic viscosity are close to that of blood at 1105 *kg/m^3* and 3.5 *cP*, respectively. The working fluid approximates blood as a Newtonian fluid.

Table 6.3: PIV Working Fluid Properties

Fluid Parameter	Predicted Value	Actual Value
Refractive Index (N_d)	1.493	1.493
Density (ρ) (kg/m^3)	1100	1105
Dynamic Viscosity (μ) (cP)	3.82	3.57
Kinematic Viscosity (ν) (cSt)	3.52	3.23
Fluid Temperature (T_s) (^{o}C)	57	50

The viscosity of the working fluid was measured using a Canon-Fenske viscometer (Model 100, Fisher Scientific, Pittsburgh, Pa). The index of refraction was measured using a

refractometer (Model# 300034, Sper Scientific, LTD., Scottsdale, AZ). Density was measured using a hydrometer (Model K334, Fisher Scientific, Pittsburgh, Pa).

The addition of heat and ethanol mildly affects the refractive index, but both strongly affect the viscosity of the solution. The fluid properties of the solution were tightly controlled and constantly monitored. The ethanol forms a covalent bond in solution with the diethyl phthalate so that evaporative effects are minimized. Preliminary testing has shown that the fluid properties of the solution do not change if the solution is exposed to air. This is important since the fluid system cannot be run as a completely closed system due to the static pressure head tanks which require venting to the atmosphere.

The fluid temperature was maintained using a hot water reservoir to supply the copper coil heat exchanger. The hot water reservoir was heated using a 1875W electric heating element positioned in an aluminum basin (Cajun Injector Brand, Bruce Foods Corp., New Iberia, LA). The copper coil inside of the fluid reservoir functioned as a countercurrent flow shell heat exchanger. The temperature was regulated using a commercial PID controller (Model #4130, The Control Company, Friendswood, TX).

6.3.3. Materials Selection

Materials used in the system were selected based on chemical compatibility. Some preliminary research on chemical compatibility of materials is found in the literature with the work of Miller, *et al.* However, their findings were inconclusive since material degradation was found to vary with the DEP / ethanol concentration of the solution in preliminary studies. This is also true of the water/glycerin solution as well. A search was performed to look for economical materials with reasonable design life spans and reasonable resistant to degradation. All

components of both solutions were compared to the Cole-Parmer Chemical Resistance Database (www.coleparmer.com/Chemical-Resistance) to guide in the decision making. DEP was not listed in the database, so chemical resistive behavior for the material was approximated with a sister molecule, ethyl benzoate. This proved to be an accurate choice since DEP ($C_{12}H_{14}O_4$) is a symmetric molecule composed of a benzene ring and two chains composed of hydrogen and oxygen. Ethyl benzoate ($C_9H_{10}O_2$) is composed of a benzene ring with a single chain. Any type of chemical effects from ethyl benzoate would be very similar, if not double, to that of DEP. Prospective materials had separate chemical resistant testing that was performed with various solutions of DEP and ethanol in a 96 hour test. Chemical compatibility testing for solutions of water/glycerin have been performed previously [5].

Some materials are inherently impervious to DEP, such as resins and metals, but not to the water/glycerin solution. For this reason, materials were carefully selected and tested. The constant pressure head tanks used in the system are constructed from polyvinyl chloride (PVC, Sch. 40, Charlotte Pipe Co., Charlotte, NC), but are coated internally with epoxy resin to seal the plastic against chemical attack from both fluids. Chemical resistance in the fluid distribution system was accomplished by using separate tubing and pipes for each fluid. Since PIV and power efficiency experiments were not run concurrently, all other components of the system were reused except for the tubing and pipes to prevent residual water / glycerin or DEP / ethanol solutions from mixing. The pump assemblies, tanks, and fluid reservoirs were easily cleaned of residual fluid. Fluid distribution for the DEP / ethanol was accomplished through copper pipes and fittings (Type M, NIBCO, Inc., Elkhart, IN) with brass ball valves and polypropylene tubing fittings (McMaster-Carr, Elmhurst, IL). Fluid distribution for the water / glycerin was ensured through CPVC pipes and fittings (Charlotte Pipe Co., Charlotte, NC) with CPVC ball valves

with PVC tubing fittings. The pump testing apparatus was modified slightly by replacing the clear acrylic tube with a section of machined copper pipe because of chemical attack on the acrylic tube. The copper pipe was internally diameter matched the internal diameter of the acrylic tube (Tube diameter = 20 *mm*).

6.4. Design of Experiment

All of the experiments were run under steady-state, steady flow conditions with laminar flow being present prior to reaching the inlet side of the pump. The horizontal placement of the TCPC in the test rig corresponded anatomically to a patient lying in the supine position at rest. A physiologically-valid cardiac output or flow rate was selected at 3 *L/min*. Fontan patients are more likely to have cardiac outputs of approximately 3 to 4 *L/min* at rest conditions, depending upon age and body surface area [122].

As was noted in the introduction, the cardiac output returning to the lungs through the TCPC comes from the superior vena cava (SVC) due to blood draining from the head and upper body and the inferior vena cava (IVC) due to return blood flow from the lower body and extremities. We constructed the hydraulic flow loop to allow for the appropriate flow distribution in the TCPC. This distribution, or the percentage of blood flow from the IVC and SVC, are subject to several factors, including age, body surface area, and the condition of the ventricle. Most healthy infants are born with a flow distribution of 50% / 50% in the SVC / IVC flow, which adjusts to 40% / 60%, respectively, in teenagers and 30% / 70% in adults. All measurements were taken based on flow distributions of 40% / 60%, in the SVC / IVC vessels, respectively to correspond to the pediatric population that the pump is designed to treat.

Similarly, while the incoming blood flow to the TCPC junction is subject to a flow distribution, the outgoing flow from the TCPC junction into the left and right pulmonary arteries (LPA and RPA, respectively) is also dependent upon a flow distribution. Recall that blood flow from the LPA and RPA supplies the lungs with blood to facilitate gas exchange. Any variability in the outgoing flow distribution arises from flow resistance due to lung structure and morphology or vascular need in the pulmonary vessel beds. For these experiments, the outgoing flow distribution of the LPA and RPA vessels was set to 50% / 50%, which would be expected to dominate a normal physiological state for Fontan patients. For equal pulmonary resistances, it is possible to experimentally determine if one pulmonary artery will be dominant in receiving more IVC flow, than the opposing pulmonary artery. The basis of the distribution of IVC blood to either pulmonary artery in Fontan patients for normal physiologic function is not well understood [126]. The condition that some IVC flow must be sent to either pulmonary artery with and without pump support is made to be certain that IVC flow will not be excessively directed toward one pulmonary artery or the other.

These experiments were conducted to measure the fluid dynamics of the following configurations: 1) rigid-impeller pump, 2) impeller with a cage having straight filaments with diffuser blades on the cage (super-diffuser cage), 3) impeller with a cage having partially twisted filaments in the opposite direction of the impeller blades and partially twisted filaments in the same direction of the diffuser blades (against-with cage) [33, 120, 121]. The pump rotational speeds were chosen to be 1000, 2000, 3000 and 4000 RPM, with an additional test case corresponding to a zero RPM or stall condition for the pump in all three cases. A separate control experiment to identify the native fluid mechanics inside of the anatomic TCPC model with the selected physiologic conditions was also performed.

Table 6.4: Experimental Conditions and Settings

No Pump Configuration: Control Case		
Flow Rate (L/min)	**Flow Split (SVC/IVC)**	**Rotational Speed (RPM)**
3	**40/60**	**0**

Pump Configuration 1: Impeller only		
Flow Rate (L/min)	**Flow Split (SVC/IVC)**	**Rotational Speed (RPM)**
	40/60	**0**
	40/60	**1000**
3	**40/60**	**2000**
	40/60	**3000**
	40/60	**4000**

Pump Configuration 2: Super Diffuser Cage		
Flow Rate (L/min)	**Flow Split (SVC/IVC)**	**Rotational Speed (RPM)**
	40/60	**0**
	40/60	**1000**
3	**40/60**	**2000**
	40/60	**3000**
	40/60	**4000**

Pump Configuration 3: Against-Width Cage		
Flow Rate (L/min)	**Flow Split (SVC/IVC)**	**Rotational Speed (RPM)**
	40/60	**0**
	40/60	**1000**
3	**40/60**	**2000**
	40/60	**3000**
	40/60	**4000**

6.5. Particle Image Velocimetry

Figure 6.9 displays a flowchart of the experimental methods that were involved in carrying out the PIV measurements in this dissertation. It is important to remember that PIV is dependent upon the experimental setup and therefore the development of a PIV system is an iterative process leading up to the actual measurements. After the PIV measurements are made, the image data needs to be carefully processed to extract the velocity data.
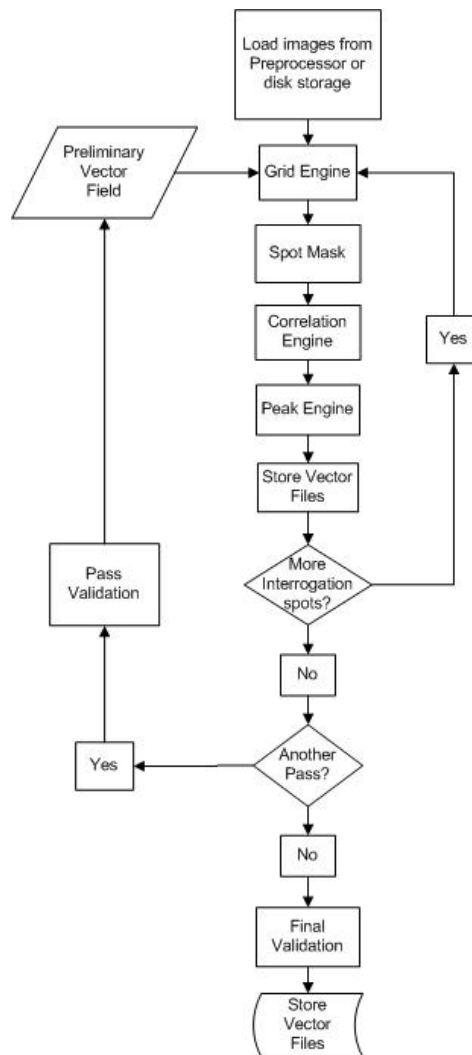
Figure 6.9: PIV Processing Flowchart [5]

6.5.1. Hardware

The PIV measurements were taken using a commercially available DPIV system which was manufactured by TSI, Incorporated, (TSI, Inc., Shoreview, MN). The laser was a double pulsed Nd:YAG laser (New Wave Research, Inc., Fremont, CA), which is used in combination with a lens array to create a laser sheet 1 *mm* in thickness. The lens array (ThorLabs, Inc., Newton, NJ) is shown in **Figure 6.10**.
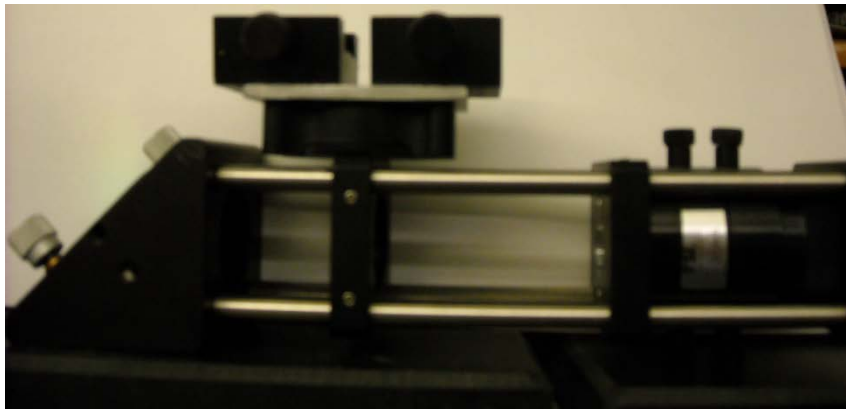
Figure 6.10: Lens Array

The software package that was used for data acquisition and analysis was Insight 3G, version 9.1 to operate the computer controlled synchronizer (TSI Model No. 610035). Images were collected using two high speed cameras (TSI Model No. 630066, PowerView 1.4MP) and mounted on to a sliding traverse structure. A short range lens was used on the camera (AF Micro Nikkor 60mm lens, Nikon Camera Co., Melville, NY). A narrow band color filter (λ=545 TSI Model No. 610072) was utilized to collect the light emitted from the seed particles and to block other light reflections. The camera aperture was set to an f-stop value of 32, which was deemed acceptable for all experiments.

The anticipated blood flow conditions inside of the anatomic model are known to be a highly three-dimensional fluid flow field. Therefore, it is necessary to take a volumetric approach to analyzing the fluid velocities to successfully capture these unsteady flows, which cannot be resolved using 2-D PIV alone. Stereo-PIV allows for all 3 components of velocity to be extracted from the fluid flow field. Thus, to configure a Stereo-PIV arrangement, the camera support assembly was mounted to a sliding traverse in order to allow for data collection to occur by slicing the model into layers and measuring the three-dimensional velocities, both x, y, and z-components in each layer. The thickness of a single layer was defined by the thickness of the laser sheet which is 1 *mm*.

To acquire volumetric data, a traverse structure was designed and constructed from aluminum construction rails (Metric 2525-Series, T-slotted profile, 80/20, Inc., Columbia City, IN) to move the measurement plane through the model. The laser and cameras must be moved simultaneously such that this distance between them is maintained. If the cameras were stationary and the laser sheet was moved, then the observed image would change in size within the camera field of view. Additionally, a separate calibration image would be required for each measurement plane in the model. A digital gage (ABSOLUTE Digimatic Series 572, Mitutoyo, Kawasaki, Kanagawa, Japan) is mounted to the stationary frame and the moving camera assembly to display the movement of the measurement plane through the model.

The cameras are positioned 30 *cm* away from the model to measure the velocities in the plane of the laser sheet. The use of one camera allows for 2-D PIV, while the introduction of a second camera that is positioned at an angle of 30 *degrees* from the first camera in a Scheimpflug configuration allows for 3-D PIV.
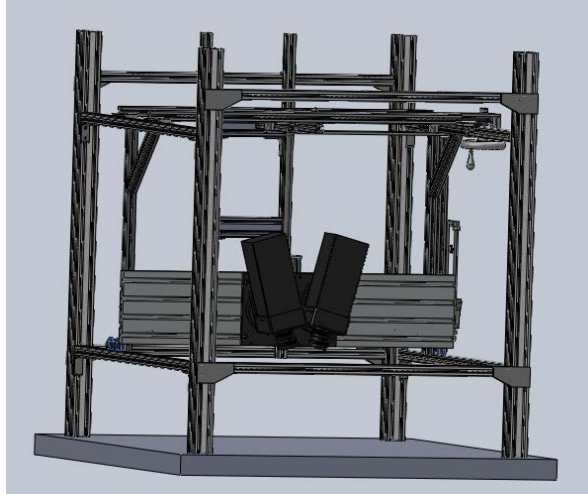
Figure 6.11: Traverse structure for stereo-PIV experiments

6.5.2. Parameters for Data Acquisition

The solution fluid was mixed and placed into the fluid system. The working fluid was seeded with neutrally buoyant, rhodamine B particles (Fluostar, EBM, Incorporated, Model No. FF1015-01) with a nominal diameter of 13 *microns* and a density of 1,100 *kg/m³*. These particles absorbed the laser light and fluoresced at 622 *nm* (orange light) which was then collected by the cameras. The SNR was increased through use of an optical filter (TSI Model No. 610072) attached to each camera lens.

Sufficient particles were added to the system to create uniformly seeded flow. To prevent overseeding, particles were removed from the system after each experiment using a filter, which also served to block any contaminants from entering the system. Initially, 2 *mL* of concentrated particles in working fluid were injected into the system. For every run of the experiment, an additional 1 *mL* of concentrated particles was added to compensate for particle deposition within the system. Adequate seeding was determined by capturing a set of ten test images using the PIV system set the temporal parameters.

Particle deposition occurs due to the constant pressure head tanks that are present to regulate the system pressures. These tanks each contain an adjustable standpipe to set the fluid height and particles may become trapped at the base of this structure and do not follow the exiting fluid flow that returns to the system. The particles are then deposed in the bottom of the tanks.

Recall from **Section 4.5** that there are three main temporal settings that are controlled during the PIV measurement. Each PIV measurement occurs by taking two successive images at a known value of time apart. Recall that this value of time is called the delta t value (δt) which must be optimized based upon the estimated velocity magnitude of the flow being measured. The δt value ranged from 800 to 1000 μs depending upon the measurement plane within the model where the data was collected. A range of δt values is to be expected since the anatomic model will not have uniform velocities throughout the entire model. Regions of stagnant flow with vortices require a large δt value in order to resolve the instantaneous velocity magnitude. In comparison, mainstream regions near the inlets will require a lower δt value in order to resolve the velocity profile. Care is taken to optimize δt value to insure an instantaneous particle residence time. The remaining temporal parameters for the PIV system can be view in **Table 6.5**.

Table 6.5 PIV Temporal Settings

Temporal Quantity	Value
Delta t value (δt)	800-1000μs
Laser pulse delay	250μs
Camera shutter time	500μs

By capturing test images and the application of a grid using INSIGHT3G software, the distance that a group of particles moved in a region was compared between the two successive images. If seeding was deemed to be insufficient, then particles were added to the system. If the relative motion of the particles was outside of the estimate interrogation window on the grid, then the δt value was adjusted. The rules put into place by Adrian *et al.* [77] from **Section 4.5.3** were then utilized. The size of the applied grid was set to 16 x 16 pixels, which is the intended size of the interrogation region to be used during the vector processing stage.

A table of estimated values of velocity based on the flow rate is shown in **Table 6.6**. The Reynolds number measures the ratio of the inertial forces to the viscous forces in the fluid flow and determines the steadiness of the flow. The approximate Reynolds numbers for the flow rates were calculated using the internal tube diameter of 20 *mm* as the characteristic length.

Table 6.6: Fluid Flow Characteristics [5]

Flow rate (L/min)	Velocity (m/s)	Reynolds Number
1	1.15E-01	4.90E+02
2	2.29E-01	9.81E+02
3	3.44E-01	1.47E+03
4	4.59E-01	1.96E+03
5	5.74E-01	2.45E+03
6	6.88E-01	2.94E+03
7	8.03E-01	3.43E+03

A spatial calibration was performed using a special 4-axis metal calibration plate for Stereo-PIV measurements with 10 *mm* dot spacing. The calibration plate was place on top of the model and the centers of the cameras and center of the laser light sheet were brought into a common alignment. The cameras were adjusted to provide a rough alignment for the Schempinflug condition between the two cameras. The dots on the calibration target are too large to provide a fine-tuned alignment, which can only be performed using particle image

pairs. Five calibration images were collected of the calibration plate. In order to fine-tune the Schempinflug angle of the camera lenses, the calibration plate was removed and the working fluid was seeded with particles. The laser light sheet and the cameras were moved to the region of principle flow or as close to the true centerline of the model as possible or approximately 25 *mm* from the top surface. The cameras were set to continuous capture in order to continuously collect images as a video feed. The laser was set to continuous fire. The Schempinflug angles on both cameras were fine-tuned so that the particles were in focus continuously across the field of view. Once the calibration images are collected, INSIGHT3G is able to determine the correct mapping function in order to dewarp the images and determine the correct pixel/mm conversion.

6.5.3. Experimental Procedures

Care was taken to remove all air bubbles from the system. Initially, the hydraulic flow loop was operated with only the pump housing present and the pump and shaft assembly removed. A machined cap was screwed into place to cover the hole left by the removal of the shaft sleeve. PIV measurements were performed based upon aforementioned flow rates and distributions from the SVC / IVC and into the LPA / RPA. Baseline measurements were taken without the pump for comparison to numerical simulations of a geometrically similar model.

After the baseline measurements were taken, each impeller test case was examined. The impeller prototype was mounted to the drive shaft in addition to a cage prototype, if one is required in that configuration. The impeller was operated at rotational speeds of 0 to 4000 RPM. The impeller prototype was located at a distance of 10 *cm* from the inlet tube in IVC of the TCPC model. A brushless DC motor was controlled using a motor controller (MicroMo

Electronics, Inc., Clearwater, FL) in combination with a 10 $k\Omega$ potentiometer to regulate the speed of rotation. Three inductors were connected in-line between the motor and the controller to protect the motor from being damaged due to excessive current draw. The rotational speed was measured using a digital oscilloscope to read the Hall sensors located inside the motor [5, 28].

In addition, using a calibrated pressure transducer (DP15-36, Validyne Engineering, Northridge CA), the pressure rise across the impeller prototype was measured as a function of increasing rotational speed. A Labjack A/D board (Labjack, Inc., Lakewood, CO) was employed for the pressure measurement. **Table 6.4** describes all of the flow and pump operating conditions evaluated and measured during these PIV experiments.

Using the previously discussed experimental setup, PIV measurements were taken of the TCPC model using the frame-straddling technique which utilized δt values appropriate to the corresponding flows within the model. Three hundred successive image pairs were capture and stored to the computer hard disk. These images were then processed to retrieve the velocity magnitude data.

Data collection and analysis were performed using Insight 3G software. The sample size was chosen to be 300 image pairs to satisfy data sampling needs in order to maintain resolution. The data was processed using a Recursive Nyquist grid to provide a 50% overlap between the image pair and to utilize the multi-pass cross-correlation method. The initial interrogation window size was set to 32 x 32 pixels and the final interrogation region size was set to 16 x 16 pixels. A Gaussian curve was used to locate the correlation peak. A validation scheme was conducted using local vector validation scheme utilizing a universal median test after pass. The mean and standard deviation of the x and y components of velocity were calculated in a 3 x 3 interrogation regions perimeter around each interrogation region. The tolerance limits for the

standard deviation of velocity is specified to be 2 standard deviations from the mean value. Bad vectors are removed and no data replacement is performed. The vector processor is set to store one secondary peak in memory from the cross-correlation calculations for use in the data replacement scheme used for post-processing. Ensemble averaging is carried out across 300 cross-correlation peaks in order to produce an averaged cross-correlation peak. This yields an averaged velocity vector field.

The vector post-processing filter is configured in the Insight 3G vector post-processor uses similar criteria that are used for data validation in the vector processor to remove erroneous vectors. The validation criteria do not need to be as strict as in the vector processor where self-propagating errors are a concern. The velocity tolerance was set to remove vectors that were outside of 3 standard deviations from the mean value. Further post-processing applied a universal median test to remove any remaining erroneous vectors in a 5 x 5 perimeter. The vector conditioning scheme is set to fill in holes in a 3 x 3 region with a valid secondary peak, or the local median. For velocity flow fields that were particularly noise, the stricter validation criteria was used. The tolerance limits for the standard deviation of velocity is specified to be 2 standard deviations from the mean value. The universal median tested is applied for a 3 x 3 perimeter for each interrogation region. The vector conditioning option is set to fill in holes in a 3 x 3 region with a valid secondary peak, or the local median.

The 3-D velocities in each level of the model are measured by moving the lasersheet and the cameras through the model and taking a Stereo-PIV measurement at each location. A total of 45 slices that are 1 *mm* in thickness were taken through the model to accurately gauge the volumetric velocity flow field. These individual layers can then be reconstructed to form a volumetric plot of velocity inside of the model and to allow for an interpretation of the z-

component of velocity. Volumetric velocity magnitude plots and streamline plots provide important information about the fluid dynamics and will be compared to the numerical data. Data from these Stereo-PIV studies will assist in evaluating the fluid dynamics as well as the pump performance in the three pump configurations.

The data files were processed using MATLAB 2012 (The Mathworks, Inc., Natick, MA) in conjunction with a custom written MATLAB code utilizing the Image Processing Toolbox. This toolbox provides image processing functions which were used to segment noise from the boundaries of the PIV data. Specifically, the active contours function *activecontours()* was used on a dewarped PIV image to reconstruct the boundaries of the physical model for the measurement location within the model. The 3-D velocity data points were plotted over the filtered image and the boundary function *inpolygon()* was used to remove data points that were found to be outside of the boundary. A separate MATLAB code was written to reconstruct the volumetric representation of velocity. Finally, all data files were plotted using TecPlot Focus 2009 (TecPlot, Inc. Bellevue, WA) for inspection of the final velocity vector fields.

6.5.4. Volumetric Data Reconstruction

Volumetric reconstruction of the processed PIV data fields is performed in a custom MATLAB code. **Figure 6.12** illustrates the volumetric data reconstruction methodology. PIV data is collected in individual slices through the patient-specific TCPC model in the z-direction, from the top to the bottom of the model. The individual slices of PIV data are cleaned of noise and the boundaries of the data which correspond to the physical boundaries of the model are reconstructed using the MATLAB code discussed in the previous section. A Delaunay mesh generator is used to provide connectivity between the velocity magnitude data points in a

125

tetrahedral mesh [127, 128]. In order to provide continuity between the individual planes of data, the *interpn()* function in MATLAB 2012 is used to provide bicubic spline interpolation of the velocity data to increase the number of data points to form a solid volume. The experimental methods described are consistent with those recommended by Li *et al.* [100] and Boring *et al.* [99] for the reconstruction of a data volume from individual Stereo-PIV measurements. A similar methodology is described in Kitajima *et al.* [51] for volumetric reconstruction of PIV data related to a patient-specific Fontan model. The volumetric data files were plotted using TecPlot Focus 2009 (TecPlot, Inc. Bellevue, WA) for inspection of final volumetric velocity flow field.
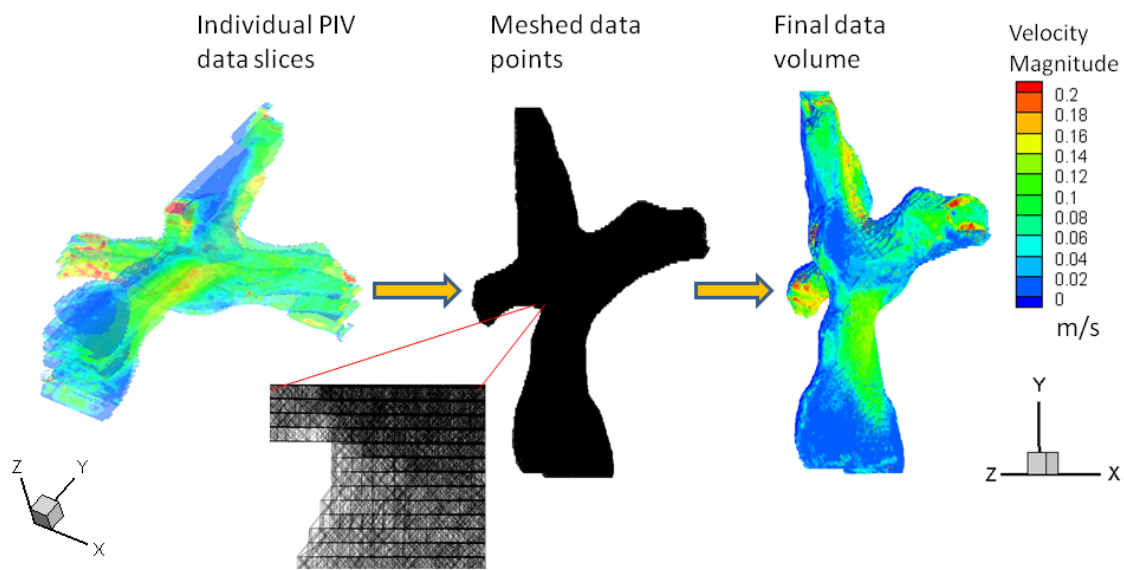
Figure 6.12: Volumetric Data Reconstruction

6.6.   Power Efficiency Studies

The changes in pressure and flow through a TCPC provide quantitative information about the power efficiency, that is, the rate of power gain or loss in the cavopulmonary circulation. Power loss refers to the amount of energy that is expended within the model due to unsteady flows and mixing. The addition of a pump into the TCPC will decrease the power loss and

increase the flow energetics since the pump inherently adds potential energy and rotational force to the fluid flow as balanced with resistance [33, 122].

The methodology described here is consistent with accepted practice for determining the physical power efficiency of a Fontan model as is found in the literature [14, 41, 50, 129, 130]. Pressure taps were located in the inlet and outlet connections to the model such that three differential pressure transducers (DP15-36, Validyne Engineering, Northridge, CA) were able to determine the pressure rise across the pump and to determine the overall affect on the power loss on the model. Data collection software (LabJack Corporation, Lakewood, CO) was used to simultaneously measure the pressure rise and flow rate at a sampling rate of 100 Hz. The data acquisition software also enabled us to measure rotational speed (RPM) from the motor controller. A water/glycerin mixture (60% / 40% by weight) was used as the fluid medium and blood analog solution. The test conditions examined a cardiac output of 3 *L/min* with SVC / IVC flow split of 40% / 60% and with RPA / LPA flow split of 50% / 50%. The pump operating conditions were 0 to 4000 RPM. All of the flow rates through the hydraulic loop and TCPC model were measured using ultrasonic flow probes (PXL-16, Transonic Systems, Ithaca, NY).

The power loss in the model was computed using the differential static pressures and flow rates on each side of the model. The differential pressures were measured with respect to the IVC. This eliminates probable errors which can arise from measuring the static gage pressure at both the inlet and outlet. The power loss experiments were performed three times for each rotational speed with each pressure being switched to a different position to eliminate the prospect of sensor bias. The power efficiency calculations were performed in Microsoft EXCEL 2007 (Microsoft Corp., Seattle, WA). The power efficiency equations are available in **Chapter 3** [131].

Some researchers have opted to include corrections to the experimental data to account for frictional losses or other factors to correct the data to provide a more accurate value of the power efficiency [41, 130, 131]. The only correction which is added to the measured data is the correction recommended by Ryu *et al*. [40] which compensates for the static pressure head bias which is present as a result of the constant pressure head tanks in the system. Compensating for this bias has the positive effect of correcting for a zero-offset in the data [130]. No corrections are required for the data collected from the numerical simulations in **Chapter 5**. A comparison of the experimental and numerical power efficiency results is given in **Chapter 8**.
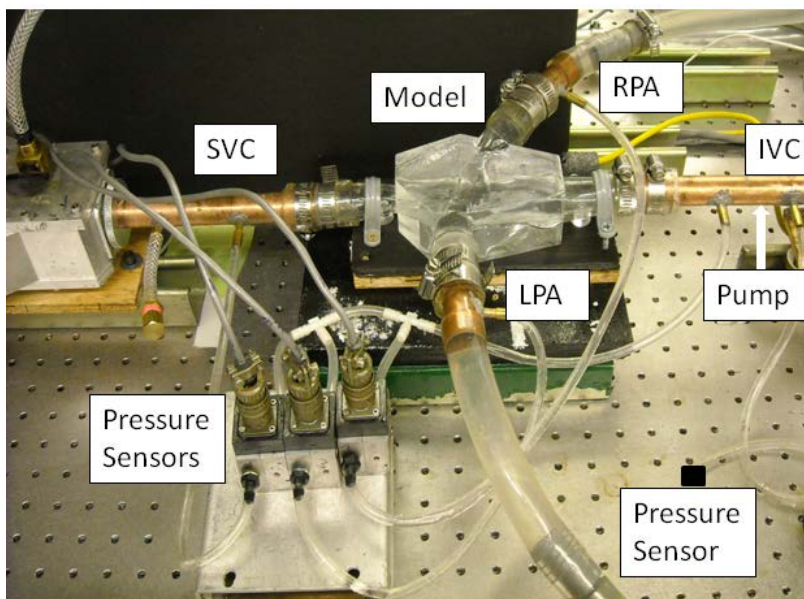
Figure 6.13: Power Efficiency Experimental Setup

6.7.   Chapter Summary

This chapter detailed the experimental methods behind examining the interactive fluid dynamics between a prototype blood pump design and an anatomical univentricular Fontan circulation. The experiments were conducted in two separate configurations. First, hydraulic testing was utilized in order to determine the effects of the operating conditions on the anatomic

model and the three prototype impeller configurations. Additionally, power efficiency measurements were conducted. Second, PIV experiments were conducted on the model in two separate cases. Control studies of the anatomic model were performed to measure the fluid dynamics inside of the model without pump assistance. Then, an axial pump prototype with and without diffuser blades were positioned into the IVC of the model to measure the effect of the pump. These studies aided in the assessment of the impact of the internal fluid dynamics inside of the TCPC.

CHAPTER 7: NUMERICAL ESTIMATIONS AND STUDY RESULTS

The numerical simulations were performed using ANSYS-CFX (ANSYS Incorporated, Canonsburg, PA) to simulate flow through a geometric model of the TCPC and intravascular blood pump. This chapter presents the results of the computational analyses in support of this dissertation research and for ultimate comparison to PIV measurements.

7.1. Computational Model and Mesh Generation

The computational model consists of the following four separate regions: 1) impeller pump domain; 2) IVC pipe from the outlet of the pump to the IVC inflow junction of the TCPC; 3) IVC patient-specific vessel structure to the TCPC junction; and 4) SVC inflow and TCPC junction itself having outflow right and left pulmonary arteries. **Figure 7.1** illustrates the computational model as generated from the patient-specific TCPC model and impeller design.
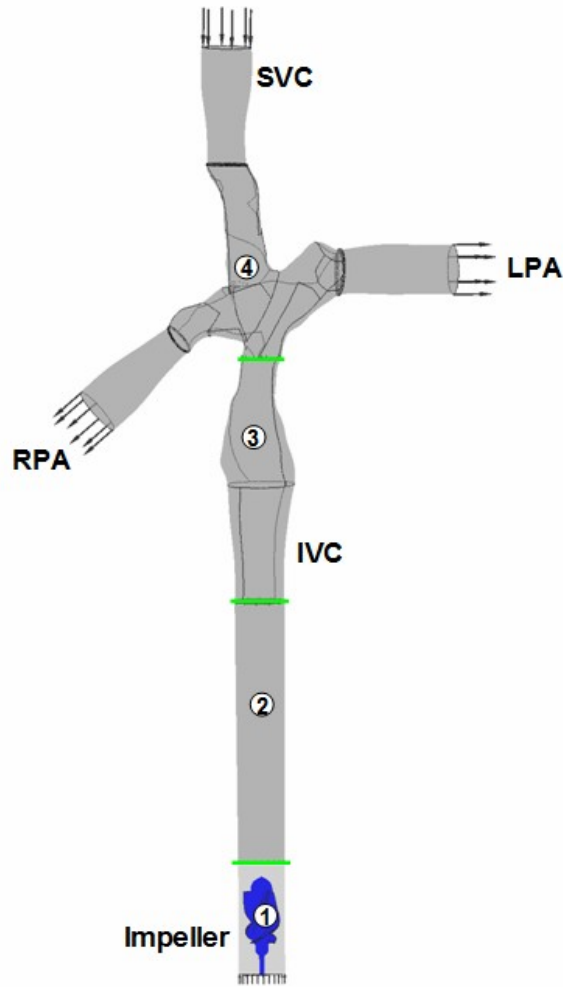
Figure 7.1: Computational Model of the Impeller and Patient-Specific TCPC, including four regions: 1) impeller pump domain; 2) IVC pipe from the outlet of the pump to the IVC inflow junction of the TCPC; 3) IVC patient-specific vessel structure to the TCPC junction; and 4) SVC inflow and TCPC junction itself having outflow right and left pulmonary arteries.

In order to achieve appropriate standards of mesh generation for the implementation of the two primary turbulence models, two separate meshed models were created. Each turbulence model required a different first nodal location or relative y+ value to satisfy constraints and abide by the inherent physics in the model. The k-ε and SST turbulence models call for y+ values along boundary surfaces to be greater than 11 and less than 2, respectively. **Figure 7.2** shows the distribution of the y+ values along the boundary surfaces in each region for the k-ε based computational model. The mesh generation and grid density study produced a mesh

with only 1.3% of the surface nodes having y+ value less than 11. Similarly, **Figure 7.3** illustrates the distribution of y+ values along the surface in each region of the SST-based model. The mesh generation and grid density study produced a mesh with only 0.15% of the surface nodes having y+ value greater than 2. Both turbulence model constraints were satisfied. **Figure 7.4** displays the mesh for the TCPC, the vessel connections to the TCPC, and the pump domain.

For both models, skew angles were maintained above 20 degrees, and aspect ratios were no larger than 50 for the meshes. A grid convergence study was conducted at densities of approximately 1.0, 2.0, 3.0, 5.0, 7.0, 8.0, and 10.0 million elements in order to demonstrate mesh independence. The analyses for the k-ε and SST models indicated that 2 million and 7 million elements, respectively, were sufficient with a deviation being less than 3% for dozens of velocities in all regions and hydraulic performance characteristics. **Table 7.1** lists the final mesh densities for the computational models.

Table 7.1: Element Numbers for Each Pump and TCPC Model

Domain Region	k-ε Meshed Model	SST Meshed Model
Impeller	499,302	4,357,924
Vessel Connection	562,269	690,764
TCPC_IVC	556,749	1,113,423
TCPC_SVC	499,194	869,502
Total Elements	*2,117,514*	*7,031,613*
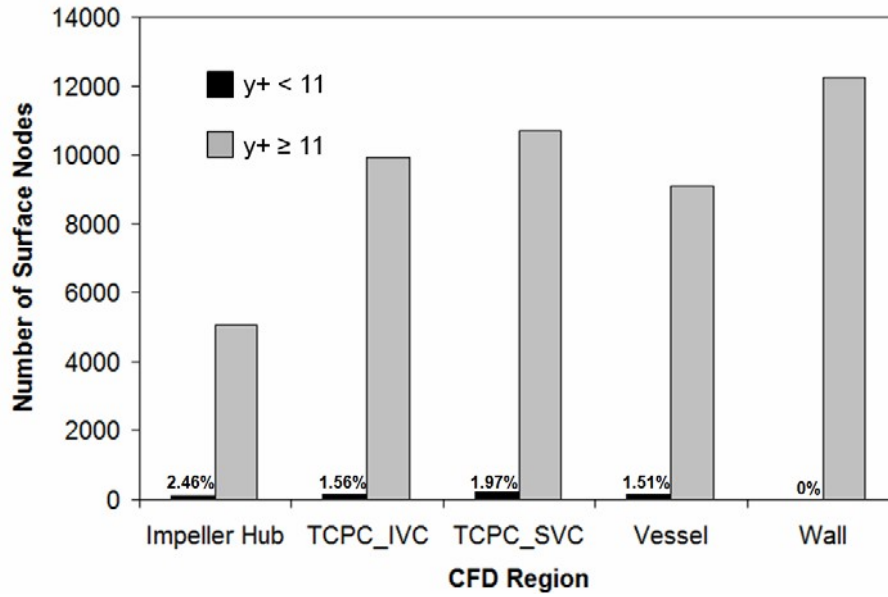
Figure 7.2: Distribution of the y+ nodal values along the boundary surfaces in each region for the k-ε based computational model.
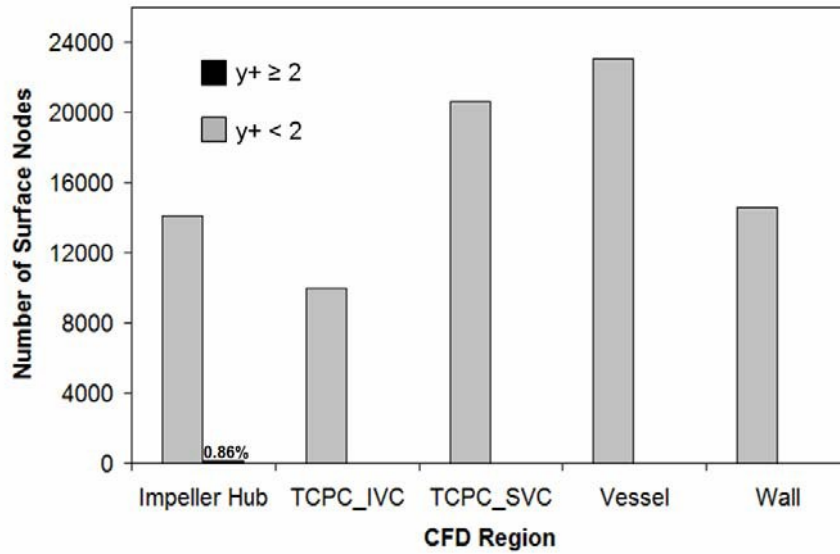
Figure 7.3: Distribution of the y+ nodal values along the boundary surfaces in each region for the SST based computational model.
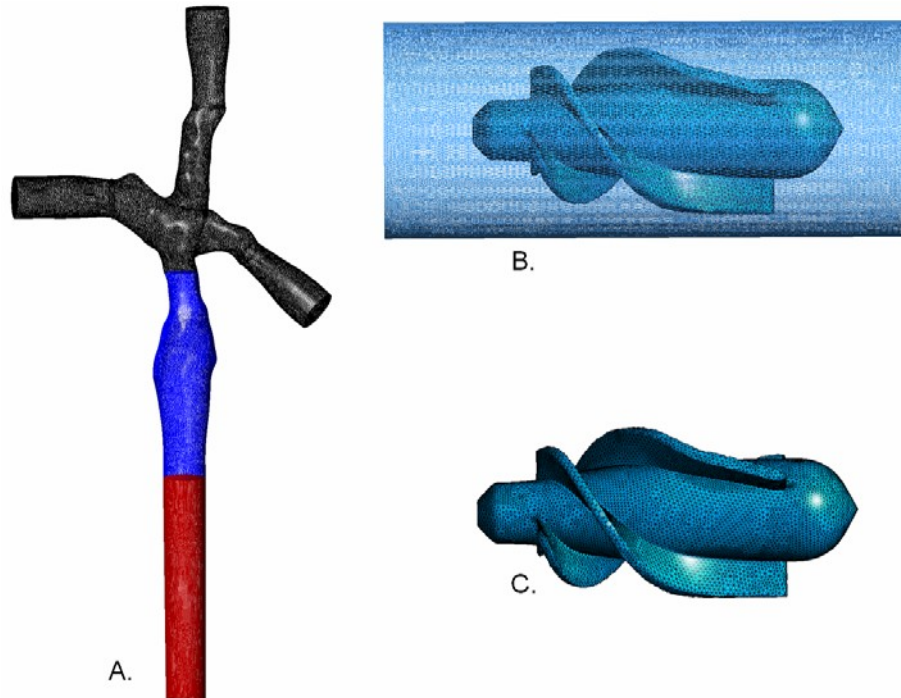
Figure 7.4: Tetrahedral Mesh for TCPC and Pump Model. A) TCPC and vessel connections; B) Vessel wall and pump; and C) Impeller hub surface.

7.2. Steady Flow Simulations

The frozen rotor interface linked regions of differing reference frames between the impeller domain and vessel wall [132]. A uniform mass inflow rate (i.e. cardiac output of 3 L/min) and rotational speed (i.e. 3000 RPM) were specified for each simulation. A range of rotational speeds (i.e. 1000 to 4000 RPM) were also considered. A Newtonian constitutive model with a dynamic viscosity of 3.5 cP (i.e. hematocrit of 33%) and a density of 1050 kg/m^3 was specified for blood based on reasonably high shear rates in the flow domain of the pump (above 100 s^{-1}) [33, 113, 133]. The outlet boundary surface was specified as an opening to capture any possible irregular flow conditions at the outflow. The outlet boundary conditions, such as the left and right pulmonary arteries (LPA and RPA), were defined to have static pressures of 8, 12, 16, and 20 *mmHg*. All of the vessel walls for the IVC, SVC, and pulmonary arteries were modeled as rigid tubes in line with the physical TCPC prototype.

7.3. Hydraulic Power Calculations for the TCPC

The rate of energy augmentation due to the axial flow blood pump was computed using two computational models. A control volume approach was employed to estimate the rate of energy augmentation through the anatomic model with the impeller pump. Per the CFD simulations, **Figure 7.5** illustrates the pressure performance curves of the impeller for a cardiac output of 3 *L/min* and equal, mean pulmonary arterial pressures of 16 *mmHg*. The expected trend of the pressure generation was found, with an increasing rise at higher rotational speeds. The impeller model using the k-ε turbulence model outperformed the impeller model using the SST turbulence model by approximately 55%. The pressure rise for the k-ε model ranged from 0 to 2.2 *mmHg* at rotational speeds of 0 to 4000 RPM.

Using these hydraulic performance estimations, the rate of power gain in the computational models were calculated as shown in **Figure 7.6**. The addition of the impeller into the IVC of the TCPC positively impacted the rate of power gain or energy in the cavopulmonary circulation. The impeller enhanced the rate of power gain as a function of higher operational rotational speeds. The impeller models were found to rapidly increase in hydraulic power, and the impeller model using the k-ε turbulence model generated much higher levels of power gains in the cavopulmonary circuit.
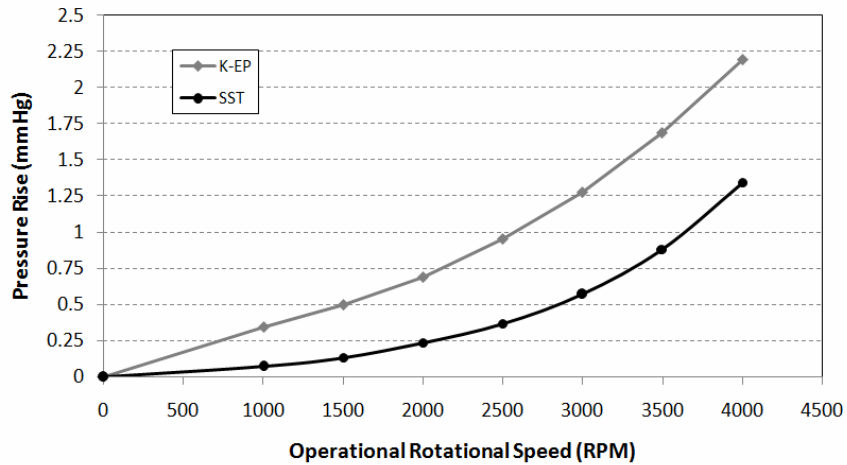
Figure 7.5: Pressure Rise Across the Pump at Equal Pulmonary Arterial Pressures of 16 *mmHg* and at a Cardiac Output of 3 *L/min.*
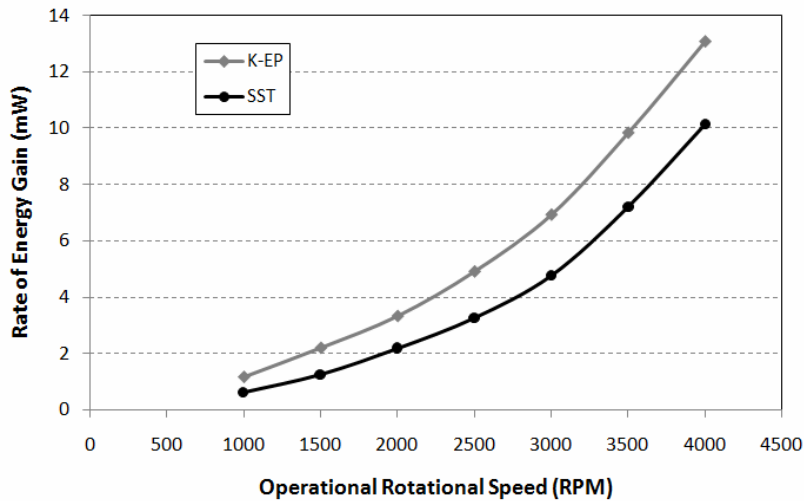
Figure 7.6**:** Rate of Power Gain for the Impeller Pump Configuration Using the k-ε and SST Turbulence Model.

7.4. Flow Streamlines

In contrast to industrial pumps, the internal flow field of blood pump is as important as the global pump performance. Irregular flow patterns and fluid streamlines throughout pump can be indicative of undesired regions of separation, high shear stresses, and possible flow stasis. The next several figures display the numerical fluid streamlines for various operating and

boundary conditions in order to assess irregular flow conditions due to the patient-specific geometry and the impact of the blood pump in the IVC.

Figure 7.7 illustrates the flow streamlines and velocity contour using the k-ε turbulence model for a pump rotational speed of 3000 RPM, cardiac output of 3 *L/min*, and equal, mean pulmonary arterial pressures of 16 *mmHg*. In this figure, the streamlines having a deep red color reflect those particles that were released at the inlet boundary of the SVC, and the streamlines having a dark blue color represent those particles that were released at the inlet boundary of the pump or IVC. It can be noted that blood flow entering the SVC almost completely shunts toward the LPA; whereas, the blood flow from the IVC flows mostly toward the RPA and a small volume does also continue toward the LPA. The velocity contour plot, as shown in **Figure 7.7 (A)**, demonstrates the strong rotational component of the flow leaving the pump and entering the TCPC junction.
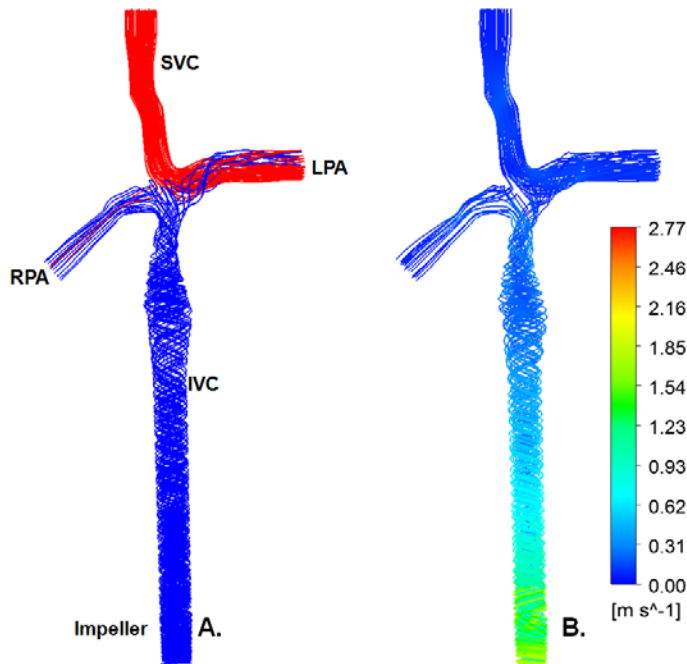
Figure 7.7: Steady Flow Streamlines (k-ε) Through the TCPC During Mechanical Cavopulmonary Assistance at 3000 RPM, Cardiac Output of 3 *L/min*, and Equal Mean Pulmonary Arterial Pressures of 16 *mmHg*. A) Red streamlines reference flow entering from the SVC, whereas dark blue streamlines reference flow entering at the pump inlet and IVC; B) Velocity color contour of the flow streamlines (m/s).

Figure 7.8 displays the velocity streamlines using the k-ε turbulence model for a pump rotational speed of 3000 RPM, cardiac output of 3 *L/min*, equal pulmonary arterial pressures of 16 *mmHg* and rotational speeds of 2000 RPM, 3000 RPM, and 4000 RPM. Higher rotational energy is observed in the blood flow at higher operating rotational speeds. All of these cases illustrate the strong rotational component leaving the impeller design.
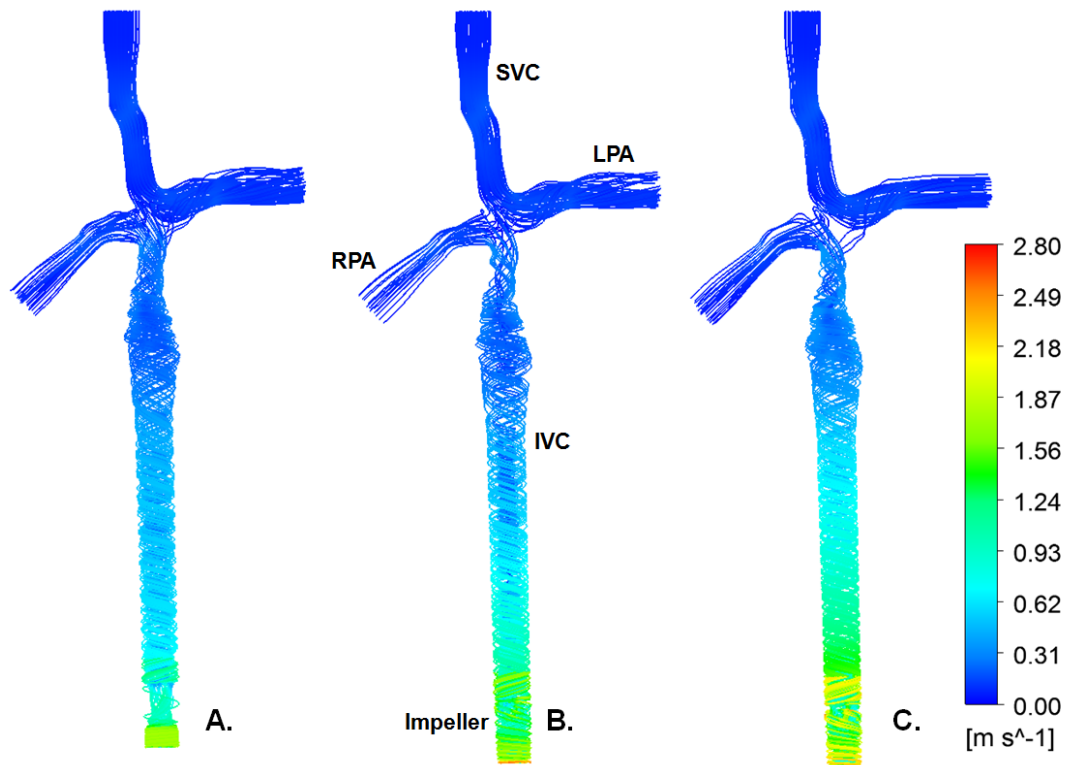
Figure 7.8: Steady Flow Velocity Streamlines (k-ε) Through the TCPC During Mechanical Cavopulmonary Assistance for a Cardiac Output of 3 *L/min* and Equal Mean Pulmonary Arterial Pressures of 16 *mmHg*. A) 2000 RPM; B) 3000 RPM; C) 4000 RPM.

Figure 7.9 illustrates the flow streamlines using the k-ε turbulence model for a cardiac output of 3 *L/min*, equal pulmonary arterial pressures of 16 *mmHg*, and rotational speeds of 2000 RPM, 3000 RPM, and 4000 RPM. Similarly, the streamlines having a deep red color reflect those particles that were released at the inlet boundary of the SVC, and the streamlines having a dark blue color represent those particles that were released at the inlet boundary of the pump or

IVC. At the higher rotational speeds, the computational estimations reveal that blood flow entering the SVC shunts toward the LPA; whereas, at the lower speeds, a volume of the SVC flow does flow into the RPA. On the contrary, blood flow from the IVC shunts more dominantly toward the LPA with small volume flowing toward the RPA. In this case, a larger volume of blood was found to flow toward the RPA at lower rotational speeds.
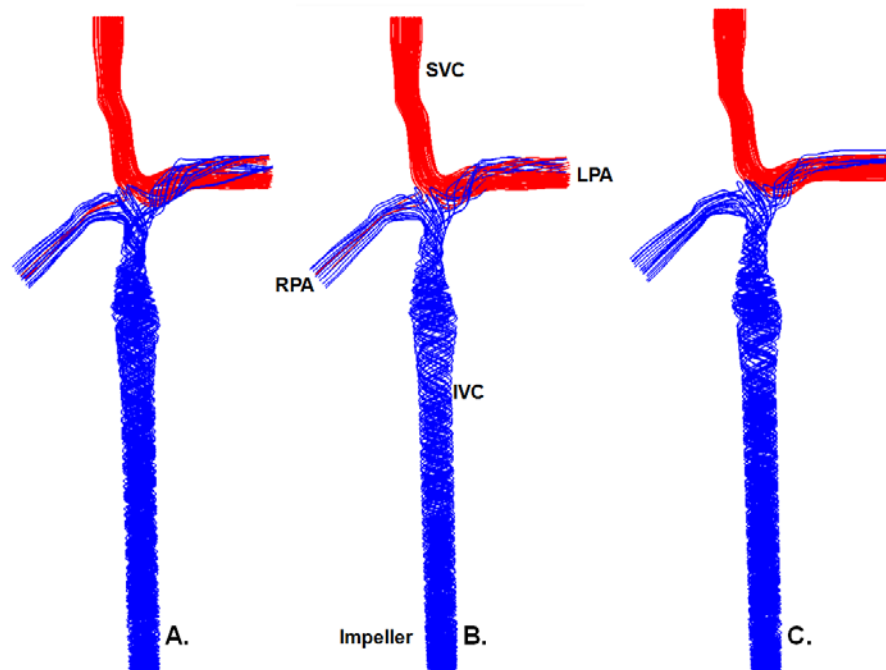
Figure 7.9: Steady Flow Streamlines (k-ε) Through the Cavopulmonary Circulation During Mechanical Cavopulmonary Assistance for a Cardiac Output of 3 *L/min* and Equal Mean Pulmonary Arterial Pressures of 16 *mmHg*. A) 2000 RPM; B) 3000 RPM; C) 4000 RPM. Red streamlines reference flow entering from the SVC, whereas dark blue streamlines reference flow entering at the pump inlet or IVC.

Figure 7.10 demonstrates the flow streamlines using the k-ε turbulence model for a cardiac output of 3 *L/min*, rotational speed of 3000 RPM, and equal and pulmonary arterial pressures of 8 *mmHg*, 12 *mmHg*, and 16 *mmHg*. A similar color convention as found in the previous figure can be seen. Interestingly, higher pulmonary arterial pressures drive a more uniform volume distribution in the LPA and RPA based on the numerical studies. As observed in the prior cases, the SVC blood volume flows dominantly into the LPA.

Figure 7.11 shows the flow streamlines using the k-ε and SST turbulence model for a cardiac output of 3 *L/min*, equal and pulmonary arterial pressures of 16 *mmHg*, and rotational speeds of 2000 RPM, 3000 RPM, and 4000 RPM. A description of the results using the k-ε was previously discussed. The modeling using SST yielded different streamlines and flow distributions than found with the k-ε. The SST simulations show more laminar flow characteristics having an equal split of flow from the SVC inlet into the LPA and RPA. For the 3000 and 4000 RPM cases, more blood flow from the IVC also enters the LPA, which is the opposite of that indicated with the k-ε. In the 2000 RPM case, the SST simulation indicates a substantial percentage of the IVC blood flow enters the LPA, as opposed to the RPA. In addition, this simulation for all rotational speeds reveals a weaker rotational velocity component exiting the impeller. The differences that occur between the k-ε and SST turbulence models are the result of the fact there is no one turbulence model than can completely predict all of the fluid flow patterns, particularly with regard to highly three-dimensional flows. The streamlines in the model suggest that mixing of the IVC flow does occur but the solvers disagree as to whichever pulmonary artery the IVC flow will be directed toward.
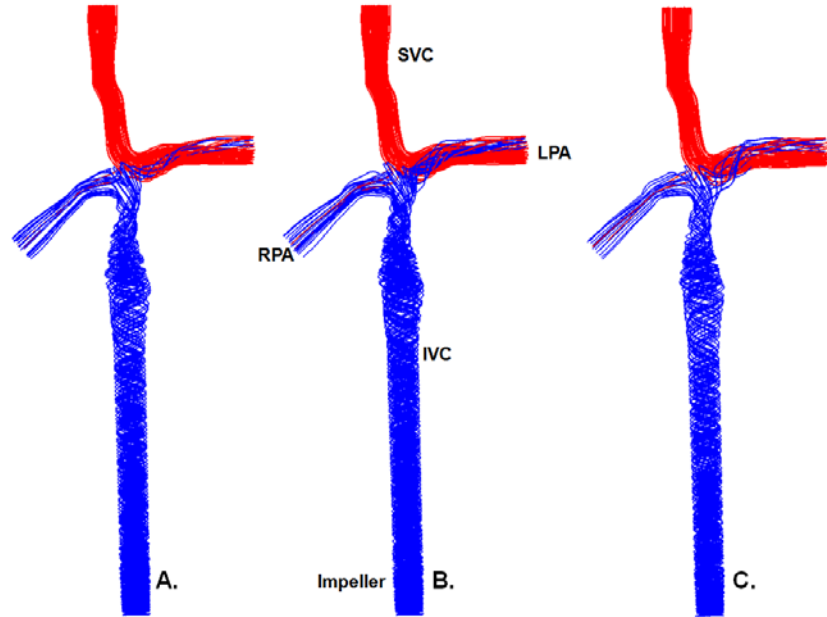
Figure 7.10: Steady Flow Streamlines (k-ε) Through the Cavopulmonary Circulation During Mechanical Cavopulmonary Assistance at 3000 RPM and Cardiac Output of 3 *L/min.* A) Equal and mean pulmonary arterial pressures of 8 *mmHg*; B) Equal and mean pulmonary arterial pressures of 12 *mmHg*; C) Equal and mean pulmonary arterial pressures of 16 *mmHg*. Red streamlines reference flow entering from the SVC, whereas dark blue streamlines reference flow entering at the pump inlet and IVC.
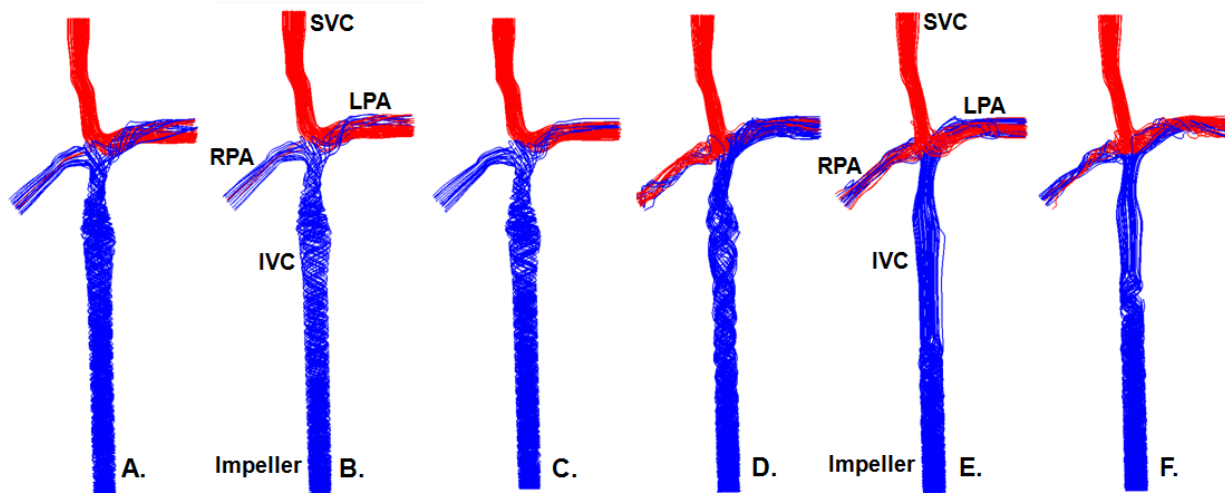
Figure 7.11: Steady Flow Streamlines Through the Cavopulmonary Circulation During Mechanical Cavopulmonary Assistance for a Cardiac Output of 3 *L/min* and Equal Pulmonary Arterial Pressures of 16 *mmHg*. A) 2000 RPM using k-ε; B) 3000 RPM using k-ε; C) 4000 RPM using k-ε; D) 2000 RPM using SST; E) 3000 RPM using SST; and F) 4000 RPM using SST. Red streamlines reference flow entering from the SVC, whereas dark blue streamlines reference flow entering at the pump inlet and IVC.

7.5. Blood Damage Analysis

A blood damage analysis using a total of 1920 particle streamlines based on a power law construct was applied to estimate the potential for hemolysis and thrombosis for this blood-contacting intravascular blood pump. This analysis has been employed as a predictive tool in the development of blood pumps [111, 115, 134]. This approach as detailed in Song *et al.*[115] uses a power law relationship between the fluid scalar stress level and the exposure time to levels of stress. The power equation provides a statistical estimate of damage to blood cells traveling through the model as a blood damage index. Half of the particles are release at the model inlets, the SVC and IVC and allowed to flow to the outlets, the RPA and LPA [55, 115].

Scalar fluid stress values were numerically estimated (k-ε turbulence model) at each nodal location in the computational flow field. **Figure 7.12** illustrates the maximum scalar stress level that was estimated in numerical flow domain for increasing rotational speeds. Higher rotational speeds led to much larger scalar stress values, but the magnitude of the scalar stress never exceeded the cutoff of 460 *Pa*. **Figure 7.13** depicts the scalar stress distribution along the rotating impeller surfaces at 3000 RPM. As expected, the highest fluid stresses were found at the leading edge of the impeller blades and along the blade tips. The highest fluid stresses of 110 *Pa* were estimated to exist along a small regional surface area (9%) of the rotor hub for 4000 RPM.
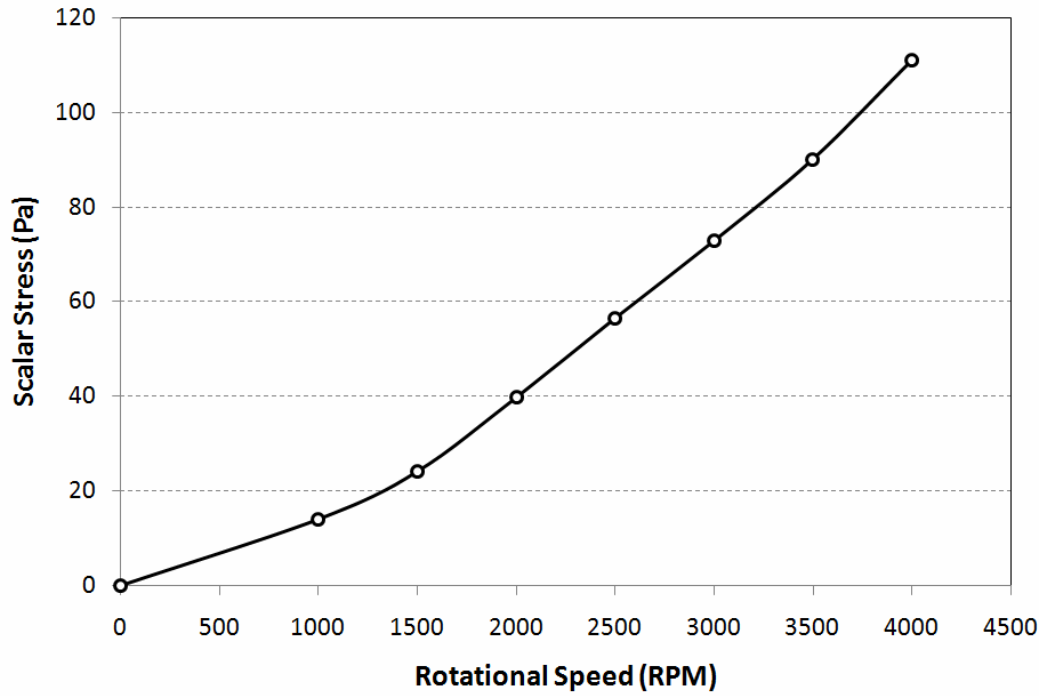
Figure 7.12: Maximum Scalar Stress Levels in the Computational Model as a Function of Increasing Rotational Speeds.
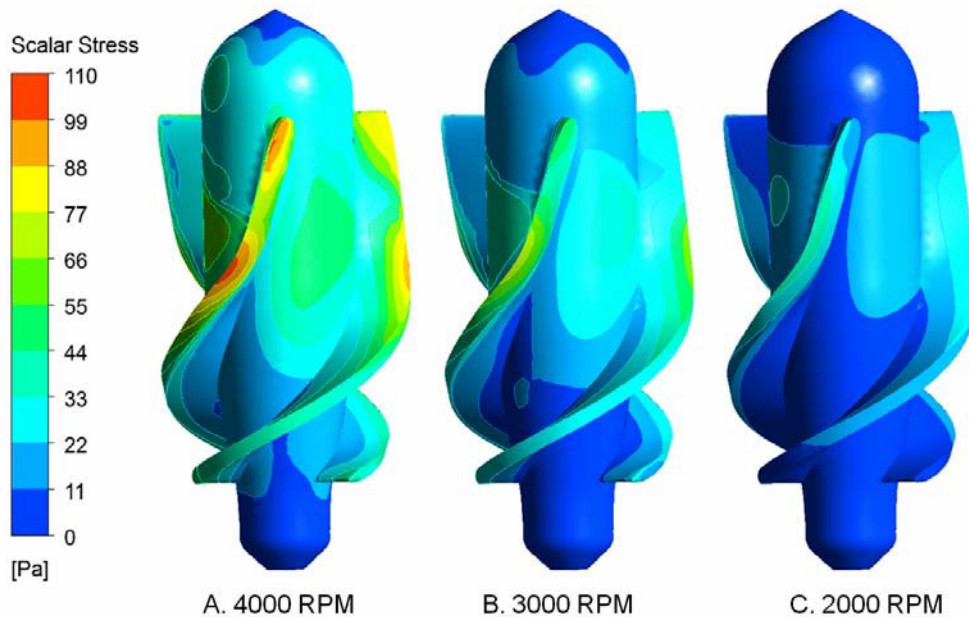
Figure 7.13: Scalar Stress Distribution Along the Rotating Impeller Surfaces for a Cardiac Output of 3 *L/min* and Equal, Mean Pulmonary Arterial Pressures of 16 *mmHg*. A) Rotational speed of 4000 RPM, B) Rotational speed of 3000 RPM, and C) Rotational speed of 2000 RPM.

Similarly, **Figure 7.14** shows the scalar stress distribution along the inlet IVC vessel surfaces immediately prior to the TCPC junction with a cardiac output of 3 *L/min* and equal, mean pulmonary arterial pressures of 16 *mmHg* for 2000, 3000, and 4000 RPM. Due to the vorticity of the flow coming from the rotating impeller, the scalar stress levels continued to remain elevated into the vessel toward the TCPC junction, but the magnitude was reduced. In the SVC and TCPC junction, **Figure 7.15** illustrates that the magnitude of the scalar stress levels dropped considerably before flow entered the pulmonary arteries and exited the cavopulmonary circulation. Scalar stress levels were very low at around 2 *Pa* for these operational conditions.
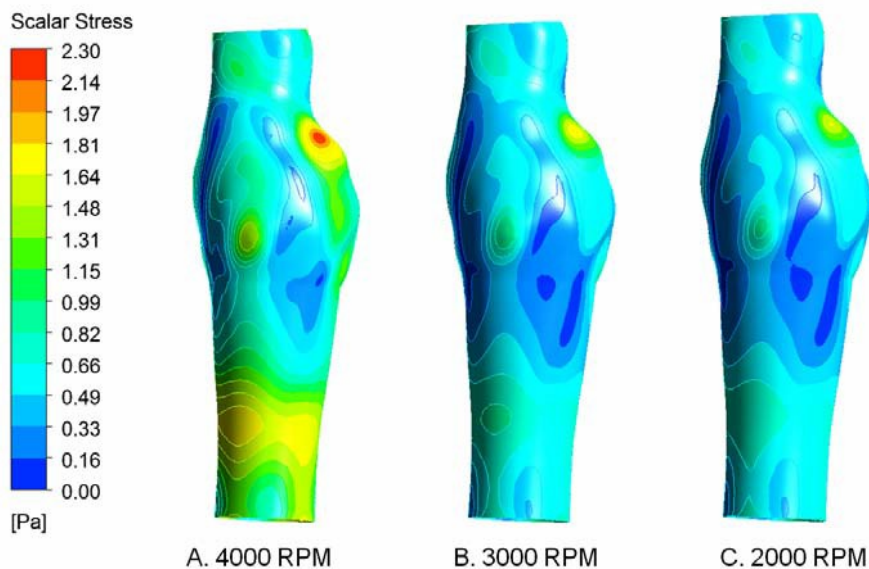
Figure 7.14: Scalar Stress Distribution Along the Inlet IVC Vessel Surfaces Immediately Prior to the TCPC Junction at a Cardiac Output of 3 *L/min* and Equal, Mean Pulmonary Arterial Pressures of 16 *mmHg*. A) Rotational speed of 4000 RPM, B) Rotational speed of 3000 RPM, and C) Rotational speed of 2000 RPM.
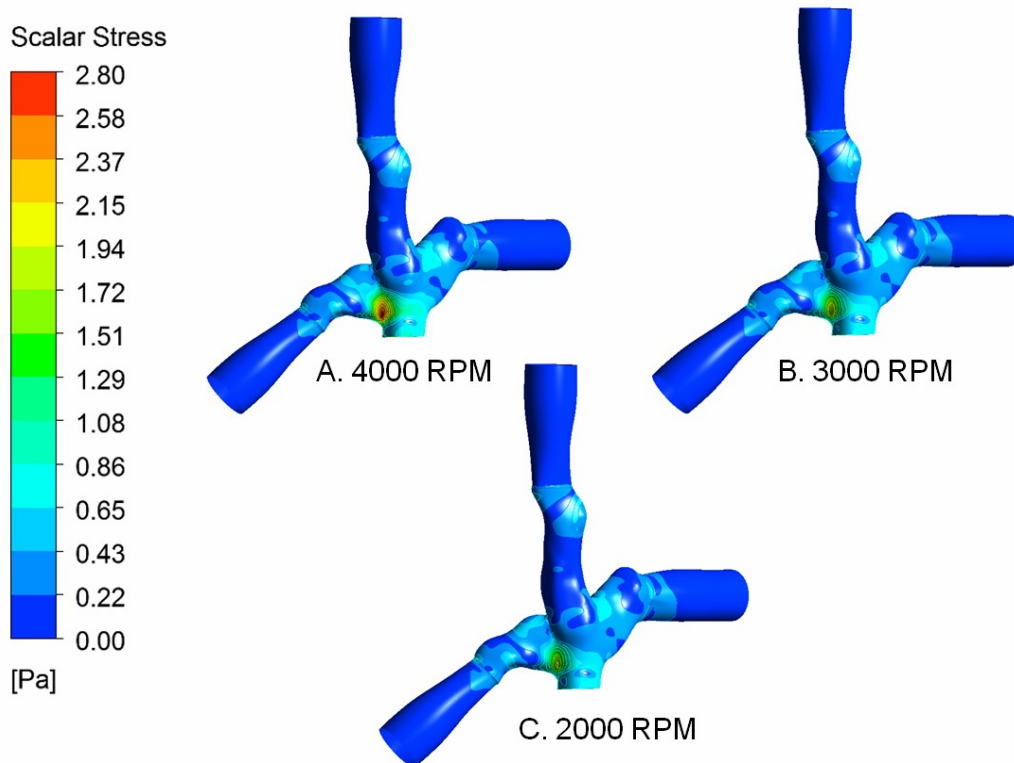
Figure 7.15: Scalar Stress Distribution Along the SVC Vessel Surfaces and TCPC Junction for a Cardiac Output of 3 *L/min* and Equal, Mean Pulmonary Arterial Pressures of 16 *mmHg*. A) Rotational speed of 4000 RPM, B) Rotational speed of 3000 RPM, and C) Rotational speed of 2000.

As part of this analysis, the model (k-ε turbulence model) was separated into two sections (i.e. IVC and SVC / TCPC junction) in order to maximize the number of possible particles to be released along streamlines and to investigate 4 rotational speeds (i.e. 1000, 2000, 3000, and 4000 RPM). The left and right pulmonary arterial pressures were 16 *mmHg*, and the cardiac output was maintained at 3 *L/min* for these simulations. The mean particle residence times for the SVC and TCPC junction side exited the model for all rotational speeds much faster, and flow was shunted toward the left pulmonary artery. In contrast, due to the impact of the impeller on the flow vorticity, particle residences times on the IVC flow side into the TCPC junction were extended close to and beyond 10 seconds with blood flow shunting toward the right pulmonary artery.

Mean particle residence times were less than 1 second at higher operating rotational speeds, in accordance with prior work [32, 54, 55]. **Figure 7.16** shows the damage indices for the impeller model (k-ε) based on a total of 1920 particle streamlines for the pump rotational speed of 2000 RPM, a cardiac output of 3 *L/min*, and 40% / 60% inflow conditions at the SVC inlet and at the IVC inlet and equal, mean left / right pulmonary arterial pressures of 16 *mmHg*. In comparison, **Figure 7.17** illustrates the damage indices under the same conditions at 4000 RPM. As expected, the higher rotational speed resulted in larger predicted damage indices and a wider distribution of such quantities. **Table 7.2** lists the blood damage analysis for each region and as a function of the rotational speeds. In general, the mean damage indices under all of the operating conditions were found to be less that the target value of 2%, which is encouraging. The maximum damage indices, however, were determined to be higher than anticipated with levels reaching slightly above 3%, which are likely due to the rotational vorticity of the flow leaving the trailing edge of the impeller blades.
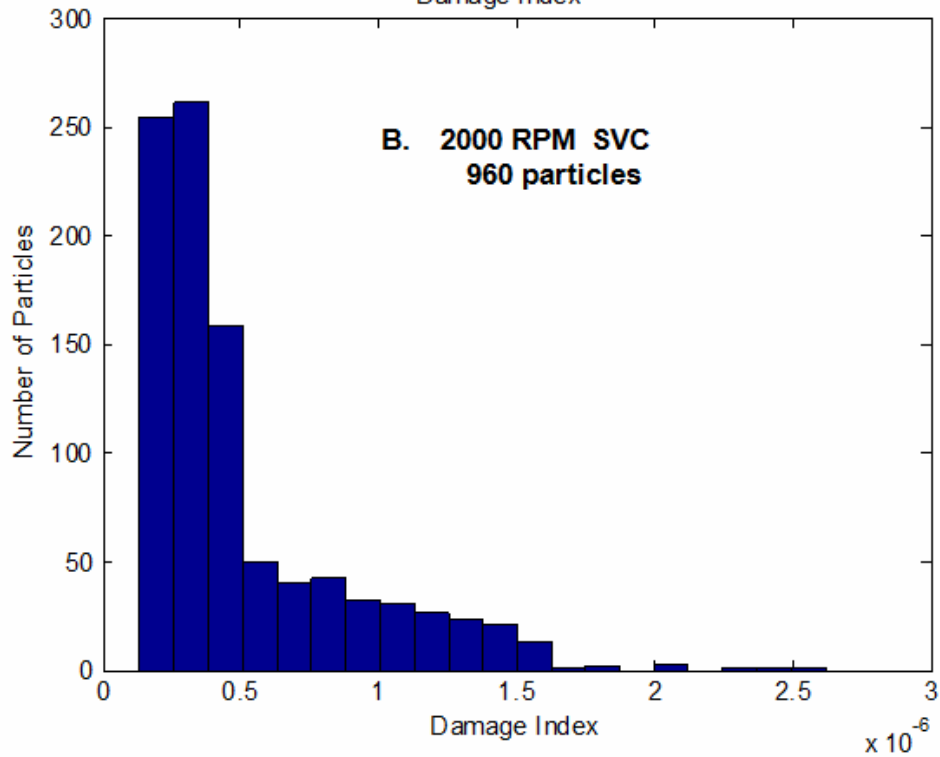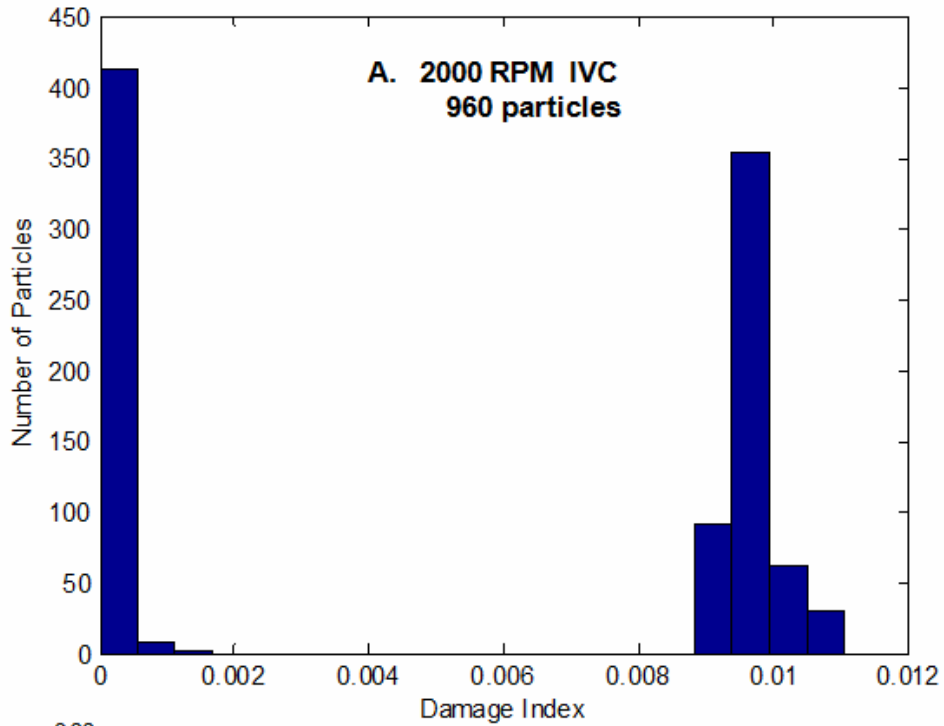
Figure 7.16: Damage Indices for the Impeller Model (k-e) at based on 1920 Particle Streamlines for an Operational Condition of 2000 RPM, Cardiac Output of 3 L/min, and Equal, Mean, Left I Right Pulmonary Arterial Pressures of 16 mmHg. A) 960 particles released at the IVC inlet, B) 960 particles released at the SVC inlet.
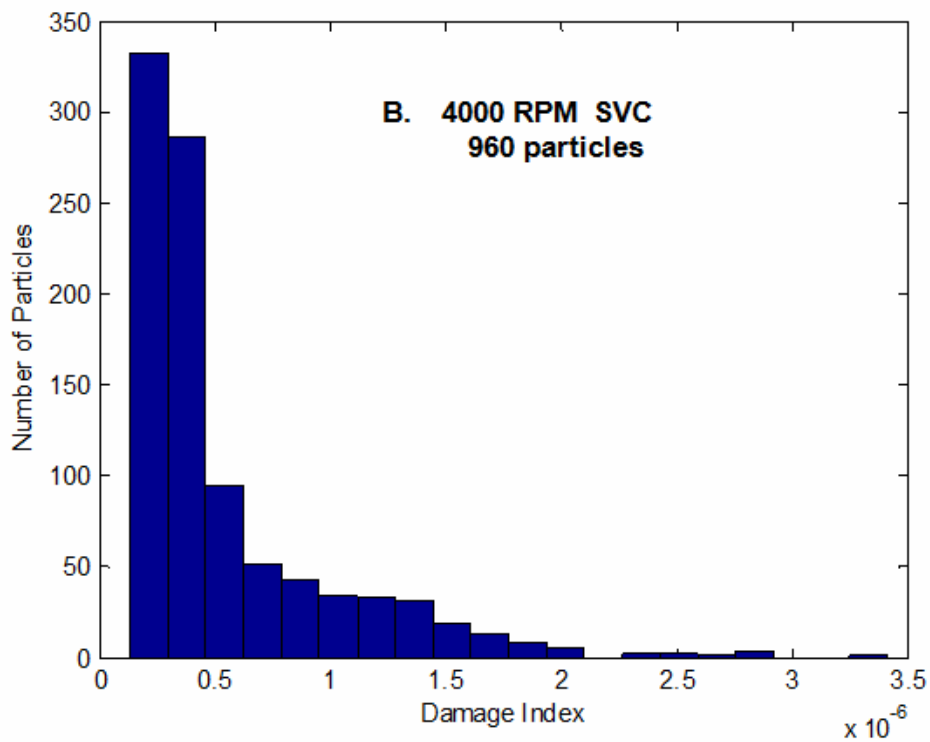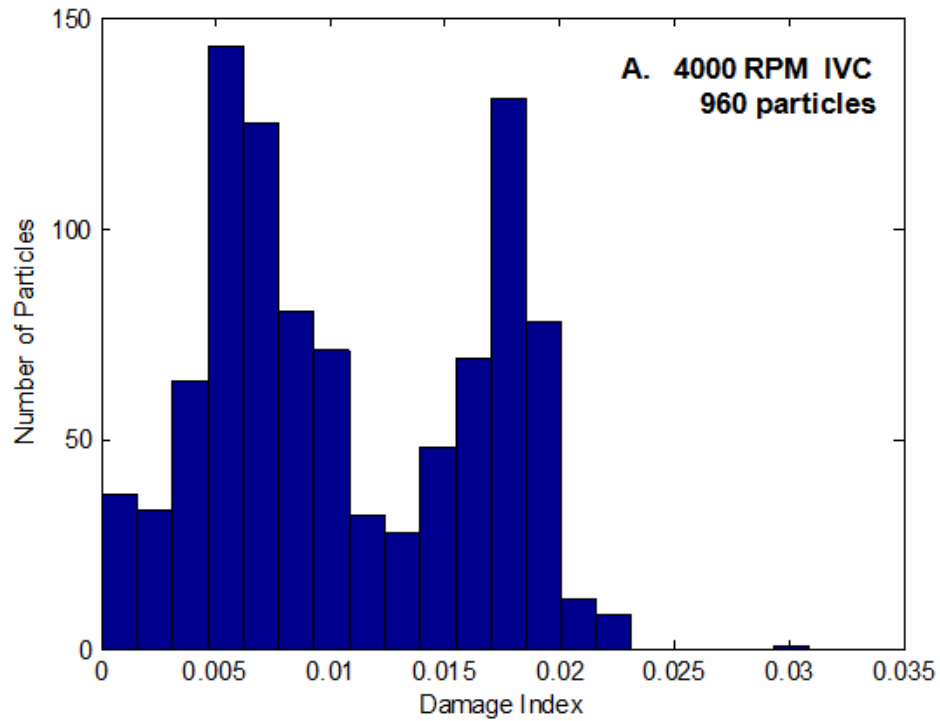
Figure 7.17: Damage Indices for the Impeller Model $(k\text{-}\varepsilon)$ at based on 1920 Particle Streamlines for an Operational Condition of 4000 RPM, Cardiac Output of 3 L/min, and Equal, Mean, Left / Right Pulmonary Arterial Pressures of 16 *mmHg*. A. 960 particles released at the IVC inlet, B. 960 particles released at the SVC inlet.

Table 7.2: Blood Damage Analysis Results for a Cardiac Output of 3 *L/min* and Pulmonary Arterial Pressures of 16 *mmHg*.

Impeller Cavopulmonary Modeling Conditions	Mean Residence Time (sec)	Mean Residence Time (sec)	Mean Damage Index (%)	Max Damage Index (%)
1000 RPM – IVC Region	2.41	13.8	4.72×10^{-2}	0.13
1000 RPM – SVC Region	0.89	2.83	4.86×10^{-5}	2.02×10^{-4}
2000 RPM – IVC Region	1.78	11.7	0.56	1.11
2000 RPM – SVC Region	0.88	2.91	5.12×10^{-5}	2.62×10^{-4}
3000 RPM – IVC Region	1.18	8.72	1.83	2.89
3000 RPM – SVC Region	0.87	2.67	5.18×10^{-5}	2.21×10^{-4}
4000 RPM – IVC Region	0.89	8.75	1.06	3.09
4000 RPM – SVC Region	0.84	3.22	3.86×10^{-5}	3.41×10^{-4}

7.6.   Chapter Summary

This chapter discusses the results for the numerical methods from **Chapter 5**. Data for the velocity magnitude, shear stress, power efficiency, and blood damage were examined and analyzed and found to be supportive of the use of an axial flow pump in the IVC of a patient-specific TCPC. The next chapter will cover the results from the physical experiments of **Chapter 6** with a comparison between the numerical and experimental results occurring shortly thereafter.

CHAPTER 8: Experiment Results

8.1. Introduction

This chapter outlines the results from the experiments conducted in **Chapter 6**. We will begin by discussing the results from the hydraulic testing of the anatomic TCPC model and the pump with and without cages. This testing was important in providing a fundamental understanding of the pressure generation that the pump is capable of producing, as well as in providing an assessment the fluid system performance in providing a mock circulation of Fontan physiology. These experiments also served to verify the testing conditions for the PIV studies. In addition, the effects of the pump and the use of the protective cages or stents were studied to determine the effect on the power efficiency of the anatomic model. The PIV results of the anatomic model will be presented later with the chapter concluding with comparisons of the PIV results to an idealized model as well as to our predictive numerical model from **Chapter 5**.

8.2. Power Efficiency Studies

The following results demonstrate the gain in energy that is provided by the pump to the patient-specific cavopulmonary circulation. **Figure 8.1** shows the pressure performance curves of the impeller with and without the cages for a cardiac output of 3 *L/min* and equal pulmonary arterial pressures of 16 *mmHg*. The trend of the pressure generation was found to increase with higher rotational speeds. The *against-with* cage was found to reach a higher pressure rise of 5 *mmHg* at a lower rotational speed (i.e. 4000 RPM) than compared to the impeller alone and the *super-diffuser* design. The performance of the *against-with* cage exceeded that of the impeller alone and the *super-diffuser*. The impeller alone was found to produce higher pressures than the impeller having the *super-diffuser* cage.

More detailed measurements of differential changes in the system were determined, as shown in **Table 8.1. Table 8.1** presents the differentials or changes in system pressures and vessel flow rates under conditions of equal LPA and RPA pressures of 16 *mmHg*. Positive values directly indicate an increase in the respective measurement, whereas, negative values indicate a subsequent decrease. The IVC flow rate for the *against-with* and *super-diffuser* cage was determined to approximately double the initial flow rate at 3500 RPM and 3000 RPM, respectively. The increase in IVC flow was found to augment the PA flow, having only a small impact on the pressure and flow in the SVC. Flow into the TCPC from the SVC was measured to be slightly reduced at higher rotational speeds. Retrograde flow into the SVC was neither observed, nor measured, for the range of operating conditions evaluated in this study [122].

For rotational speeds of 0 to 4000 RPM, the system response curves of **Figure 8.2** illustrate the changes in measured static pressure of the SVC, IVC, RPA, and LPA with the impeller in the flow circuit at a cardiac output of 3 *L/min* and then in direct comparison to the impeller having the cage configurations. For the *against-with* case, as displayed in **Figure 8.2 (A)**, the impeller and cage combination produced a more rigorous reduction in IVC pressure by 5 *mmHg* while increasing the pressure into the pulmonary arteries by 2 *mmHg* over the operating speeds. Similarly, for the *super-diffuser* case, as displayed in **Figure 8.2 (B)**, the impeller and cage combination generated a more gradual decline in IVC pressure by 3 *mmHg* while increasing the pressure into the pulmonary arteries by 1.5 *mmHg*. **Figure 8.2 (C)** shows the case with only the impeller, which was capable of only modestly augmenting the pulmonary pressures and reduced the IVC pressure by a maximum of 1.5 *mmHg*. The SVC pressure was found to increase in both instances where a cage was coupled to the impeller, and it was measured to remain reasonably constant when the impeller alone was tested.

Table 8.1: Pump and Cage Performance Characteristics

Configuration	Rotational Speed (RPM)	ΔQ: SVC (L/min)	ΔQ: IVC (L/min)	ΔQ: RPA (L/min)	ΔQ: LPA (L/min)	ΔP: SVC (mmHg)	ΔP: IVC (mmHg)	ΔP: RPA (mmHg)	ΔP: LPA (mmHg)	ΔP: Across Pump (mmHg)	Δ Power (mW)
Impeller	0	0.00	0.00	0.00	0.00	0.00	0.00	0.00	0.00	-0.40	0.00
	1000	-0.01	0.00	0.00	-0.02	-0.04	-0.05	0.01	0.00	-0.52	0.30
	1500	0.05	-0.02	0.01	0.04	-0.09	-0.05	0.00	-0.01	-0.36	1.41
	2000	-0.02	0.00	-0.01	-0.03	-0.07	-0.06	0.12	-0.01	0.09	2.87
	2500	-0.02	0.01	-0.01	-0.01	-0.07	-0.04	0.16	0.00	0.57	4.59
	3000	-0.01	0.01	-0.01	0.00	-0.06	-0.11	0.15	0.02	1.20	6.59
	3500	-0.01	0.04	0.01	0.00	-0.08	-0.20	0.14	0.03	1.73	9.19
	4000	-0.02	0.05	0.02	-0.01	-0.07	-0.31	0.11	0.04	2.72	12.51
Super-Diffuser	0	0.00	0.00	0.00	0.00	0.00	0.00	0.00	0.00	-0.53	0.43
	1000	-0.02	-0.01	0.02	-0.01	-0.03	-0.71	-0.05	-0.07	0.25	0.75
	1500	-0.03	0.10	0.05	0.04	0.07	-1.25	-0.05	-0.07	0.90	0.87
	2000	-0.04	0.40	0.22	0.17	-0.06	-1.88	0.02	0.04	1.57	1.91
	2500	-0.07	0.87	0.39	0.36	0.15	-2.26	0.20	0.30	2.29	4.06
	3000	-0.10	1.54	0.70	0.67	0.38	-2.85	0.35	0.53	3.38	7.99
	3500	-0.06	1.89	1.01	1.11	0.63	-3.51	0.39	0.54	4.59	13.50
	4000	-0.12	2.58	1.12	1.27	0.78	-4.40	0.47	0.69	5.96	19.03
Against-With	0	0.00	0.00	0.00	0.00	0.00	0.00	0.00	0.00	-1.16	0.19
	1000	-0.03	0.00	0.01	0.00	0.04	-0.55	-0.90	0.01	-0.45	0.35
	1500	-0.08	0.26	0.10	0.03	0.07	-1.02	-0.81	0.03	0.13	0.88
	2000	-0.15	0.80	0.40	0.23	0.19	-1.40	-0.58	0.20	0.80	1.21
	2500	-0.21	1.44	0.66	0.51	0.42	-1.69	-0.43	0.45	1.73	3.78
	3000	-0.23	1.89	1.00	0.76	0.66	-2.01	-0.30	0.76	2.65	7.21
	3500	-0.28	2.66	1.36	1.04	1.13	-2.38	-0.20	1.12	3.97	12.49
	4000	-0.29	2.80	1.39	1.31	1.43	-2.69	-0.12	1.25	4.90	14.49

The rate of power gain measurements for the anatomic model is shown in **Figure 8.3**. The addition of the pump into the IVC of the TCPC had a significant impact on the rate of power gain or energy in the cavopulmonary system. All of the pump configurations enhanced the rate of power gain and increased the efficiency by adding energy and rotational force to the fluid flow. **Figure 8.3 (A)** shows the introduction of the *super-diffuser* cage to the anatomic model with an additional improvement in efficiency and achievement of higher hydraulic powers at lower rotational speeds. The *against-with* cage, as seen in **Figure 8.3 (B)**, performed reasonably well in augmenting the rate of power gain in the cavopulmonary circuit and also achieved higher gains at lower rotational speeds in comparison to the performance of the impeller alone. The impeller and *super-diffuser* cage were found not to generate as much power as rapidly as the *against-with*

configuration; however, the impeller and against-with cage demonstrated a rapid increase, but then leveled its power gain at 4000 RPM.
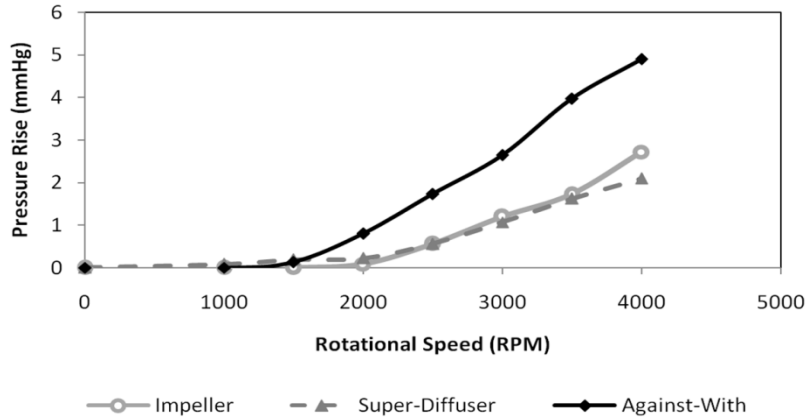
Figure 8.1: Pressure Rise Across the Pump at Equal Pulmonary Arterial Pressures of 16 *mmHg* and at a Cardiac Output of 3 *L/min.*
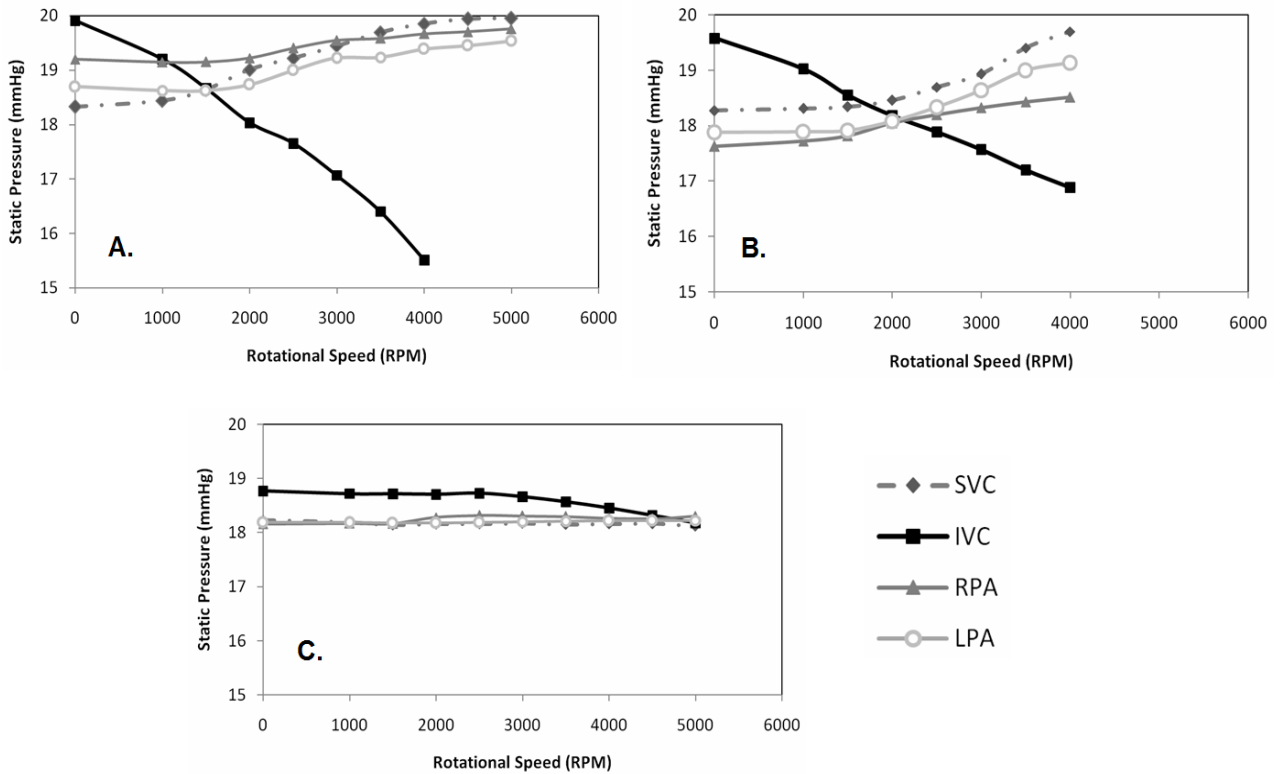
Figure 8.2: System Static Pressure Response Curves for Three Pump Configurations at a Cardiac Output of 3 *L/min.* A) Super-diffuser cage, B) Against-with cage, C) Impeller.
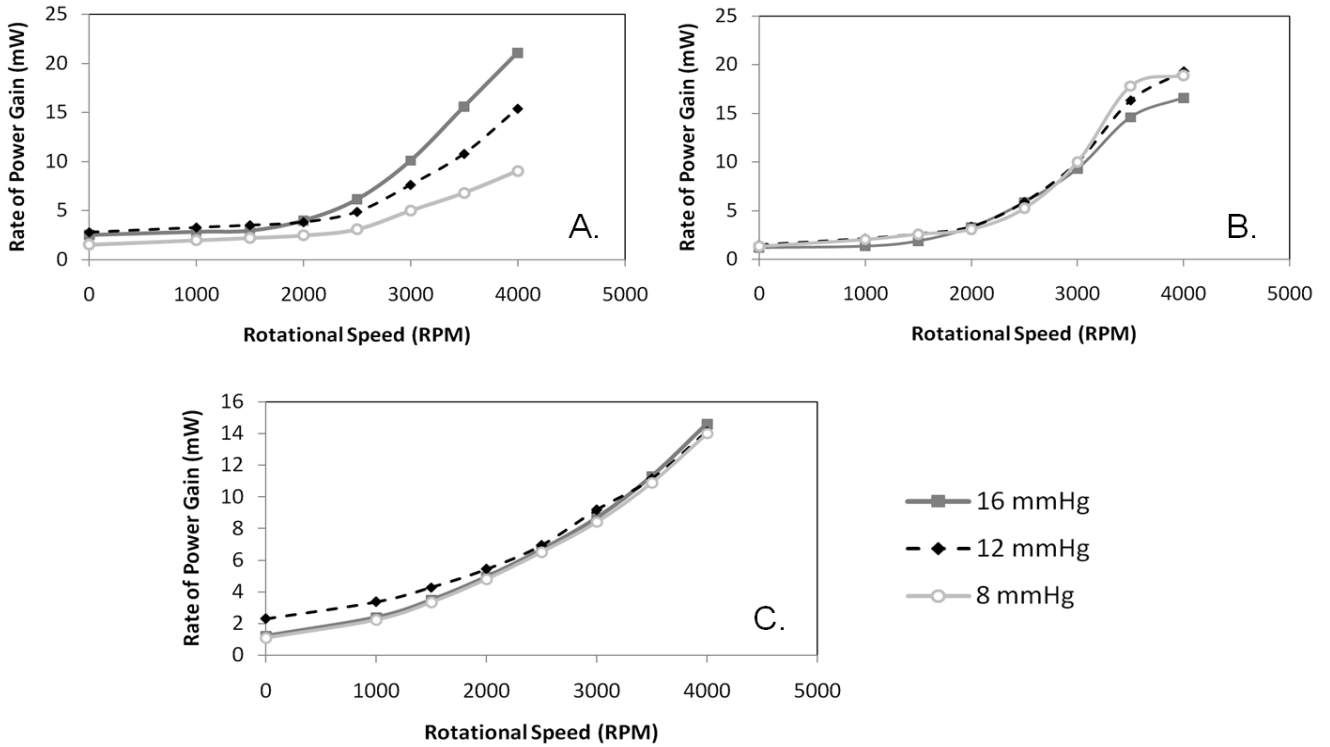
Figure 8.3: Rate of Power Gain for Three Pump Configurations. A) Super-diffuser cage,
B) Against-with cage, C) Impeller.

8.3. PIV Studies

8.3.1. Introduction

The PIV studies that were performed as part of this research project are displayed in this chapter. The goal of these PIV measurements was to obtain 3-D global velocity profiles of a patient-specific anatomic TCPC model under conditions of mechanical cavopulmonary assistance. The methods that were utilized to produce these profiles were set forth in **Chapter 6**. To better understand the fluid mechanics of the pump and TCPC interaction, the 3-D velocity profile can be resliced into planes in 3-D space which permit the observation of local phenomena and 3-D velocities at any location. For the purpose of presenting the data in the most efficient manner, an isometric view is applied to the volumetric PIV data in order to more closely examine the complex 3-D flow structures of interest, while a frontal view is reserved solely for

planar slices through the volume. **Figure 8.4** shows the velocity distribution for a set of slices in the Y-direction. For clarity, every 5th slice is shown to effectively visualize the velocity plots. Streamlines can be applied to a volumetric velocity profile or to planar slices in order to visualize the flow phenomena.
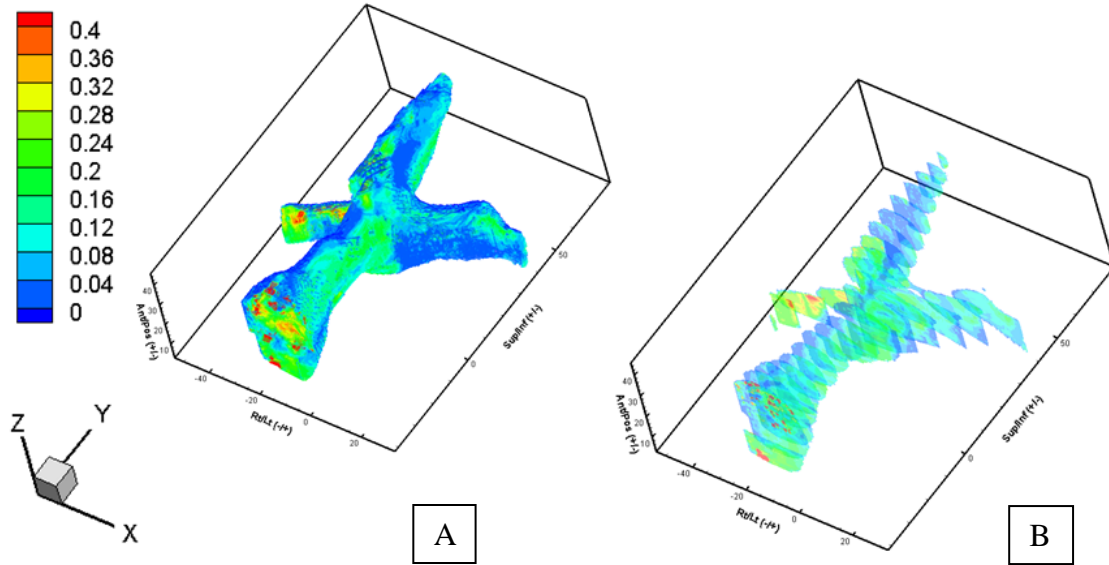
Figure 8.4: A) PIV volumetric data for the case of the impeller rotating at 3000 RPM, B) Slices in the Y-direction through the data volume. Scale: mm.

8.3.2. Control Case

Figure 8.5 **(A)** and **(B)** show the anterior and posterior views of the anatomic model. In the anterior view, it is possible to see the nature of the entering caval flows. Further analysis reveals that there are a total of four vortices present in this model due to stagnant flow patterns. The three vortices in the anastomosis are due to the colliding vena cavae flows. These vorticies to be expected given the nature of the flow patterns that have been observed in an idealized TCPC model. The fourth vortex is present in the IVC and is due to a bulge created by the rapid tapering of the larger diameter IVC vessel to be able to connect to the much smaller diameter

155

pulmonary artery. The fluid stagnates in the bulge and forms a recirculation region, which may promote conditions favorable for a thrombus formation.

The flow in the TCPC anastomosis is strongly three-dimensional, as would be expected from the colliding flows and uneven vasculature surfaces. There is a vessel offset present in this anatomic model as well as flaring of the vessel walls at the anastomosis sites for the vena cavae. These geometric structures inherently affect the fluid flow patterns in the model. Close up views of the anterior side shown in **Figure 8.6** combined with planar vessels slices shown in **Figure 8.7** allow us gain some additional insight into the recirculation regions that exist in this model.
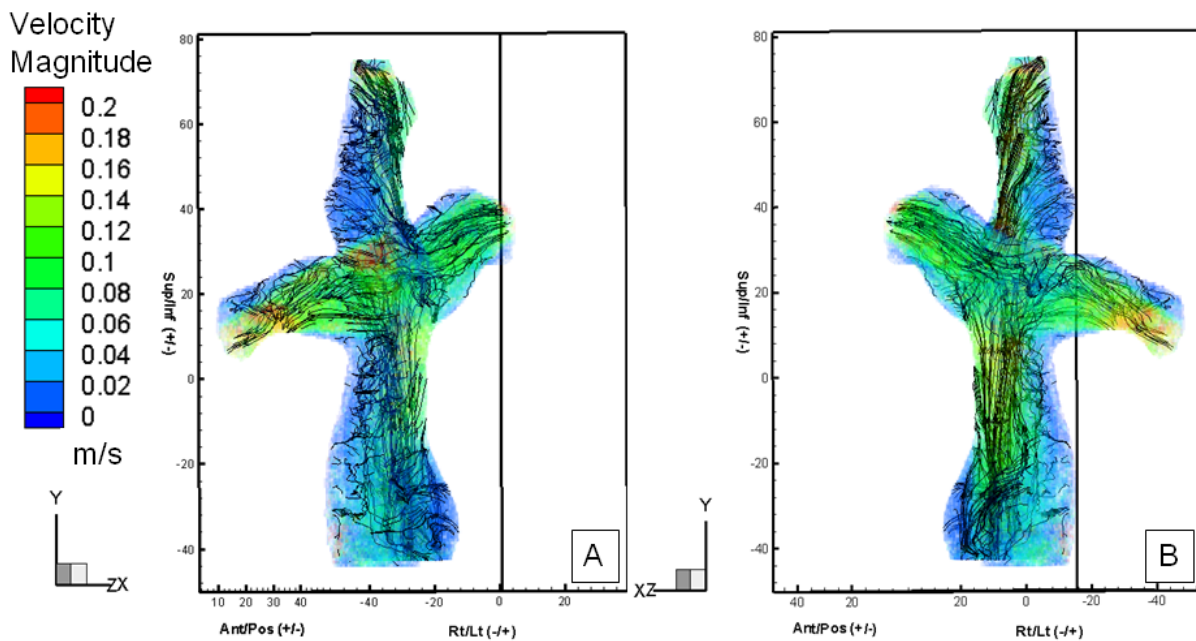
Figure 8.5: Control Case: A) Anterior side, B) Posterior side. Scale: mm.
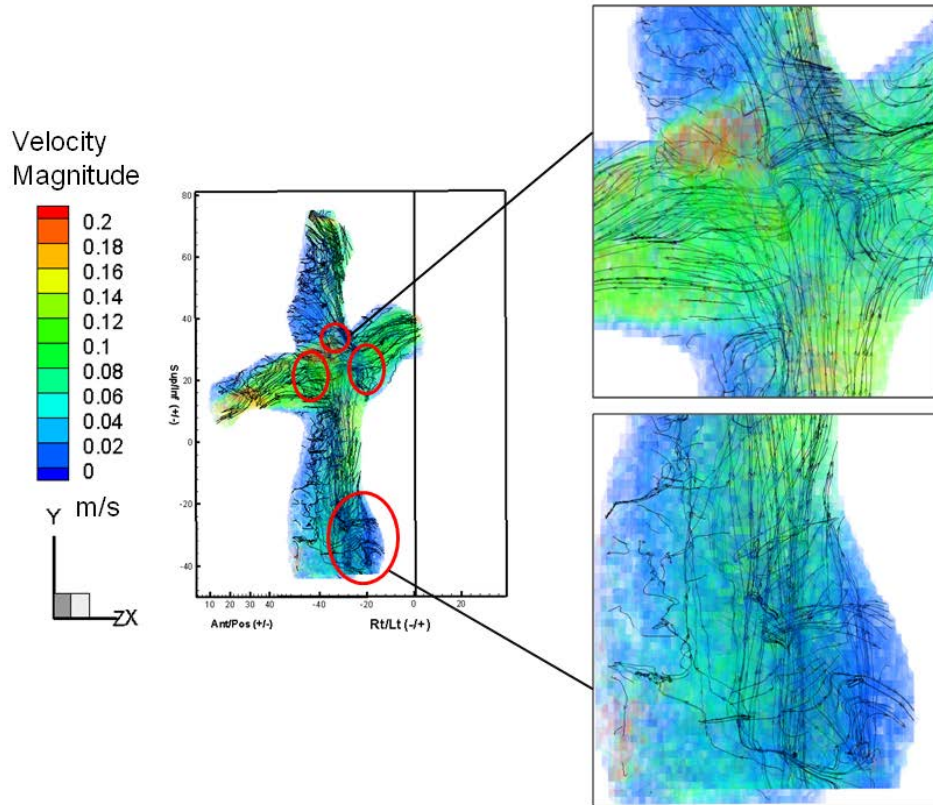
Figure 8.6: Control Case: Anterior side: Vortices outlined in red circle. Scale: mm.

Figure 8.7 displays the true nature of the entering and exiting flows. The slices are taken prior to the vena cavae connections to the TCPC junction and just past the anastomosis site leading to the left and right pulmonary arteries. **Figures 8.7 (A)**, **(B)**, **(C)**, represent the RPA, LPA, and IVC, respectively. All three vessels exhibit a spiraling or helical flow pattern. The SVC in **Figure 8.7 (D)** does not have a helical flow pattern present when flow enters the anastomsis. The helical pattern in the RPA and LPA has been noted previously as occurring as a result of the colliding vena cavae flows. The helical nature of the IVC is most likely due to the ellipsoid vasculature structure combined with the uneven, undulating vessel walls.
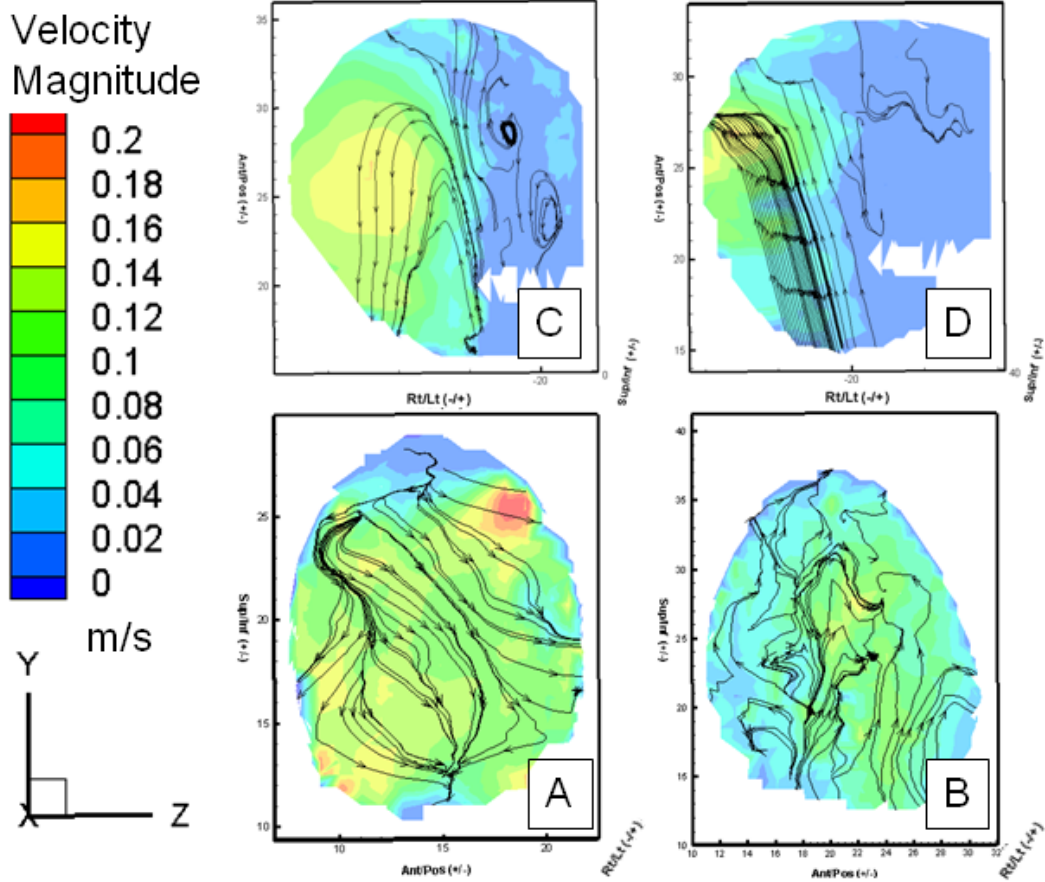
Figure 8.7: Side Slices: A) RPA, B) LPA, C) IVC, D) SVC

8.3.3. Impeller only case

The introduction of the impeller in **Figure 8.8** has a modest effect on the flows at low rotational speeds but a dramatic effect on the flows at higher rotational speeds. **Figure 8.8 (B)** illustrates the 1000 RPM case for the impeller without a set of protective cage filaments or a set of diffuser blades present. The effects of the pump are visible as the streamlines that curve toward the wall of the model in the bulge portion of the IVC. Some of the rotating flow from the impeller is able to make it out of the bulge and follow the IVC up into the anastomosis. This flow pattern is visible as the familiar swirling jet fluid flow structure of an axial flow pump that is visible as a set of streamlines that impacts onto the flared vessel wall of the SVC on the right

158

side. The pump is not strong enough to provide any type of rotational force to fluid flow in the PAs. The 2000 RPM case shown in **Figure 8.8 (C)** begins to show the impeller starting to affect the flows in the PAs. The pump primarily affects flow in the LPA, as is shown by the streamlines curving toward the right side.

Figures 8.8 (C) and **(D)** illustrate the pump interfering with the main recirculation region in the center of the anastomosis. **Figure 8.8 (D)** shows how the pump is able to begin to break up the recirculation region and drive the fluid toward the LPA. However, the recirculation region is not completely dissolved at the highest rotational speed for this case.
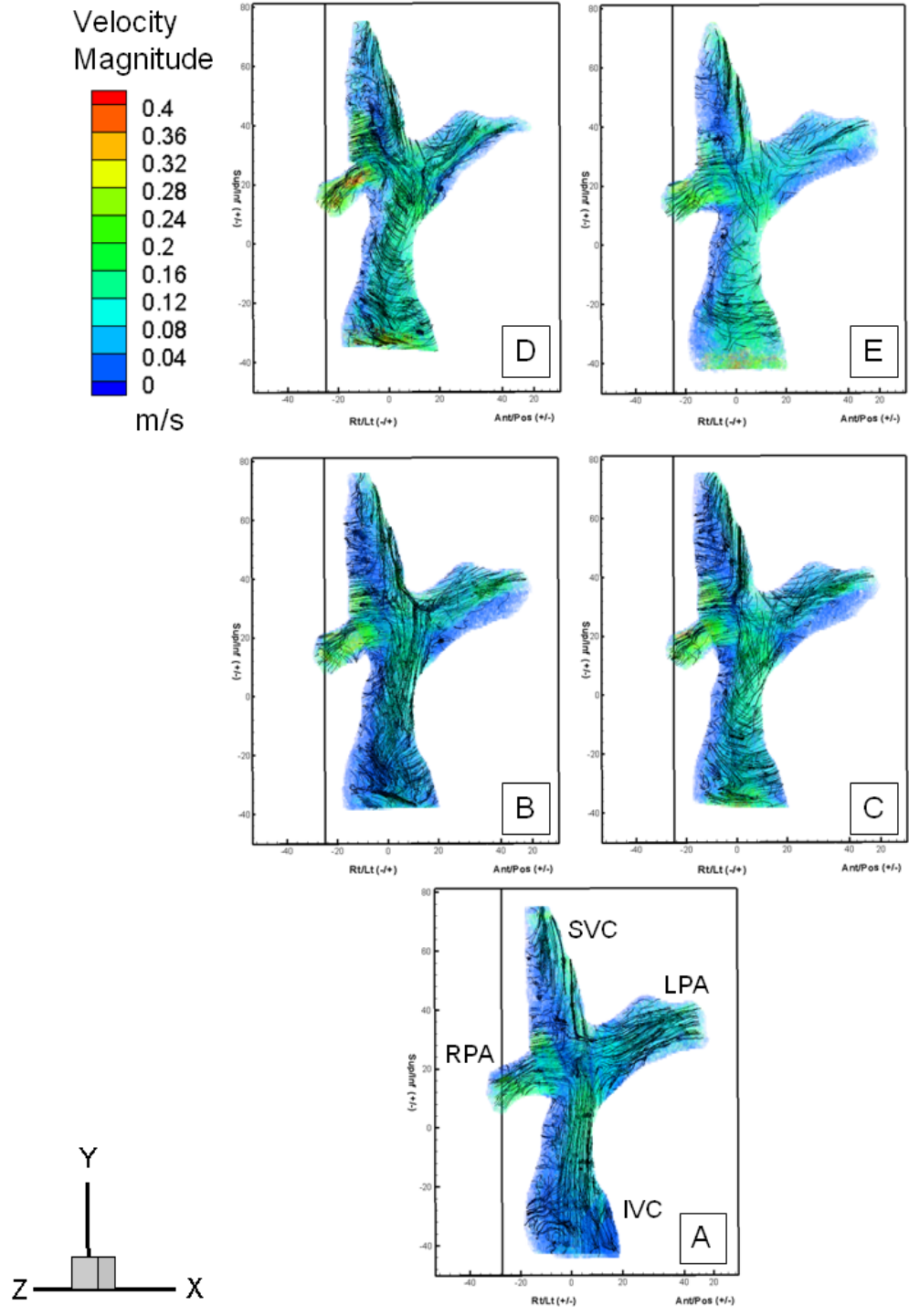
Figure 8.8: Velocity Magnitude Plots: Pump Test Case: Impeller Case Comparison: A) Control case; B) Pump operating at 1000 RPM; C) Pump operating at 2000 RPM; D) Pump operating at 3000 RPM; E) Pump operating at 4000 RPM. Scale: mm

8.3.4. Super-Diffuser case

The cage design with straight filaments the super-diffuser cage is added to the pump to function in conjunction with the impeller. This protective cage includes straight filaments with an attached set of diffuser blades. **Figure 8.9** provides the results for these PIV studies. **Figure 8.9 (A)** represents the control case and provides a comparison to the stall case in **Figure 8.9 (B)**. The effect of the diffuser with the impeller stopped is visible in the base of the IVC as a cluster of streamlines that rises gradually up the vessel. However, this effect dissipates before it reaches the mouth of the IVC. **Figure 8.9 (C)** illustrates the impeller rotating at 1000 RPM. The rotating streamlines coming off of the pump travel up the IVC and then shift toward the LPA. The recirculation region that is present in the bulge in the IVC is flushed out, while the recirculation region present in the anastomosis is only minimally affected. At 2000 RPM in **Figure 8.9 (D)**, the effects of the pump begin to dissolve the central recirculation region. We see the formation of the jet structure from the pump with a noticeable increase in velocity magnitude in the PAs. In the 3000 RPM and 4000 RPM cases shown in **Figure 8.9 (E)** and (**F**), the jet structure from the pump passes from the IVC through the anastomosis and impinges on the opposing vessel wall. This is made clear by the streamlines that all converge toward a common point in the LPA, indicating a stagnation point. It unclear, however, if this is the same stagnation point that is present in the control case from the IVC flow, which creates the helical flow patterns in the PAs. In **Figure 8.9 (F),** we begin to see the beginning of what could be retrograde flow into the SVC. This is visible as the cluster of streamlines located in the center of the velocity magnitude plot the moves from the impinging flow from the IVC and up and to the left into the mouth of the SVC. This is an important find since it validates the behavior the super-diffuser cage in hydraulic testing causing a small increase in SVC pressure and a small reduction in SVC flow rate.
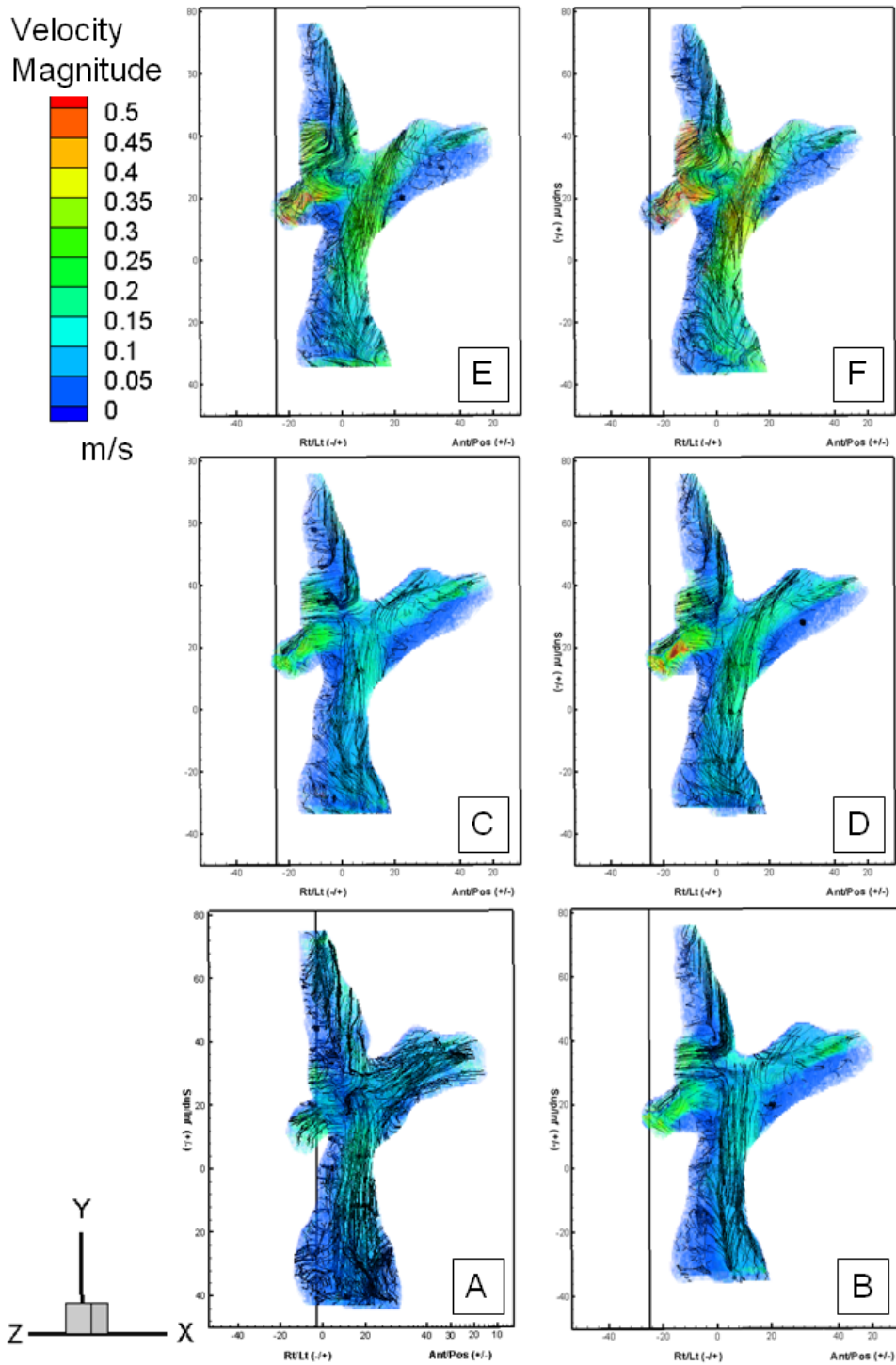
Figure 8.9: Velocity Magnitude Plots: Pump Test Case: Comparison of the Super-Diffuser Cage Cases: A) Control case without the pump present; B) Pump at stall; C) Pump operating at 1000 RPM; D) Pump operating at 2000 RPM; E) pump operating at 3000 RPM; F) pump operating at 4000 RPM. Scale: mm

8.3.5. Against-With Case

The cage design with twisted filaments the against-with cage is added to the pump to function in conjunction with the impeller. This protective cage has a set of hydrodynamically designed revolving filaments attached to a set of diffuser blades. The cage having straight filaments the super-diffuser cage was introduced to the pump and studied in the previous section. **Figure 8.10** illustrates the results for these PIV studies. **Figure 8.10 (A)** represents the control case and provides a comparison to the stall case in **Figure 8.10 (B)**. The presence of the diffuser with the impeller not rotating is visible as a cluster of streamlines in the base of the IVC that travel up the vessel toward the anastomosis. This effect appears to dissipate the further up the IVC it goes. It is able to reach the mouth IVC, but it does not have any effect on the flow patterns present in the anastomosis. A similar effect was present in the super-diffuser case, however the effect of the diffuser on the flow was less prominent with the visible flow pattern dissipating prior to reaching the mouth of the IVC. The added rotational effect can be partially attributed to the hydrodynamically designed filaments providing some rotational force to the flow in addition to the diffuser blades. **Figure 8.10 (C)** illustrates the impeller rotating at 1000 RPM with rotating streamlines coming off of the pump traveling toward the LPA. The recirculation region that is present in the bulge in the IVC is flushed out. The recirculation region in the anastomosis is perturbed by the flow coming from the pump in the IVC. Thick clusters of streamlines coming from the IVC prove that the wrapped filaments of the against-with cage are able to provide additional thrust. This is a dramatic improvement over the super-diffuser cage for the same rotational speed.

At 2000 RPM in **Figure 8.10 (D)**, the effects of the pump have begun to dissolve the recirculation region that is present in the TCPC junction. We see the formation of the jet

structure from the pump with a noticeable increase in velocity magnitude in the PAs, particularly in the RPA. In the 3000 RPM and 4000 RPM cases shown in **Figure 8.10 (E)** and **(F)**, the jet structure from the pump rise out of the IVC crosses the TCPC junction impinges on the opposing vessel wall. This is made clear by the cluster of streamlines that all collide toward a stagnation point in the LPA. As in the super-diffuser case, it is unclear if this is the same stagnation point that is present in the control case and provides the helical flow patterns in the PAs. In **Figure 8.10 (F)**, we begin to see the beginning of what could be retrograde flow into the SVC. This is visible as the thick cluster of streamlines that is visible in the center of the velocity magnitude plot the moves from the normal impinging flow from the IVC and which moves to the left into the mouth of the SVC and then moves across the open to merge with the exiting RPA flow. As in the super-diffuser case, this flow pattern represents an important find since it validates the behavior of the against-with cage that was observed in hydraulic testing. A small increase in SVC pressure and a small reduction in SVC flow rate were observed. The flow structure seen in **Figure 8.10 (F)** indicates the flow from the pump is not entering into the SVC but is rather moving across the mouth of the vessel and inhibiting the fluid flow. This is not likely an indication of retrograde flow into the SVC but an indication of an errant flow pattern arising from the IVC as a result of the against-with cage being used in conjunction with the pump. Although, a similar flow pattern was observed in the super-diffuser case, the finding was less definitive since it is not clear if the flow from the IVC completely crosses the mouth of the SVC or is simply impacted and diverted by it.

Figure 8.10: Velocity Magnitude Plots: Pump Test Case: Comparison of the Against-With Cage Cases: A) Control case without the pump present; B) Pump at stall, C) Pump operating at 1000 RPM; D) Pump operating at 2000 RPM; E) Pump operating at 3000 RPM; F) Pump operating at 4000 RPM. Scale: mm

165

8.3.6. Comparison of Test Cases

8.3.6.1.   Cage Configuration Comparison: Stall Condition

The comparison of the stall cases is shown in **Figure 8.11**. It is important to note that the stall case for the impeller will be identical to the control case. This is to be expected since the cavopulmonary assist device is designed to not be obstructive to the flow and to allow flow through it. The impeller will only provide a minimum amount of rotational force to the local fluid region when it is stopped. This flow disturbance is assumed to rapidly to dissipate in the 100 *mm* inlet tube which connects the pump testing apparatus to the IVC inlet of the anatomic TCPC model. Since this region is before the inlet to the IVC, it is outside of the available field of view for the high-speed camera, so it is unlikely that it would show up in the PIV data. The stall cases for the two cage prototypes exhibit some spiraling streamlines that are primarily localized in the bulge of the IVC. The streamlines from the against-with cage are able to make it past this region and up to the mouth of the IVC but do not impact the flow patterns in the TCPC junction.
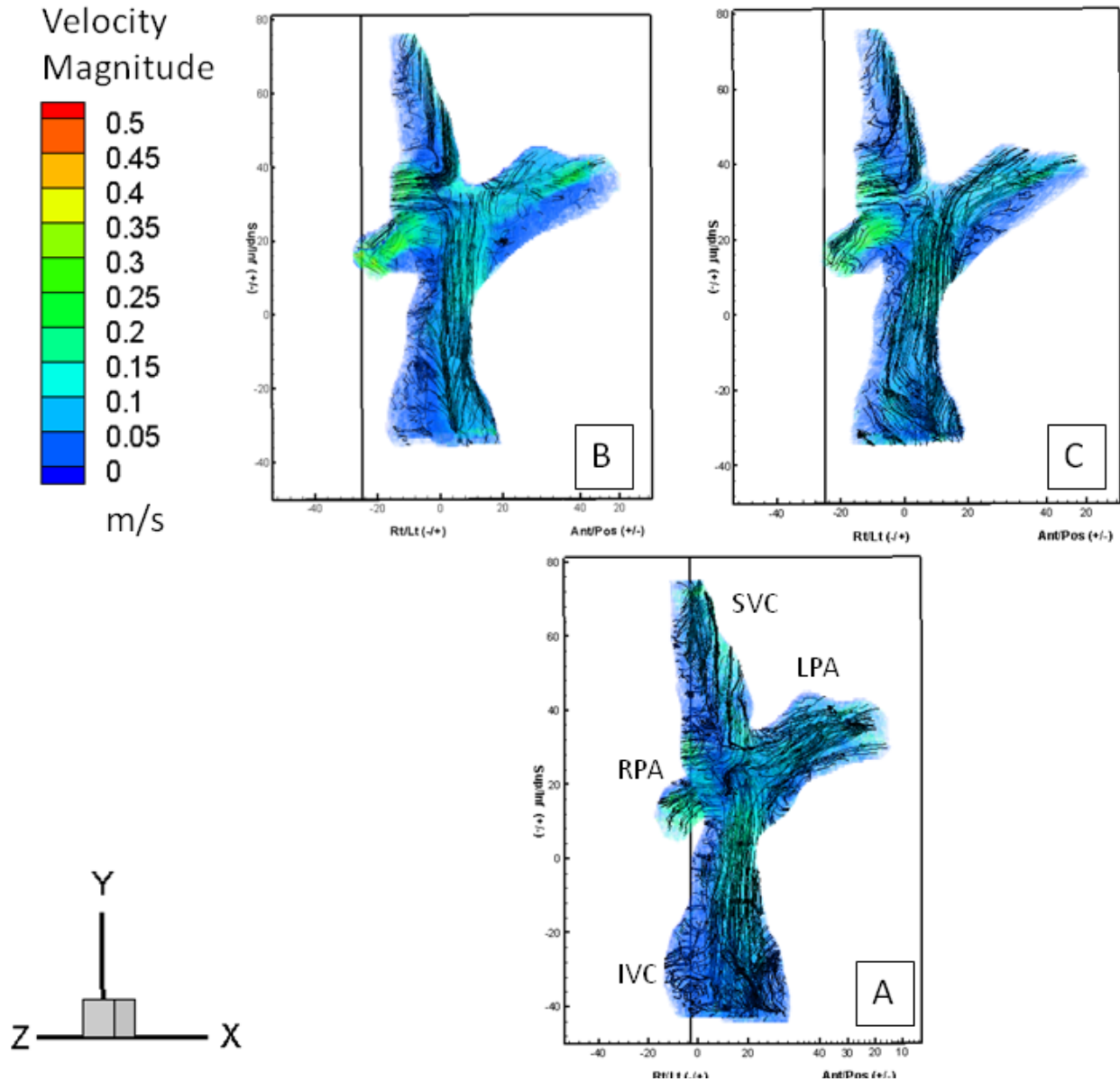
Figure 8.11: Velocity Magnitude Plots: Comparison of Test Cases: Comparison of the stall condition: A) Impeller with pump at stall; B) Super-diffuser cage with pump at stall; C) Against-with cage with pump at stall. Scale: mm

8.3.6.2. Cage Configuration Comparison: 1000 RPM

When the 1000 RPM cases are compared in **Figure 8.12**, the presence of pump is more clearly recognized. This can be observed in all cases as a set of streamlines that gradually spirals up out of the IVC. The against-with case in **Figure 8.12 (C)** shows the strongest presence of the pump with noticeable higher velocities and more streamlines being diverted toward the RPA and

LPA and then in the other two cases. The impeller case does not appear to have much effect on the flow patterns in the TCPC junction as 1000 RPM. This supports the claim that the pump is running outside of its design range and simple creating a swirling vortex but only moving a very small amount of fluid. The diffuser blades help to increase the pump output as is illustrated in the super-diffuser case and further complemented by the diffuser blades and twisted filaments in the against-with case.
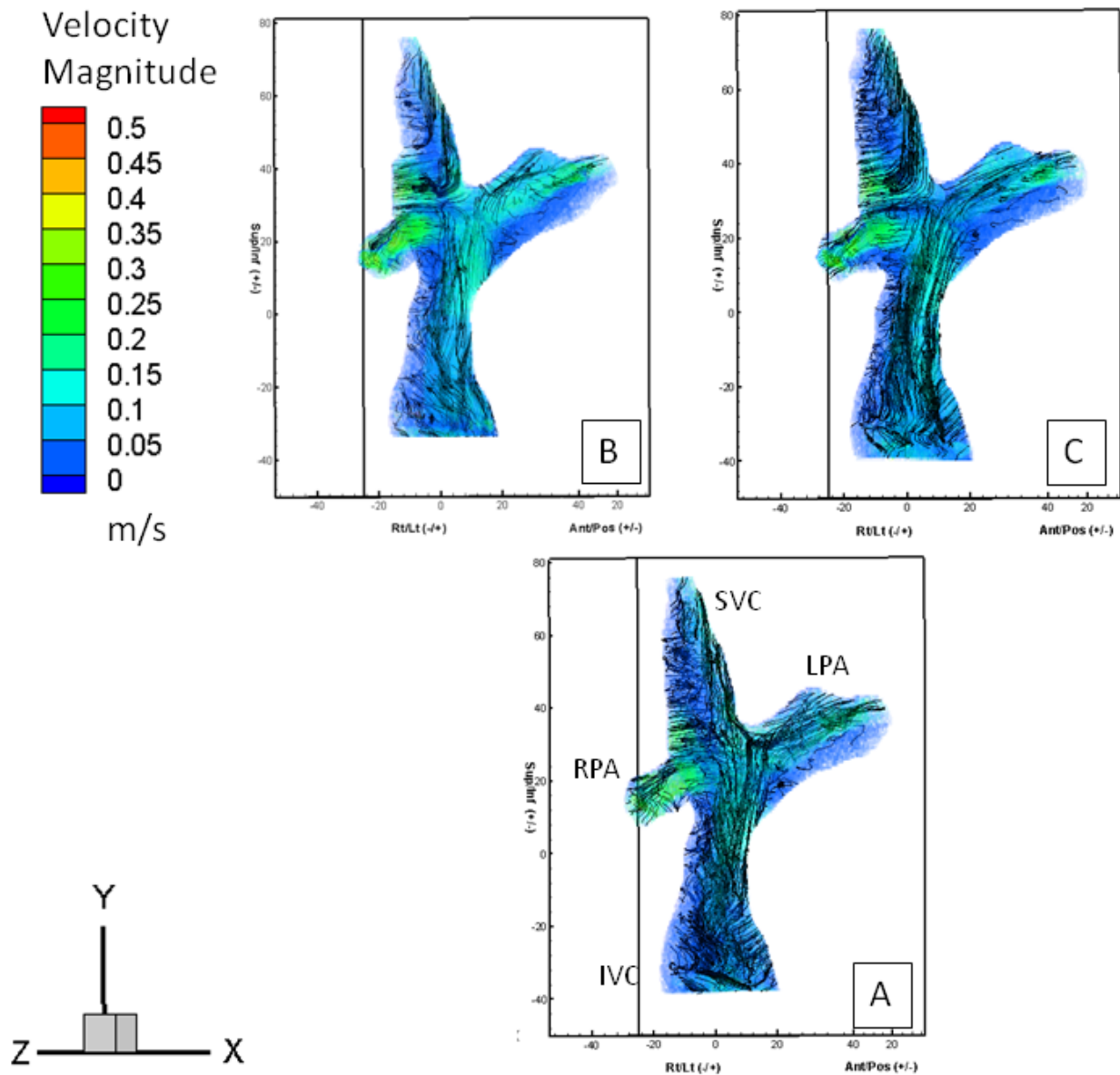
Figure 8.12: Velocity Magnitude Plots: Comparison of Test Cases: Comparison of the 1000 RPM condition: A) Impeller only, B) Super-diffuser cage, C) Against-with cage. Scale: mm.

8.3.6.3.   Cage Configuration Comparison: 2000 RPM

Figure 8.13 displays the comparison between the 2000 RPM test cases. The against-width case outperforms the other two cases by providing a clean set of streamlines and directs flow primarily toward the LPA. There is also an increase in flow toward the RPA as well. In the cases with the cages, it is noted that the flow appears to curve into the LPA likely following the flare of the IVC and the SVC.
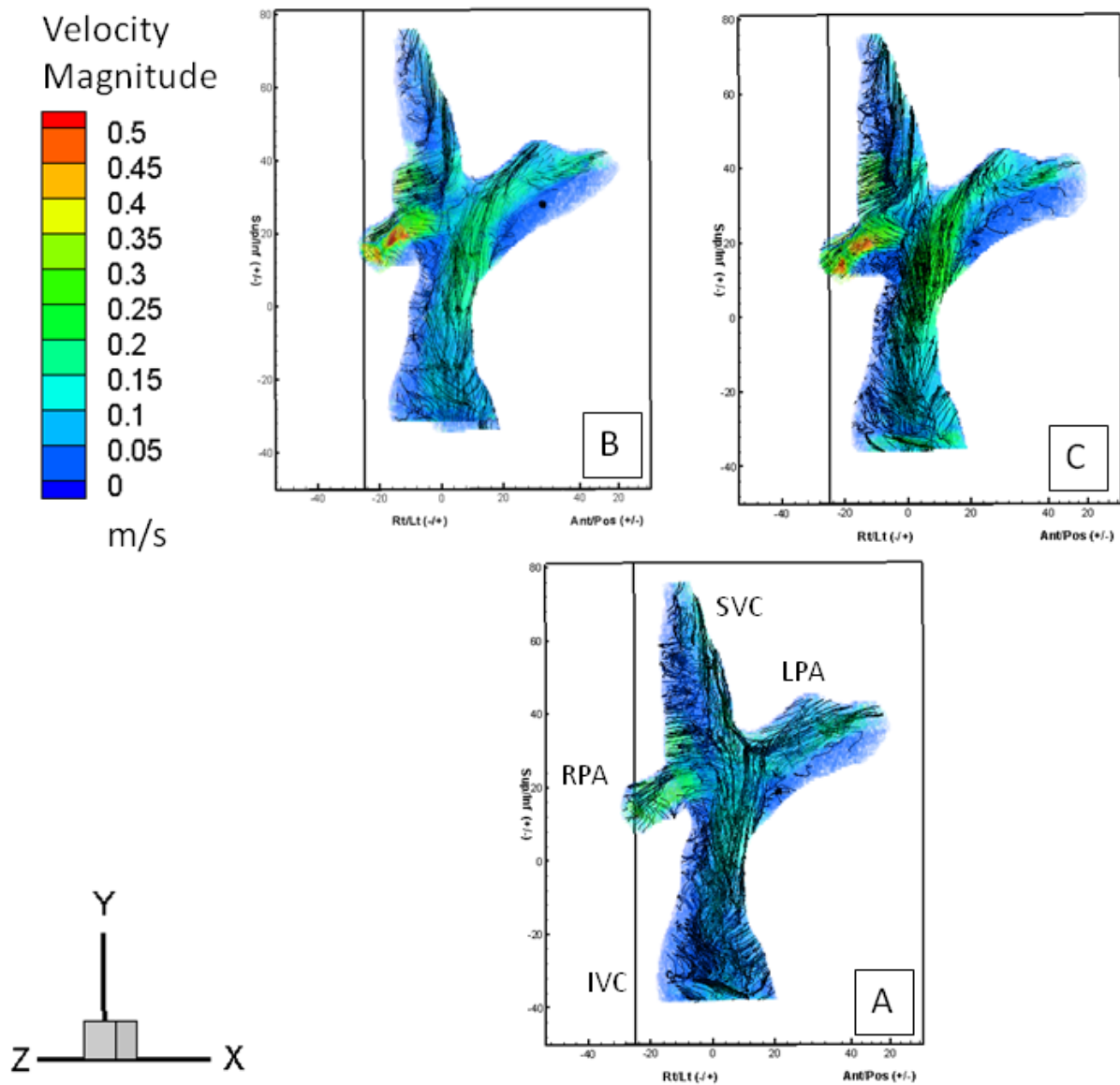
Figure 8.13: Velocity Magnitude Plots: Comparison of Test Cases: Comparison of the 2000 RPM condition: A) Impeller only, B) Super-diffuser cage, C) Against-with cage. Scale: mm.

8.3.6.4.   Cage Configuration Comparison: 3000 RPM

For the comparison of the 3000 RPM case shown in **Figure 8.14**, the against-with case displays a large amount of swirling and mixing of the fluid flow. The jet structure from the pump is less clearly defined than in the super-diffuser case. The impeller case has the lowest velocities of the three plots showing some improvement from the normal stagnation of the fluid flow seen in the control case.
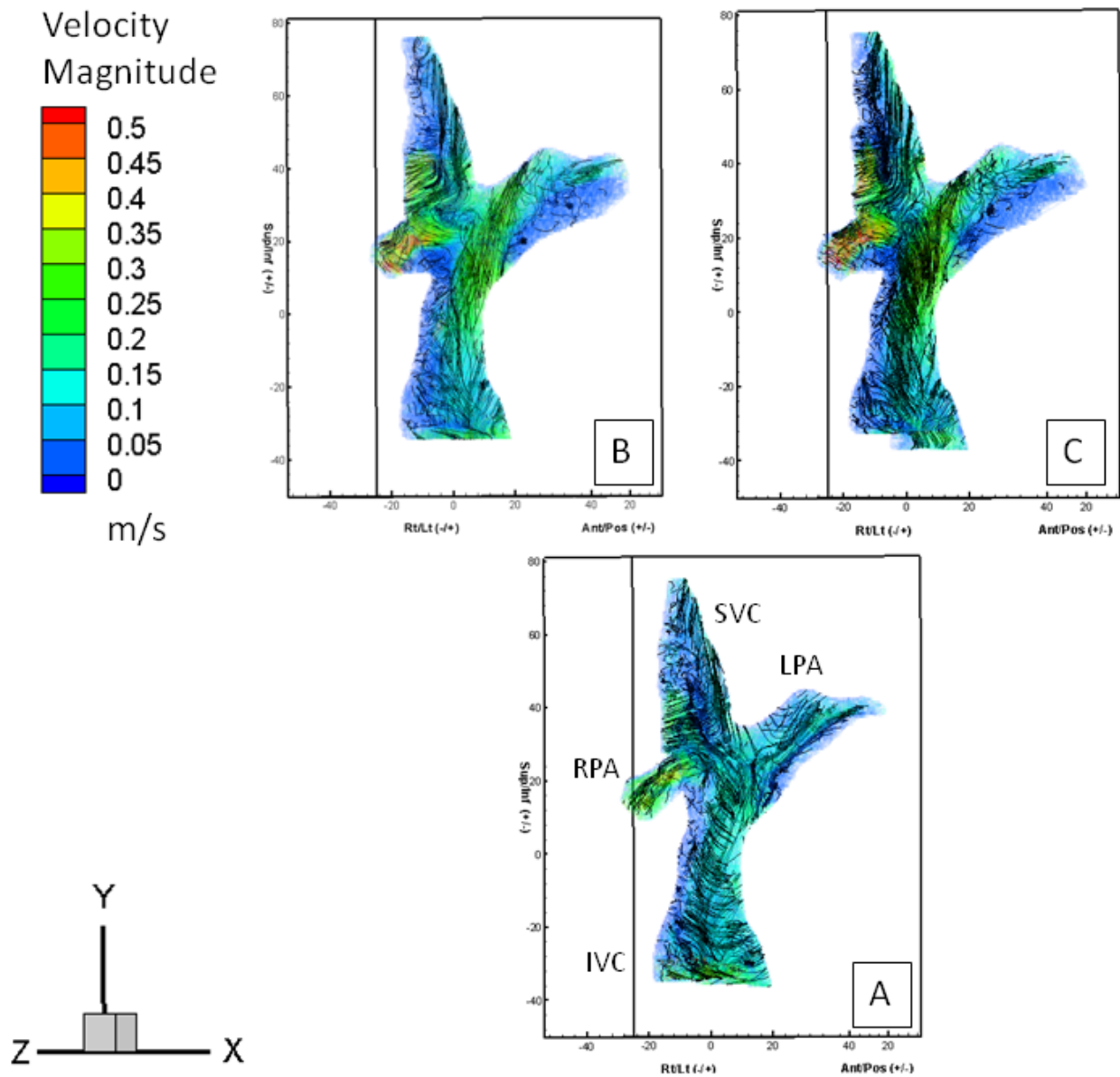
Figure 8.14: Velocity Magnitude Plots: Comparison of Test Cases: Comparison of the 3000 RPM condition: A) Impeller only, B) Super-diffuser cage, C) Against-with cage. Scale: mm.

8.3.6.5. Cage Configuration Comparison: 4000 RPM

For the comparison of the 4000 RPM case shown in **Figure 8.15**, the against-with case displays a very large amount of swirling and mixing of the fluid flow. A streak of high velocities are shown entering into the LPA, with some entering into the RPA as well. The flow in the base of the IVC becomes very chaotic, showing an increase in the unsteady flow patterns present in this model. The onset of retrograde flow into SVC is clearly visible in **Figure 8.15 (B)** and **(C)**. A cluster of streamlines that typically enters into the vortex in the center of the anastomosis is being pushed back toward the SVC by the IVC flow before in exits into the RPA.

As was previously observed in **Figure 8.10 (F)** and illustrated in this case comparison as **Figure 8.15 (C)** for the against-with cage, flow from the pump does not enter into the SVC but rather moves across the opening and inhibits the entering the fluid flow. This flow pattern in not an indication of retrograde flow into the SVC but an indication of an errant flow pattern arising from the IVC as a result of the against-with cage being used in conjunction with the pump. In **Figure 8.9 (F)** and illustrated in this case comparison in **Figure 8.15 (B)** showed that a similar flow pattern was observed in the super-diffuser cage, however the finding was less definitive since it is not clear if the flow from the IVC completely crosses the mouth of the SVC or is simply impacted and diverted by it.
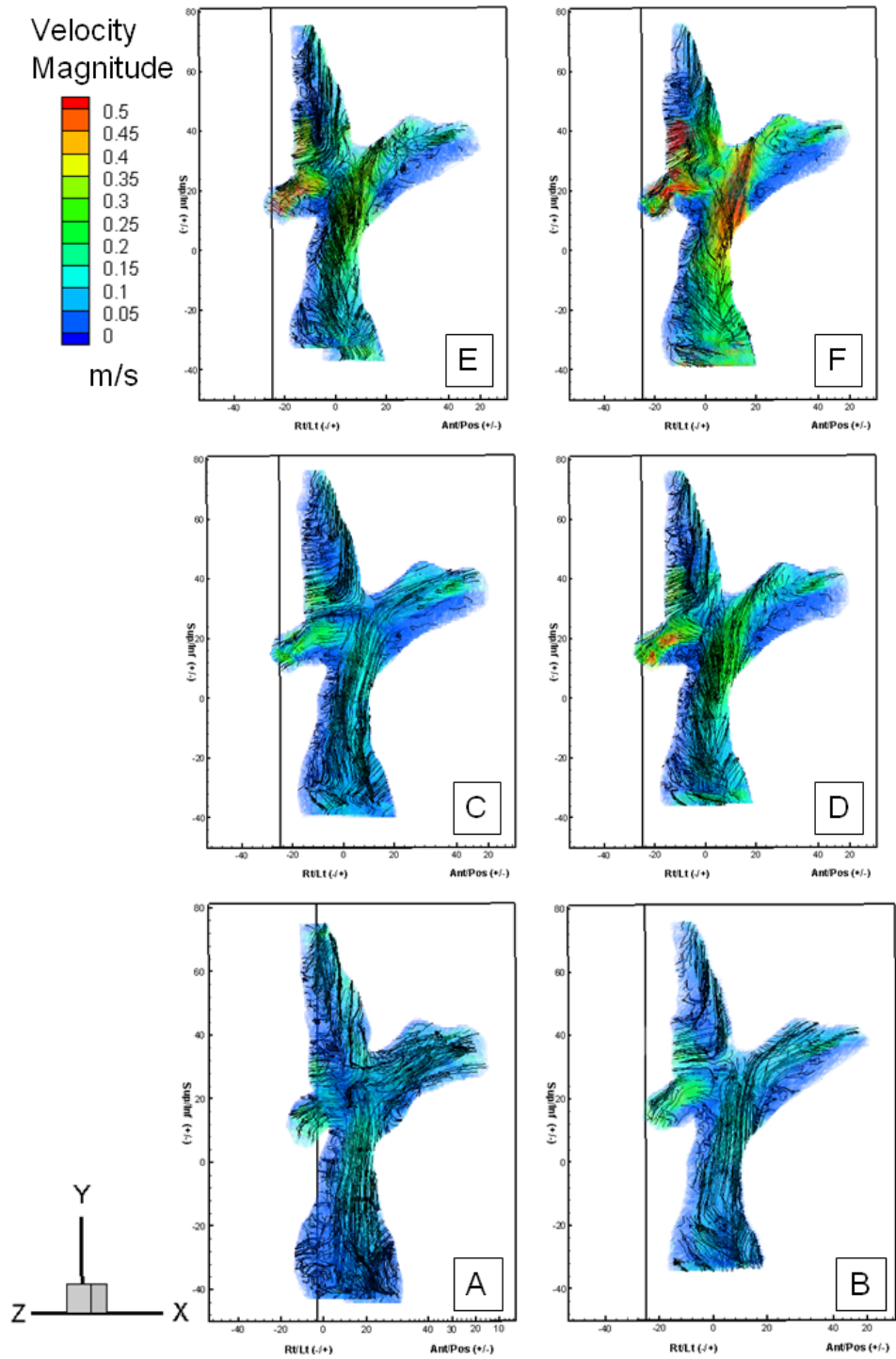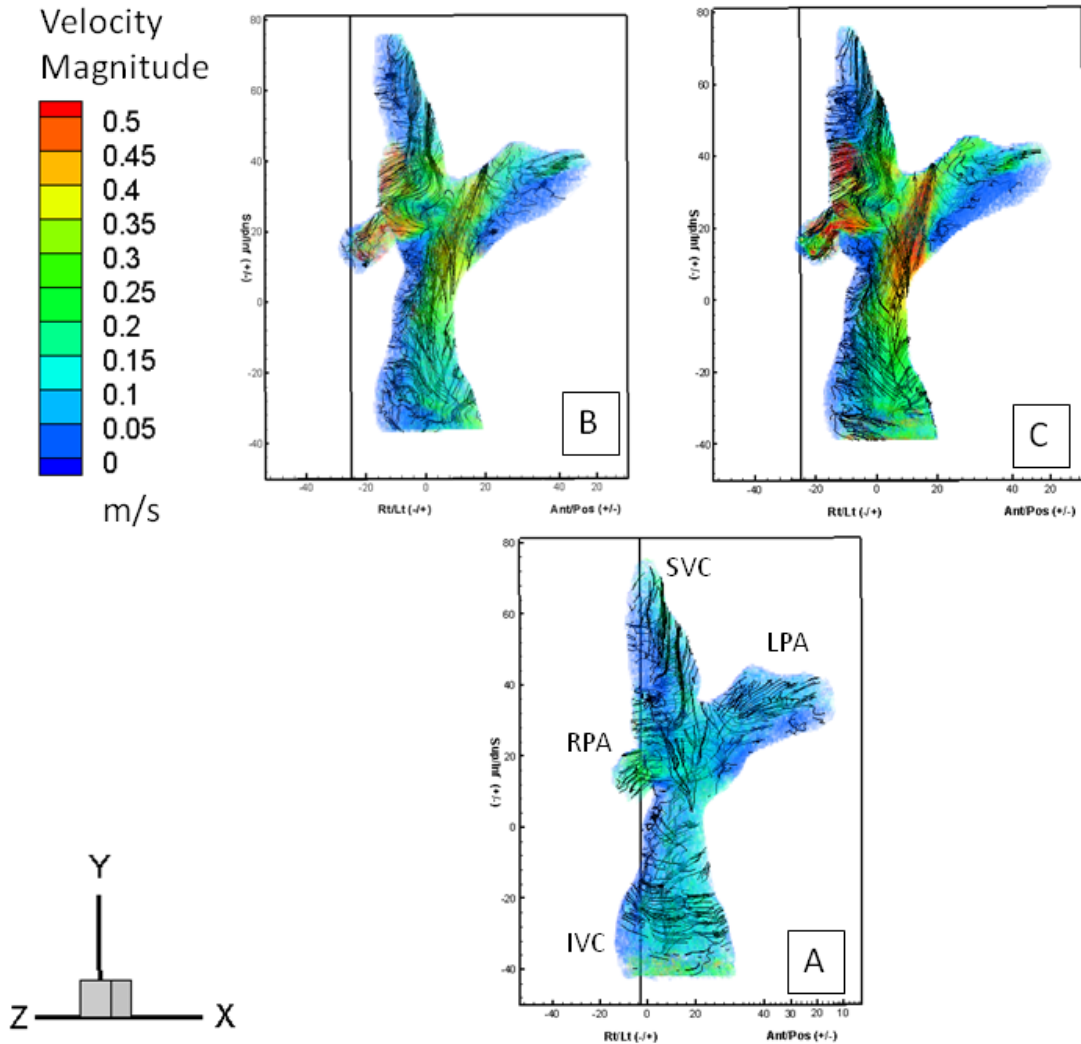
Figure 8.15: Velocity Magnitude Plots: Comparison of Test Cases: Comparison of the 4000 RPM condition: A) Impeller only, B) Super-diffuser cage, C) Against-with cage. Scale: mm.

The three pump configurations are shown in **Figure 8.16** for the operating conditions of 3 *L/min* with a 40%/60% flow split between the SVC and IVC with a pulmonary flow split of 50%/50% at a pump rotational speed of 3000 RPM. The data volume representing velocity magnitude is sliced to show the velocity distribution for a set of slices in the Y-direction. For clarity, every 5th slice is shown in order to effectively visualize the velocity plots. The slices reveal the changes in the velocity distribution inside of the data volume. The flow behavior present in IVC for all three cases indicates that the pump is driving flow up the IVC into the

TCPC junction. Flow in the anastomosis site is affected by the pump and we see the velocity

distribution that occurs in the anterior to posterior direction along the Z-axis. The flow behavior

present in the super-diffuser case and the against-with case is not present in the impeller only

case. The against-with case shown in **Figure 8.16 (C)** shows the highest velocities being present

in the RPA. A similar region is present in the super-diffuser case, the velocity magnitude is lower

and occurs in a much smaller region.
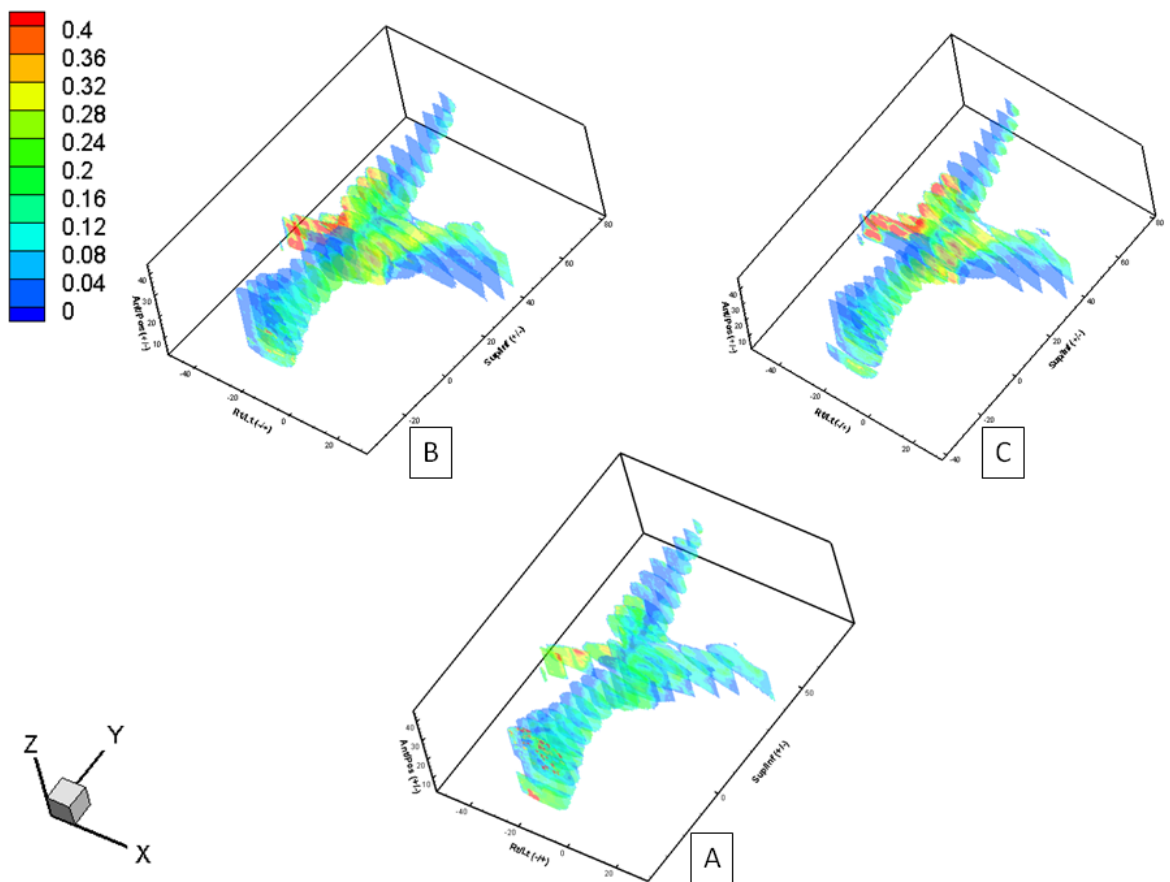
Figure 8.16: Slices in the Y-direction through the PIV data volume for the case of the impeller operating at 3000 RPM: A) Impeller only, B) Super-Diffuser Cage, C) Against-With Cage. Scale: mm.

8.3.7. Comparison of TCPC Models

8.3.7.1. Idealized TCPC Model verses Anatomic TCPC Model: Control Case Comparison

Recall from **Chapter 1** that the total cavopulmonary connection consists of two inlets with flows entering from the SVC and IVC and two outlets with flows exiting into the pulmonary arteries. The principal flow patterns in the idealized model used in this study have been previously identified by Ensley *et al.*[135]. Further research was performed by Sharma *et al.* [131] who realized the complex, rotational flow patterns and unsteadiness of the flow in the TCPC in a much larger study of glass idealized TCPC models. Similar flow instabilities have been observed in other simplified geometries [40]. The complexity of the flow has also been found to increase with increasing flow rate and Reynolds numbers [49].

The idealized TCPC requires a brief historical account. The idealized TCPC was studied extensively in the early 2000s with researchers using both numerical and experimental tools to assess the internal fluid dynamics. The ultimate goal of this prior research was to increase the hemodynamic efficiency of the TCPC by reducing the resistance through modifications in the geometry and morphology performed during the palliative surgical procedure. These improvements involve changes in geometry such as off-setting the vena cava (caval offset), curvature of the inlets, flaring of the vena cava anastomoses, and enlargement of the IVC inlet connection [16, 17]. These recommendations have the effect of increasing the power efficiency in the TCPC.

A vessel offset alters the flow patterns of the SVC and IVC to prevent direct collisions of the flows has the unintended effect of allowing the vena cavae flows to impinge onto the opposite walls upon entering. This forms a stagnation point that alters the flow structure and the flow direction. A vortex is formed between the two entering flows with a secondary helical flow

pattern existing between the two exiting flows. Flaring of the vessel walls attempts to minimize the flow separation from the walls and to turn the flow such that it would follow the curvature of the vessel walls into the pulmonary arteries [16].

Given the large recirculation region in the TCPC junction, the three-dimensional nature of the flow cannot be entirely neglected. Helical pulmonary flow as a result of the colliding caval flows has been observed in most TCPC models, both physical and numerical [16, 49, 136]. Ensley *et al.* [16] theorize that this flow pattern have a positive impact as it minimizes pulmonary flow separation and prevents the formation of stagnation regions. The effects of the recirculation region are still under investigation and its consequences, beneficial or adverse, are not well understood [16, 49, 50].

Chopski *et al.* [28] previously examined the interactive fluid dynamics of an idealized TCPC with an axial flow pump located in the inferior vena cava using PIV. The results of this study indicated that the blood pump was able to successfully augment pressure in the IVC and push flow into the pulmonary arteries. It was shown the pump was able to remove the large recirculation region is formed by the vena cavae flows. This study enabled the continued development of the cavopulmonary assist device.

The idealized TCPC model is designed after a similar model pioneered by Ensley, *et al.* [16] using MRI data from an 8-year-old child. The TCPC model includes uniform tube diameters of 13.4 *mm* with a one caval diameter offset between the vena cavae with flaring incorporated toward the pulmonary arteries [16, 17, 40].

A comparison of the velocity magnitude plots for the division of the cardiac output between the superior and inferior vena cavae with flow splits of 40%/60%, is shown in **Figure 8.17. Figure 8.17 (A)** displays the control case of the anatomic TCPC without the pump present

in the IVC. **Figure 8.17 (B)** displays the idealized TCPC. There are three main fluid flow structures that are present in the idealized TCPC which have been previously identified by Sharma *et al.* [131]. These structures arise as the result of the geometry of the TCPC model and are important because of a probable increase in the presence of unsteady flow which may occur from an interaction with the pump. The large concentration of streamlines which passes from the IVC through the center of the TCPC is due to the abrupt change in direction of the flow being forced to make a 90 degree bend. This fluid structure occurs in the SVC as well and is very prevalent in **Figure 8.17 (B)**. There is a large recirculation region in the center which rotates counterclockwise which is mainly propelled by the more powerful IVC flow. The third fluid flow structure is present as a result of the flaring of the vessels in the model, which aids in redirecting the flow into left or right pulmonary arteries. Boundary layer separation only occurs on the outside of the layer of the entering caval flows while the inside layer follows the flaring through the curvature into the PAs. The outside layer continues forward to collide with the opposing flow and form the recirculation region.

The anatomic model in **Figure 8.18 (A)** shows similar fluid flow structures to the idealized TCPC. It is important to note the loss of information for a 2-D slice as compared to the volumetric velocity magnitude plots shown in **Section 8.3.2**. It is important to note that for a 2-D slice through the centerline of both models, the fluid flow structures are similar. The flaring of the vessel walls is present which aids in the directing of flow into the PAs. A recirculation region is present between the vena cavae and the PAs in the center of the TCPC junction. Straight streamlines enter and exit through the models implying steady flow at the centerline slice, but negates mixing in 3-D flow fields above or below this region. The secondary helical flow

176

patterns are not visible in the planar slices since the rotation is perpendicular to the measurement plane.
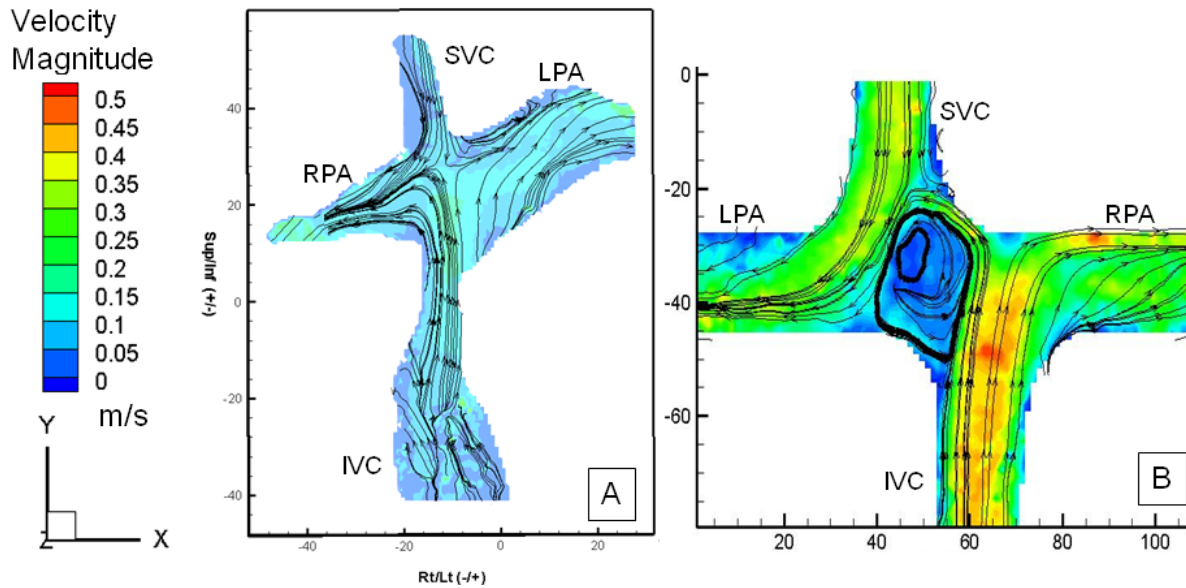
Figure 8.17: Velocity Magnitude Plots: Comparison of Anatomic TCPC verses Idealized TCPC: Control case: A) Anatomic TCPC, slice=20, B) Idealized TCPC, centerline, slice=6. Scale: mm

8.3.7.2. Idealized TCPC Model verses Anatomic TCPC Model: 4000 RPM Case Comparison

Figure 8.18 introduces the pump into the inferior vena cava of the TCPC with a rotational speed of 4000 RPM. **Figure 18 (A)** displays the anatomic TCPC with the pump present in the IVC and **Figure 18 (B)** displays the idealized TCPC. Similar flow structures are present between the two cases.

Figure 8.18 (A) displays the centerline slice of the anatomic model with the pump operating at 4000rpm and illustrates the flow from the inferior vena cava being directed toward the LPA. The flaring of the vessels between the vena cavae and the PAs is more uneven that in the control cases, but it effectively aids in redirecting the flow from the pump into left or right

177

pulmonary arteries. The recirculation region that is present within the control case has been dramatically reduced in size.

Figure 8.18 (B) displays the centerline slice of the idealized model with the pump operating at 4000rpm. The pump causes a notable shift in the recirculation region to the lower left side of the junction. The IVC flow is also more directed toward the RPA and more closely follows the flare into the RPA, and the pump helps to push flow to the RPA. The contribution from the pump is noted by the increase in the number of streamlines curving to the RPA.

The fluid structures in the SVC are very similar between **Figures 8.18 (A)** and **(B)**, such that straight streamlines enter the TCPC junction. The curved fluid streamlines coming from the IVC are a result of the rotating impeller. It is important to note that the streamlines in the idealized case direct IVC flow toward the RPA, with the remaining flow entering into the LPA. The anatomic model shows that flow from the pump will predominate toward the LPA but that there is mixing that occurs and flow also is directed toward the RPA. The concentrated streamlines which occur on the left side of the IVC for both cases are the result of the swirling jet structure that is created by the impeller of an axial flow pump.
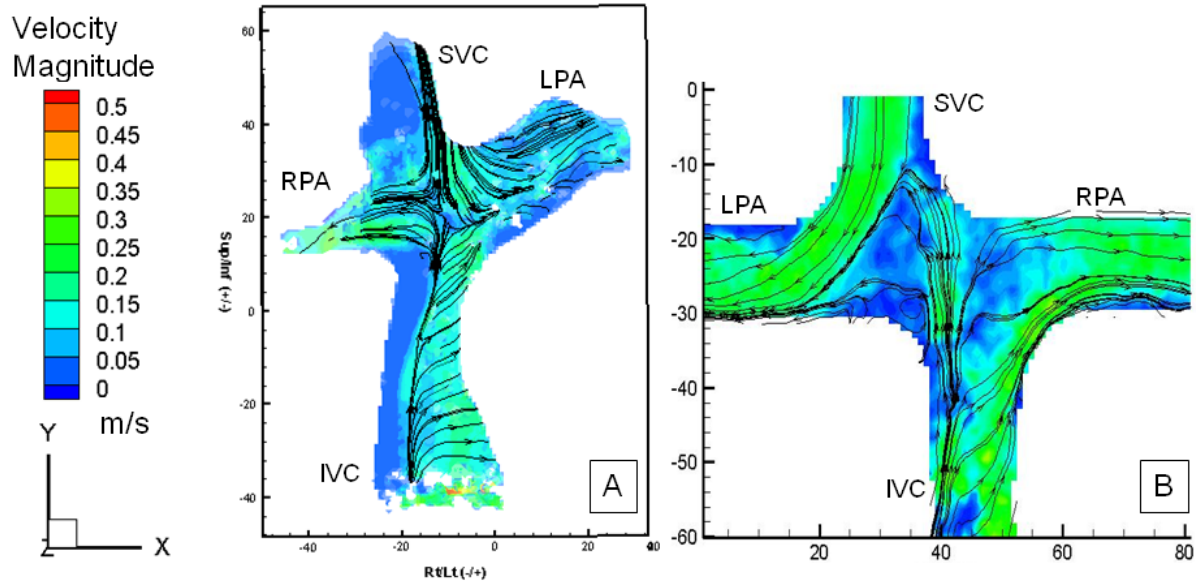
Figure 8.18: Velocity Magnitude Plots: Comparison of Anatomic TCPC verses Idealized TCPC: 4000 RPM case: A) Anatomic TCPC, slice=20, B) Idealized TCPC, centerline, slice=6. Scale: mm

8.4. Comparison Between Computational and Experimental Results

8.4.1. Hydraulic Power Calculations for the TCPC

The numerically estimated pump pressure performance curves from **Chapter 7** are compared against the performance curves acquired on the physical TCPC model in **Section 8.1** in **Figure 8.19**. The flow conditions of a total cardiac output of 3 *L/min* with an equal mean pulmonary arterial pressure of 16mmHg are chosen for comparison. It is noted that in comparing the numerical estimates, the k-ε model predicted a higher pressure rise than the SST model. In contrast, the data collected from the physical pump experiments show that the physical pump was able to generate a higher pressure at 4000 RPM than the k-ε estimate. The physical pump was also able to generate a much lower pressure rise in the lower RPM range below 2500 RPM. This reduction in pressure generation is expected based off of pressure-flow curves that were generated for the pump design specifications [53]. The physical impeller was able to generate pressures of 0 to 2.75 *mmHg* for rotational speeds of 0 to 4000 RPM, while the k-ε model was

179

able to generate pressures of 0 to 2.2 *mmHg* for rotational speeds of 0 to 4000 RPM, and the SST model was able to generate pressure of 0 to 1.15 *mmHg* for rotational speeds of 0 to 4000 RPM.

The rate of power gain or the improvement in energy efficiency was numerically estimated for the flow conditions of a total cardiac output of 3*L/min* with an equal mean pulmonary arterial pressure of 16*mmHg* and was chosen for comparison to the experimental results in **Figure 8.20.** Both the numerical and experimental results show a positive impact on the energetic of the TCPC. Higher rotational speed of the impeller in the physical model increased the power efficiency beyond the estimates of the k-ε and SST models to 14 *mW*.
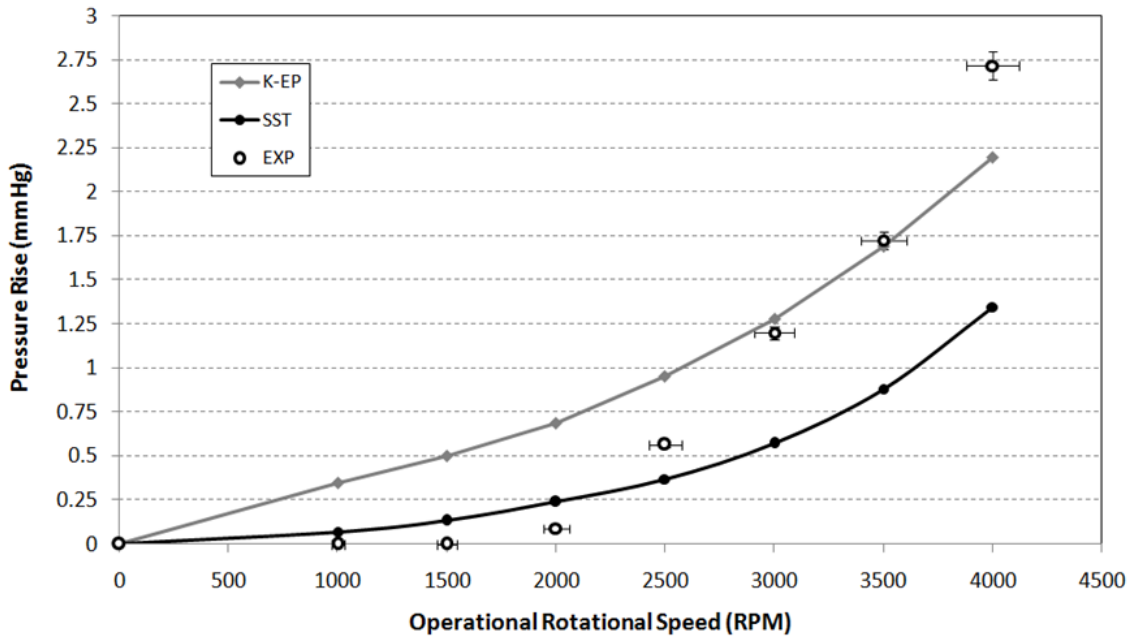
Figure 8.19: Pressure Rise Across the Pump at Equal Pulmonary Arterial Pressures of 16 *mmHg* and at a Cardiac Output of 3 *L/min.*
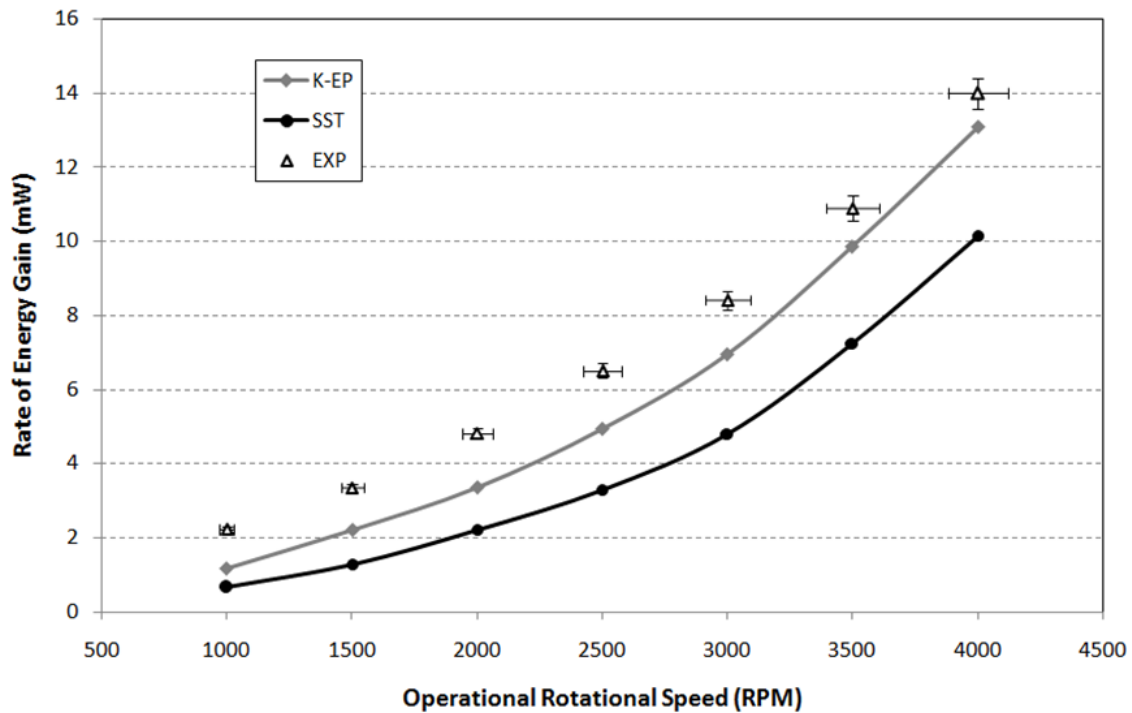
Figure 8.20: Rate of Power Gain for the Impeller Pump Configuration Using the k-ε and SST Turbulence Model.

8.4.2. Flow Streamlines

A comparison of the CFD streamline predictions to the PIV measurements for the 3 *L/min* cardiac output with a 40% / 60% flow split for the SVC / IVC and with 16*mmHg* equal mean pulmonary pressures was performed. The importance of such a comparison cannot be over-emphasized. The agreement between the CFD simulation and the PIV results will provide guidance for future pump design iterations and allow us to draw solid conclusions about the fluid dynamics within the TCPC due to the blood pump located in the IVC.

Figure 8.21 illustrates the comparison between the k-ε model, the SST model and the PIV results for the previously described operating conditions over rotational speeds of 2000 to 4000 RPM. For the numerical models, streamlines that have a deep red color represent flow coming from the SVC and streamlines having a deep blue color represent flow coming from the

IVC. It is important to remember that the PIV data that is presented here is truncated compared to the numerical data. This is due to the limited field of view that can be obtained by the PIV camera. The impeller and the inflow tube are connected to the physical model but there is no data available for these locations.

Figures 8.21 (A), (D), and (E) compares the k-ε and the SST models to the PIV data for the 2000 RPM case. At a low rotational speed, SVC flow will move toward the RPA. The PIV data clearly shows a vortex in the upper right corner. As the rotational speed is increased, the vortex shifts. Figures 8.21 (B), (F), and (G) compares the k-ε and the SST models to the PIV data for the 3000 RPM case. The vortex begins to shift toward the SVC in the PIV data. Figures 8.21 (C), (H), and (I) compare the k-ε and the SST models to the PIV data for the 4000 RPM case. At the higher rotational speed, blood in the SVC is shunted toward the LPA in the k-ε case. The vortex is dissolved with increased mixing caused by the pump.
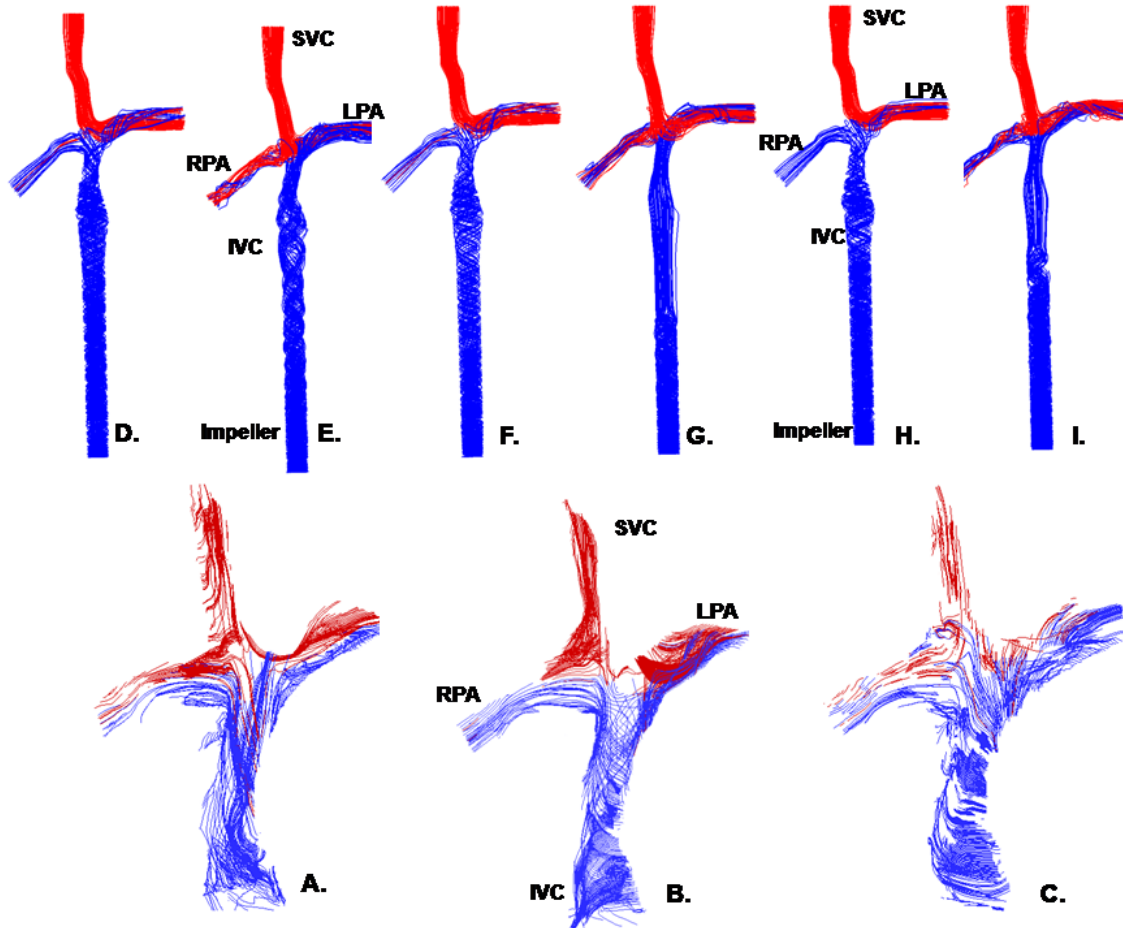
Figure 8.21: Steady Flow Streamlines Through the Cavopulmonary Circulation During Mechanical Cavopulmonary Assistance for a Cardiac Output of 3 *L/min* and Equal Pulmonary Arterial Pressures of 16 *mmHg*. Comparison of numerical and experimental streamlines. A) 2000 RPM PIV result; B) 3000 RPM PIV result; C) 4000 RPM PIV result; D) 2000 RPM k-ε model; E) 2000 RPM SST model; F) 3000 RPM k-ε model; G) 3000 RPM SST model; H) 4000 RPM k-ε model; and I) 4000 RPM SST model. Red streamlines reference flow entering from the SVC, whereas dark blue streamlines reference flow entering at the pump inlet and IVC.

8.4.3. Slice Comparison

The following figures illustrate comparisons between the numerical results and the PIV results for five planar slices through the TCPC. These planes occur at key areas of interest, specifically at the four sides of the anastomosis, so that the connections of the SVC and IVC represent the incoming flow patterns and the connections to the RPA and LPA represent the outgoing flow patterns. Additionally, a slide is made diagonally through the anastomosis in order

183

to visualize the vortices that are present. The numerical data is displayed for the pump

configuration of the impeller only without a protective cage present. **Figures 23-27** show the

slices for the 2000 *RPM* case and **Figures 28-32** show the 3000 *RPM* case.
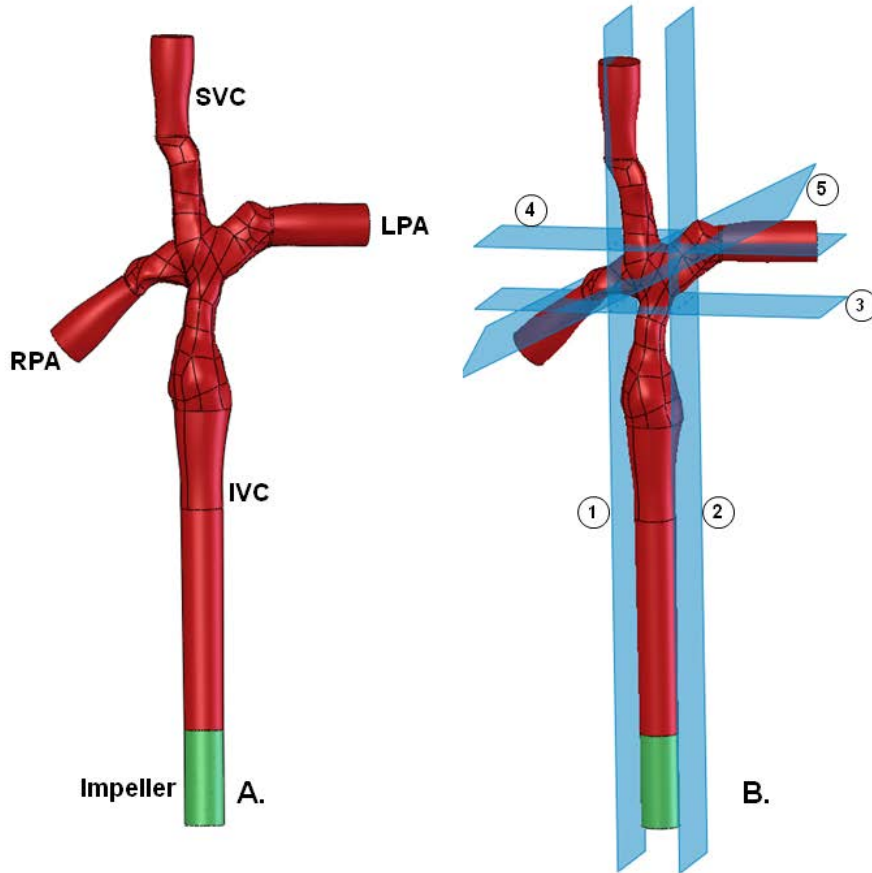
Figure 8.22: A) Numerical Model Solid Body; B) Slice locations inside of the TCPC Model: 1) RPA, 2) LPA, 3) IVC, 4) SVC, 5) Anastomosis Site.

8.4.3.1.   CFD-PIV Case Comparison for 2000 RPM Case

The planar slice through the SVC for the 2000 RPM case is shown in **Figure 23**. A

comparison shown between the PIV data in **Figure 23 (A)** with the two numerical estimates

using the k-ε and the SST turbulence models is present in **Figure 23 (B)** and **Figure 23 (C)**. The

PIV data is in good agreement with both models. The velocity magnitudes have similar

distributions with the SST model predicting a higher velocity in the center of the vessel. The k-ε

model provides a closer match to the velocity distribution of the PIV data, than the SST model.

The PIV data shows a vortex present in the right side of the slice with streamlines flowing from

it. The k-ε model is unable to detect the vortex but shows some vorticity. The SST model is able

to detect the vortex and some additional vorticity in the fluid flow.

Figure 8.23: Planar slice through the SVC for the 2000 RPM rotational speed with cardiac output of 3 *L/min* and mean pulmonary arterial pressures of 16 *mmHg*. A) PIV data, B) k-ε model and C) SSTmodel.

Figure 8.24 shows the IVC slice for the experimental and numerical data. The numerical

models predict higher velocities in the IVC than the PIV data reports. The k-ε model shows a

vortex rotating in the center of the image. The vortex is present in the SST model and in the PIV

data, but in a different location. It is observed in the lower right corner of the vessel in **Figure 8.24 (A)** and in **Figure 8.24 (C)**. The SST model closely matches the representative streamlines in the PIV data such there is vorticity present in the fluid flow. The k-ε more closely resolves the jet flow structure which produced by the rotating impeller in the lower portion of the IVC.

Figure 8.24: Planar slice through the IVC for the 2000 RPM rotational speed with cardiac output of 3 *L/min* and mean pulmonary arterial pressures of 16 *mmHg*. A) PIV data, B) k-ε model and C) SSTmodel.

Figure 8.25 shows the planar slice for the LPA. There is good agreement between the numerical models and the PIV data. The PIV data shows a vortex occurring in the center-left of the image. The k-ε model shows a vortex in the bottom-right with the SST model having a vortex in the upper left corner. The velocity magnitudes that are present are similar between the PIV

data and the k-ε model. Higher velocities were predicted in the SST model showing flow past the

vortex in the lower left portion of the image in **Figure 8.25 (C)**.

Figure 8.25: Planar slice through the LPA for the 2000 RPM rotational speed with cardiac output of 3 *L/min* and mean pulmonary arterial pressures of 16 *mmHg*. A) PIV data, B) k-ε model and C) SSTmodel.

Figure 8.26 displays the planar slices for the RPA. The velocity distributions in the PIV

data and the SST model are very similar with the k-ε model predicting lower velocities than

either the SST or the PIV data. The PIV data shows a more uniform velocity distribution in

Figure 8.26 (A). All three images display a vortex in the RPA. This vortex is present either from

the pump driving flow into the RPA or from the native helical flow structure that is present in the

control case. The location of the vortex varies, however, with the vortex being present in the

upper left corner of the image for the PIV data, but in the lower right corner for the k-ε model

and in the upper right corner for the SST model. A second vortex is present in the SST model in

187

Figure 8.26 (C) which is shown by the low velocity distribution on the right side of the image. This flow structure is only present in the SST model. Two possibilities exist for the vortex not being present in the PIV data. Either the vortex is not well resolved by the PIV data or the vortex in the RPA is distorted due to the uneven walls vessel walls.
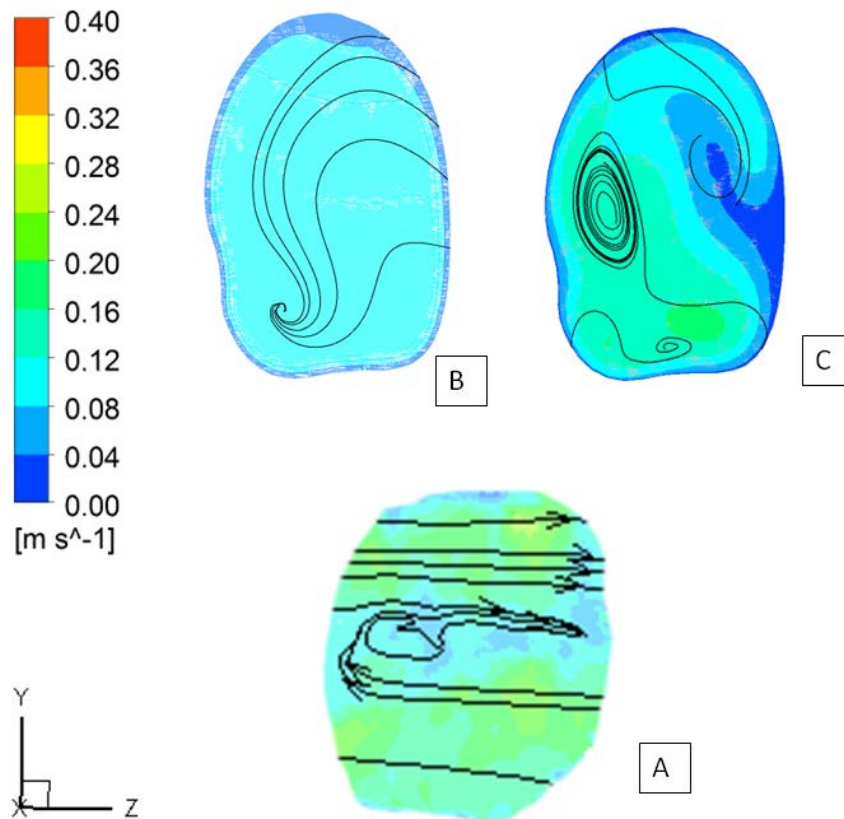
Figure 8.26: Planar slice through the RPA for the 2000 RPM rotational speed with cardiac output of 3 *L/min* and mean pulmonary arterial pressures of 16 *mmHg*. A) PIV data, B) k-ε model and C) SSTmodel.

Figure 8.27 shows the slice through the anastomosis. The numerical models are in good agreement with the PIV data having similar velocity magnitude distributions. The PIV data shows a distinctly unsteady fluid flow pattern. A vortex is present in the center with helical flow patterns present in the RPA. A helical pattern is present in the LPA but the streamlines show that the flow patterns become steadier and more stable as flow exits the TCPC as can be seen by the

188

straight streamlines on the far right of the LPA. The vortex in the center of the anastomosis is well resolved by the k-ε model but is not resolved by the SST model. Neither numerical model is able to resolve the helical flow patterns of the PAs but show straight streamlines exiting the TCPC.
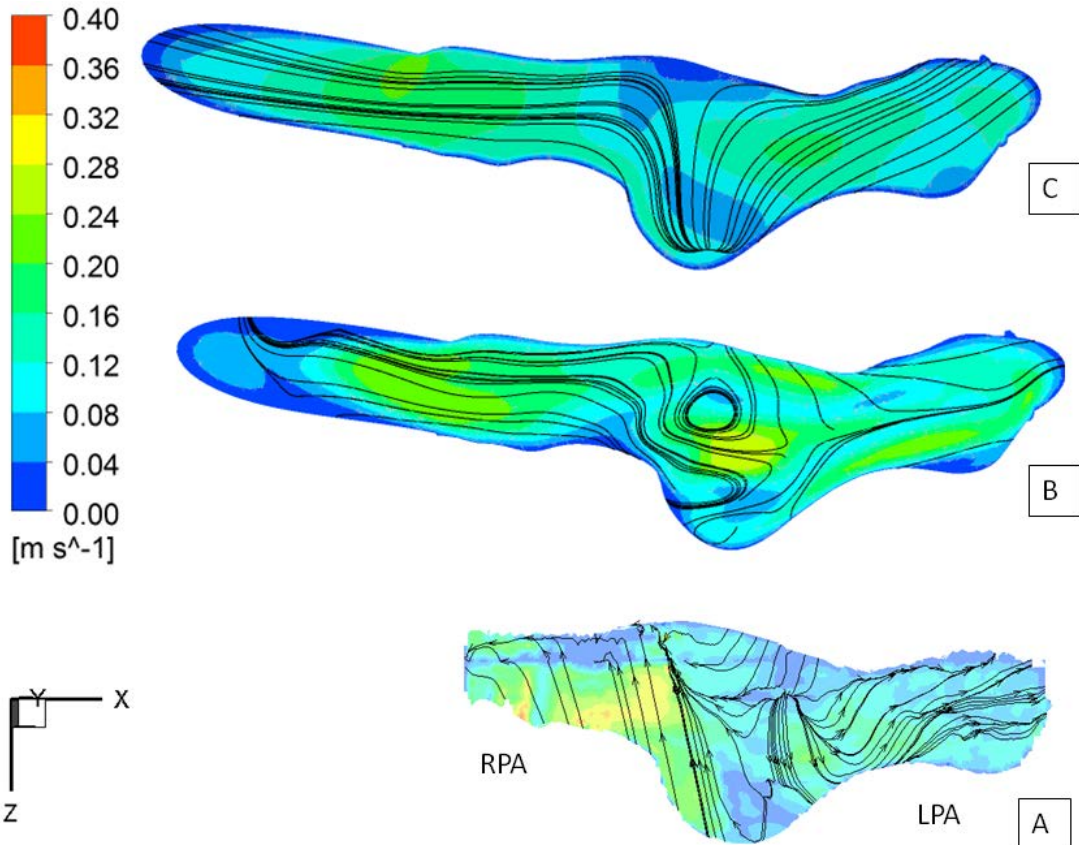
Figure 8.27: Planar slice through the anastomosis for the 2000 RPM rotational speed with cardiac output of 3 *L/min* and mean pulmonary arterial pressures of 16 *mmHg*. A) PIV data, B) k-ε model and C) SSTmodel.

8.4.3.2. CFD-PIV Case Comparison for 3000 RPM Case

Figure 8.28 illustrates the fluid flow patterns in the SVC for the pump rotational speed of 3000 RPM. The flow in the PIV data in **Figure 8.28 (A)** shows a complex flow pattern with a vortex being present in the upper center portion of the vessel. A vortex is present in the SST

model in **Figure 8.28 (C)**, however the vortex is shifted toward the upper left. The PIV data

shows a high velocity magnitude distribution than either the k-ε model or the SST models. A

vortex is not resolved by the k-ε model as is evident by the straight streamlines.
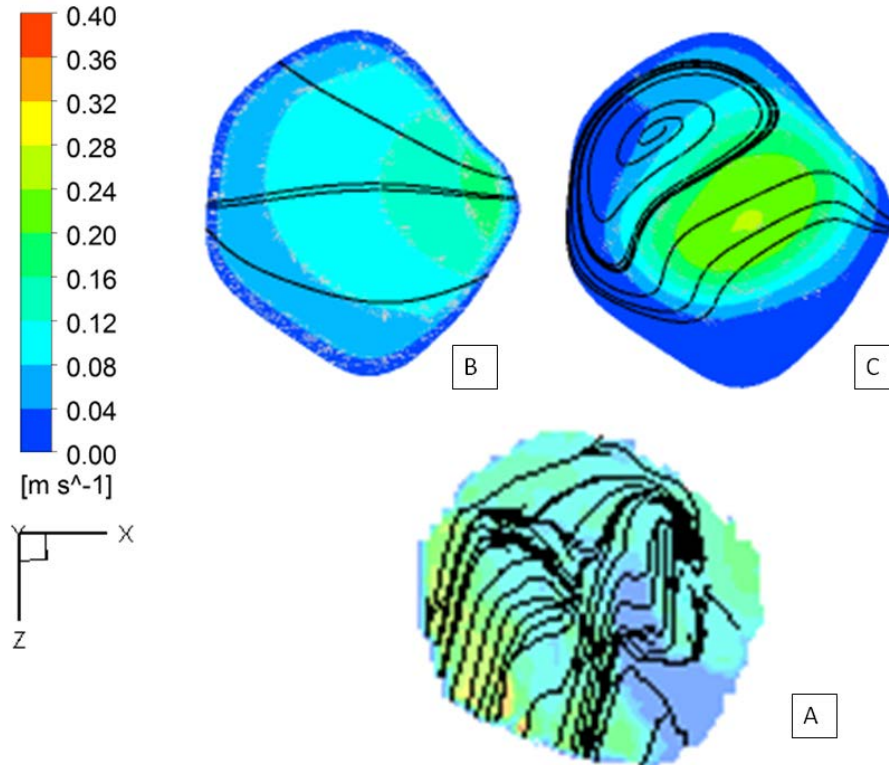
Figure 8.28: Planar slice through the SVC for the 3000 RPM rotational speed with cardiac output of 3 *L/min* and mean pulmonary arterial pressures of 16 *mmHg*. A) PIV data, B) k-ε model and C) SSTmodel.

Figure 8.29 (A) shows the PIV data for the IVC planar slice. The vortex from the pump

is well resolved by the PIV data in the bottom of the vessel. A similar vortex is shown in **Figure**

8.29 (B) by the k-ε model near the center of the vessel. The velocity distributions are different

with lower velocities being shown in the PIV data and higher velocities being predicted by the

effect of the pump in the k-ε model. The SST model does not predict a vortex being present in

the IVC. It also predicts a higher velocity magnitude in the vessel than the PIV data reveals.
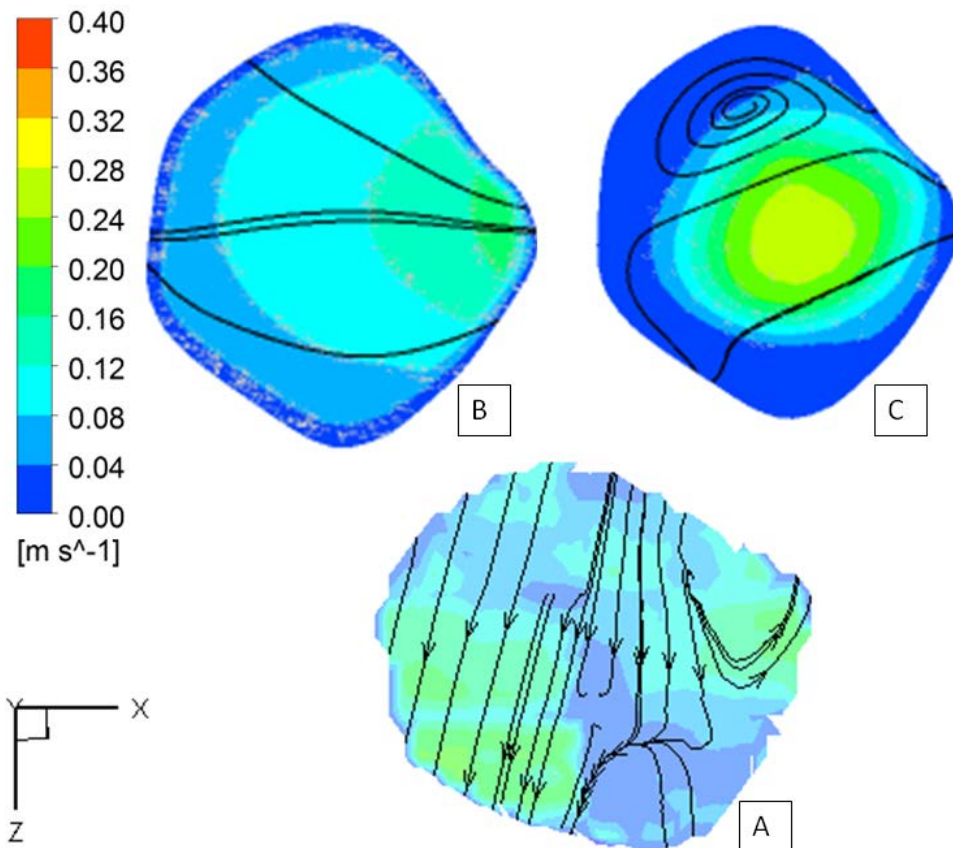
190
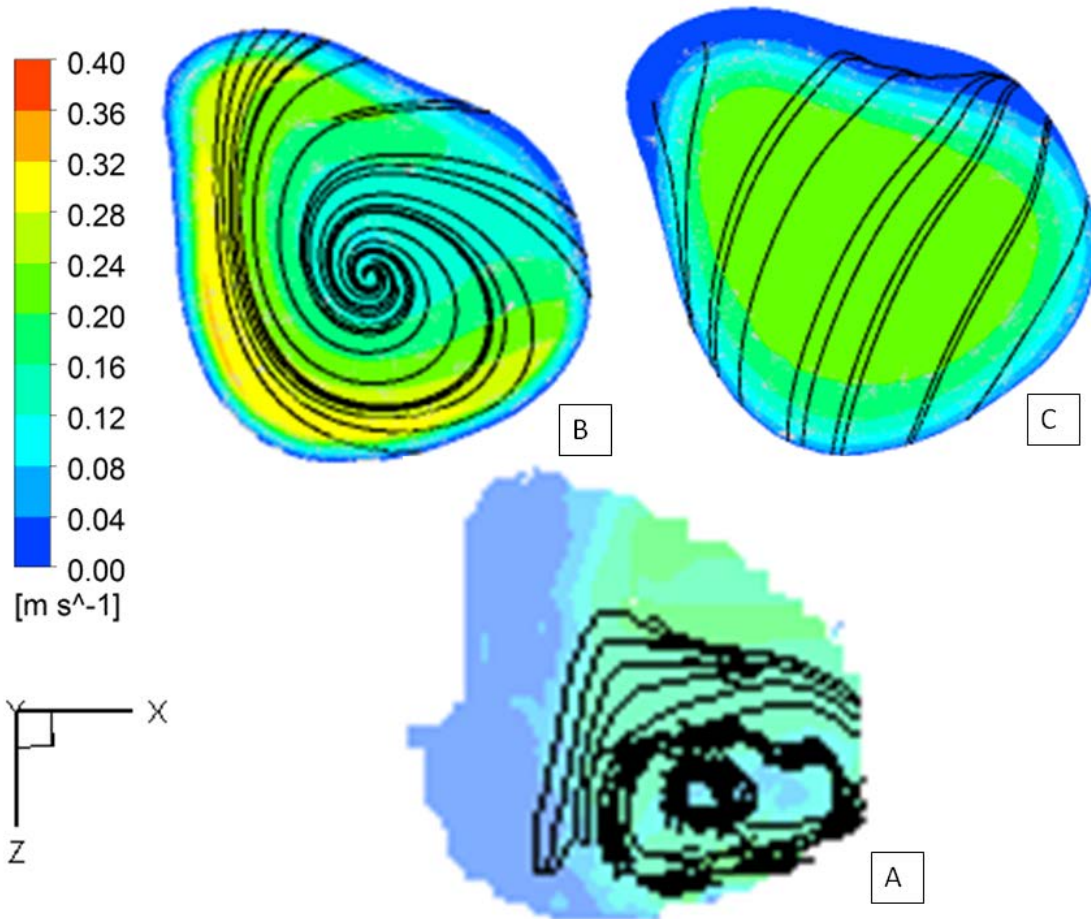
Figure 8.29: Planar slice through the IVC for the 3000 RPM rotational speed with cardiac output of 3 *L/min* and mean pulmonary arterial pressures of 16 *mmHg*. A) PIV data, B) k-ε model and C) SSTmodel.

Figure 8.30 illustrates the planar slice for the LPA. The numerical and PIV data are in good agreement with similar velocity magnitude distributions. The PIV data shows a complex fluid flow profile with mixing of the fluid. Vortices are present in all three images. The k-ε model shown in **Figure 8.30 (B)** predicts a single vortex to occur in the lower right corner of the model. This is in contrast to the PIV data in **Figure 8.30 (A)** which shows two separate vortices present in the upper left and lower right portions of the vessels. These flow patterns are similarly predicted by the SST model with a vortex occurring in the lower left and lower right of the

vessel. The vortex in the lower right is not well resolved except for the presents of lower
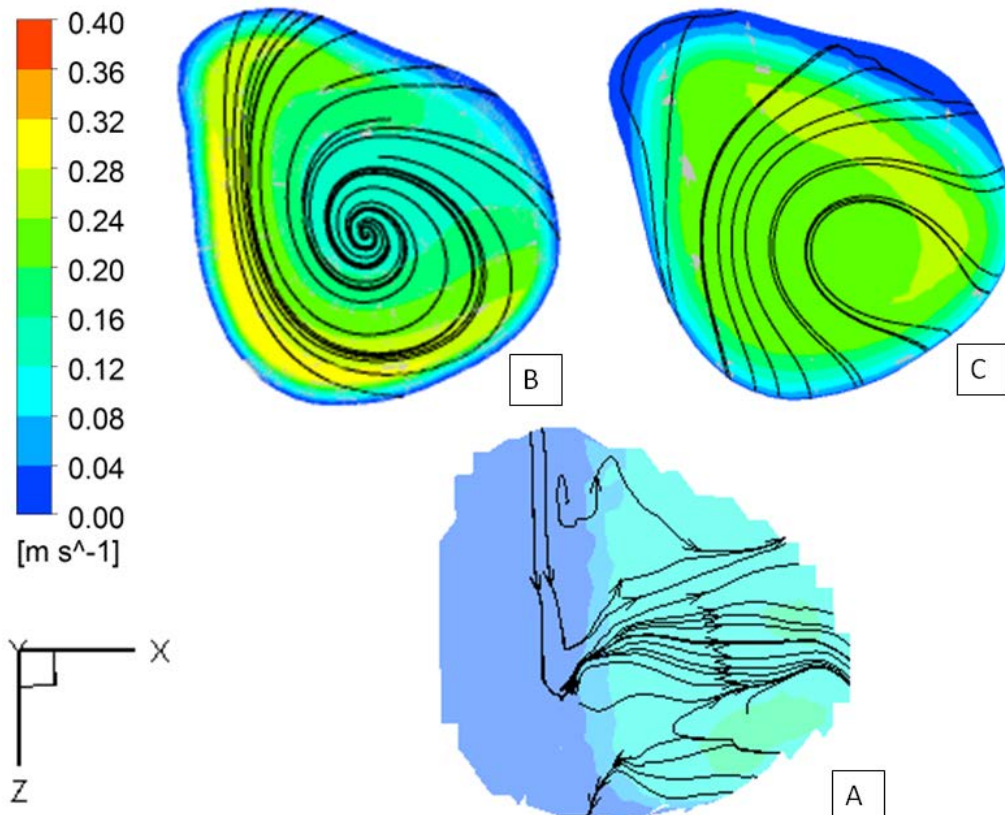
velocities.
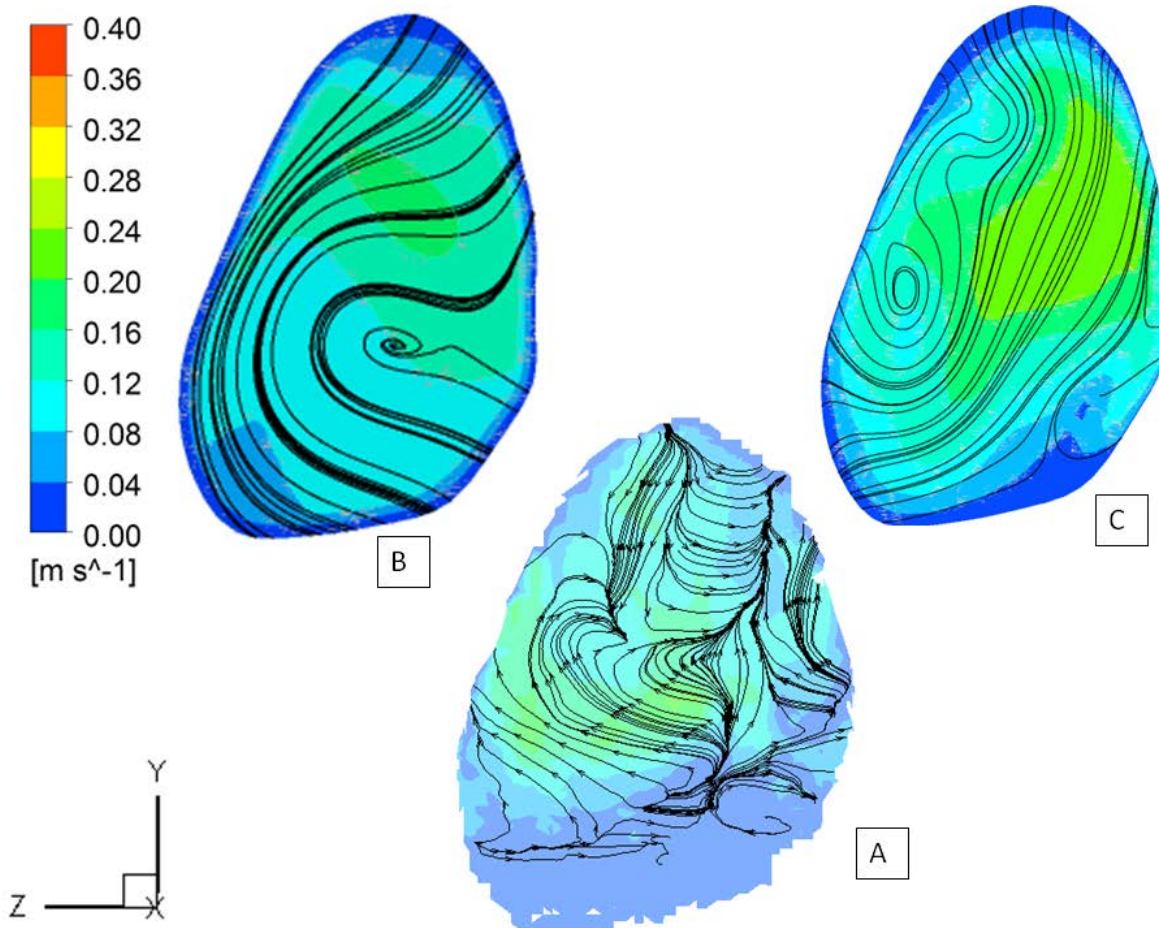
Figure 8.30: Planar slice through the LPA for the 3000 RPM rotational speed with cardiac output of 3 *L/min* and mean pulmonary arterial pressures of 16 *mmHg*. A) PIV data, B) k-ε model and C) SSTmodel.

The planar slice for the RPA is displayed in **Figure 8.31**. The RPA shows a complex

fluid flow profile like the LPA. The velocity magnitude distribution for the PIV data is similar to

the numerical data. The k-ε model predicts a vortex to occur in the bottom left corner of the

vessel. A vortex is shown in the SST model in a similar location but is not as well resolved. The

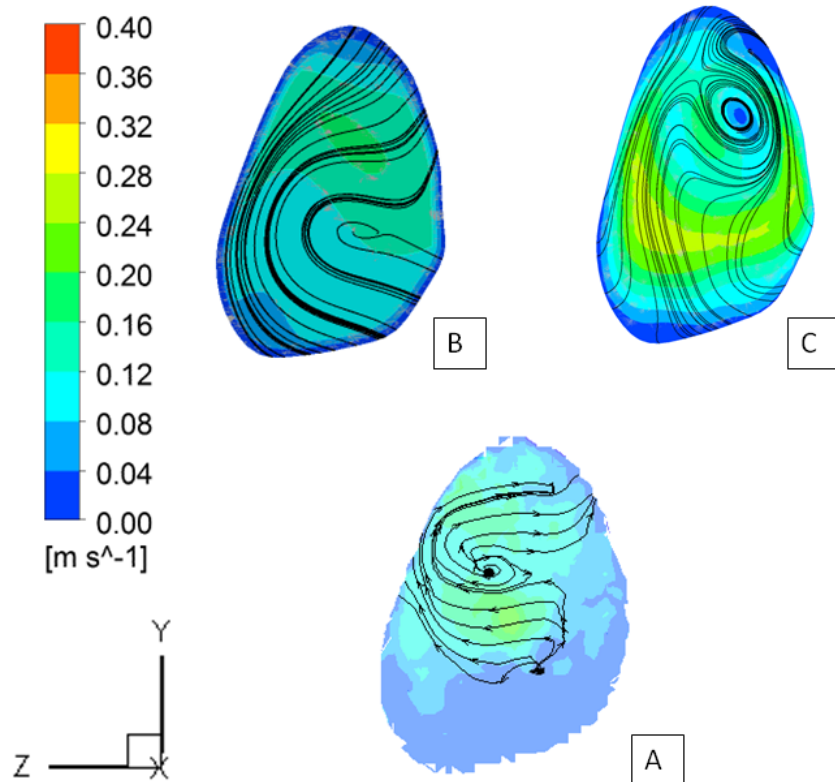PIV data shows the vortex being present in the dead center of the model.
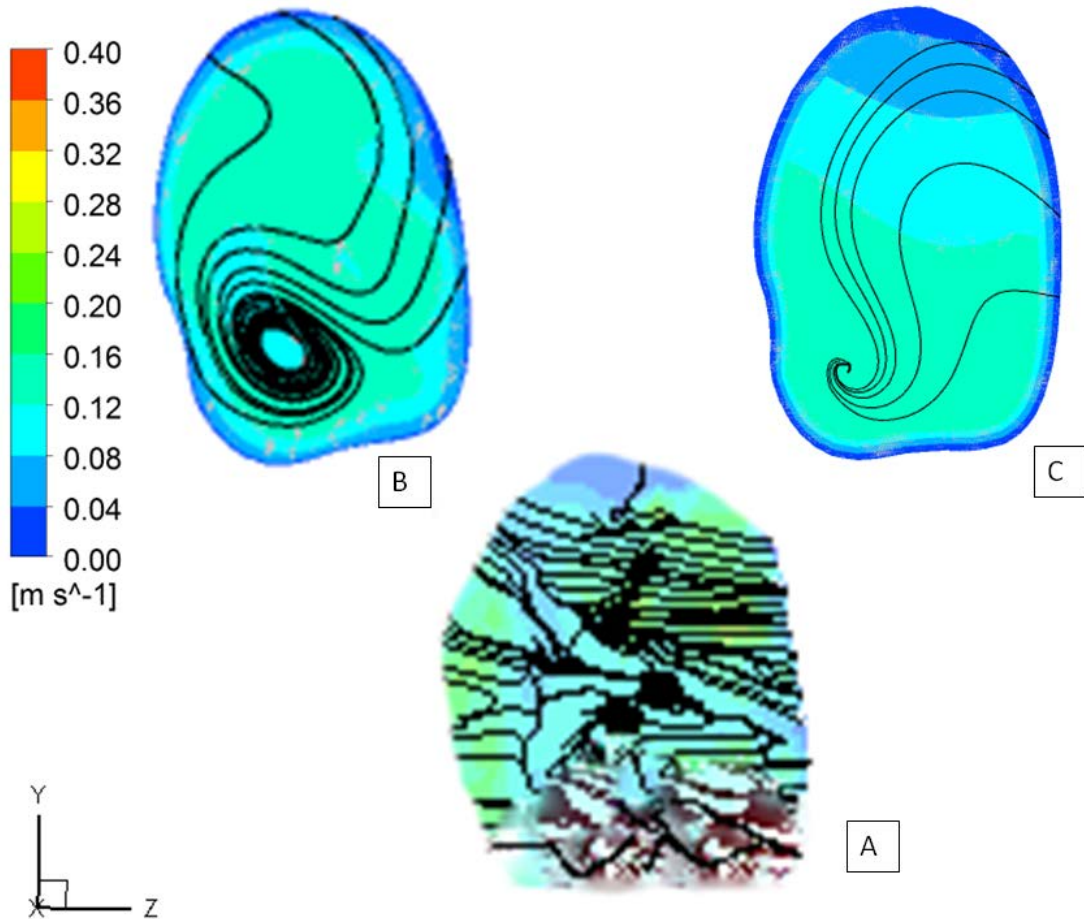
Figure 8.31: Planar slice through the RPA for the 3000 RPM rotational speed with cardiac output of 3 *L/min* and mean pulmonary arterial pressures of 16 *mmHg*. A) PIV data, B) k-ε model and C) SSTmodel.

The slice through the anastomosis of the TCPC is shown in **Figure 8.32**. Helical flow patterns are present in the PAs in the PIV data, but are not resolved in the numerical models. The SST model is able to resolve the vortex in the center of the anastomosis. A similar vortex is present in a similar location in the PIV data. The same vortex is not resulted by the k-ε model in **Figure 8.32 (B)**. As was observed in the anastomsis slice in the PIV data in the 2000 *RPM* case in **Figure 8.27 (A)**, the swirling flow in the LPA in **Figure 8.32 (A)** is able to stabilize as it exits the vessel. The velocity magnitude plots have similar distributions between the PIV and numerical models.
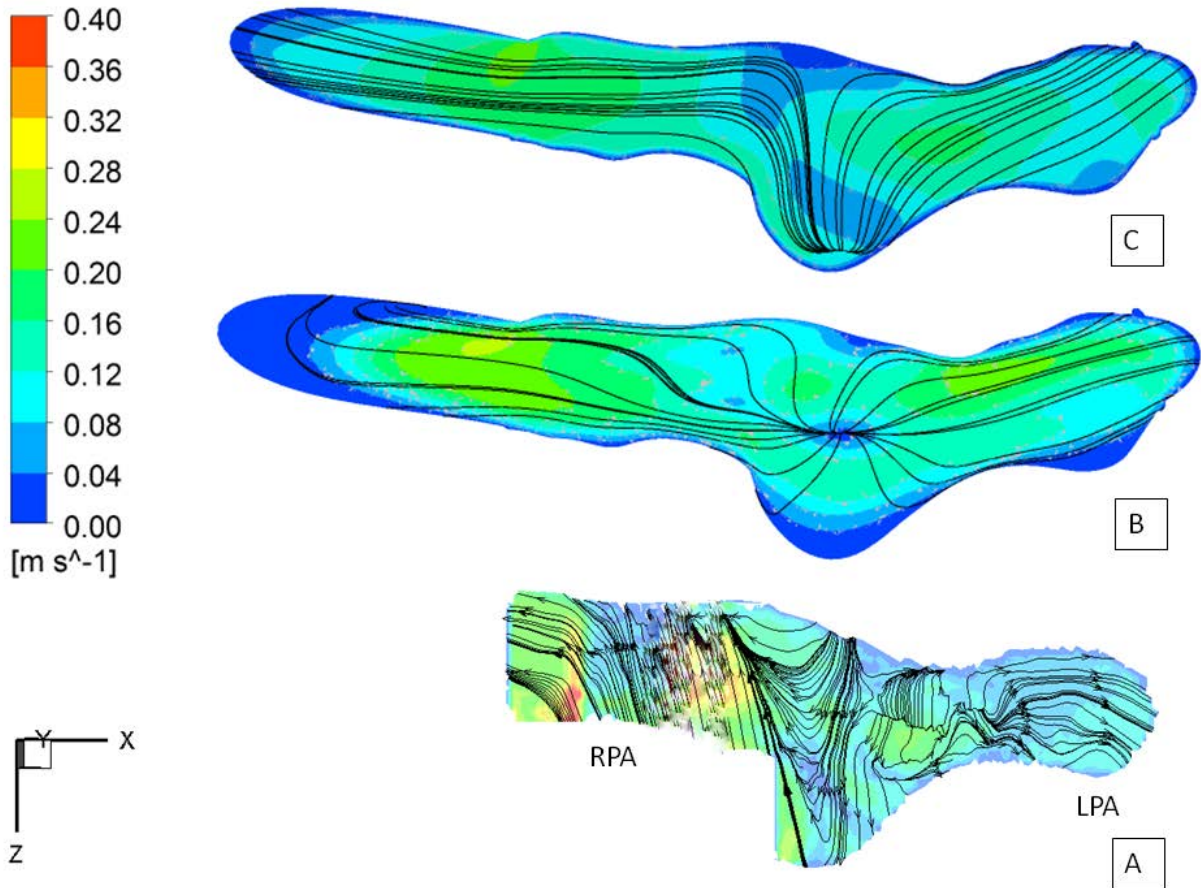
Figure 8.32: Planar slice through the anastomosis for the 3000 RPM rotational speed with cardiac output of 3 *L/min* and mean pulmonary arterial pressures of 16 *mmHg*. A) PIV data, B) k-ε model and C) SSTmodel.

8.5. Chapter Summary

In this chapter, the experimental results from the methods described in **Chapter 6** were presented. A comparison of these experimental findings to the numerical estimations from **Chapter 7** was performed and the results were found to be in good agreement. The inconsistencies that were found when comparing the numerical estimates to the PIV data can be attributed to limitations of any numerical model. No one turbulence model exists that can completely predict all of the fluid flow patterns, particularly with regard to highly three-dimensional flows. Further discussions of the results will follow in the next chapter, **Chapter 9**.

CHAPTER 9: Discussion

The incidence of single ventricle anomalies is approximately 2,000 babies per year in the U.S. [1, 3]. A single ventricle anomaly occurs as a result of an incomplete or abnormal development of the fetal heart during pregnancy. In addition to an underdeveloped ventricle, other structural defects in the heart may exist including holes in the septum, malformed vasculature, and missing or poorly formed valves. In these patients exhibiting a single ventricle anomaly, the vasculature connecting to the heart must be surgically repaired and reconfigured to form a single ventricle physiology. A single ventricle physiology uses a single functioning ventricle to provide the energy that is required to drive blood flow through the entire cardiovascular system, such that one ventricle does the equivalent workload of two normal ventricles.

Infants that are born with complex congenital heart defects experience distress shortly after birth. Closure of the ductus arteriosus transitions the cardiovascular system from receiving oxygen dependently from the mother's body to receiving oxygen independently from the lungs. A hole in the ventricular septum will allow oxygenated blood from the lungs to mix with the deoxygenated blood from the body resulting in a condition called cyanosis. This mixing of blood causes inadequate oxygen to reach the tissues and end organs. The malformed heart is unable to take the increased workload of both the pulmonary and systemic circulations and goes into congestive heart failure. Immediate medical intervention is required to preserve life. The infant will be given medications to reopen the ductus arteriosus and to mediate the congestive heart failure [6-8].

Palliative surgical intervention will follow within the first 4 weeks of life with subsequent surgeries to follow being conditional on the growth and development of the baby. In some cases where the child is experiencing poor development due to hemodynamic instability and limited oxygen reaching the tissues, a minimum of two additional surgeries will be performed. The ultimate goal of these surgeries is to repair and gradually off-load the single ventricle heart, while providing time for the growth and development of the child [137].

Before the fifth year of life, children with single ventricle physiologies will have undergone three invasive cardiovascular surgeries, the Norwood, the Glenn or Hemi-Fontan, and the Fontan conversion. The extra-cardiac Fontan, which is the most common performed procedure, results in a complete right heart bypass in which the superior and inferior vena cava intersect directly with the pulmonary artery. This surgery results in a complete separation of the systemic and pulmonary circulations [11]. In a single ventricle physiology the most developed or functional ventricle becomes the systemic ventricle and drives blood through the body and tissues. However, since there is no pulmonary ventricle in this configuration, venous blood returning from the body must flow passively into the pulmonary arteries through the total cavopulmonary connection [9]. Blood in the body is meant to be dynamic, such that it is always active and moving. In the TCPC, the passive flow can cause stagnation of blood, which requires extensive use of pharmacologic medications to prevent thrombus formation [6].

The requirements for a successful Fontan procedure are increased ventricular function and cardiac output with no arterial hypertension, an unrestricted inflow to the ventricle without regurgitation, and a complete separation of the pulmonary and systemic circulations. The pulmonary system requires normal vascular resistance in the lungs, unrestricted inflow from the superior and inferior vena cava into the left and right pulmonary arteries, and an unrestricted

outflow from the pulmonary veins into the heart [9, 13]. Ideally, these conditions will promote stable and definitive hemodynamics of the single ventricle physiology, but a failure of one of these conditions can lead to congestive heart failure.

Unfortunately, the Fontan procedure is an imperfect solution for complex cardiac defects with late stage mortality and morbidity occurring months to years after the surgery. A progressive decline takes place in the effectiveness of the Fontan procedure with time due to mounting physiologic complications, which progressively lead to congestive heart failure (CHF) [13, 138]. These complications may involve cardiac arrhythmias, increased venous and pulmonary pressures, low cardiac output, and hepatic and gastrointestinal dysfunction [139]. Surgical intervention to restore hemodynamic stability of the single ventricle physiology is possible, but the surgery may be complicated due to the presence of scar tissue from previous surgeries. The only definitive solution for these patients is a heart transplant for which a limit number of donor organs are available. Alternative therapeutic options are severely limited for these patients.

An emerging valid treatment option that is gaining widespread approval and use is the application of a blood pump to mechanically alleviate the chronic volume overload of the single ventricle circulation in order to slow or reverse the onset of congestive heart failure by reducing pressures in the venous system through increasing pressure in the pulmonary arteries.

There are many blood pumps or ventricular assist devices (VADs) that are being developed and in various stages of clinical trials or use. Progress in the development of pediatric VADs continues to achieve new milestones with newer generations of compact, pediatric VADs. All current devices were designed fit the specific operating conditions of patients with congestive heart failure with normal biventricular physiologies and generate pressures that exceed the desired range for venous-to-pulmonary or cavopulmonary support in the Fontan.

197

In order to address a public health concern and to provide hope for a targeted patient population in need of therapeutic options, the BioCirc Lab of VCU is developing a mechanical blood pump specifically designed to increase pressure in the great veins in order to augment flow through the lungs and reverse the Fontan paradox in adolescent and adult patients with failing single ventricle physiologies. During bridge-to-transplant, this pump would provide hemodynamic stability until a donor organ is located. Alternatively, the application of this pump as a bridge-to-recovery would potentially prevent the onset of many of the late co-morbidities, such as congestive heart failure. The functional parameters for a pump to operate in the anatomic and physiologic conditions of a cavopulmonary connection are unlike standard requirements for systemic left ventricular assist [11, 53, 54]. It has been postulated that a pressure adjustment of only 2-5 *mmHg* would be sufficient to improve hemodynamic stability [19]. We have generated promising data through numerical modeling and particle image velocimetry measurements to demonstrate the feasibility of this approach. The pump prototypes delivered 2-25 *mmHg* for flow rates of 0.5-4 L/min at 1500-9000 RPM [28, 54, 55].

This dissertation research sought to further validate the use of mechanical cavopulmonary assistance through modeling a steady-flow Fontan venous circulation with an anatomically accurate TCPC and a prototype blood pump located in the IVC. Computational modeling was performed using ANSYS-CFX to conduct the computational studies for a range of pump operating conditions and physiologically relevant parameters. These studies examined pump pressure generation, power efficiency estimates, blood trauma predictions, shear stress levels, fluid streamlines, and velocity profiles. Physical experiments were performed in order to validate the numerical models. These experiments included hydraulic testing and particle image velocimetry studies. The hydraulic testing measured the pump pressure generation as well as the

power efficiency of the TCPC with cavopulmonary assistance for a range of physiological parameters. The particle image velocimetry studies measured the three-dimensional velocity flow field inside of the TCPC for irregular flow patterns that might be created by the pump and could cause of regions of high shear stress or regions of stagnant flow. These studies were performed for three impeller cases in order to evaluate the impeller alone and the two cage designs, the super-diffuser cage and the against-with cage [32, 54, 120, 121].

9.1　　　Study Implications

The research studies conducted in this dissertation work are the first to present numerical predictions and experimental measurements of the impact of mechanical cavopulmonary assistance of the TCPC using a blood pump that is specifically designed for Fontan patients. The interactive fluid dynamics which can occur when a prototype axial flow pump is implanted into the inferior vena cava of a patient-specific total cavopulmonary connection to provide mechanical cavopulmonary assistance were extensively studied.

The CFD analysis for this dissertation research applied the k-ε and SST turbulence models for comparison with PIV and power efficiency experiments. The k-ε turbulence model has been used previously in designing other pump prototypes and has been used successfully by other researchers designing and optimizing numerous other blood pumps with experimental validation [11, 107-111]. The SST turbulence model was chosen for its ability to make up for the shortcomings of the k-ε model in modeling near wall regions which are important in pump design. This model served as a second numerical model that could be used for comparison to the experimental results.

The numerical simulations were applied to the patient-specific TCPC with an axial flow pump located in the IVC. The numerical models used a Newtonian constitutive model with a dynamic viscosity of 3.5 cP (i.e. hematocrit of 33%) and a density of 1050 kg/m^3 to model blood based on reasonably high shear rates in the flow domain of the pump (above 100 s^1) [33, 113, 133]. The pump rotational speeds were evaluated at 1000-4000 RPM. Under steady flow conditions, a cardiac output of 3 *L/min* based on a 60% / 40% flow split between the IVC and SVC was specified for each simulation. The outlet boundary conditions, such as the left and right pulmonary arteries (LPA and RPA), were defined to have static and equal mean pressures of 8, 12, 16 and 20 *mmHg* [54, 55].

A blood damage analysis based on a power law construct was applied to estimate the potential for hemolysis and thrombosis for this blood-contacting intravascular blood pump. This analysis has been employed as a predictive tool in the development of blood pumps [111, 115, 134]. This approach uses a power law relationship between the fluid scalar stress level and the exposure time to levels of stress [115]. The power equation provides a statistical estimate of damage to blood cells traveling through the model as a blood damage index [55, 115].

Higher rotational speeds resulted in larger predicted damage indices and a wider distribution of such quantities. In general, the mean damage indices under all of the operating conditions were found to be less that the target value of 2%. The maximum damage indices, however, were determined to be higher than anticipated with levels reaching slightly above 3%, which are likely due to the rotational vorticity of the flow leaving the trailing edge of the impeller blades. This finding requires further investigation of flow patterns around the trailing edge of the blade tips and will be investigated as part of future work.

Scalar fluid stress values were numerically estimated u s i n g t h e k-ε turbulence model at each nodal location in the computational flow field. Higher rotational speeds led to much larger scalar stress values, but the magnitude of the scalar stress never exceeded the cutoff of 460 *Pa*. The highest fluid stresses were found at the leading edge of the impeller blades and along the blade tips. The findings are very promising and support the continued development of this pump prototype.

The rate of energy augmentation due to the axial flow blood pump was computed using both the k-ε and SST turbulence models. Hydraulic testing of the physical impeller was used to validate the numerical predictions. The numerical models used a control volume approach to estimate the rate of energy augmentation through the anatomic model with the impeller pump. The flow conditions used a cardiac output of 3 *L/min* and equal, mean pulmonary arterial pressures of 16 *mmHg*. The pump was operated in the range of 1000-4000 RPM rotational speeds. An increase in pressure generation with increasing rotational speeds was observed. It is noted that in comparing the numerical estimates, the k-ε model predicted a higher pressure rise than the SST model. In contrast, the data collected from the physical pump experiments shows that the physical pump was able to generate a higher pressure at 4000 RPM than the k-ε estimate. The physical pump was also able to generate a much lower pressure rise in the lower RPM range below 2500 RPM. This reduction in pressure generation is expected based off of pressure-flow curves that were generated for the pump design specifications [53]. In the numerical model, the impeller model using the k-ε turbulence model outperformed the impeller model using the SST turbulence model. The physical impeller was able to generate pressures of 0 to 2.75 *mmHg* for rotational speeds of 0 to 4000 RPM, while the k-ε model was able to

generate pressures of 0 to 2.2 *mmHg* for rotational speeds of 0 to 4000 RPM, and the SST model was able to generate pressure of 0 to 1.15 *mmHg* for rotational speeds of 0 to 4000 RPM.

The rate of power gain or the improvement in energy efficiency was numerically estimated for the flow conditions of a total cardiac output of 3 *L/min* with an equal, mean pulmonary arterial pressure of 16 *mmHg* and was chosen for comparison to the experimental results. Both the numerical and experimental results show a positive impact on the energetics of the TCPC. Higher rotational speed of the impeller in the physical model increased the power efficiency beyond the estimates of the k-ε and SST models to 14 *mW*.

Physical experiments investigated the performance of the axial flow blood pump with two protective cages designs using hydraulic testing to measure their impact on the cavopulmonary circulation using a patient-specific Fontan model. The effect of the different pump configurations on the system pressures and flows in the mock circulatory loop were investigated to collect quantitative data on the power efficiency and pump pressure generation. The PIV experiments investigated the interactive fluid dynamics inside of the TCPC for the pump and the two cage designs. The experiments were conducted for 3 mechanical support configurations: 1) axial flow pump in the inferior vena cava (IVC) of the anatomic model; 2) axial flow pump with the *super-diffuser* stent in IVC; and, 3) axial flow pump having the *against-with* cage in the IVC.

The addition of a blood pump into the IVC of the TCPC should theoretically enhance fluid power in the cavopulmonary circulation by adding kinetic energy and rotational force to the fluid flow as balanced with the vessel resistance. The effect of the protective cages was to enhance the pressure generation of the pump. The impeller that was coupled with the *against-with* cage design demonstrated superior pressure generation as compared to the super diffuser

cage and the impeller configuration. The *against-with* configuration provided the most rapid increase in the rate of power gain for all of the pulmonary pressures examined. A higher pump pressure generation over the flow range and rotational speeds was also achieved [120, 121]. At higher rotational speeds, the *against-with* configuration, however, demonstrated a leveling in the rate of power gain that must be further investigated in future studies [122].

Pressure generation is only one aspect to consider in blood pump design. Streamlined flow conditions in the pump outlet with minimal turbulent vortices and lower shear stresses are highly desired to reduce the risk of hemolysis and thrombosis. Only the pressure generation and power efficiency of the two cage configurations were investigated in this dissertation work. Future work will allow for the further development of these protective cages by investigating fluid streamlines, hemolysis estimates and shear stresses using numerical models.

The results for the control case of the TCPC for the physical power efficiency studies were in agreement with similar studies performed by other researchers. The results in this power efficiency study are similar to those obtained by Dasi *et al.* [140] and Amodeo *et al.* [50] for similar patient specific geometries under similar experimental conditions performing a power flow analysis. The pressure and flow data are similar to those obtained by Haggerty *et al.* [141] for a patient-specific geometry using the Impella blood pump, which was developed for left ventricular failure in normal, biventricular circulations, to augment central venous pressure and to increase left atrial return. The power efficiency experiments were limited to investigating the augmentation of pressure and flow only into the pulmonary arteries.

Volumetric PIV data was created by stacking individual slices of stereo-PIV data to form a data volume. This provided the ability to view the global velocity profiles of the patient-specific anatomic TCPC model under conditions of mechanical cavopulmonary assistance. The

3-D velocity profile could be resliced into planes to permit the observation of local flow phenomena. 3-D streamlines can be applied to a volumetric velocity profile or to planar slices in order to visualize the flow phenomena. This provided a basis for comparison to the numerical models for the case of the impeller without a cage configuration present.

The PIV control case examined the TCPC without pump support present. The anatomic TCPC model had the expected flow patterns which are known to be present from previous work conducted by other researchers [16, 40, 41, 51, 142]. The flow in the TCPC anastomosis is strongly three-dimensional, as would be expected from the colliding flows and uneven vasculature surfaces. A large recirculation region is present at the anastomosis site. Ensley *et al.* [16] have theorized that the central recirculation region in the TCPC junction may have a positive impact as it minimizes pulmonary flow separation and prevents the formation of stagnation regions. The effects of the recirculation region are still under investigation and its consequences, beneficial or adverse, are not well understood [16, 49, 50]. The presence of the recirculation region in the TCPC junction can cause high shear stresses and irregular flow patterns to persist into the pulmonary arteries leading to blood trauma. The PIV studies are important for determining the impact the pump has on this recirculation region for its benefits in mediating it. For this TCPC model, additional smaller vortices were present. A small vortex was present in the IVC as a result of a small indentation in the vessel wall. Helical flow patterns were present in the pulmonary arteries as a result of the colliding caval flows. This flow pattern has been observed in most TCPC models, both physical and numerical [16, 49, 51, 136].

The introduction of the impeller without a set of diffuser blades had a modest effect on the flows at low rotational speeds but a dramatic effect on the flows at higher rotational speeds. In the lower rotational speeds, the effects of the pump are confined to the mainly to the IVC

vessel. A small amount of the rotational force is able to make it out of the IVC and into the anatomosis with the pump attempting to direct flow toward the LPA. The pump is not strong enough to provide any type of rotational force to fluid flow in the PAs.

The higher rotational speeds of the pump interfered with the main recirculation region in the center of the anastomosis. At 4000 RPM, the pump was able to begin to break up the stagnant region and drive the fluid toward the LPA. The recirculation is not completely dissolved at the highest rotational speed for this case. The helical flow patterns in the LPA are influenced by the pump.

The super-diffuser cage was tested over operating conditions of 0-4000 RPM. The 0 RPM case represented a stall case in order to determine the impact of the protective cage with the pump not rotating. The stall case was found to have only a minimal effect on the flow in the IVC and provide sufficient flow through so as not to be obstructive. The effect of the diffuser blades was immediately apparent with flow at lower rotational speeds driving flow toward the LPA while only mildly affecting the recirculation region present in the anastomosis. At higher rotational speeds pump is able to dissolve the central recirculation region and direct the flow into the PAs. The 4000 RPM case displayed the beginning of retrograde flow into the SVC. This flow structure was visible as the small region of flow that moved from the main impinging flow from the IVC to the left across the mouth of the SVC in order to exit through the RPA. This flow structure was noted to be concurrent with pressure and flow behavior that was observed in the super-diffuser cage during hydraulic testing. This cage configuration at the 4000 RPM rotational speed caused a small increase in SVC pressure and a small reduction in SVC flow rate.

The against-with cage was found not to be obstructive to the flow in the IVC in the stall case. The effects of the against-with cage were more pronounced at lower rotational speeds than

in the impeller case or the super diffuser case. The against-with cage was able to begin to dissolve the recirculation region in the anastomosis and direct flow into the LPA. At higher rotational speeds, the pressure and flow are directed into the PAs. For the 4000 RPM case, a similar flow structure that was also present in the super-diffuser case arises. This flow structure is the beginning of retrograde flow into the SVC. This was visible as a stream of flow that branches to the left from the impinging flow of the IVC and moves across the mouth of the SVC to merge with the exiting RPA flow. This flow pattern is indicative of the behavior that was observed for the against-with cage during hydraulic testing. A small increase in SVC pressure and a small reduction in SVC flow rate were observed.

The against-with cage design demonstrated superior pressure generation as compared to the super diffuser cage and the impeller configuration during the hydraulic testing. The against-with configuration had a higher pump pressure generation over the flow range and rotational speeds was also achieved [120, 121]. Representative flow structures present in the PIV data showed that there is an increase with flow in addition to the pressure rise. The pump was able increase pressure and drive flow from the IVC in order to dissolve the central recirculation region and move fluid into the pulmonary arteries. This finding supports the further development of this cage design.

In all three pump configurations, it was noted that the fluid flow field did not contain irregular flow patterns which could lead to issues with hemolysis or thrombus formation. The mixing caused by the pump may cause high shear stresses at rotational speeds in excess of 4000 RPM. This rotational speed was able to remove the central recirculation region in the TCPC but care must be taken when disturbing this mixing region to prevent blood cell trauma from occurring.

Numerical modeling of the internal flow field of the blood pump located in the IVC of an anatomic TCPC model provides information about the pump performance. Three-dimensional fluid streamlines throughout the pump can be indicative of undesired regions of separation, high shear stresses, and possible recirculation regions. The numerical fluid streamlines for various operating and boundary conditions in order to assess irregular flow conditions due to the patient-specific geometry and the impact of the blood pump in the IVC were examined. The flow streamlines were generated using the k-ε and STT turbulence models for a pump rotational speed range of 1000-4000 RPM, cardiac output of 3 *L/min*, and equal, mean pulmonary arterial pressures of 16 *mmHg*. A comparison of the CFD streamline predictions to the PIV measurements was performed at identical experimental conditions was performed.

Shunting of blood flow from the SVC and IVC was noted to prefer either the RPA or the LPA in the numerical models. The PIV on the other hand displayed a more even mixing of the caval flows to the PAs. The disagreement that was found when using the k-ε and STT turbulence models to generate the flow streamlines can be attributed to the limitations inherent to any numerical model. No one turbulence model exists that can completely predict all of the fluid flow patterns, particularly with regard to highly three-dimensional flows. The streamlines in the model suggest that mixing of the IVC flow does occur but the numerical models disagree as to whichever pulmonary artery the IVC flow will be directed toward. The PIV data also takes into account additional physical conditions which would otherwise complicate a numerical model.

Although not explicitly examined in this study, shunting of IVC blood has clinical relevance with regard to failure of Fontan physiology. IVC blood is believed to carry the liver factors which are necessary for proper development and function of the lungs [143]. An equal flow split is desired since this would allow equal amounts of IVC blood to be distributed to both

lungs. Since preferential shunting was predicted to occur, one lung could end up not receiving sufficient IVC blood flow. This can be alleviated by better controlling and directing the pump exit flow. Increasing the mixing that naturally occurs in the TCPC junction while removing the congestion of blood would be an important step toward restoring hemodynamic stability [140, 142, 144].

Comparisons between 2-D slices of data generated using the k-ε model and the SST model to the PIV results for the operating conditions over rotational speeds of 2000 to 4000 RPM provided valuable insight into the internal fluid dynamics as well as the limitations of the numerical models. The rotational speed of 1000 RPM was not included in this comparison because the volumetric PIV data showed the pump had only a very small impact on the flows in the TCPC and as such would not provide useful information. The slices were taken at five key areas of interest through the TCPC, specifically at the four sides of the anastomosis, so that the connections of the SVC and IVC represent the incoming flow patterns and the connections to the RPA and LPA represent the outgoing flow patterns. Additionally, a slice is made diagonally through the anastomosis in order to visualize the vortices that are present.

The numerical models are in good agreement with the PIV data having similar velocity magnitude distributions for the impeller case. The PIV data shows a distinct unsteady fluid flow pattern, which is fairly well resolved by the numerical data. The numerical data is limited as to the fluid flow structures that it can resolve. The presence and location of vortices in the fluid flow field differed between the PIV and numerical predictions.

There are limitations present in both the numerical simulations and the PIV data. The numerical simulations are recognized as a predictive tool to gain insight into the complex three-dimensional flow profiles of the TCPC and the pump. There is a limitation present in the degree

to which the numerical simulations are able to resolve these three-dimensional velocities. Some fluid flow structures are resolved, but these represent primarily vortices and regions of stagnant fluid flow. Regions with complex flow patterns are not well resolved or resolved at all in the case of the slices through the TCPC anastomosis. This is an inherent limitation to numerical simulations such that simple to moderate fluid flow structures can be resolved, but the solver has difficulty in resolving complex fluid flow structures.

The PIV data was able to capture the complex fluid flow structures of the TCPC however PIV has a limit as well. The technique used here was developed as a compromise between cost and data resolution. If the fluid flow pattern becomes too complex, then it may not be possible to measure the instantaneous velocity with this technique. A higher resolution PIV system to collect velocity data in the form of tomographic PIV is possible but would be difficult to implement due to the additional hardware constraints that are required [92, 145].

There are functional and clinical limitations with implementing mechanical cavopulmonary assistance. Firstly, a concern that arises with the use of an axial flow pump in the IVC is the disturbance of the internal flow balance between the incoming caval blood flows and the outgoing pulmonary flows at the TCPC junction. Secondly, an additional limitation is that of excessive retrograde flow into the SVC, which could hinder or halt blood flow in the appropriate direction toward the TCPC junction. Measurements during this study showed that flow into the TCPC from the SVC was slightly reduced at higher rotational speeds, which is likely due to the pressure elevation and higher volume flow into the PAs. No retrograde flow was observed or measured during these experiments, which is encouraging despite competing flow conditions. This finding reinforces the need for careful control and understanding of the operational limitations of the pump in consideration of the cardiophysiology and anatomy of the TCPC and

SVC inflow conditions. Thirdly, risk of IVC vessel suction and collapse due to pump rotation remains a constraint. Vessel trauma or damage due to varying levels of suction must also be examined. *In vivo* findings by Riemer et al. [25] demonstrated a collapse of the IVC at 6000 RPM using the Thoratec HeartMate II. The Thoratec HeartMate II blood pump, however, was designed to support a normal biventricular circulation having a left ventricular failure and was not developed for the unique anatomic configuration of the TCPC. Previous *in vitro* research has investigated the probability of vessel suction and collapse of the vein on the inlet side of our pump [30, 55]. In the case of the impeller alone without a supportive protective cage, venous collapse did not occur at rotational speeds below 9000 RPM and only minimal deformation occurred over the entire range of rotational speeds [55]. Additionally, the physiologic effects of the suction effect of the pump is not known since the pump must draw from the liver and the venous system but not draw an excessively large amount of volume that could cause a significant pressure drop leading to venous collapse. The pump rotational speed of 4000 RPM for the case of the impeller alone was chosen to be the best operating condition because it is able to provide the necessary balance of reducing the IVC pressure without increasing the SVC pressure, but still proving pressure into the PAs.

All three pump and cage configurations showed promise in promoting the blood flow energetics in the TCPC. The numerical data and the experimental data supported the claim that mechanical cavopulmonary assistance is viable therapeutic option for Fontan patients with failing physiologies. The limits to the benefits of cavopulmonary support in the unique hemodynamics of the TCPC that must be further addressed for the clinical approach in future research.

9.2   Impact of Experiment Error

There are several possible sources of error that are present with the numerical analyses. The boundary conditions in the CFD models are set to be steady flow analyses. Additional studies which include transient flow simulations, fluid structure interaction studies, in the incorporation of additional physiologic parameters of the Fontan circulation would provide more accurate information about the interactive fluid dynamics between the pump and the TCPC. These parameters include pulsatile flow, vessel impedance and compliance, and respiratory effects. The use of more complex models of the Fontan will be investigated in future work.

The blood damage analyses conducted in this research did not consider platelet activation or transient effects as a result of the blade rotation in the fluid flow. The blood damage analyses applied a power law model which tends to overestimate the levels of hemolysis. This provides a factor of safety in the pump design since the true hemolysis level would be below the predicted values. Hemolysis testing using physical prototypes in a test rig would provide a more realistic approximation of the actual blood trauma levels due to the pump. Further development needs to done on the cages including numerical simulations and physical experiments to determine the blood trauma levels.

There are several possible sources of experimental error, which can occur during hydraulic testing or when using particle image velocimetry to measure fluid flow velocity. In PIV studies, a key source of error is the choice of the delta t value prior to data collection and the interrogation window size that is used during image processing to extract the velocity vectors. Delta t values must be chosen with care because an improper choice can negatively impact the velocity measurements by giving velocity magnitude values which may be lower than the actual value. Likewise, a larger interrogation window size reduces the effective resolution of the

measurement. For the experiments performed this study, a 16x16 interrogation window was used, which is an acceptable size.

Background noise in the captured image is a problem. This noise occurs as a result of reflection and refraction of the laser light within the model. There is a trade-off between the available resolution and the background noise in the image. A smaller interrogation window is possible but at the expense of noise amplification, which would require additional methods in the experimental setup to increase the signal to noise ratio significantly.

Aberations in the field of view can arise due to the air-liquid interface of a model when the cameras must look through a thick liquid layer. These imaging effects can distort the particle images in the radial direction, that is, into the image plane. Prasad and Jensen[146] proposed a liquid prism, a clear glass structure with angled sides that is filled with the working fluid. This would create an orthogonal axis to the camera lenses and air-liquid interface. This ensures paraxial image recording and corrects for the radial distortion of the particle images. Typically, this prism structure will take on the form of a trapezoid with the angled sides for the camera view perspective. This would be necessary if a wide angle is used since total internal reflection within a given model with occur at approximately 45 degrees of camera angle tilt [146, 147].

In our TCPC model, this trapezoid structure is not used since the camera angle is only 15 to 20 degrees of tilt due to the limited optical access from the small surface area of the model. This is consistent with the work of Hill *et al.*[148] who have shown that the camera angle has only a weak dependence on the in-plane and out of plane errors with regard to 3-D particle motion. Moreover, since our model is made from resin, this would require the inclusion of a solid trapezoidal block on top of the model which would further limit the optical access. In addition, the anatomic structure is imbedded into a solid block so aberrations would occur at the side of

the block, which is distant from the TCPC which is positioned in the center of the camera field of view.

The 3-D motion of particles within and through the image plane is also problematic since particles that move out of the lightsheet by moving up and down as opposed to left to right within the plane, cannot be used in the determination of velocity vectors. The current study used only two cameras to collect stereo-PIV data about the out of plane motion and velocities. This data is limited in its resolution since more cameras will naturally provide a higher data resolution. Typically with anatomic models of all kinds of structures, three or four cameras are used in order to capture the true three-dimensional nature of fluid flow field [149, 150]. The velocity data that is collect is based off of two-component data, e.g. x and y velocity data each from two cameras which are combined to gain information about the z-direction. PIV systems that provide three-component data are under-development with 3-D cross-correlation aiming to overtake the standard 2-D cross-correlation in a few years. Additionally, measuring a full 3-D displacement vector rather than having to utilize data interpolation to complete the volumetric representation of the PIV data, would increase the accuracy of the data. Measuring the complete displacement vector remains a gold standard for PIV, and has only recently been made possible through advances in the hardware and technology. Equipment cost still remains an issue, but the cost of cameras as well as CCD chips continues to decline due to advances in microelectronics development [98].

Additional sources of error are fabrication errors due to differences in CAD models and the finished product. It is possible that the axial flow prototype may not have been created exactly as the Solidworks model, even with minimal manufacturing tolerance. This is also true of the anatomic TCPC model, which is produced as a reasonably accurate replica. The method

described by de Zelicourt, *et al.*[47] is used for this model which is an extension to the methods developed by Budwig *et al.*[123] and Bale-Glickman *et al.*[46] for creating PIV models. Technological advances are currently underway to increase the accuracy of rapid-prototyped models. The model used in this study was done using a casting system. Two models were rapid-prototyped of the vessel lumen to several as negatives. The casting resin was then injected into the molds to form a positive solid. The two halves were then glued together to get the complete model. There is always a chance for slight misalignment of the individual halves despite the best efforts to limit manufacturing defects and to properly align the halves for permanent adhesion. The prototype cages are inherently difficult to rapid-prototype. The cage corresponds to a large amount of open space internally which requires the use of support structures which must then be removed. The cage filaments used in this study were rigid and had to be manufactured to be robust into withstand the vigorous testing. This required thickening of the filaments so that the cages would not be excessively fragile and prone to sudden catastrophic failure due to broken cage filaments. Prior experience with cage designs by Throckmorton *et al.*[121] have supported this design change. Additionally, it is difficult to manufacture circular shapes without forming an oval due to the stacking process of the RP resin layers. The manufacturing tolerances had to be careful chosen to form a circular structure for the attachment collar for the shaft housing as well as a circular structure for the cage as a whole but to form ellipsoidal shaped cage filaments.

9.3   Study Limitations and Future Work

Mock circulation of the Fontan remains a challenge with researchers gradually developing improved physiologic models. The model of the Fontan used in this study is a simple model used by researchers studying the Fontan circulation in the early 2000's [14, 27, 151]. The venous system largely supports laminar flow conditions, however more recent research has

shown that flow through the TCPC is somewhat pulsatile due to respiration effects. This has lead to the development of more complex models of the Fontan circulation to include the pulsatility as well as contributing effects from the liver, spleen and greater venous system. These represent more complex scenarios that the pump may be tested under in future studies [152].

Stereo-PIV was applied to the patient-specific model to measure interactive fluid dynamics that occur as result of a pump located in the IVC to provide cavopulmonary assistance. Flow into the total cavopulmonary connection (TCPC) from the SVC was measured to be slightly reduced at higher pump rotational speeds. Retrograde flow was neither observed, nor measured, into the SVC. At higher rotational speeds with the protective cages and the diffuser blades in place, retrograde flow will occur since the pressure generation is much greater. In essence, balance is in place between the inflow and outflow pressures such that the pump generation cannot exceed a certain percentage of the SVC pressure. The threshold for the effective pressure rise of the pump, without causing retrograde flow is not well defined. This is an important area for future work since in provides a limitation on the operating conditions of the pump.

Further research is currently underway to include extensive numerical analysis to allow for better, optimized pump designs. An assessment is currently underway for the implementation of the *against-with* cage design in multiple, patient-specific models. These studies will provide important information about the abilities of the pump to function in multiple patient-specific anatomies and to insure that the pump can be safely implemented in a diverse patient population.

Although the results of this dissertation work are encouraging, additional investigation is required. Transient simulations and fluid-structure interaction studies would provide more insight into the fluid dynamics in the pump, especially the fluid layers closest to the stent

filaments. A general enhancement of the boundary conditions must be performed to include physiologic and varying inlet and outlet impedances, vessel compliance, and lung compliance. This requires the assessment of more complex Fontan physiologic models to effectively model pump support. Animal studies would also provide information about the ability of the blood pump to support a Fontan patient and to maintain biocompatibility, implantability, and pressure generation. The intravascular blood pump in this study meets the requirements to mechanically support these patients, but additional development phases are need to address limitation and to ensure translational success [122].

CHAPTER 10: Conclusions

A mechanical circulatory support alternative in the form of a blood pump is being specifically developed to increase the pressure in the vena cavae to improve the hemodynamic stability in adolescent and adult Fontan patients exhibiting congestion in the cavopulmonary circulation. The blood pump is capable of producing pressure rises in the range suitable to mechanically support adolescent and adult Fontan patients.

The scientific studies performed in this dissertation work investigated the interactive fluid dynamics between a patient-specific total cavopulmonary connection and an axial flow pump located in the inferior vena cava to facilitate cavopulmonary assist. Through estimating the impact of the pump numerically using computational fluid dynamics simulations, positive conclusions were drawn that the cavopulmonary circulation is capable of interacting with a blood pump. Quantitative data about the impact the pump had on patient-specific TCPC located in a mock circulatory loop was assessed using hydraulic testing and stereo-PIV experiments. These experiments were conducted for three mechanical support configurations, which included the pump impeller alone in the inferior vena cava (IVC) and with two different prototype cage designs. All three pump configurations led to an increase in pressure and flow in the mock circulatory system. Further development will continue on the against-with cage design which showed superior performance over the other two configurations.

In this dissertation research, a contribution was made to the advancement of intravascular blood pump technologies through developing an advance cage prototype with hydrodynamically optimized filaments. The positive impact on the pressure and flow through the use of a set of twisted protective cage filaments in conjunction with an impeller proves that the shape of the

filaments are capable of positively enhancing pressure generation across the pump. Future work will concentrated on further developing the against-with cage design.

The numerical data and the experimental data supported the claim that mechanical cavopulmonary assistance is a viable therapeutic option for adolescent and adult Fontan patients. The limits to the benefits of cavopulmonary support in the unique hemodynamics of the TCPC must be further addressed for the clinical approach in future research. This scientific research aided in attaining the long-term goal of developing an alternative therapeutic treatment option for adolescent and adult Fontan patients, who have limited therapeutic options available.

Literature Cited

1.   Association AH. *Facts and Statistics*. Congenital Heart Defects August 2009 [cited 2010 February 2]; Available from: http://www.americanheart.org.

2.   Law SM, Sahn DJ, *Congestive Heart Failure Secondary to Congenital Heart Disease*, in *Moss and Adams' Heart Diseases in Infants, Children, and Adolescents: including the fetus and young adult*, Allen HD, Editor. 2008, Lippincott and Williams: Philadelphia, PA. p. 354-372.

3.   Foundation MoD. *Congential Heart Defects*. Medical Reference August 2008 [cited 2010 February 2]; Available from: http://www.marchofdimes.com/professionals/14332_1212.asp#surgery.

4.   Costanzo LS: *Physiology*. Philadelphia, PA, USA, Elsevier, 2006.

5.   Chopski SG, *Particle Image Velocimetry Measurements of the Total Cavopulomary Connection with Circulatory Flow Augmentation*. M.S. Thesis in *Mechanical Engineering*. Richmond, VA, Virginia Commonwealth University: p. 1-150, 2010.

6.   Khairy P, Fernandes SM, Mayer JE, Jr.*, et al.*: Long-term survival, modes of death, and predictors of mortality in patients with Fontan surgery. *Circulation* 117: 85-92, 2008.

7.   Hosein RBM: Factors influencing early and late outcome following the Fontan Procedure in the current era. The 'Two Commandments'? *European Journal of Cardio-thoracic surgery* 31: 344-353, 2007.

8.   Myers CD, Ballman K, Riegle LE*, et al.*: Mechanisms of systemic adaptation to univentricular Fontan conversion. *J Thorac Cardiovasc Surg* 140: 850-856, 856 e851-856, 2010.

9.   Gewillig M: The Fontan circulation. *Heart* 91: 839-846, 2005.

10.   Throckmorton AL, Chopski SG: Pediatric circulatory support: current strategies and future directions. Biventricular and univentricular mechanical assistance. *ASAIO J* 54: 491-497, 2008.

11.   Throckmorton AL, Kapadia J, Madduri D: Mechanical axial flow blood pump to support cavopulmonary circulation. *Int J Artif Organs* 31: 970-982, 2008.

12.   Ohuchi H, Kagisaki K, Miyazaki A: Impact of the Evolution of the Fontan Operation on Early and Late Mortality: A single-center experience over 3 decades. *Ann Thorac Surg* 92: 1457-1467, 2011.

13.   Fontan F, Kirklin JW, Fernandez G*, et al.*: Outcome after a "perfect" Fontan operation. *Circulation* 81: 1520-1536, 1990.

14.   Grigioni M, Amodeo A, Daniele C*, et al.*: Particle image velocimetry analysis of the flow field in the total cavopulmonary connection. *Artif Organs* 24: 946-952, 2000.

15.   de Leval MR, Kilner P, Gewillig M, Bull C: Total cavopulmonary connection: a logical alternative to atriopulmonary connection for complex Fontan operations. Experimental studies and early clinical experience. *J Thorac Cardiovasc Surg* 96: 682-695, 1988.

16.   Ensley AE, Lynch P, Chatzimavroudis GP*, et al.*: Toward designing the optimal total cavopulmonary connection: an in vitro study. *Ann Thorac Surg* 68: 1384-1390, 1999.

17.   DeGroff CG, Carlton JD, Weinberg CE*, et al.*: Effect of vessel size on the flow efficiency of the total cavopulmonary connection: in vitro studies. *Pediatr Cardiol* 23: 171-177, 2002.

18.   Rodefeld MD, Boyd JH, Myers CD*, et al.*: Cavopulmonary assist: circulatory support for the univentricular Fontan circulation. *Ann Thorac Surg* 76: 1911-1916, 2003.

19.	de Leval MR: The Fontan Circulation: What have we learned? What to expect? *Pediatr Cardiol* 19: 316-320, 1998.
20.	Throckmorton AL, Ballman KK, Myers CD*, et al.*: Performance of a 3-bladed propeller pump to provide cavopulmonary assist in the failing Fontan circulation. *Ann Thorac Surg* 86: 1343-1347, 2008.
21.	Rodefeld MD, Frankel SH, Giridharan GA: Cavopulmonary assist: (em)powering the univentricular fontan circulation. *Semin Thorac Cardiovasc Surg Pediatr Card Surg Annu* 14: 45-54, 2011.
22.	Rodefeld MD, Coats B, Fisher T*, et al.*: Cavopulmonary assist for the univentricular Fontan circulation: von Karman viscous impeller pump. *J Thorac Cardiovasc Surg* 140: 529-536, 2010.
23.	Giridharan GA, Koenig SC, Kennington J*, et al.*: Performance evaluation of a pediatric viscous impeller pump for Fontan cavopulmonary assist. *J Thorac Cardiovasc Surg*, 2012.
24.	Boni L, Sasaki T, Ferrier WT*, et al.*: Challenges in longer-term mechanical support of fontan circulation in sheep. *ASAIO J* 58: 60-64, 2012.
25.	Riemer RK, Amir G, Reichenbach SH, Reinhartz O: Mechanical support of total cavopulmonary connection with an axial flow pump. *J Thorac Cardiovasc Surg* 130: 351-354, 2005.
26.	Tsuda S, Sasaki T, Maeda K*, et al.*: Recovery during mid-term mechanical support of fontan circulation in sheep. *ASAIO J* 55: 406-411, 2009.
27.	Wang R, Lacour-Gayet FG, Lanning CJ*, et al.*: Initial experience with the development and numerical and in vitro studies of a novel low-pressure artificial right ventricle for pediatric Fontan patients. *ASAIO J* 52: 682-692, 2006.
28.	Chopski SG, Downs E, Haggerty CM, Yoganathan AP, Throckmorton AL: Laser flow measurements in an idealized total cavopulmonary connection with mechanical circulatory assistance. *Artif Organs* 35: 1052-1064, 2011.
29.	Day SW, McDaniel JC: PIV measurements of flow in a centrifugal blood pump: steady flow. *J Biomech Eng* 127: 244-253, 2005.
30.	Throckmorton AL, Lopez-Isaza S, Downs EA*, et al.*: A viable therapeutic option: mechanical circulatory support of the failing Fontan physiology. *Pediatr Cardiol* In Press, 2013.
31.	Downs EA, Moskowitz WB, Throckmorton AL: Steady Flow Analysis of Mechanical Cavopulmonary Assistance in MRI-Derived Patient-Specific Fontan Configurations. *Artif Organs* 36: 972-980, 2012.
32.	Kapadia JY, Pierce KC, Poupore AK, Throckmorton AL: Hydraulic testing of intravascular axial flow blood pump designs with a protective cage of filaments for mechanical cavopulmonary assist. *ASAIO J* 56: 17-23, 2010.
33.	Throckmorton AL, Kishore RA: Design of a protective cage for an intravascular axial flow blood pump to mechanically assist the failing Fontan. *Artif Organs* 33: 611-621, 2009.
34.	Khunatorn Y, Shandas R, DeGroff C, Mahalingam S: Comparison of in vitro velocity measurements in a scaled total cavopulmonary connection with computational predictions. *Ann Biomed Eng* 31: 810-822, 2003.

35. Hsia TY, Migliavacca F, Pittaccio S*, et al.*: Computational fluid dynamic study of flow optimization in realistic models of the total cavopulmonary connections. *J Surg Res* 116: 305-313, 2004.

36. Pekkan K, de Zelicourt D, Ge L*, et al.*: Physics-driven CFD modeling of complex anatomical cardiovascular flows-a TCPC case study. *Ann Biomed Eng* 33: 284-300, 2005.

37. Pekkan K, Kitajima HD, de Zelicourt D*, et al.*: Total cavopulmonary connection flow with functional left pulmonary artery stenosis: angioplasty and fenestration in vitro. *Circulation* 112: 3264-3271, 2005.

38. Migliavacca F, Dubini G, Bove EL, De Leval MR: Computational fluid dynamics simulations in realistic 3-D geometries of the total cavopulmonary anastomosis: The influence of the inferior vena caval anastomosis. *J Biomech Eng* 125: 805-813, 2003.

39. Whitehead K, Pekkan K, Kitajima H, Paridon SM, Yoganathan A: Nonlinear power loss during exercise in single ventricle patients after the Fontan: insights from computational fluid dynamics. *Circulation* 116: I165-171, 2007.

40. Ryu K, Healy TM, Ensley AE*, et al.*: Importance of accurate geometry in the study of the total cavopulmonary connection: computational simulations and in vitro experiments. *Ann Biomed Eng* 29: 844-853, 2001.

41. de Zelicourt DA, Pekkan K, Wills L*, et al.*: In vitro flow analysis of a patient-specific intraatrial total cavopulmonary connection. *Ann Thorac Surg* 79: 2094-2102, 2005.

42. Raffel M, Willert C, Wereley S, Kompenhans J: *Particle Image Velocimetry: A Practical Guide*. New York, Springer, 2007.

43. Adrian R: Particle-imaging techniques for experimental fluid mechanics. *Annu. Rev. Fluid Mech.* 23: 261-304, 1991.

44. Day SW, *Measurements of Flow in a Centrifugal Blood Pump using Particle Image Velocimetry*. Dissertation in *Mechanical and Aerospace Engineering*. Charlottesville, VA, University of Virginia: p. 1-271, 2003.

45. Patel SM: The Status of Failure and Reliability Testing of Artificial Blood Pumps. *ASAIO* 51: 440-451, 2005.

46. Bale-Glickman J, Selby K, Saloner D, Savas O: Experimental flow studies in exact-replica phantoms of atherosclerotic carotid bifurcations under steady input conditions. *J Biomech Eng* 125: 38-48, 2003.

47. de Zelicourt D, Pekkan K, Kitajima H, Frakes D, Yoganathan AP: Single-step stereolithography of complex anatomical models for optical flow measurements. *J Biomech Eng* 127: 204-207, 2005.

48. Brunette J, Mongrain R, Laurier J, Galaz R, Tardif JC: 3D flow study in a mildly stenotic coronary artery phantom using a whole volume PIV method. *Medical Engineering & Physics* 30: 1193-1200, 2008.

49. Bolzon G, Pedrizzetti G, Grigioni M*, et al.*: Flow on the symmetry plane of a total cavo-pulmonary connection. *J Biomech* 35: 595-608, 2002.

50. Amodeo A, Grigioni M, Oppido G*, et al.*: The beneficial vortex and best spatial arrangement in total extracardiac cavopulmonary connection. *J Thorac Cardiovasc Surg* 124: 471-478, 2002.

51. Kitajima HD, Sundareswaran KS, Teisseyre TZ*, et al.*: Comparison of particle image velocimetry and phase contrast MRI in a patient-specific extracardiac total cavopulmonary connection. *J Biomech Eng* 130: 041004, 2008.

52. Day SW, McDaniel JC, Wood HG*, et al.*: Particle image velocimetry measurements of blood velocity in a continuous flow ventricular assist device. *ASAIO J* 47: 406-411, 2001.

53. Kapadia JY, *Development of a Mechanical Cavopulmonary Assist Device for the Failing Fontan*. M.S. Thesis in *Mechanical Engineering*. Richmond, Virginia, Virginia Commonwealth University: p. 1-102, 2009.

54. Bhavsar SS, Kapadia JY, Chopski SG, Throckmorton AL: Intravascular mechanical cavopulmonary assistance for patients with failing Fontan physiology. *Artif Organs* 33: 977-987, 2009.

55. Throckmorton AL, Carr JP, Tahir SA*, et al.*: Mechanical cavopulmonary assistance of a patient-specific Fontan physiology: numerical simulations, lumped parameter modeling, and suction experiments. *Artif Organs* 35: 1036-1047, 2011.

56. Warsi Z: *Fluid Dynamics: Theoretical and Computational Approaches.* Boca Raton, FL, CRC Press, 1999.

57. Wendt J: *Computational Fluid Dynamics: An Introduction.* Berlin, Germany, Springer-Verlag, 1992.

58. Peyret R: *Handbook of computational fluid mechanics*. London, Academic Press, 1996.

59. Cebeci T: *Analysis of Turbulent Flows*. Amsterdam, Elsevier Ltd., 2004.

60. White FM: *Fluid Mechanics*. Boston, McGraw-Hill, 2008.

61. Schlichting H, *Boundary-Layer Theory*. 1979, McGraw-Hill: New York.

62. Warsi Z: *Fluid Dynamics: Theoretical and Computational Approaches*. Boca Raton, FL, CRC Press, 1999.

63. Zhang Y, Zhan Z, Gui X-M*, et al.*: Design Optimization of an Axial Blood Pump With Computational Fluid Dynamics. *ASAIO* 54: 150-155, 2008.

64. Xuan Y, Chang Y, Gu K, Gao B: Hemodynamic Simulation Study of a Nove Intra-Aorta Left Ventricular Assist Device. *ASAIO* 58: 462-469, 2012.

65. Karmonik C, Partovi S, Loebe M*, et al.*: Influence of LVAD Cannula Outflow Tract Location on Hemodynamics in the Ascending Aorta: A Patient-Specific Computational Fluid Dynamics Approach. *ASAIO* 58: 562-567, 2012.

66. Toptop K, Kadipasaoglu K: Design and Numeric Evaluation of a Novel Axial-Flow Left Ventricular Assist Device. *ASAIO* 59: 230-239, 2013.

67. ANSYS Technology: Engineering Software Manuals for BladeGen and TascFlow., July 2000.

68. Kundu PK, Cohen IM: *Fluid Mechanics*. Boston, Elsevier, 2008.

69. Menter F: Two-Equation Eddy-Viscosity Turbulence Models for Engineering Applications. *AIAA Journal* 32: 1598-1605, 1994.

70. Day SW, McDaniel JC, Wood HG*, et al.*: A prototype HeartQuest ventricular assist device for particle image velocimetry measurements. *Artif Organs* 26: 1002-1005, 2002.

71. Su B, Chua LP, Wang X: Validation of an axial flow blood pump: computational fluid dynamics results using particle image velocimetry. *Artif Organs* 36: 359-367, 2011.

72. Liu G, Zhang Y, Chen H*, et al.*: Flow visualization in the outflow cannula of an axial blood pump. *Biomed Mater Eng* 23: S117-122, 2012.

73. Melling A: Tracer particles and seeding for particle image velocimetry. *Measurement Sci. Technol.* 8: 1406-1416, 1997.

74. Mei R: Velocity fidelity of flow tracer particles. *Exp Fluids* 22: 1-13, 1996.

75. *1.4MP PowerView Camera Model 630066 spec sheet*. 2008.

76. *TSI Insight 3G Data Acquisition, Analysis, and Display Platform, User's Manual*, 2008.

77.   Adrian R, Keane R: Optimization of particle image velocimeters. Part 1: Double pulsed systems. *Measurement Sci. Technol.* 1: 1202-1215, 1990.
78.   Adrian R: Dynamic ranges and spatial resolution of particle image velocimetry. *Measurement Sci. Technol.* 8: 1393-1398, 1997.
79.   Keane J, Adrian R: Theory of cross-correlation analysis of PIV images. *Appl. Sci. Res.* 49: 191-215, 1992.
80.   Papoulis A: *Signal Processing*. New York, McGraw-Hill, 1977.
81.   Westerweel J, Dabiri D, Gharib M: The effect of a discrete window offset on the accuracy of cross-correlation analysis of PIV recordings *Exp Fluids* 23: 20-28, 1997.
82.   Meinhart CD, Wereley S, Santiago JG: A PIV Algorithm for Estimating Time-Average Velocity Fields. *Journal of Fluids Engineering* 122: 285-288, 2000.
83.   Nobach H, Bodenschatz E. *New resolution limits in PIV image processing*. in *13th Int symp on Applications of Laser Techniques to Fluid Mechanics*. 2006. Lisbon, Portugal.
84.   *Peaks*.   [cited; Available from: www.dsp.stackexchange.com.
85.   Nogueira J, Lecuona A, Rodriguez PA: Data validation, false vectors correction and derived magnitudes calculation on PIV data. *Measurement Sci. Technol.*, 1997.
86.   Westerweel J: Efficient detection of spurious vectors in particle image velocimetry data. *Exp Fluids* 16: 236-247, 1994.
87.   Huang H, Dabiri D, Gharib M: On errors of digital particle image velocimetry. *Measurement Sci. Technol.* 8: 1427-1440, 1997.
88.   Prasad AK: Stereo particle image velocimetry. *Exp Fluids* 29: 103-116, 2000.
89.   Giordano R, Astarita T: Spatial resolution of the Stereo PIV technique. *Experiments in Fluids* 46: 643-658, 2009.
90.   Zang W, Prasad AK: Performance evaluation of a Scheimpflug stereocamera for stereoscopic particle image velocimetry. *Appl. Opt.* 36: 8738-8744, 1997.
91.   Wieneke B: Volume self-calibration for 3D particle image velocimetry. *Exp Fluids* 45: 549-556, 2008.
92.   Willert C: Stereoscopic digital particle image velocimetry for application in wind tunnel flows. *Measurement Sci. Technol.* 8: 1465-1479, 1997.
93.   Scarano F, David L, Bsibsi M, Calluaud D: S-PIV comparative assessment: image dewarping + misalignment correction and pinhole + geometric projection. *Exp Fluids* 39: 257-266, 2005.
94.   Soloff SM, Adrian RJ, Liu Z-C: Distortion compensation for generalized stereoscopic particle image velocimetry. *Measurement Sci. Technol.* 8: 1441-1454, 1997.
95.   Willert C, Gharib M: Digital particle image velocimetry. *Exp Fluids* 10: 181-193, 1991.
96.   Wieneke B: Stereo-PIV using self-calibration on particle images. *Exp Fluids* 39: 267-280, 2005.
97.   Prasad AK, Adrian RJ: Stereoscopic particle image velocimetry applied to liquid flows. *Exp Fluids* 15: 49-60, 1993.
98.   Kitzhofer J, Brucker C, Nonn T: Generation and visualization of volumetric PIV data fields. *Exp Fluids* 51: 1471-1492, 2011.
99.   Boring E, Pang A, *Directional visualization of vector fields*, in *Proceedings of IEEE visualization*. 1996. p. 389-392.
100.   Li G-S, Tricoche X, Weiskopf D, Hansen C: Flow Charts: visualization of vector fields on arbitrary surfaces. *IEEE Trans Vis Comput Graph* 14: 1-14, 2008.

101. Frakes DH, Pekkan K, Dasi LP, *et al.*: Modified control grid interpolation for the volumetric reconstruction of fluid flows. *Exp Fluids* 45: 987-997, 2008.
102. Frakes D, Smith M, de Zelicourt D, Pekkan K, Yoganathan A: Three-dimensional velocity field reconstruction. *J Biomech Eng* 126: 727-735, 2004.
103. Baldwin J, Deutsch S, Petrie H, Tarbell J: Determination of Principal Reynolds Stresses in Pulsatile Flows After Elliptical Filtering of Discrete Velocity Measurements. *Transactions of the ASME* 115: 396-403, 1993.
104. Scharnowski S, Hain R, Kahler CJ. *Estimation of Reynolds Stresses from PIV measurements with single pixel resolution*. in *15th International Symp on Applications of Laser Techniques to Fluid Mechanics*. 2010. Lisbon, Portugal.
105. Bendat J, *Random Data: Analysis and Measurement Procedures*. 1986: New York.
106. Bludszuweit C: Model for General Mechanical Blood Damage Prediction. *Artificial Organs* 19: 583-589, 1995.
107. Miyazoe Y, Sawairi T, Ito K, Konishi Y, Yamane T, Nishida M, Asztalos B, Masuzawa T, Tsukiya T, Endo S, and Taenaka Y.: Computational Fluid Dynamics to Establish the Design Process of a Centrifugal Blood Pump: Second Report. *Artificial Organs* 23: 762-768, 1999.
108. Anderson J, Wood HG, Allaire PE, and Olsen DB.: Numerical Analysis of Blood Flow in the Clearance Regions of a Continuous Flow Artificial Heart Pump. *Artificial Organs* 24: 492-500, 2000.
109. Allaire P, Wood HG, Awad RS, and Olsen DB.: Blood Flow in a Continuous Flow Ventricular Assist Device. *Artificial Organs* 23: 769-773, 1999.
110. Takiura K, Masuzawa T, Endo S, Wakisaka Y, Tatsumi E, Taenaka Y, Takano H, Yamane T, Nishida M, Asztalos B, Konishi Y, Miyazoe Y, and Ito K.: Development of Design Methods of a Centrifugal Blood Pump with In Vitro Test, Flow Visualization, and Computational Fluid Dynamics: Result in Hemolysis Tests. *Artificial Organs* 22: 393-398, 1998.
111. Throckmorton A, Untaroiu A, Allaire PE, Wood HG, Matherne GP, Lim DS, Peeler BB, and Olsen DB.: Computational Analysis of an Axial Flow Pediatric Ventricular Assist Device. *Artificial Organs* 28: 881-891, 2004.
112. Paul R, Apel J, Klaus S, *et al.*: Shear stress related blood damage in laminar couette flow. *Artif Organs* 27: 517-529, 2003.
113. Long J: Viscoelasticity of pediatric blood and its implications for the testing of a pulsatile blood pump. *ASAIO* 51: 563-566, 2005.
114. Bludszuweit C: Three-dimensional numerical prediction of stress loading of blood particles in a centrifugal pump. *Artif Organs* 19: 590-596, 1995.
115. Song X, Throckmorton AL, Wood HG, Antaki JF, Olsen DB: Quantitative Evaluation of Blood Damage in a Centrifugal VAD by Computational Fluid Dynamics. *J. Fluids Eng.* 126: 410-418, 2004.
116. Heuser G, Opitz R: A Couette viscometer for short time shearing of blood. *Biorheology* 17: 17-24, 1980.
117. Weiss WJ: Pulsatile pediatric ventricular assist devices. *ASAIO J* 51: 540-545, 2005.
118. Song X, Throckmorton AL, Wood HG, Antaki JF, Olsen DB: Computational fluid dynamics prediction of blood damage in a centrifugal pump. *Artif Organs* 27: 938-941, 2003.

119. Throckmorton AL, Carr JP, Tahir S: Mechanical Cavopulmonary Assistance of a Patient-Specific Fontan Physiology: Numerical Simulations, Lumped Parameter Modeling, and Suction Experiments. *Artif Organs* 35: 1036-1047, 2011.

120. Throckmorton AL, Downs EA, Hazelwood JA, Monroe JO, Chopski SG: Twisted cardiovascular cages for intravascular axial flow blood pumps to support the Fontan physiology. *Int J Artif Organs* 35: 369-375, 2012.

121. Throckmorton AL, Carr JP, Moskowitz WB*, et al.*: Uniquely shaped cardiovascular stents enhance the pressure generation of intravascular blood pumps. *J Thorac Cardiovasc Surg* 144: 704-709, 2012.

122. Chopski SG, Rangus OM, Moskowitz WB, Throckmorton AL: Experimental Measurements of Energy Augmentation for Mechanical Circulatory Assistance in a Patient-Specific Fontan. *Artif Organs* In Press, 2013.

123. Budwid R: Refractive index matching methods for liquid flow investigations. *Experiments in Fluids* 17: 350-355, 1994.

124. Hopkins L, Kelly J, Wexler A, Prasad A: Particle image velocimetry measurements in complex geometries. *Experiments in Fluids* 29: 91-95, 2000.

125. Nguyen TT, Biadillah Y, Mongrain R*, et al.*: A method for matching the refractive index and kinematic viscosity of a blood analog for flow visualization in hydraulic cardiovascular models. *J Biomech Eng* 126: 529-535, 2004.

126. Dasi LP, Whitehead K, Pekkan K*, et al.*: Pulmonary hepatic flow distribution in total cavopulmonary connections: Extracardiac versus intracardiac. *J Thorac Cardiovasc Surg* 1-8, 2010.

127. Persson P-O, *Mesh Generation for Implicit Geometries*. PhD Dissertation in *Department of Mathematics*. Cambridge, Massachusetts Institute of Technology, 2004.

128. Persson P-O, Strang G: A Simple Mesh Generator in MATLAB. *SIAM Review* 46: 329-345, 2004.

129. Grigioni M, Daniele C, Del Gaudio C*, et al.*: Numerical simulation of a realistic total cavo-pulmonary connection : Effect of unbalanced pulmonary resistances on hydrodynamic performance. *Int J Artif Organs* 26: 1005-1014, 2003.

130. Grigioni M, D'Avenio G, Amodeo A, Di Donato RM: Power dissipation associated with surgical operations' hemodynamics: critical issues and application to the total cavopulmonary connection. *J Biomech* 39: 1583-1594, 2006.

131. Sharma S, Goudy S, Walker P*, et al.*: In vitro flow experiments for determination of optimal geometry of total cavopulmonary connection for surgical repair of children with functional single ventricle. *J Am Coll Cardiol* 27: 1264-1269, 1996.

132. Elder R, Tourlidakis A, Yates M, *Advances of CFD in Fluid Machinery Design*. 2003, John Wiley and Sons, Inc.: Hoboken, NJ.

133. Throckmorton AL, Untaroiu A, Allaire PE*, et al.*: Numerical design and experimental hydraulic testing of an axial flow ventricular assist device for infants and children. *ASAIO J* 53: 754-761, 2007.

134. Throckmorton AL, Lim DS, McCulloch MA*, et al.*: Computational design and experimental performance testing of an axial-flow pediatric ventricular assist device. *ASAIO J* 51: 629-635, 2005.

135. Ensley AE, Ramuzat A, Healy TM*, et al.*: Fluid mechanic assessment of the total cavopulmonary connection using magnetic resonance phase velocity mapping and digital particle image velocimetry. *Ann Biomed Eng* 28: 1172-1183, 2000.

136. Migliavacca F, Kilner PJ, Pennati G, *et al.*: Computational fluid dynamic and magnetic resonance analyses of flow distribution between the lungs after total cavopulmonary connection. *IEEE Trans Biomed Eng* 46: 393-399, 1999.

137. O' Donnell CP, Landzberg MJ: The 'failing' Fontan circulation. *Progress in Pediatric Cardiology* 16: 105-114, 2002.

138. Rogers LS, Glatz AC, Ravishankar C, *et al.*: 18 years of the Fontan operation at a single institution: results from 771 consecutive patients. *J Am Coll Cardiol* 60: 1018-1025, 2012.

139. Rychik J, Goldberg DJ, Dodds K: Long-term results and consequences of single ventricle palliation. *Prog Pediatr Cardiol* 29: 19-23, 2010.

140. Dasi LP, Pekkan K, Katajima HD, Yoganathan AP: Functional analysis of Fontan energy dissipation. *J Biomech* 41: 2246-2252, 2008.

141. Haggerty CM, Fynn-Thompson F, McElhinney DB, *et al.*: Experimental and numeric investigation of Impella pumps as cavopulmonary assistance for a failing Fontan. *J Thorac Cardiovasc Surg* 144: 563-569, 2012.

142. Sundareswaran KS, Pekkan K, Dasi LP, *et al.*: The total cavopulmonary connection resistance: a significant impact on single ventricle hemodynamics at rest and exercise. *Am J Physiol Heart Circ Physiol* 295: H2427-2435, 2008.

143. KrishnankuttyRema R, Dasi LP, Pekkan K, *et al.*: Quantitative analysis of extracardiac versus intraatrial Fontan anatomic geometries. *Ann Thorac Surg* 85: 810-817, 2008.

144. Dasi LP, Krishnankuttyrema R, Kitajima HD, *et al.*: Fontan hemodynamics: importance of pulmonary artery diameter. *J Thorac Cardiovasc Surg* 137: 560-564, 2009.

145. Scarano F: Tomographic PIV: principles and practice. *Measurement Science and Technology* 24: 012001.

146. Prasad AK, Jensen K: Scheimpflug stereocamera for particle image velocimetry. *Appl. Opt.* 34: 7092-7099, 1995.

147. Westerweel J, van Oord J, *Stereoscopic PIV measurements in a turbulent boundary layer*, in *Particle Image Velocimetry : progress toward industrial application*, Stanislas M, Kompenhans J, and Westerweel J, Editors. 1999: Kluwer, Dordrecht.

148. Hill DF, Sharp KV, Adrian RJ: Stereoscopic particle image velocimetry by streaked-particle-imaging velocimetry. *Exp Fluids* 12, 1999.

149. Elsinga GE, Scarano, F., Wieneke, B., Van Oudheusden, B. W.,: Tomographic particle image velocimetry. *Experiments in Fluids* 41: 933-947, 2006.

150. Watanabe Y, Hideshima Y, Shigematsu T, Takehara K: Application of three-dimensional hybrid stereoscopic particle image velocimetry to breaking waves. *Measurement Sci. Technol.* 17: 1456-1469, 2006.

151. Khunatorn Y, Mahalingam S, DeGroff CG, Shandas R: Influence of connection geometry and SVC-IVC flow rate ratio on flow structures within the total cavopulmonary connection: a numerical study. *J Biomech Eng* 124: 364-377, 2002.

152. Vukicevic M, Chiulli J, Conover T, *et al.*: Mock Cirulatory System of the Fontan Circulation to Study Respiration Effects on Venous Flow Behavior. *ASAIO* 59: 253-260, 2013.

Appendix A

Diethyl Phthalate-Ethanol Constitutive Equations

The following is a summary of the constitutive relationship for the diethyl phthalate-ethanol working fluid used in the particle image velocimetry experiments. The fluid model is laid out in further detail in Nguyen *et al.*[125].

The temperature dependence of the refractive index of two liquids is given by **Equations 1** and **2**, where **a** and **b** are empirical constants related to the fluid properties, the subscript numerals are with regard to the first and second liquids, respectively, n is the refractive index and **T** is the liquid temperature in *K*.

$$n_1 = a_1 + b_1 T \qquad \qquad 1.$$

$$n_2 = a_2 + b_2 T \qquad \qquad 2.$$

By combining and mixing the two liquids in quantities of p and (1-p) (0-100% of volume), a linear interpolation can be created from **Equations 1** and **2** to form **Equation 3**.

$$n_{target} = n_1 p + n_2 (1-p) = p(a_1 + b_1 T) + (1-p)(a_2 + b_2 T) \qquad 3.$$

In order to build a model for the relationship of dynamic viscosity of the final mixed fluid, an Arrhenius relation for the temperature dependence of dynamic viscosity is used to model each fluid independently in **Equations 4** and **5**. The terms are μ is the dynamic viscosity, μ_0 is the asymptotic dynamic viscosity at a very high temperature, R is the universal gas constant, d is the activation energy of the liquid, and e and f are condensed variables.

$$\ln(\mu_1) = \ln(\mu_{01}) + \frac{d_1}{RT} = e_1 + \frac{f_1}{T}, \ f_1 = -\frac{d_1}{R} \qquad 4.$$

$$\ln(\mu_2) = \ln(\mu_{02}) + \frac{d_2}{RT} = e_2 + \frac{f_2}{T}, \ f_2 = -\frac{d_2}{R} \qquad 5.$$

The final viscosity of the mixture of the two liquids is modeled as a Grunberg-Nissan model of type I in **Equations 6** and **7**. The term α is a dimensional scaling factor, the substript is the reference or accepted value for viscosity, the subscript mixture is target value for the final mixture of the two liquids, d_{12} is the activation energy of the final mixture.

$$\ln(\mu_{mixture}) = \ln(\alpha \mu_r) = (p) * \ln(\mu_1) + (1-p) * \ln(\mu_2) + (p)*(1-p)*d_{12} \quad 6.$$

$$\ln(\mu_{mixture}) = (p) * \left(e_1 + \frac{f_1}{T}\right) + (1-p) * \left(e_2 + \frac{f_2}{T}\right) + (p)*(1-p)*d_{12} \quad 7.$$

The temperature dependence for temperature can be modeled based general empirical relations. **Equations 8** and **9** display this relationship, where T_0, ρ_0 is the temperature at a known density and g, h and s are empirical constants for each of the liquids.

$$\rho_1 = \rho_{01} * \left(\frac{T_{01}}{T_1}\right)^{s_1} = g_1 * \left(\frac{h_1}{T}\right)^{s_1} \qquad\qquad 8.$$

$$\rho_2 = \rho_{02} * \left(\frac{T_{02}}{T_2}\right)^{s_2} = g_2 * \left(\frac{h_2}{T}\right)^{s_2} \qquad\qquad 9.$$

In order to determine the final density for the mixture, final mixture is assumed to follow the volume additive rule shown in **Equation 10**.

$$\rho_{mixture} = \sum_i p_i * \rho_i * \left(\frac{T_{02}}{T_2}\right)^{s_2} = g_2 * \left(\frac{h_2}{T}\right)^{s_2} \qquad\qquad 10.$$

The temperature dependence for the kinematic viscosity of the final mixture can be determined through the relationship between dynamic viscosity and density by combining expressions together to form **Equation 11**.

$$\upsilon_{mixture} = \frac{\mu_{mixture}}{\rho_{mixture}} = \frac{\exp((p)*(e_1+\frac{f_1}{T}) + (1-p)*(e_2+\frac{f_2}{T}) + (p)*(1-p)*d_{12})}{p*(g_1*(\frac{h_1}{T})^{s1}) + (1-p)*(g_2*(\frac{h_2}{T})^{s2})} \qquad 11.$$

Rearranging **Equation 3** to solve for temperature and inserting into **Equation 11** allows for the formation of the final equation in **Equation 13** for the kinematic viscosity.

$$T = \frac{\eta_{target} - a_2 - p*(a_1 - a_2)}{b_2 - p*(b_1 - b_2)} \qquad\qquad 12.$$

$$\upsilon_{mixture} = \frac{\mu_{mixture}}{\rho_{mixture}} = \frac{\exp((p)*(e_1+\frac{f_1(b_2 - p*(b_1 - b_2))}{\eta_{target} - a_2 - p*(a_1 - a_2)}) + (1-p)*(e_2+\frac{f_2(b_2 - p*(b_1 - b_2))}{\eta_{target} - a_2 - p*(a_1 - a_2)}) + (p)*(1-p)*d_{12})}{p*(g_1*(\frac{h_1(b_2 - p*(b_1 - b_2))}{\eta_{target} - a_2 - p*(a_1 - a_2)})^{s1}) + (1-p)*(g_2*(\frac{h_2(b_2 - p*(b_1 - b_2))}{\eta_{target} - a_2 - p*(a_1 - a_2)})^{s2})} \qquad 13.$$

.

In principle, the refractive index of any material can be matched between the values of 1.362 and 1.526 with this model. The model can be applied to a mixture of diethyl phthalate and ethanol

using a simple Microsoft Excel spreadsheet to apply the above equations. Predicted and actual values can be found in Table 6.3.

Table A1: Fluid Property Constants

Liquid	Refractive index (n)	Dynamic viscosity (μ) (PS)	Density (ρ) (kg/m^3)
D-limonene	1.473	.8	.85
Diethyl Phthalate	1.504	12	1.18
Methyl Salicylate	1.526	4.09	1.18
Mineral Oil	1.460	21.2	.82
Ethanol	1.362	1.17	.79
Glycerol	1.47	11.50	1.26
Water	1.333	1	1

Table A2: Fluid Empirical Constants

Liquid	a	b	E	f	g	h	s
D-limonene	1.6065	-.0005	-.57772	-218.87	.85	293	.84
Diethyl Phthalate	1.6193	-.0004	-13.765	2768.3	1.18	293	.2437
Methyl Salicylate	1.6726	-.0005	-6.6441	280.45	1.18	293	.3596
Mineral Oil	1.5748	-.0004	-12.378	2546.2	.82	293	.652
Ethanol	1.4766	-.0004	-11.737	1479.9	.79	293	.3015
Glycerol	1.4563	-.0002	-20.534	6040.2	1.26	293	.1185
Water	1.3774	-.0002	-13.115	1831.1	1	293	.17

The empirical constant d_{12} was reported by Nguyen *et al.*[125] as having a value of -1.84 J/mol for a mixture of diethyl phthalate and ethanol.

VITA

Steven G. Chopski was born April 12, 1985 in Roanoke, Virginia, USA. He attended William Byrd High School and graduated in June 2004. He entered into the Biomedical Engineering program in the School of Engineering at Virginia Commonwealth University in the fall of 2004. A Bachelors of Science degree in Biomedical Engineering was completed in May 2008. He entered into the graduate Mechanical Engineering program in the fall of 2008 and began working in the Biodevices for Biocirculatory Flow Augmentation (BioCirc) Laboratory under the guidance of Dr. Amy Throckmorton. He completed his Master of Science degree in Mechanical Engineering in May 2010. He entered into the Mechanical Engineering PhD program in fall 2010. In January 2011, he was awarded the U.S. Department of Education, GAANN fellowship. He has authored six publications.